ABSTRACT

Title of Dissertation: AEROSOL EFFECTS IN HIGH SUPERSONIC FLOWS

Antonio Giovanni Schöneich
Doctor of Philosophy, 2024

Dissertation Directed by: Professor Stuart Laurence
Department of Aerospace Engineering

The understanding of high-speed aerodynamics is becoming evermore pertinent with the growth of space tourism, continued interest in space exploration, and pursuit of advanced high-speed aircraft for both military and commercial use. For initial investigations, ground test facilities are preferred to flight tests as they are far cheaper and carry significantly less risk, although wind tunnels can only replicate a subset of the conditions experienced in actual flight. One of these conditions that has not been adequately captured in wind tunnels is the effect of particulates in the atmosphere.

Typical wind tunnels use a pure, clean gas (air, nitrogen, etc.) for testing, but this does not capture the aerosolized nature of the atmosphere, where humidity and condensation can produce a distribution of liquid droplet sizes ranging from the average rain drop of 2 mm to sub-micron diameter particles. Similarly, volcanic eruptions and ever-present wildfires result in solid particles exhibiting a variety of species and sizes that are transported to every layer of the atmosphere. At supersonic speeds, encounters with particulates have been shown to lead to detrimental effects,

such as material erosion and boundary layer transition.

Previous attempts to study this problem in wind tunnels have focused mainly on sub-micron sized solid particles, since aerosol settling time is a major limiting factor. On the other hand, most high-speed experiments involving large liquid droplet impacts have been carried out in gas guns or ballistic ranges due to the difficulty of trying to accelerate a droplet to high speeds without causing it to break up. While these facilities can be used to study impacts, the moving model means that detailed aerodynamic studies are nearly impossible, leading to a large gap in knowledge.

To perform high-speed wind tunnel testing with liquid aerosols representative of cloud-like environments (5-20 μm), a Mach-4 facility, referred to as the Multi-phase Investigations Supersonic Tunnel (MIST) has been designed and developed at the University of Maryland (capable of producing supersonic, particle-laden flows). This range of aerosol sizes makes MIST a unique facility with significant potential for expanding the state of the art in high-speed multi-phase flows. The present work discusses the design and characterization of MIST as well as two major experimental investigations carried out using this new facility. The first investigation examines the force augmentation on a free-flying sphere exposed to supersonic, particle-laden flows. Free-flight measurements are performed with five different particle size and concentration combinations. When comparing the results for particle-free flow in the same facility, the drag coefficient of the sphere was shown to be 1.75-4.5% greater for all multi-phase cases; this is significantly higher than simple estimates based on the increased momentum flux in the freestream would indicate.

In addition to force measurements, an experimental investigation into the effect of particle-laden flows on boundary-layer transition was conducted. It is important to characterize the distur-

bance environment in wind tunnels since they typically do not represent the levels in atmospheric flight and can lead to earlier onset of boundary-layer transition. In performing such measurements using a single-point Focused Laser Differential Interferometer, it was discovered that the presence of particles in the flow could significantly attenuate the acoustic disturbances generated by the wind tunnel. This finding was further reinforced when investigating the boundary-layer transition on a 5° half-angle, sharp cone using high-speed schlieren visualization. For each case presented in this work, the boundary-layer disturbance amplitudes were reduced and transition Reynolds numbers increased in the particle-laden flow cases. This was contrary to expectations, given that prior numerical studies have indicated that particles can induce early transition. These findings potentially open a path to substantially reduce freestream disturbance levels in conventional hypersonic wind tunnels.

AEROSOL EFFECTS IN HIGH SUPERSONIC FLOWS

by

Antonio Giovanni Schöneich

Dissertation submitted to the Faculty of the Graduate School of the
University of Maryland, College Park in partial fulfillment
of the requirements for the degree of
Doctor of Philosophy
2024

Advisory Committee:
Professor Stuart Laurence, Chair/Advisor
Professor Kenneth Yu
Professor Christopher Cadou
Professor Christoph Brehm
Professor Johan Larsson

Acknowledgments

I would first like to thank my advisor, Professor Stuart Laurence, for giving me the opportunity to conduct research on such an interesting topic. I would also like to thank Professors Kenneth Yu, Christopher Cadou, Christoph Brehm, and Johan Larsson for serving on my committee and providing additional support and guidance. Thank you as well to my past professors, especially Shawn Keshmiri and Ron Barrett-Gonzalez, at the University of Kansas who have encouraged me to pursue my career goals.

To my lab-mates in the High-Speed Aerodynamics and Propulsion Lab, thank you for your assistance, advice, and friendship throughout the years. I am also grateful to Bruce Rowley, Jack Touart, and Leslie Lorenz, without whom I would not have been able to build, troubleshoot, and modify the wind tunnel and its components.

I owe a lot of my success to Professor Chris Hogan, Austin Andrews, and Bernard Olson who invited me to their lab at the University of Minnesota and provided guidance and assistance with the development of the aerosol feature for the wind tunnel. The development of this feature made all of the research with MIST possible. I also had the pleasure of working with an incredible team at NASA Langley on a different project during my grad school journey; most of all, I would like to thank Greg Buck for his incredible mentorship.

A massive thank you of all of my friends who have shown their support from all over the world. To my teammates on all of my soccer teams: The Big Slow, Minion Squad, Columbia FC,

Pilar, etc., thank you for giving me the great joy of playing the beautiful game.

I would like to acknowledge financial support from the Office of Naval Research (ONR) for all the projects discussed herein, and the University of Maryland Clark Doctoral Fellowship Program.

Finally, thank you to my family. To my mother and father, it is impossible to express my gratitude for the lifetime of love, encouragement, and support. To my brother and sister, thank you for the frequent visits and phone calls that have kept us close. To my aunt, uncles, cousins, and grandmothers, thank you for all of your support from overseas and the countless care packages of Italian and German food. Thank you. Grazie. Dankeschön.

Table of Contents

Bibliography 171

List of Tables

List of Figures

Nomenclature

Acronyms

AEDC	Arnold Engineering Development Center
APS	Aerodynamic Particle Sizer
CFD	Computational Fluid DYnamics
DEHS	Di-Ethyl-Hexyl-Sebacat
FLDI	Focused Laser Differential Interferometry
MDG	Monodispersed Aerosol Generator
MIST	Multi-phase Investigations Supersonic Tunnel
PIV	Particle Image Velocimetry
PSD	Power Spectral Density
RMS	Root Mean Square
RTD	Resistance Temperature Detector

Variables

a	Acceleration
A	Area
A^*	Sonic throat area
C	Concentration
C_D	Drag coefficient
d_0	Initial diameter
d_{aero}	Aerodynamic particle diameter
d_{cro}	Cross-sectional diameter
d_d	Droplet diameter
d_p	Particle diameter
f	Frequency
F_D	Drag force
k	Wavenumber
m	Mass
M	Mach number
M_{CT}	Post-expansion charge tube Mach number
m_p	Particle mass
Oh	Ohnesorge number
p	Pressure
p_{CT}	Post-expansion charge tube pressure
p_{fill}	Charge tube fill pressure

Q	Liquid flow rate
r	Radius
Re	Reynolds number
Re_∞	Freestream Reynolds number
s	Standard deviation
$S(a)$	Standard error in the acceleration
Stk	Stokes number
t	Time
T	Temperature
T_{CT}	Post-expansion charge tube temperature
T_{fill}	Charge tube fill temperature
u	Velocity in the x-axis direction
V	Volume
w	Relative particle velocity
We	Weber number
x	Streamwise coordinate
y	Vertical coordinate
δ	Boundary layer thickness
γ	Specific heat ratio
ϵ	Density ratio
μ	Dynamic viscosity
ρ_{eff}	Effective density
ρ_g	Gas density
ρ_p	Particle density
σ	Surface tension
τ	Nondimensional time
τ_d	Particle dynamic relaxation time
ω	Circular frequency

Chapter 1: Introduction

1.1 Motivation

Aerosols, both solid and liquid, are present throughout the atmosphere and can cause significant adverse effects to high-speed projectiles and aircraft. These aerosols come from a variety of sources and are distributed throughout the atmosphere via several natural processes as demonstrated in Fig. 1.1. Their distribution and size have been studied for over a century, and continues to this day as the atmosphere is ever-changing. Recent work by Turco [12], Deshler et al. [13,14], Renard et al. [15,16], and Habeck et al. [17] provided aerosol measurements made using weather balloons over specific locations showing particles spanning a vast range of diameters and concentrations throughout the atmosphere. The presence of aerosols in the upper atmosphere has increased in recent years for a variety of reasons [1], and with the increase of strong and erratic weather events caused by global warming, the chance of a high-speed vehicle encountering potentially damaging conditions will become increasingl likely and less predictable.

At lower altitudes, the average rain drop (1-2 mm diameter) possesses a relative kinetic energy on the order of 0.5-4 J with respect to a Mach-4 vehicle or projectile. At such high Mach numbers, because of the short transit time from the shock front to the body of the vehicle, rain drops have been shown to survive the physical forces they experience in this region and impact the surface, although not in their initial spherical shape [18]. Within clouds, the incident aerosol

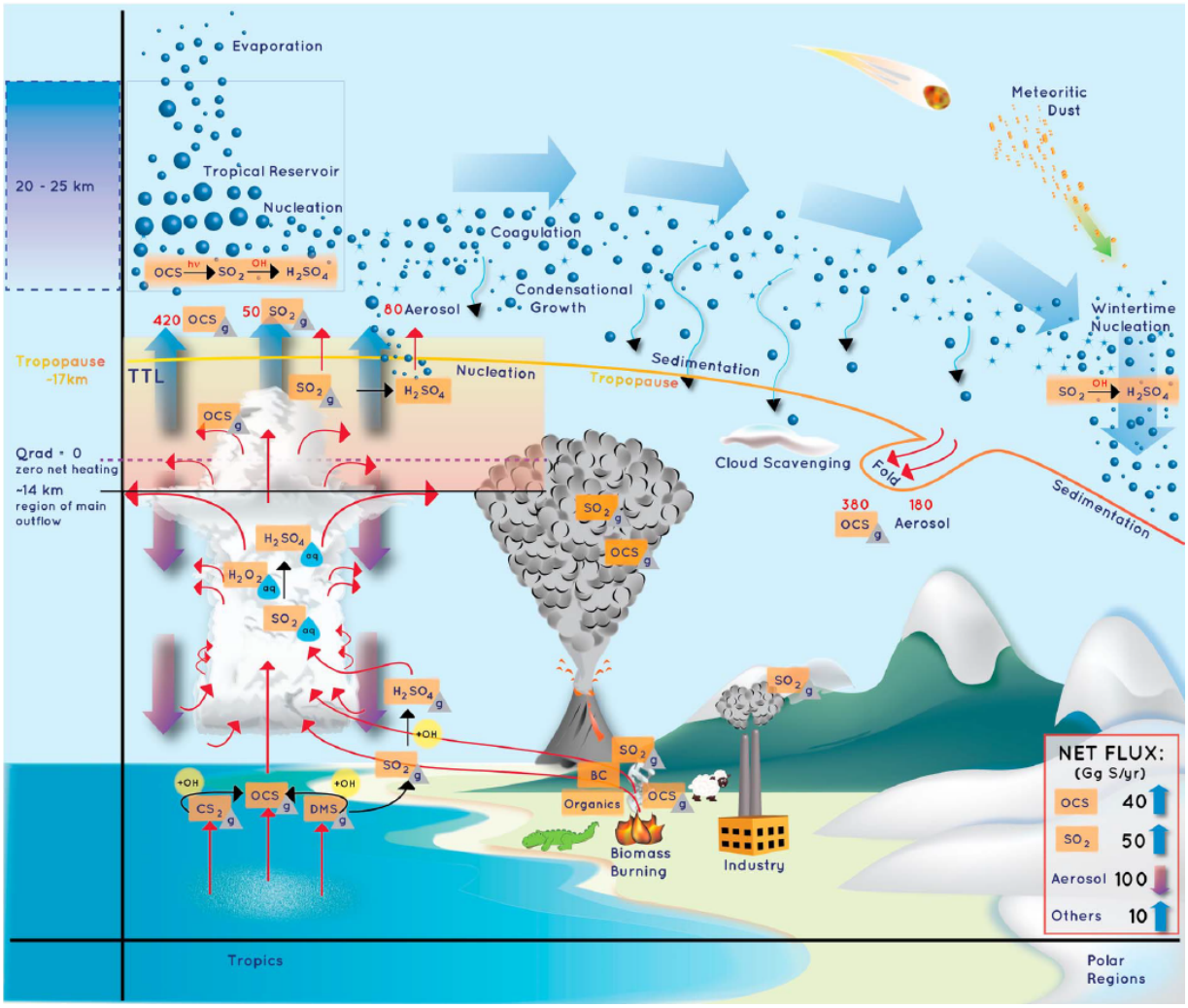

Figure 1.1: Schematic of the relevant processes that govern the stratospheric aerosol life cycle and distribution [1].

kinetic energy (scaling with the cube of the aerosol diameter and square of the vehicle flight speed) decreases mostly due to the decrease in particle size (2-30 μm diameter [19]), but the possibility of detrimental effects remains. Smaller particles have been shown to cause disturbances in the boundary layer that induce transition ahead of where natural transition might occur [4]. Even at typical cruise altitudes for hypersonic vehicles (above 24 km), in situ measurements have revealed particulates with sizes ranging from 0.2 to 50 μm [17]. Impact simulations for these particles with their respective concentration distributions identified the 6–8 μm range as the main contributors for the transfer of energy [20]. High-speed impacts can also result in surface erosion [21], which could in turn also affect boundary-layer transition by altering the surface roughness.

Ground testing in wind-tunnel facilities is fundamental to the pursuit of advancing high-speed flight capabilities. It is a relatively affordable and low-risk method for investigating aerodynamic phenomena by reproducing aspects of a real flight environment. Since a major limitation to ground testing is the inability to completely capture all characteristics of the true flight conditions, most wind tunnels are tailored to model a desired subset of them. For this work, a new wind tunnel (the Multi-phase Investigations Supersonic Tunnel - MIST) was designed, developed, and commissioned for the purpose of studying the effect of multi-phase flows on flight geometries at Mach 4 in the High-Speed Aerodynamics and Propulsion Lab (HAPL) at the University of Maryland College Park. While this wind tunnel provides the ability to study multi-phase flows, it is a cold tunnel and therefore does not replicate the flow enthalpies experienced during high-speed atmospheric flight.

Wind-tunnel facilities to study the effects of multi-phase flows are not new; however, the dominant focus has previously been on solid-gas two-phase flows. In the early 1970s, a program

established by the Air Force Space and Missile Systems Organization led to both the modification of the Boeing Hypersonic Wind Tunnel to provide dust-laden flows and the development of the Arnold Engineering Development Center (AEDC) dust erosion test facility; results from both facilities showed a significant increase in stagnation-point heating as well as boundary-layer separation caused by the pressure communication from the wakes of rebounding particles [22]. Around the same time, the Lockheed Missiles and Space Company developed a reentry weather erosion simulator that essentially used a rocket exhaust to accelerate particle clouds (cloud diameter of about 2 inches) to around 8 kft/s [23]. Solid-gas two-phase flow capabilities were also demonstrated in the Zhukovsky Central Aerohydrodynamic Institute UT-1 wind tunnel, with results of particle impacts on a blunt body showing a nearly three-fold increase of the heat flux at the stagnation point [24].

Most experiments examining liquid-gas multi-phase flows with sufficiently large aerosols to produce surface impacts are conducted with light gas guns or on ballistic ranges such as the AEDC Hyperballistic Range G [25]. These types of facilities allow for a larger range of aerosol sizes but significantly limit the test time and make it very difficult to study both particle-induced boundary-layer transition, due to the restrictions with placement and operation of diagnostic systems, and erosion. Producing liquid-aerosolized flow in high-speed wind tunnels is not a new technique, as this is often done with the goal of then analyzing flow features using Particle Image Velocimetry (PIV). However, PIV uses very small particles with small Stokes numbers that are designed to follow the fluid and not impact surfaces and is independent of phase as both liquid or solid particles are commonly used. Due to the lack of experimental data representing supersonic flight through cloud-like environments, further investigations are needed to better understand the flow physics (forces, heating, boundary layer transition, etc.) and provide data sets for computa-

tional validation. This has motivated the development of the MIST facility to enable multi-phase flow investigation of liquid and solid aerosols in the range of 0.8-20 μm accelerated to Mach 4, representative of the particle sizes typically found in clouds.

1.2 Aerodynamic Effects of Bodies in Multi-phase Flows

Attempts to understand how weather encounters can affect the flight of an aircraft, specifically rain, date back to 1941 when Rhode first studied this phenomena at the NACA Laboratories at Langley Field [26]. Subsequent theoretical work then led to the development of an experimental facility to study this problem on a large scale [27]. While these investigations showed a decrease in aerodynamic performance, at low flight speeds, the adverse effects of flying through rain were determined to be inconsequential. Several studies in the 1960s and 1970s looked at the impact of rain under high-speed flight conditions [28], where weather encounters can have more sever consequences. However, investigations into high-speed rain encounters took a lengthy break in interest before the problem was revisited by Moylan in 2010 [29].

In the meantime, the desire to understand how multi-phase flows affects aerodynamic performance did not die, but simply the phase combination of interest changed to that of solid particles suspended in a gas. The 1970s saw a series of experiments investigating the effects of dusty hypersonic environments, leading to the finding of a noticeably higher stagnation region heat flux caused by such flows [22, 30, 31]. With growing interest in extraterrestrial exploration, studies of this kind continued with the turn of the century, including those by Vasilevskii et al., producing similar results [24, 32]. With complex geometries and flow environments, which make it difficult to obtain experimental data, numerical models are becoming evermore necessary and

a significant amount of work has been directed towards multi-phase flows recently for both solid and liquid particles [33–38].

Although the advancements in this area of study have been significant, there has been a lack of data on how fundamental aerodynamic properties are affected by the particle-laden flows. This is both necessary for the understanding of how multi-phase flows affect lift and drag of high-speed vehicles, as well as providing necessary experimental data for validation of numerical results. Chapter 3 covers the experimental setup and results pertaining to the aerodynamic measurements of free-flying spheres in high-supersonic, particle-laden flows.

1.3 Tunnel Noise in Ground Test Facilities

Laminar to turbulent boundary layer transition has drastic effects on the heat transfer, skin friction, and flow separation on a vehicle. The accurate prediction of boundary layer transition is highly dependent on the facility used in the measurements since each facility is unique in the details of its construction, operation, and testing envelope. High-speed wind tunnels in general have a much stronger noise environment compared to that of the atmosphere due to the acoustic noise radiated from the turbulent boundary layers on the nozzle walls [2]. For any new facility, it is therefore important to characterize the disturbances in the free stream so that correct scaling can be utilized to compare to atmospheric flight, computational results, and measurements in other wind tunnels.

Hot wire anemometeres were used by Kovasznay [39] in 1953 to show that the fluctuations in a viscous compressible flow can be decomposed into distinct modes: vorticity, entropy, and sound-wave. Morkovin [40] further investigated the importance of acoustic fluctuations radiating

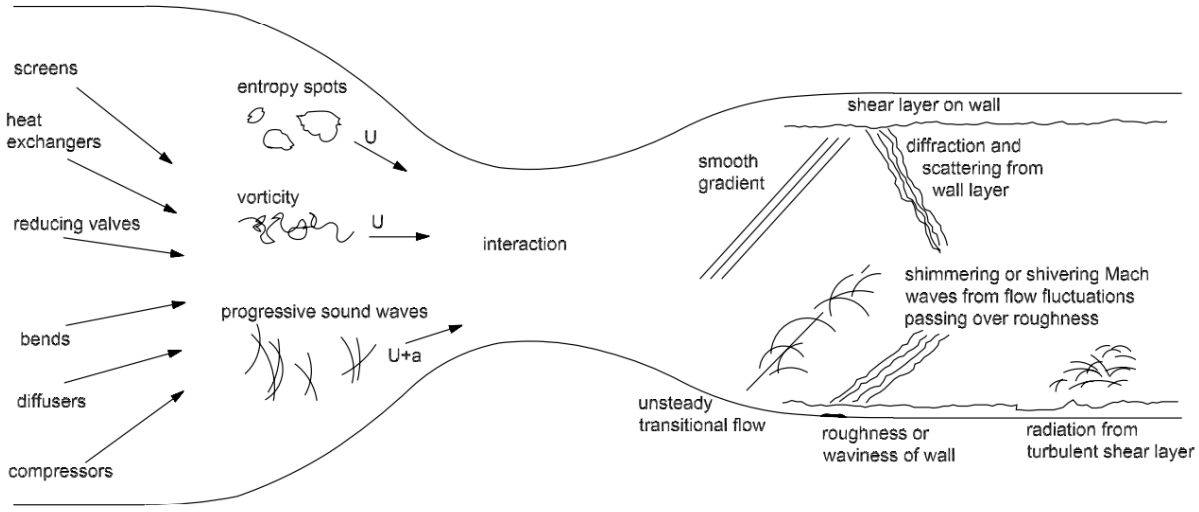

Figure 1.2: Free-stream disturbances in supersonic wind tunnels [2].

from the turbulent boundary layer as well as those caused by shivering Mach waves. These shivering Mach waves form at flaws in the nozzle contour, and oscillate as turbulent structures pass over the flaws - making them unique to the construction of each wind tunnel. Laufer [41] used hot wires to directly measure the noise radiated from the nozzle-wall boundary layer and found a relationship between the rms fluctuation in mass flow normalized by the mean and the free-stream Mach number to the fourth power. Fig. 1.2 presents schematic taken from [2] that depicts the sources for tunnel noise in high speed wind tunnels.

More recently, nonintrusive techniques such as Focused Laser Differential Interferometry (FLDI) have been employed to measure the noise environments given their ability to not disturb the flow and measure at a much higher frequency range than other physical sensors. FLDI was originally developed by Smeets and George in the 1970s [42–46] and adds lenses to the traditional Laser Differential Interferometry (LDI). The focusing effect restricts the sensitivity of the system to a very small region close to the focus, eliminating much of the noise caused by disturbances along the line of sight.

Applying this technique to high-speed facilities laid dormant until Parziale et al. [47] used it to measure the density perturbations in the T5 reflected-shock tunnel. Since then, there have been a series of improvements made to FLDI in both the physical apparatus and analytical methods. Recent work has shown the success of multi-point FLDI systems for measuring the disturbances as well as their convective velocities [48–51]. Advancements in the interpretation of the FLDI signal (see [49, 52–54]) has made this diagnostic technique extremely powerful when it comes to measuring density fluctuations in an environment where the signal amplitudes may be quite low and disturbances along the line of sight are present. While the capabilities of FLDI are extensive, this work aims to use it in its fundamental form as a means of measuring the density fluctuations in the free-stream and minimizing disturbances along the rest of the optical line of sight. Chapter 4 presents a qualitative characterization of the acoustic disturbances generated by MIST.

1.4 Attenuation of Acoustic Disturbances

The presence of entropic, vortical, and acoustic perturbations in a wind tunnel has led to efforts to develop ”quieter” wind tunnels. It has been understood that, in high-speed facilities, the dominant mechanism for generating tunnel noise are the acoustic disturbances produced in the nozzle. Therefore, methods for attenuating these disturbances were explored by several researchers dating back to the 1960s. One that has been utilized successfully is that of using mechanical means to keep the nozzle boundary layer laminar. Schneider [2] provides an extensive review on how quiet tunnels came to be, using highly polished, precision-machined nozzles that incorporate a boundary-layer suction mechanism to keep the nozzle boundary layer laminar. A major deterrent in this method though is cost, as the first hypersonic quiet tunnel at Purdue

University was reported to have incurred more than $3 million in external support.

Another mechanism for attenuating wind tunnel noise is that of using the molecular relaxation process from gas mixtures. These methods were successfully demonstrated in the T5 shock tunnel at the California Institute of Technology [55–57]. Gillespie expanded on this work by investigating the effect of the vibrational nonequilibrium processes on acoustic radiation from a compressible turbulent boundary layer [58]. By comparing the experimental results to a numerical model, it was determined that a He/CO_2 mixture can result in a acoustic disturbance amplitude reduction of 15-30%.

Another method that has shown the ability to reduce the amplitude of acoustic waves is that of the particle relaxation process, the study of which dates back over a century. In 1910, Sewell [59] published a study on the extinction of sound caused by the suspension of solid particles in a gas. Knudsen et al. [60] expanded this work on sound attenuation in multi-phase flows by studying both fog and smoke and considered particle relaxation as a cause for this behavior. Further work by Temkin and Dobbins [61] confirmed that particulate-relaxation theory predicts attenuation and dispersion of sound waves by small, heavy particles. In addition to the particle-relaxation mechanism, the vaporization process was also identified as a means of reducing acoustic disturbances [62]. More recently, Kalikmanov and Hagmeijer [63] produced a model that showed that, at higher frequencies, the attenuation coefficient diverges as $\sqrt{\omega}$ where ω is the circular acoustic wave frequency. Over the past few decades, this process has been gaining significant attention as a means of reducing the jet noise produced by rockets [64–69]. For this application, however, particles were not introduced into the nozzle, rather a water jet was injected into the developed supersonic jet. While these studies show how a multi-phase environment can attenuate acoustic disturbances, to the author's knowledge they have not been applied

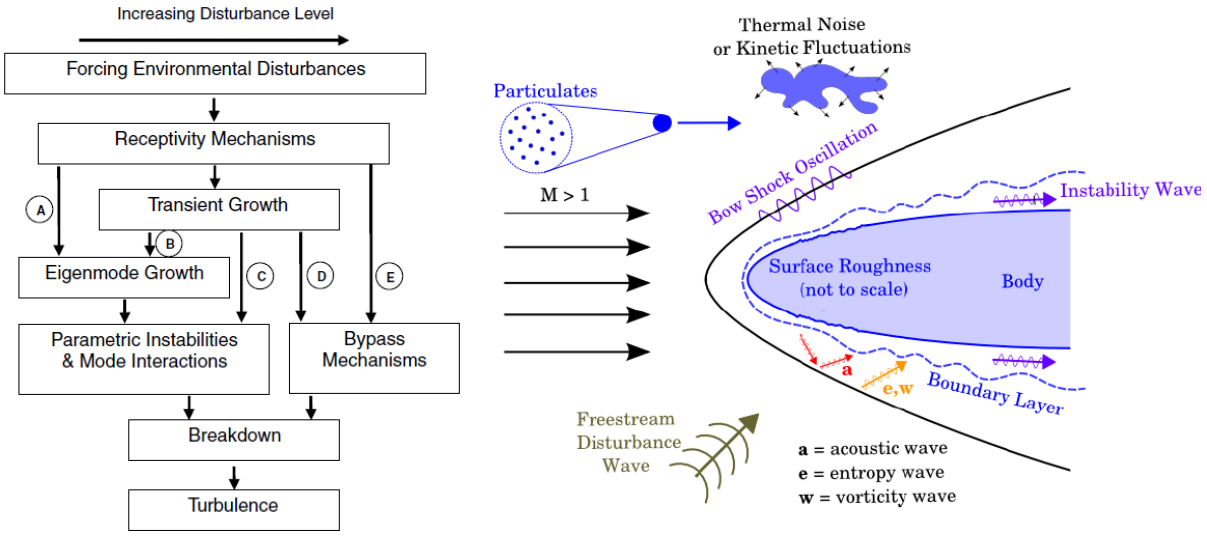

(a) (b)

Figure 1.3: Schematics depicting (a) the transition pathways [3] and (b) the various boundary layer disturbance mechanisms [4].

to high-speed wind tunnels as a mechanism to make them "quieter."

1.5 Boundary Layer Transition

In high-supersonic and hypersonic boundary layers, the transition to turbulence can result in significant increases in pressure and thermal loads [70], which has led to a considerable amount of work dedicated to understanding this problem. However, the primary difficulty remains: a large uncertainty in the prediction of the transition location. Since this leads to the over-design of vehicles, such as structural components and thermal protection systems, identifying the location with greater precision is highly valuable.

The processes that cause laminar to turbulent transition have been studied for over a century, dating back to the late 1800s with the work of Lord Rayleigh and Osborne Reynolds. Well documented descriptions of these processes can be found in works by Morkovin [71] and Reshotko [72, 73] with the summary of the pathways presented in Fig. 1.3a. The transition pro-

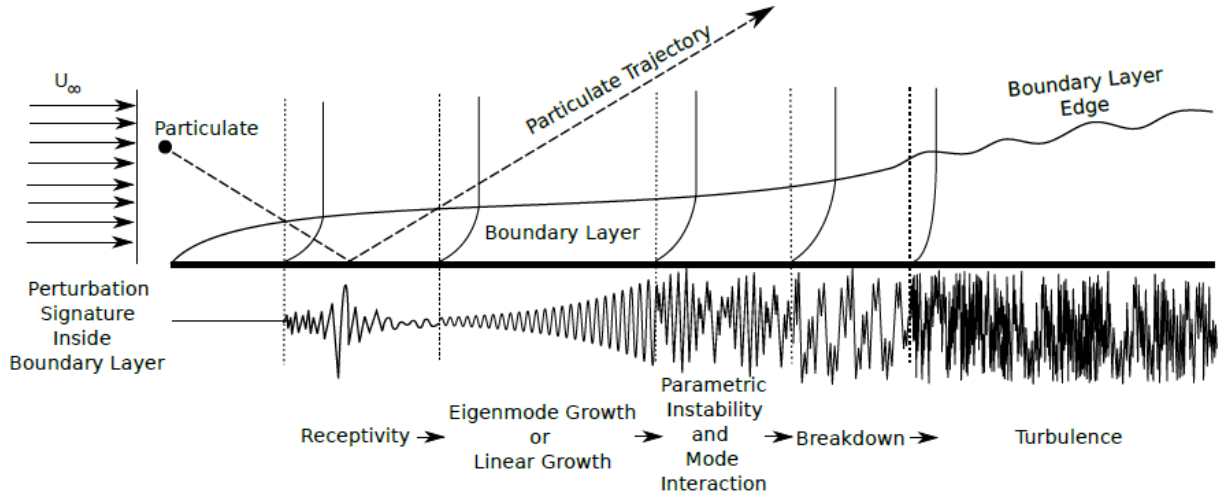

Figure 1.4: Boundary layer transition process initiated by a particle induced disturbance [5].

cess begins when an external disturbance carries the necessary amplitude to force a growth in the unstable waves. There are a multitude of sources for these disturbances (depicted in Fig. 1.3b), however, for the purpose of this work, a focus will be placed on the freestream acoustic waves and particulates. While the elements along the transition pathway caused by acoustic waves have been a major field of interest for many years, the study of the boundary layer receptivity and transition process from particulate disturbances has gained more traction within the past few decades.

Bushnell [74] notes the many ways in which particles can disturb the boundary layer: (1) inducing roughness by either sticking or damaging the surface through impacts, (2) vortex/vorticity shedding while the particle is immersed in or external to the boundary layer, (3) particle rotation and consequent fluid motions, (4) production of reverse shocklets within the vehicle flow field, and (5) rebound off the vehicle surface and subsequent interaction with the bow shock causing formation of embedded shear layers and jets. The entire transition process caused by an impinging particle is well depicted in Fig. 1.4 where the perturbation signal follows the steps from path

A in Fig. 1.3a. Identifying the lack in knowledge for this problem, Fedorov et al. [75,76] were the first to numerically investigate the boundary layer receptivity to particle-induced disturbances in high-speed flows. Others have followed suit with an agreement that particle-laden flows induce boundary layer transition [4, 5, 77, 78]. Fundamental to understanding the boundary layer transition process is the identification of the dominant instability mechanism for the given problem. For the work presented, linear stability theory [79] recognizes both the first viscous (Tollmien-Schlichting) and second inviscid (Mack) modes as the dominant instability mechanisms in the Mach 3.7-4 range. However, experiments by Jones [10] reveal the first mode to be dominant for the model and wind tunnel used.

1.6 Scope of Current Work

This study seeks to investigate the effect that multi-phase flow has on high-speed aerodynamics. In particular, the goal is to measure the drag increase experienced by a canonical geometry (sphere) when exposed to particle-laden flow, and experimentally investigate how particle-laden flow changes the noise environment of the wind tunnel as well as its influence on the boundary-layer transition on a sharp cone. The desired particle size range in this study is meant to simulate a flight path through clouds. However, since there is no such faciity for wich to conduct this work, one had to be built.

The first part of this study explores the design and characterization of the MIST facility at the University of Maryland. As with any new wind tunnel, the flow characteristics need to be established in order to accurately understand the results from any experimental campaign performed in it. In addition to these properties, the characterization of the particle size, con-

centration, and distribution in the flow are presented as they are fundamental to the following studies. Next, MIST is used to study how the drag coefficient of a sphere changes when it is exposed to various particle-laden flows. The spheres are allowed to fly freely through the test section from a release mechanism, and are optically tracked using a bi-telecentric visualization system. An edge-tracking technique is employed to ascertain the acceleration of the sphere and the flow conditions from the flow characterization study are used to calculate the drag coefficient.

Finally, the effect of multi-phase flow on tunnel noise amplitudes and boundary-layer transition are evaluated. A single-point FLDI system is used to measure the free-stream density fluctuations in MIST and compare them between the particle-laden and particle-free cases. A Schlieren visualization system is then set up to study the boundary-layer transition on a sharp, 5° half-angle cone. The conclusions and contributions of the work are then presented, along with several recommendations for facility improvements and future research.

Chapter 2: Development of a Supersonic Ludwieg-Tube Facility for Investigating High-Speed Multi-Phase Flows

2.1 Facility

2.1.1 Wind Tunnel

MIST is a conventional Ludwieg tube with a piston-driven fast-acting valve to initiate and terminate the flow (see Fig. 2.1 for a schematic of the facility). The Ludwieg-tube concept was chosen since it is an economic option that allows for significantly longer test times than a shock tunnel [80]. Furthermore, with the fast-acting valve, the time that a test article is exposed to the multi-phase flow can be precisely controlled (important for studies involving damage from aerosol impacts). The charge tube measures 851 cm long and has an inner diameter of 20.3 cm. The Mach-4 converging-diverging nozzle was designed for a pure nitrogen test gas using a Method of Characteristics approach and validated with the VULCAN-CFD solver [81]. Computed Mach-number contours within the nozzle are shown in Fig. 2.2. The nozzle was optimized for a 10 bar charge tube pressure, measures 96 cm in total length, with the converging section accounting for 11.4 cm, and has a throat and exit diameter of 6 cm and 20.8 cm, respectively. The free-jet test section has a diameter of 30.5 cm with four 15.2 cm diameter NBK7 windows oriented at 90° intervals.

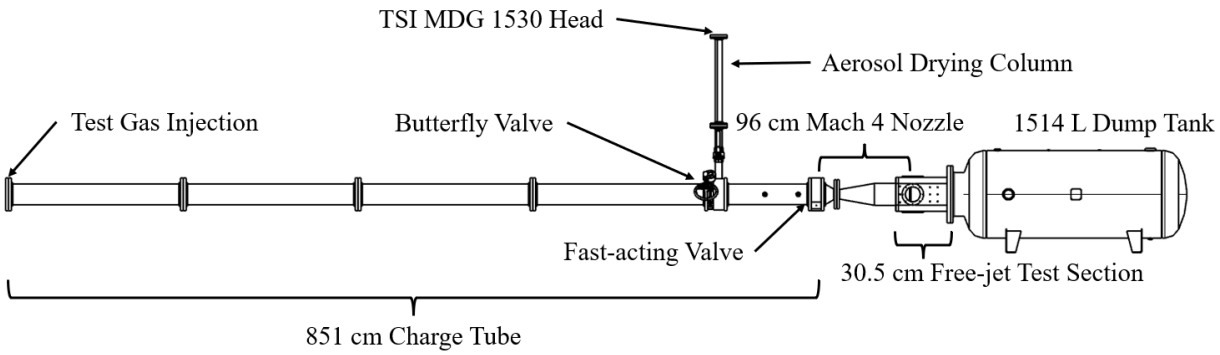

Figure 2.1: Schematic of MIST.

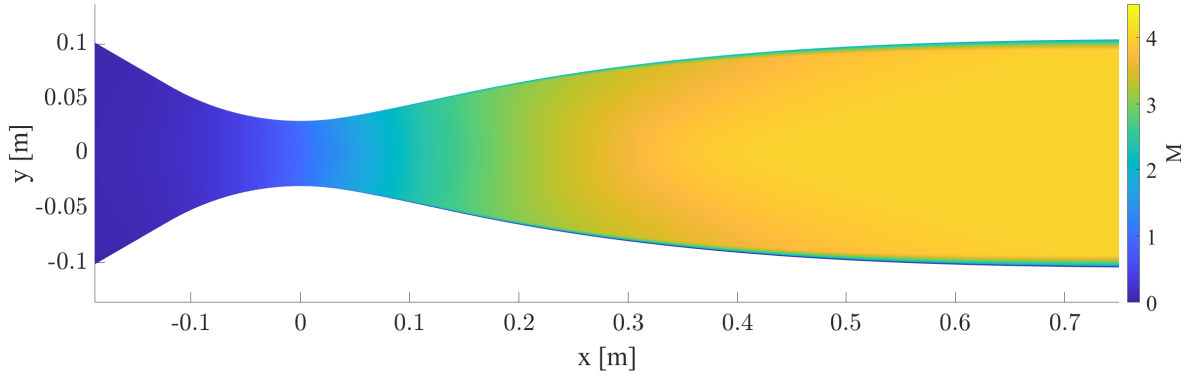

Figure 2.2: Mach number profile in the MIST nozzle generated using Vulcan.

When operating in a clean-gas mode, the test gas is injected through the upstream flange. In the multi-phase mode, a butterfly valve, placed 124.4 cm upstream of the nozzle throat, is used to divide the charge tube into two sections. The upstream section, filled with pure test gas, is filled through the upstream flange, whereas the downstream section has inserts in the flange to allow for both aerosol injection and pure test gas injection. This divided charge tube was introduced to shorten the fill times, since the aerosol generator would take hours to seed the entire charge tube to the range of desired concentrations. Instead, only the downstream section of the charge tube, which accounts for the flow during the steady test period, is seeded with the aerosol, significantly decreasing the turnaround time between tests. Both the upstream and downstream sections of the charge tube are filled to the same pressure, such that when the butterfly valve is opened immediately before the tunnel is started, there is minimal bulk transport of the aerosols into the upstream gas slug before the activation of the fast-acting valve.

An Omega® Pt100 wire wound resistance temperature detector (RTD) is placed on the charge tube 87.8 cm upstream of the nozzle throat, and a Kulite® XTEL-190S-250A piezoresistive pressure transducer is placed 118.7 cm upstream of the nozzle throat; these provide measurements of the charge tube temperature and pressure, respectively, as well as allow tracking of the unsteady expansion wave that initiates the flow. Tracking the pressure in the charge tube is essential since the total pressure during the test time will not be the same as the initial fill pressure, the unsteady expansion leading to a decrease in total pressure. However, this pressure loss is typically minimal and the charge tube pressure and temperature during the steady test time can

be calculated by applying the method of characteristics and isentropic flow relations as

$$\frac{p_{CT}}{p_{fill}} = \left(1 + \frac{\gamma - 1}{2} M_{CT}\right)^{-\frac{2\gamma}{\gamma-1}} \tag{2.1}$$

$$\frac{T_{CT}}{T_{fill}} = \left(1 + \frac{\gamma - 1}{2} M_{CT}\right)^{-2} \quad , \tag{2.2}$$

where M_{CT} is the post expansion flow Mach number in the charge tube. The Kulite® sensor in the charge tube allows for the calculation of M_{CT} through Eqn. 2.1, however, M_{CT} can also be calculated using the subsonic solution to the Area-Mach number relation:

$$\frac{A}{A^*} = \frac{1}{M^2}\left[\frac{2}{\gamma + 1}\left(1 + \frac{\gamma - 1}{2} M^2\right)\right]^{\frac{\gamma+1}{\gamma-1}} \quad . \tag{2.3}$$

The total pressure in the charge tube during the steady test time is then calculated using the isentropic relations,

$$\frac{p_0}{p} = \left(1 + \frac{\gamma - 1}{2} M^2\right)^{\frac{\gamma}{\gamma-1}} \quad , \tag{2.4}$$

where M_{CT} replaces M for the charge tube calculations. When the tunnel is started, unsteady expansion waves progress from the valve location to the upstream end of the charge tube, and reflect back towards the nozzle, as shown in Fig. 2.3. In theory, this could lead to a series of consecutive test periods as the expansion wave reflects back and forth between the nozzle throat and end wall; however, in practice, the volume of the MIST dump tank (and lack of diffuser) limits the usable test time to just one steady period before the tunnel unstarts.

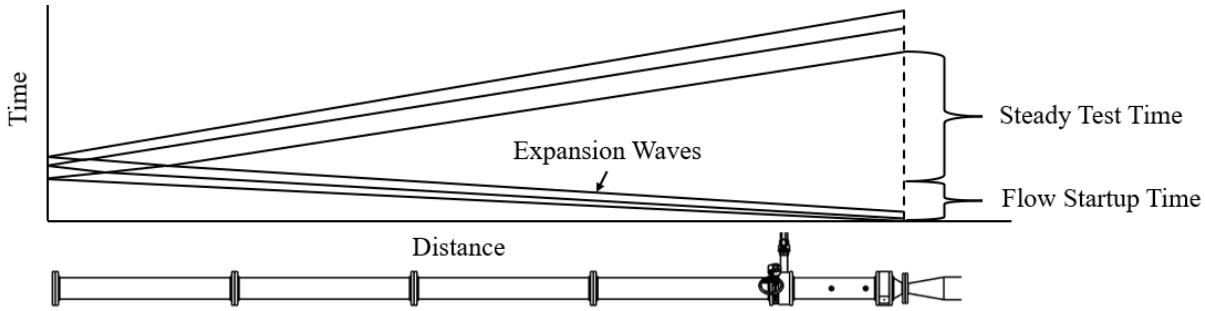

Figure 2.3: Sketch of the operation of a Ludwieg tube wind tunnel.

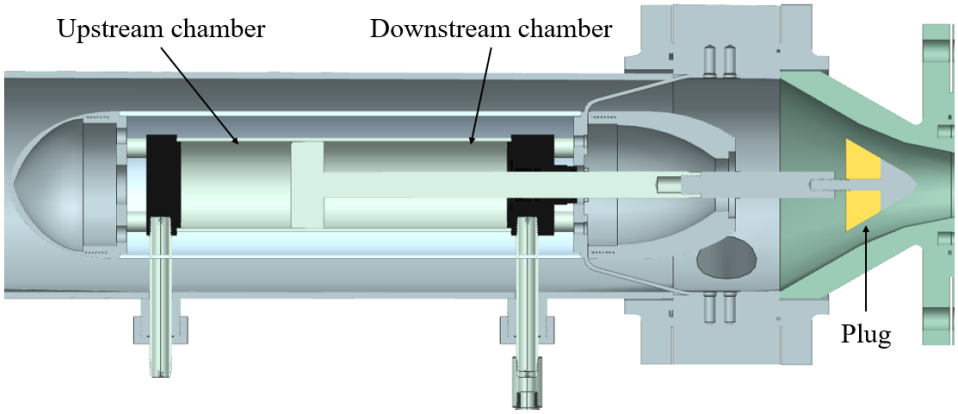

Figure 2.4: CAD rendering of the fast-acting plug valve.

2.1.2 Fast-acting Valve

The flow in MIST is initiated by pneumatically actuating the plug valve shown in Fig. 2.4. A separate high-pressure reservoir is used to provide the air to the pneumatic cylinder. When the tunnel is triggered, solenoid valves connecting the high-pressure reservoir to the downstream end of the cylinder and the upstream end of the cylinder to the ambient room open simultaneously, allowing for piston to be driven upstream and opening the plug valve. The trigger signal then passes through an adjustable time delay before triggering solenoid valves connecting the high-pressure reservoir to the upstream end of the cylinder and the downstream end of the cylinder to the ambient room, thus reversing the start-up process and closing the plug valve.

2.1.3 Aerosol Generators

MIST is currently configured for two aerosol generators, although only one will be used in the present work, that together can generate a range of liquid aerosols from 0.8–100 μm. The TSI 1530 monodispersed aerosol generator (MDG) forms droplets in the range of 0.8–93 μm when operated with water, with a flow rate in the range of 4–25 L/minute. The Topas LDG 244 can generate droplets in the range of 50–100 μm and a particle mass flow of 50–2000 gallons/hour ($\sim$ 3–126 L/minute). In the present application, both produce droplets of Di-Ethyl-Hexyl-Sebacat (DEHS), which was chosen since it is a non-toxic oil with a similar density to water (the properties of both DEHS and water are provided in Tab. 2.1). In order to produce DEHS droplets in the MDG 1530, the viscosity of the solution needs to be reduced; this is done by dissolving DEHS to a 5% solution by volume in methanol. Once the droplets are produced, the methanol evaporates off, leaving a smaller, pure DEHS droplet behind. To remove the methanol vapor from the wind tunnel, as shown in Fig. 2.5, the droplet traverses an activated-alumina-lined tube before passing into the wind-tunnel charge tube, ensuring that the methanol vapor is adsorbed by the alumina, as shown in Fig. 2.5. Within the charge tube, small, 3.2 mm diameter perforated tubes line the top and bottom of the tunnel, creating a light updraft by injecting gas through the lower tube and pulling to a vacuum through the upper tube. This updraft is intended to prevent particles from settling to the bottom of the chamber since seeding to the desired particle densities (50-150 particles/cm^3 in the free stream) requires continuous operation of the MDG for 15 to 60 minutes, much longer than the calculated settling time for the particles(which ranges from 0.5 to 8, minutes depending on the particle size). A limitation of the MDG is its operating pressure, which cannot operate at pressures much higher than 1 bar, making it difficult to operate MIST in

Table 2.1: Properties of DEHS and water.

liquid	σ (N/m)	ρ (kg/m^3)	μ (Pa s)
DEHS	3.2×10^{-2}	912	23×10^{-3}
Water	7.2×10^{-2}	997	8.9×10^{-4}

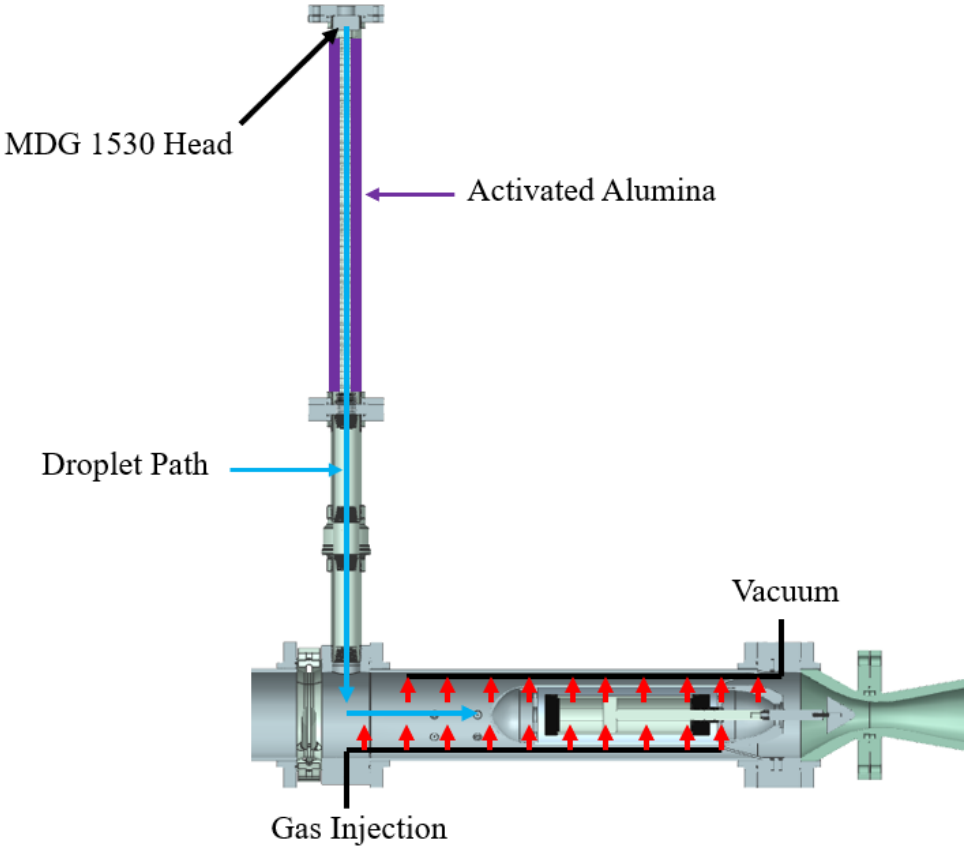

Figure 2.5: Diagram of MDG 1530 droplet generation in MIST.

the multi-phase configuration at much higher pressures.

The droplet size produced by the MDG 1530 with the 5% DEHS solution was characterized using a TSI aerodynamic particle sizer (APS) at the University of Minnesota. The APS has 1024 aerodynamic diameter size bins on a logarithmic scale from 0.523 - 19.81 μm. A particle density correction for the APS is applied using the methods of Wang et al. [82]. The geometric diameter of the particle is related to the aerodynamic diameter by $d_{\text{aero}} = \sqrt{\rho_{\text{p}}}\, d_{\text{p}}$, where here the density is in units of g/cm^3. Figure 2.6 shows the results for seven settings that were found

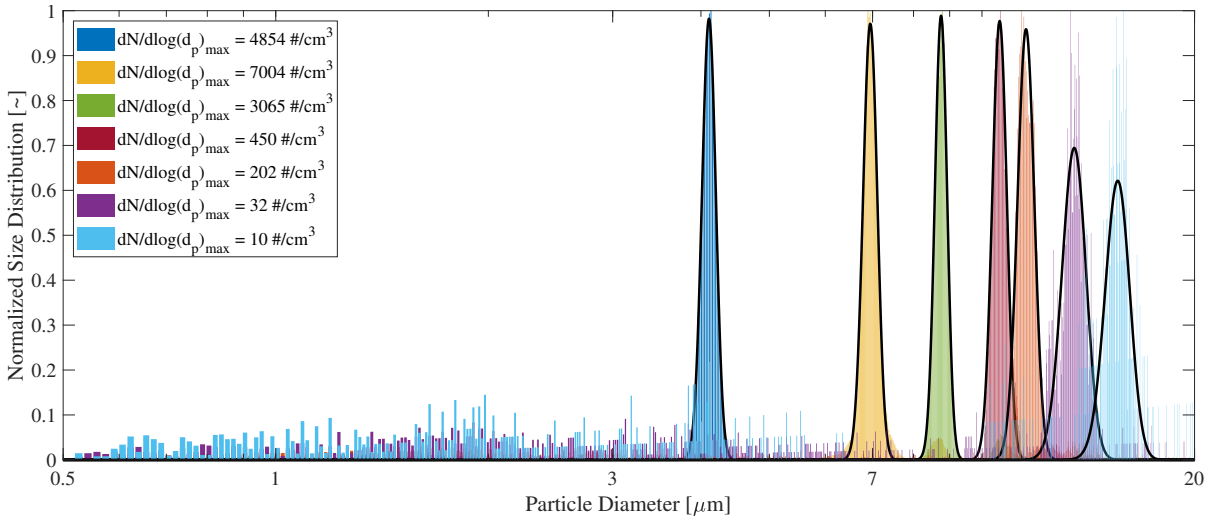

Figure 2.6: Resulting geometric particle size distribution by number count normalized by the maximum bin value for each case with a gaussian curve fitted to each data set for the pure DEHS oil droplets after the evaporation of the methanol.

to produce monodisperse droplets. Each data set is normalized by the bin with the maximum number concentration. While the number concentration is an important feature, the value of interest is the mean droplet diameter in each data set and the monodispersity (i.e. a narrow and tall peak with negligible measured diameters outside of this peak). As can be seen in the figure, each data set produces the desired shapes for monodispersity where the majority of measured particles fall inside a very narrow band of particle diameters. The small-diameter particle noise associated with the larger particle measurements (purple and light blue) but only because of the normalization process; a mass weighted distribution would essentially eliminate the relevance of those particles for the experiments. A gaussian curve is fitted to each data set and the mean and standard deviation of the geometric droplet diameters in increasing order are as follows: d_{p} = 4.11±0.13, 6.95±0.23, 8.75±0.25, 10.6±0.35, 11.6±0.45, 13.5±0.75, 15.6±0.88 μm. The TSI MDG 1530 settings used to generate these particle diameters are presented in Tab. 2.2.

Table 2.2: TSI MDG 1530 settings for production of DEHS droplets.

d_p (μm)	Q (mL/h)	$p_{\text{focusing flow}}$ (psi)	f (kHz)
4.11±0.13	8	1	35
6.95±0.23	2	1	120
8.75±0.25	4	1	122.5
10.6±0.35	4	0.8	62.5
11.6±0.45	8	0.8	90
13.5±0.75	12	0.8	70
15.6±0.88	18	0.8	71

2.2 MIST Flow Characterization in Clean Flow

2.2.1 Experimental Apparatus

A pitot rake, instrumented with Kulite® XCE-062, XCQ-062, and XCS-062 piezoresistive pressure sensors, was used to perform a flow characterization study under particle-free conditions. The rake was placed at several locations: the nozzle exit (x = 0 mm), test section viewing window (x = 76 mm and x = 84.7 mm), and back of the test section (x = 213 mm and x = 288 mm). At each location, the tunnel was operated with fill pressures at 0.1 bar increments from 0.5 bar to 1 bar and 0.5 bar increments from 1.5 bar to 5.5 bar. The rake has the capability of housing 10 probes with a spacing of 23 mm between each probe. The pressure measurements were collected by three Dewetron TRION-2402-dSTG universal input modules at 200 kHz with an antialiasing filter. A schlieren picture of the rake in the test section viewing window is shown in Fig. 2.7. Sensor attrition occurred throughout the campaign, therefore some probe locations are missing for certain rake locations and tunnel conditions.

The flow Mach number is calculated by using the Rayleigh Pitot-tube formula (Eq. 2.5), assuming a calorically perfect gas (γ = 1.4) and isentropic flow through the nozzle (Eq. 2.4). In

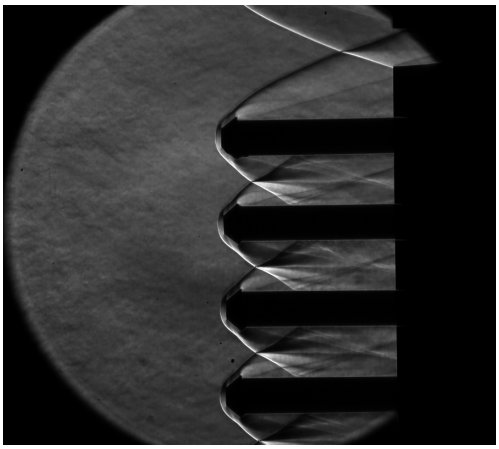

Figure 2.7: Schlieren image of the pitot rake for a charge tube pressure of 5.5 bar and a distance from the nozzle exit of 84.7 mm.

Eq. 2.5, p_{02} refers to the post-shock stagnation pressure measured by the pressure transducers and p_1 to the pre-shock freestream static pressure. Since an expansion wave travels upstream from the nozzle when the tunnel is started, the charge tube pressure during the steady test time is not the initial fill pressure. The Kulite® XTEL-190S-250A, placed 118.7 cm upstream from the nozzle throat, is used to measure the charge tube static pressure behind the expansion wave. The Mach number of the charge tube flow is found by using Eq. 2.1. The Mach number can also be found by satisfying the subsonic solution to the Area-Mach number relationship for a quasi-one-dimensional, isentropic flow to a sonic throat (Eq. 2.3), however this does not account for pressure losses due to the unsteady expansion. The solution to the Area-Mach number relation results in M_{CT} = 0.0562 whereas the charge tube Mach number that results from the relationship between the fill pressure and the post-expansion static pressure measures between M_{CT} = 0.095-0.0992. While this difference may appear to be quite large, the overall effect it has on the calculation of the freestream properties is negligible. The total pressure in the charge tube is then obtained from the isentropic relations; assuming an isentropic nozzle flow this value is also appropriate for the freestream.

$$\frac{p_{02}}{p_1} = \left(\frac{(\gamma+1)^2 M^2}{4\gamma M^2 - 2(\gamma-1)}\right)^{\frac{\gamma}{\gamma-1}} \left(\frac{1-\gamma+2\gamma M^2}{\gamma+1}\right) \tag{2.5}$$

2.2.2 Flow Characterization Results

Pressure traces from a shot at p_{fill} = 1.5 bar are presented in Figs. 2.8 and 2.9 for within the charge tube and at the nozzle exit plane. To reduce high-frequency noise, an 11-point moving average filter has been applied three times in succession to the data. The charge-tube pressure and temperature traces shows a drop corresponding to the passage of each of the initial and reflected expansion waves, with the steady test time in between. No temperature drop is picked up by the RTD sensor because the response time is on the order of seconds, while the relevant time scales here are on the order of tens of milliseconds. Therefore, for calculations, the isentropic equations are used with the total temperature calculated using Eq. 2.2 and the charge tube Mach number being the one obtained from the charge tube pressure measurements. The pressure rise and subsequent plateau seen in the Pitot traces of Fig. 2.9 correspond to a startup time of ~15 ms and steady test time of ~35 ms. The spike in some of the signals immediately following flow initiation is likely an artifact of the plug valve violently impacting its housing. These traces also show a secondary steady test period following the second pressure drop in the charge tube pressure trace; however, the sensor at r = 68.8 mm picks up the unstart shock traveling upstream early on in this test period and the remaining sensors (although not shown in the figure) follow soon after, rendering the secondary test time significantly shorter than the first. Figure 2.10 shows a statistical representation of the flow startup time, calculated as the time required for the Pitot pressure to increase from 5% to 95% of its steady value, over all rake experiments. The times

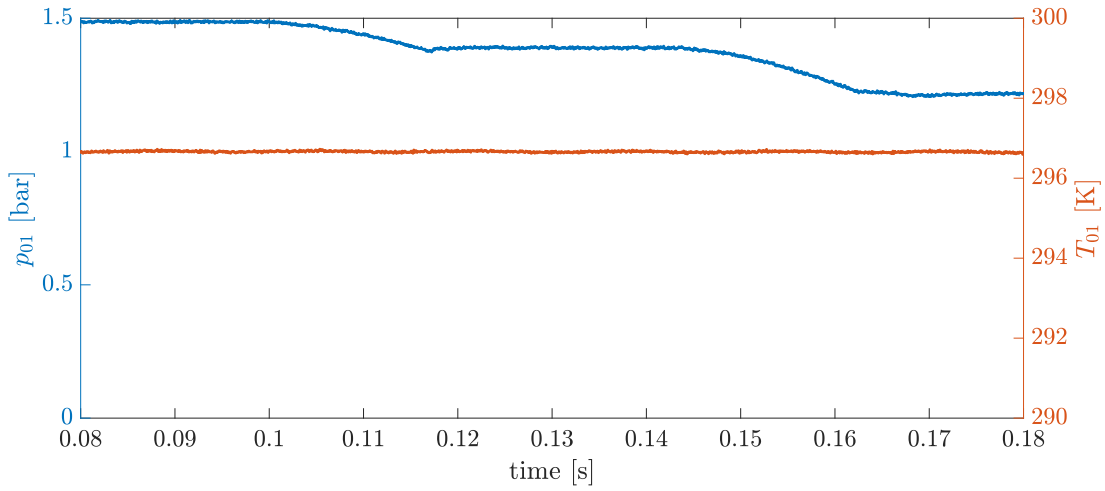

Figure 2.8: Charge tube pressure and temperature traces at x = -203.3 cm and x = -172.4 cm from the nozzle exit plane respectively.

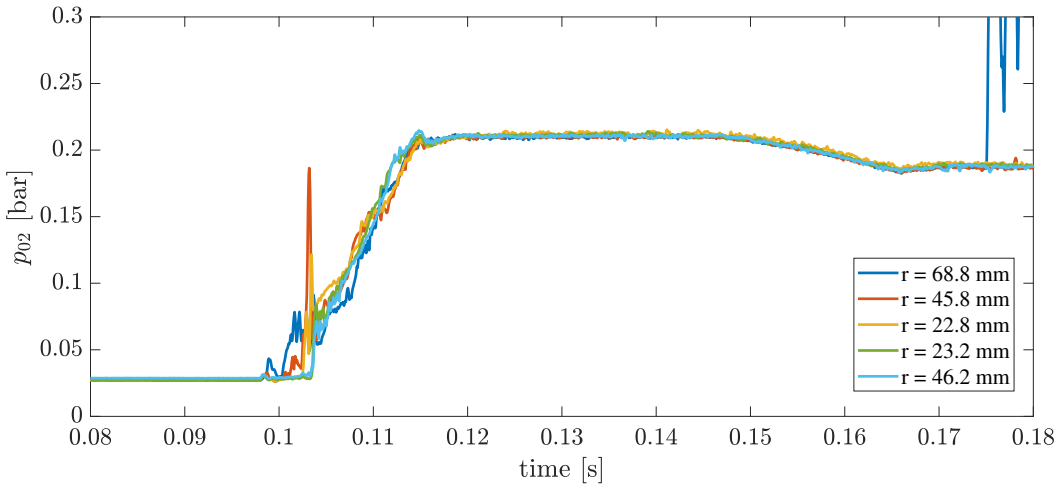

Figure 2.9: Pitot rake pressure traces for a charge tube pressure of 1.5 bar at the nozzle exit.

range from 10 ms to 24 ms, with a mean of 15 ms. The steady test times typically range from 30 ms to 40 ms but depend on the location in the test section, since the unstart shock reaches the edge of the test section first; the shape of the unstart shock is a normal shock wave in the center of the test section and oblique waves emanating from the shear layer at the edge of the free jet that then meet the normal shock wave towards the center.

Figure 2.11 shows calculated test-section Mach-number and unit-Reynolds-number dis-

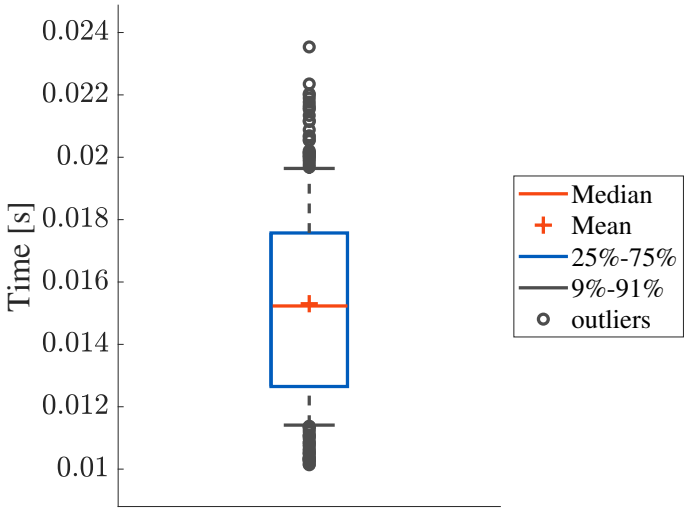

Figure 2.10: Box plot representation of the flow startup time from 5% to 95% of the total pressure rise.

tributions for $p_{\text{fill}} = 1.5$ bar. To calculate the unit Reynolds number, defined as $Re = \frac{\rho u}{\mu}$, the dynamic viscosity is obtained by applying Sutherland's law for nitrogen at the freestream temperature. From the distributions, it is evident that the core-flow region at the nozzle exit plane has a radius of 80 mm, decreasing to $r = 70$ mm at the test section viewing window and $r \approx 30$ mm at the rear of the test section. Mach-number and unit-Reynolds-number profiles at the nozzle exit for different fill pressures are shown in Figs. 2.12 and 2.13. At fill pressures below 1 bar, the resulting freestream Mach numbers fall below 4, ranging from 3.75 to 3.9 for fill pressures of 0.5 bar to 0.9 bar. This is caused by the thicker nozzle boundary layer at lower Reynolds numbers reducing the core-flow diameter. At higher fill pressures, the Mach numbers collapse to $M_\infty = 4$ inside the core flow region. The unit Reynolds number, meanwhile, increases from $Re_\infty = 2.5{\times}10^6$ m^{-1} for $p_{\text{fill}} = 0.5$ bar to $Re_\infty = 24{\times}10^6$ m^{-1} for $p_{\text{fill}} = 5.5$ bar.

A concern for tunnels with an internal fast-acting plug valve is the potential for additional disturbances in the flowfield originating from the wake of the valve. Unfortunately, when the rake

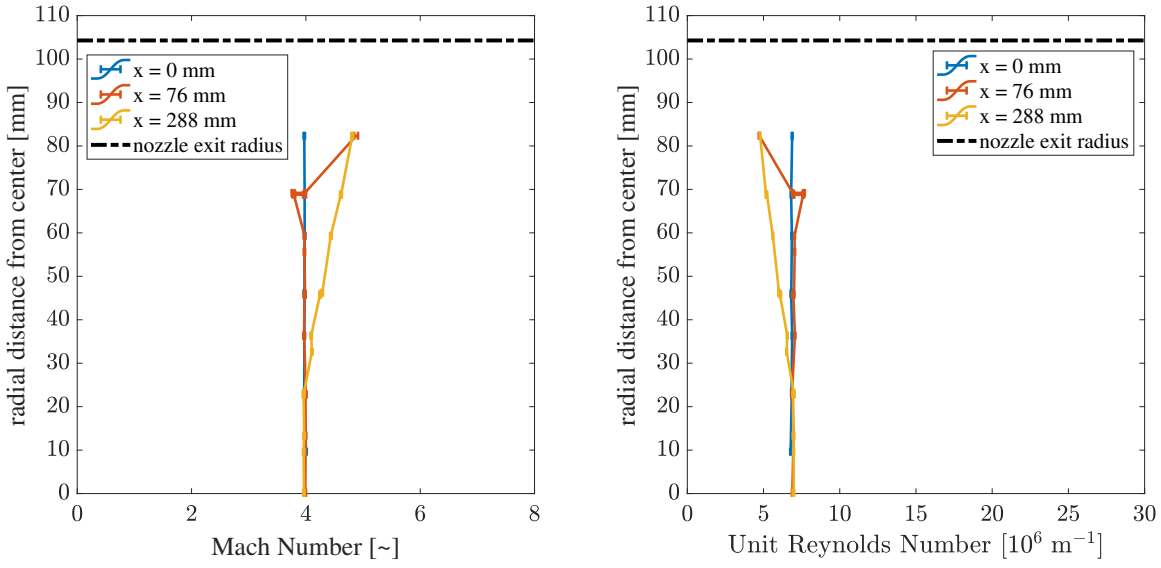

Figure 2.11: (a) Mach number and (b) Reynolds number distributions for a fill pressure of 1.5 bar with uncertainty bars.

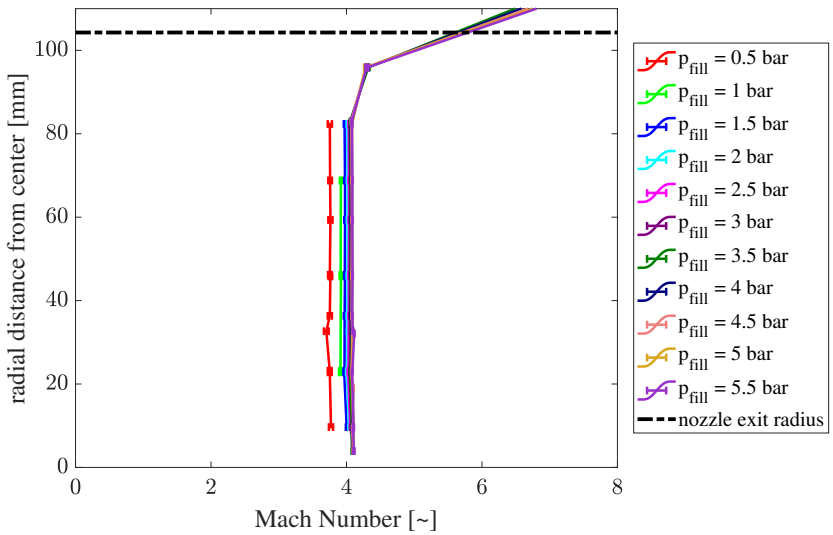

Figure 2.12: Radial Mach number distributions at the nozzle exit for fill pressures spanning 0.5 bar to 5.5 bar with uncertainty bars.

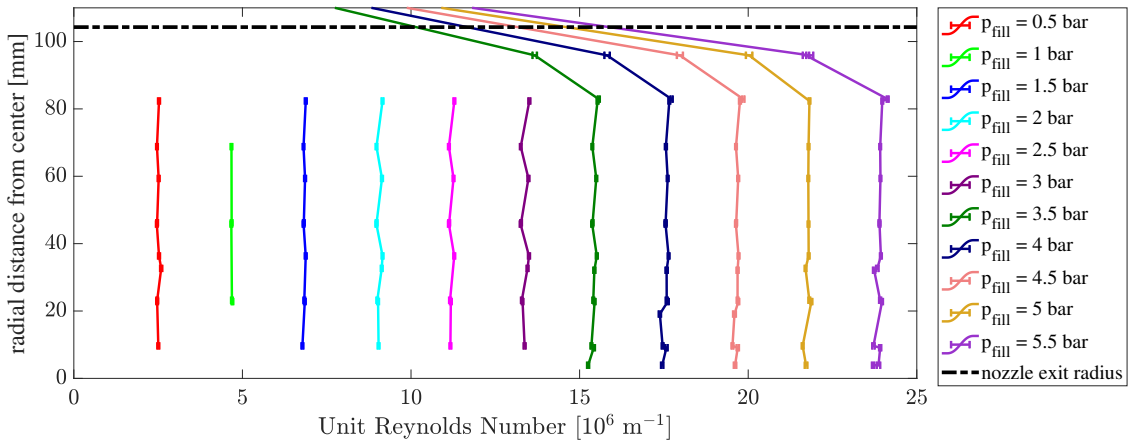

Figure 2.13: Radial Reynolds number distributions at the nozzle exit for fill pressures spanning 0.5 bar to 5.5 bar with uncertainty bars.

was positioned at the nozzle exit, the pressure transducer at r ≈ 0 was not functioning. Therefore, to assess any evidence for such a wake, selected power spectral densities of the pressure fluctuation for several sensors during the steady test time for the rake in the viewing window (x = 76 mm) are plotted in Fig. 2.14. For this shot, the probe along the centerline indicates no significantly elevated noise in the signal compared to the other pressure transducers. This result was consistent throughout all shots in the Pitot rake campaign. Furthermore, the RMS of the raw pressure fluctuation measurement at the centerline was 0.55% of the mean pressure; for comparison, the sensors at r = 22.8, r = 45.8, r = 68.8, and r = 69.2 had corresponding RMS values of 0.53%, 0.54%, 1.38%, and 0.42% respectively. This suggests that the plug valve is retracted far enough into the charge tube that it does not affect the flow through the nozzle, or that any disturbance that is produced is damped out before it reaches the nozzle exit.

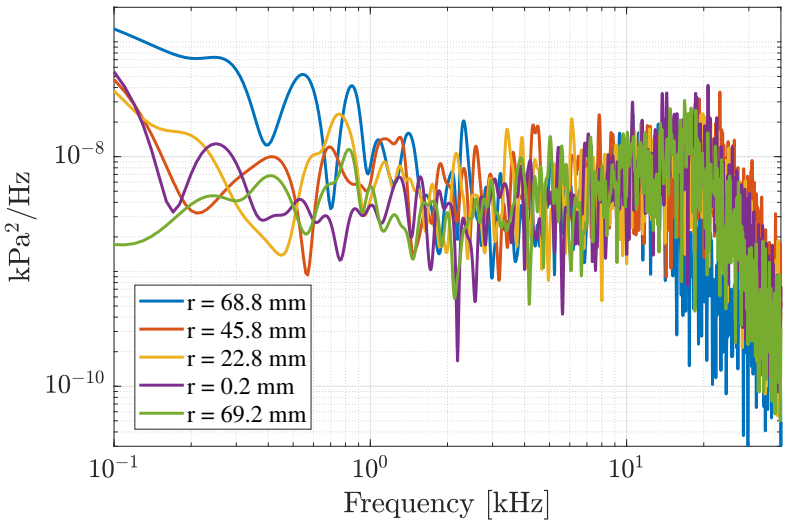

Figure 2.14: Pitot rake fluctuation pressure PSD for a charge tube pressure of 1.5 bar at the tunnel viewing window, x = 76 mm.

2.3 Particle Transport Simulations

Two primary considerations for the design of MIST were: (i) whether or not the liquid particles, once generated and suspended in the charge tube, would survive the forces caused by the acceleration through the nozzle and (ii), assuming survival, what the distribution of particles entering the test section across the nozzle exit would be. To verify this, first a simple one-dimensional simulation methodology was developed, where the local particle Weber number was compared to break-up criteria derived from previous research. This model was then extended to two-dimensional (axisymmetric) nozzle flows to predict the particle distribution in the freestream.

2.3.1 Droplet Breakup and Transport

Extensive work has been performed in the field of droplet demise over the past century: comprehensive reviews by Pilch and Erdman [6], Faeth et al. [83], and Guildenbacher et al. [8]

have captured a significant amount of the progress made to date in understanding the physical phenomena involved in droplet breakup. It has been determined that a driving condition for breakup is the magnitude of the drag or inertial force the droplet experiences compared to the magnitude its own cohesion force, a ratio that is characterized by the Weber number (We)

$$We = \frac{\rho\, V^2 d_p}{\sigma} \quad , \tag{2.6}$$

where ρ is the density of the fluid, V is the relative velocity of the droplet in the fluid, d_p is the droplet diameter, and σ is the surface tension of the droplet.

Depictions of the various types of breakup processes together with their respective Weber number ranges that drive them are given in Fig. 2.15. For a first-pass analysis on the survivability of the droplets as they are accelerated through the MIST nozzle, a precise physical model for the droplet deformation and breakup was unnecessary, instead empirical relations for given flow conditions were preferred as they would be less computationally expensive. The transition between vibrational and bag breakup mechanism was chosen as the limiting factor since it was desired that the droplets maintained their original mass through the nozzle, with the assumption that weaker vibrations in the droplet would either dampen out before impacting whichever model was placed in the wind tunnel, or have little effect on the overall momentum transferred. Hsiang and Faeth [7] compiled a model for the critical Weber number associated with each breakup regime based on the droplet Ohnesorge number, as shown in Fig. 2.16. The Ohnesorge number (Oh), that appears in this figure, relates the viscous forces to the inertial and surface tension forces:

$$Oh = \frac{\mu}{\sqrt{\rho\, d_p\, \sigma}} \quad . \tag{2.7}$$

For the properties of DEHS given in Tab. 2.1, the Ohnesorge number ranged from Oh = 2.1 for a droplet diameter of d_p = 4.11 μm to Oh = 1.08 for d_p = 15.6 μm. Based on this range, a critical Weber number of We_{crit} = 12 was selected as the limiting threshold the droplets could experience while they accelerate through the nozzle. Prior to the initiation of droplet breakup, the growth in the Weber number results in a deformation of the droplet from an initially spherical shape to a disk (see Fig. 2.17). For low Oh (Oh < 0.1) and We < 100, Hsiang and Faeth [84] found a relationship for the maximum cross-sectional diameter of the deformed droplet to its original diameter:

$$\left(\frac{d_{cro}}{d_0}\right)_{max} = 1 + 0.19\sqrt{We} \quad . \tag{2.8}$$

However, the limitation on this Ohnesorge number range was mostly due to the constraints of the experimental data available, and these are authors later postulated that such a relationship could be extended for larger Oh since the effect of increasing Oh simply delays the deformation process [7]. For the purpose of the simulations presented in sections 2.3.2 and 2.3.3, applying Eqn. 2.8 was assumed to be sufficient to account for the droplet deformations since the Ohnesorge numbers for the simulated particles were only an order of magnitude larger than the earlier postulated limit and the particle Weber numbers remained relatively low (well below 100).

The particle dynamics within the nozzle will be governed by the drag force (Eqn. 2.9) on the particle caused by the local flowfield. The Loth [85] and Singh [86] sphere-drag models, summarized in Appendix A, were utilized to calculate the local drag coefficient at each point along the trajectory, and the particle position, velocity, and acceleration were updated at each time step using the Euler method. The drag over the deformed droplet was taken into account

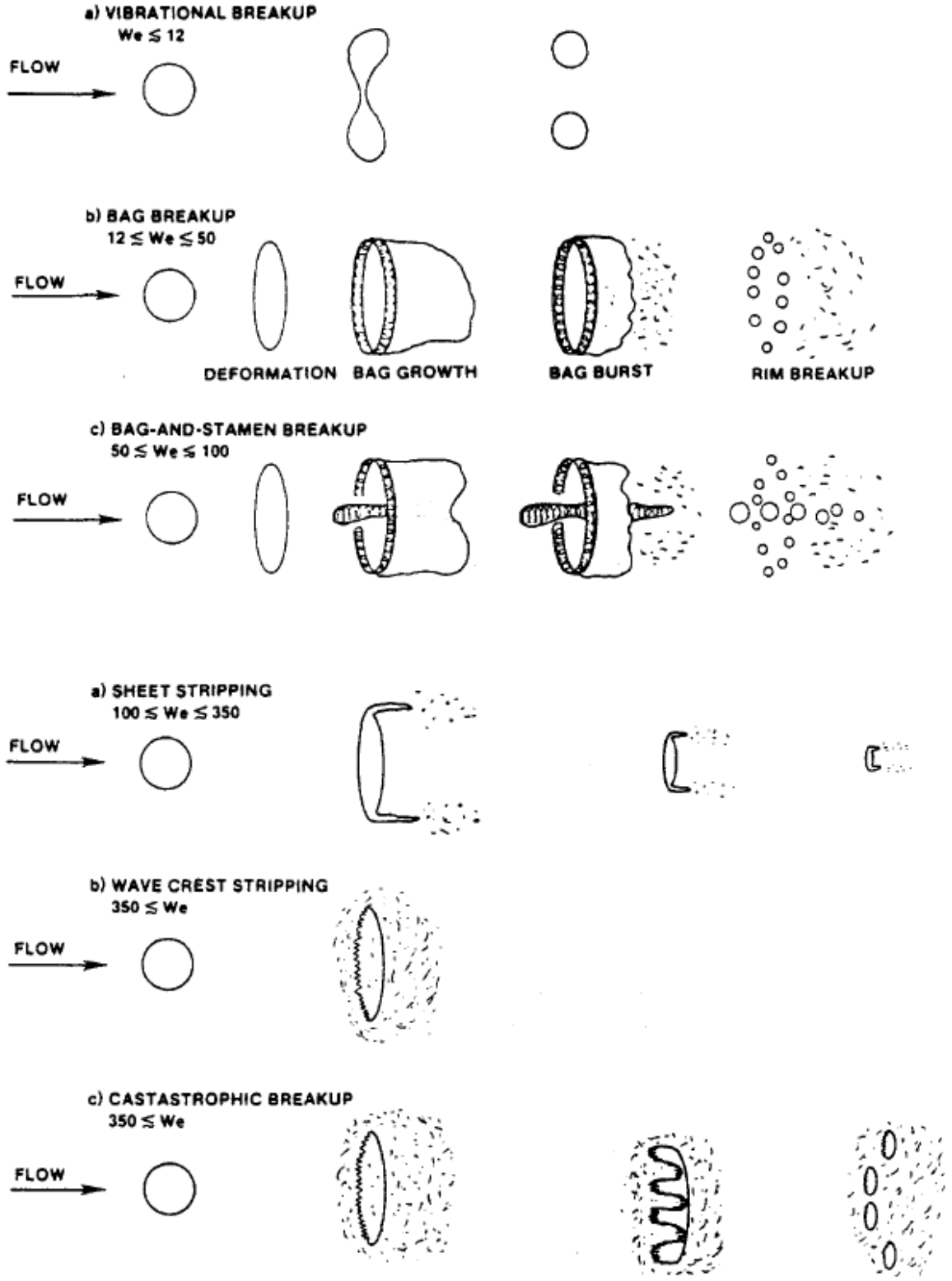

Figure 2.15: Droplet breakup mechanisms [6].

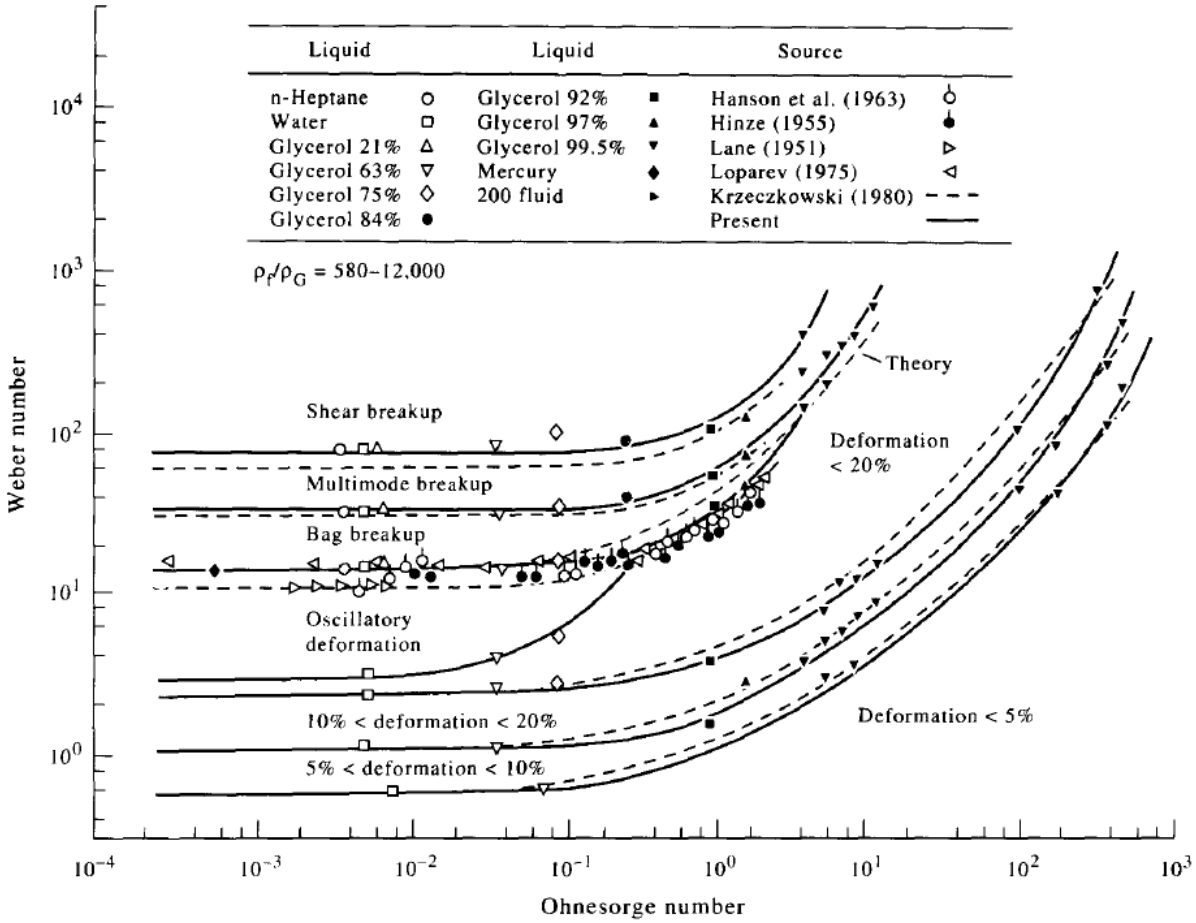

Figure 2.16: Droplet breakup mechanisms [7].

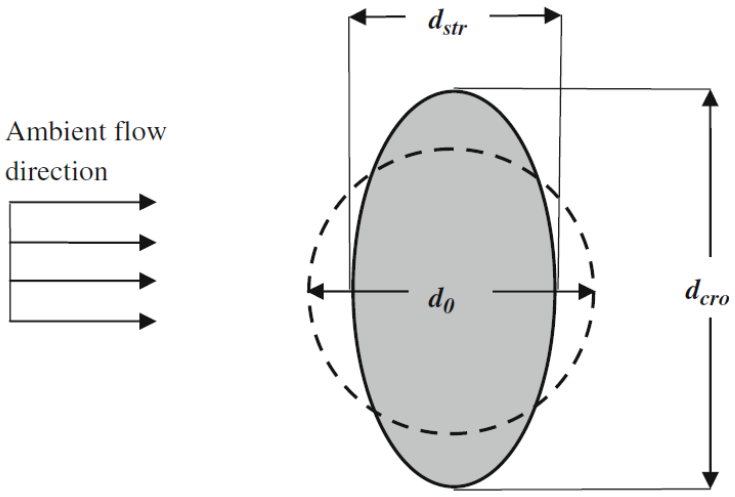

Figure 2.17: Droplet deformation [8].

using the maximum cross-sectional diameter from Eqn. 2.8.

$$F_D = -\frac{1}{8}\pi\rho_g|\mathbf{w}|\mathbf{w}\left(\frac{d_{cro}}{d_0}\right)^2 d_0^2 C_{D_{sphere}}\left(\frac{C_D}{C_{D_{sphere}}}\right) \tag{2.9}$$

Here, ρ_g is the local density of the gas, $\mathbf{w}$ is the relative particle velocity vector, and the deformed droplet drag correction factor is obtained from the model proposed by Liu et al. [87] as:

$$\frac{C_D}{C_{D_{sphere}}} = 1 + 2.632\left(1 - (d_0/d_{cro})^2\right) \quad . \tag{2.10}$$

By the author's own admission, this model has not been validated experimentally, but is sufficient for the analysis desired in these studies as Eqn. 2.10 recovers the drag coefficient of a sphere when $d_{cro} = d_0$ and the drag coefficient of a disk as (d_0/d_{cro}) approaches zero.

2.3.2 One-Dimensional Particle Acceleration through the MIST Nozzle

First, one-dimensional particle acceleration simulations were performed to estimate the Weber number experienced by particles of various diameters as they accelerate through the nozzle and to check if these values exceeded the assumed limiting critical Weber number for particle breakup, $\mathrm{We_{crit}} = 12$. The flow-field was generated by satisfying the area-Mach number relationship (Eqn. 2.3), assuming a quasi-one-dimensional, isentropic flow through the nozzle. The initial conditions were set by choosing the fill pressure from the range of achievable values for the facility, with the fill temperature assumed to correspond to room temperature ($\mathrm{T_{fill}} = 296$ K). Since a series of expansion waves emanating from the nozzle throat and traveling upstream start the flow, the subsonic solution to the area-Mach number relationship gives the flow Mach number in the charge tube, $\mathrm{M_{CT}}$. The post-expansion pressure and temperature in the charge tube were

then found using Eqns. 2.1 and 2.2, derived using the method of characteristics.

The stagnation conditions were then calculated using the steady isentropic relations, Eqns.2.4 and 2.11.

$$\frac{T_0}{T_{CT}} = \left(1 + \frac{\gamma - 1}{2} M_{CT}^2\right)^{\frac{\gamma}{\gamma-1}} \tag{2.11}$$

Knowing the stagnation conditions and nozzle geometry, along with the quasi-one-dimensional and isentropic flow assumptions, the flow conditions at each position along the length of the nozzle were obtained by satisfying Eqns. 2.3, 2.4, and 2.11. Finally, the density and viscosity were found using the ideal gas law and Sutherland's Law. Although, this latter equation is not very accurate for the low temperatures encountered near the nozzle exit [88], it is acceptable for the purposes of the desired study since, as we will see, peak We values are encountered immediately downstream of the throat and not at the nozzle exit.

The Singh drag model (see Appendix A) was used in these one-dimensional simulations to calculate the drag coefficient for the spherical droplet. The droplet, initially at rest, was placed at the entrance to the nozzle, and the position and velocity of the particle were updated at each time step using the Euler method:

$$x^n = x^{n-1} + u^{n-1}\Delta t + \left(\frac{F_D}{2m_p}\right)\Delta t^2 \tag{2.12}$$

$$u^n = u^{n-1} + \left(\frac{F_D}{m_p}\right)\Delta t \quad . \tag{2.13}$$

A convergence study showed that a time step of $\Delta t = 5\ \mu s$ was sufficient to achieve reliable results.

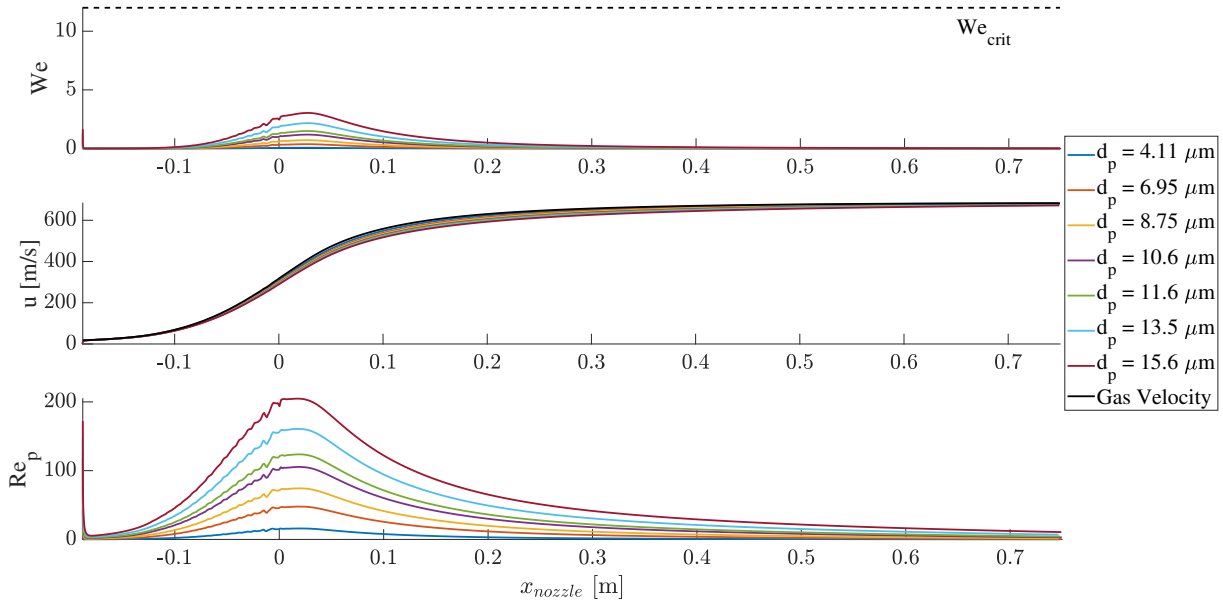

Figure 2.18: Particle Weber number, velocity, and Reynolds number as it accelerates through the MIST nozzle for initial charge tube conditions of p_{fill} = 10 bar and T_{fill} = 296 K.

Since the particle Weber number is driven primarily by the dynamic pressure, we first check the particle survivability for the high-pressure limiting case of p_{fill} = 10 bar and T_{fill} = 296 K — the design parameters chosen for the nozzle. Figure 2.18 shows the local Weber number, velocity, and Reynolds number for the particle as it moves along the nozzle, with the nozzle throat located at x_{nozzle} = 0 m. On the Weber number plot, the dashed line denotes the critical Weber number threshold previously identified to be We_{crit} = 12. Particle simulations were performed over the range of particle diameters producible by the MDG 1530, and it can be seen that even the largest particle (d_p = 15.6 μm) only experiences a maximum We of less than half the value of We_{crit}. This occurs shortly after the particle passes the nozzle throat: here, the difference between the flow velocity and particle velocity is greatest, due to the particle having too high an inertia to accelerate at the same rate of the flow. The particle velocity profiles show that, as the particles get smaller, their nozzle exit velocities approach the exit flow velocity of 684 m/s. Slight perturbations in the

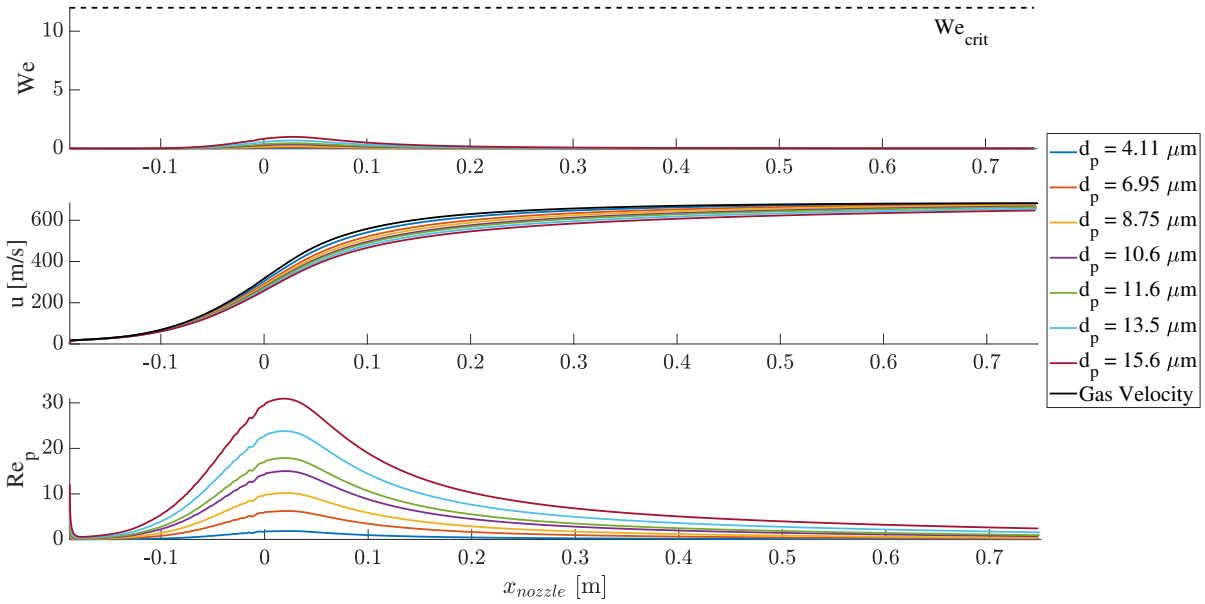

Figure 2.19: Particle Weber number, velocity, and Reynolds number as it accelerates through the MIST nozzle for initial charge tube conditions of p_{fill} = 0.7 bar and T_{fill} = 296 K.

curves are noticeable directly upstream of the nozzle throat: these were found to be caused by the application of the drag model and were present in the simulations ran using both drag models due to their piece-wise natures.

Of greater relevance to the present work are the 0.7 and 1 bar fill-pressure cases. Figure 2.19 shows the corresponding results for p_{fill} = 0.7 bar and it is evident that the external disturbances to the particles as they travel through the nozzle are minimal, as shown by the low We along their path. However, the velocity profiles indicate that, with such a low driving pressure, even the smallest particles fail to accelerate to the flow velocity at the nozzle exit: the particle exit velocities in ascending order for the particle sizes are 681 m/s, 678 m/s, 673 m/s, 668 m/s, 664 m/s, 656 m/s, and 648 m/s, respectively. A similar trend is noticeable for the p_{fill} = 1 bar results, where the exit velocities for the larger particles fall well below the nozzle exit velocity. The particle velocities for the three cases described above are summarized in Table 2.3. The maximum

Table 2.3: MIST nozzle exit velocities for DEHS particles.

d_p (μm)	u_p (m/s) p_{fill} = 0.7 bar	u_p (m/s) p_{fill} = 1 bar	u_p (m/s) p_{fill} = 10 bar
4.11	681	682	682
6.95	678	679	681
8.75	673	676	680
10.6	668	671	678
11.6	664	668	677
13.5	656	661	675
15.6	648	654	672

slip velocity for all cases presented is 36 m/s, or 5.26% of the flow velocity at the nozzle exit, and is therefore minimal and will not need to be accounted for in the experiments in the present work.

2.3.3 Two-dimensional Particle Transport through the MIST Nozzle

Two-dimensional simulation of the particle trajectory was performed in order to understand the behavior of the aerosols through the converging-diverging nozzle and, in particular, to determine their radial distribution at the nozzle exit. The governing equations are the same as for the one-dimensional case whith the particle drag coefficient obtained from the Singh drag model and the particle trajectories determined by the drag force equation (Eqn. 2.9) applied with Euler time marching, (but now in two dimensions):

$$\mathbf{x}^n = \mathbf{x}^{n-1} + \mathbf{v}^{n-1}\Delta t + \begin{pmatrix} \frac{F_{D_x}}{2m_p} \\ \frac{F_{D_y}}{2m_p} - \frac{g}{2} \end{pmatrix} \Delta t^2 \quad , \tag{2.14}$$

$$\mathbf{v}^n = \mathbf{v}^{n-1} + \begin{pmatrix} \frac{F_{D_x}}{m_p} \\ \frac{F_{D_y}}{m_p} - g \end{pmatrix} \Delta t \quad . \tag{2.15}$$

The time step chosen for these simulations was based on the local characteristic time of the particle traveling through the center of the nozzle, i.e. $\Delta t = 0.5 d_p / u_g$. The nozzle flowfield was generated using the VULCAN-CFD solver for an initial charge-tube fill pressure of 10 bar. The x- and y-components of velocity from this simulation are shown in Figs. 2.20 and 2.21, respectively. To account for different initial tunnel pressures, the pressure profile outputted from the solver for the 10 bar condition was scaled linearly, and the fluid density was found by applying the perfect gas equation to the scaled pressure while keeping the same temperature profile. This method does not account for differences in boundary layer thickness as the unit Reynolds number is varied, but it is acceptable for understanding the general behavior of the particles through the core-flow region.

Simulations were run for each of the particle diameters measured with the APS (Section 2.1.3) with the initial radial location of the particle in the charge tube varied. Figure 2.22 shows an example of the results obtained for 15.6 μm droplets initialized with a 1 cm spacing at the nozzle inlet; particle path-lines generated by tracking the particles through the nozzle are shown. In the converging section of the nozzle, the particles follow the contour of the nozzle, focusing through the nozzle throat. In the diverging section of the nozzle, however, the particles react more slowly to the expansion of the gas, spreading in a roughly conical manner rather than following the shape of the nozzle. This is due to the relatively large Stokes number of these large particles, where the Stokes number, Stk, is the ratio of the characteristic reaction time of the particle to the characteristic time of the flow. If we evaluate the characteristic time of the flow based on

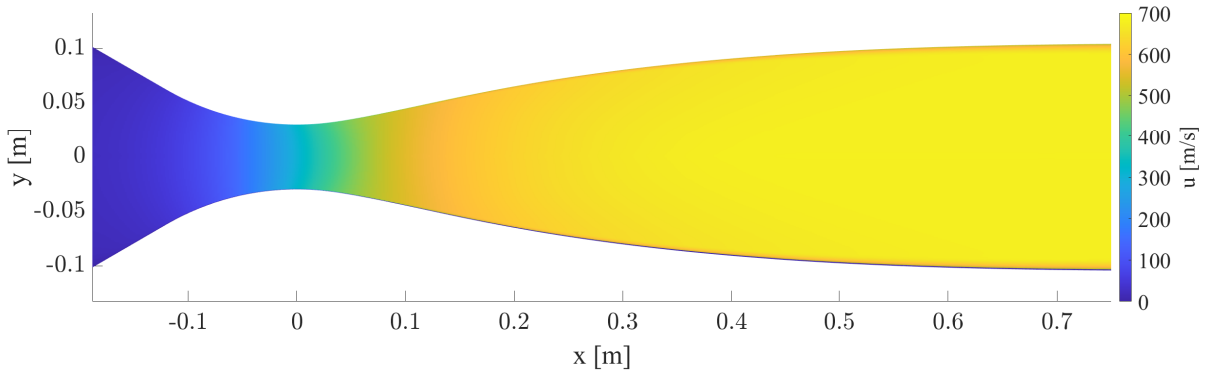

Figure 2.20: Axial component of velocity in the MIST Mach-4 nozzle.

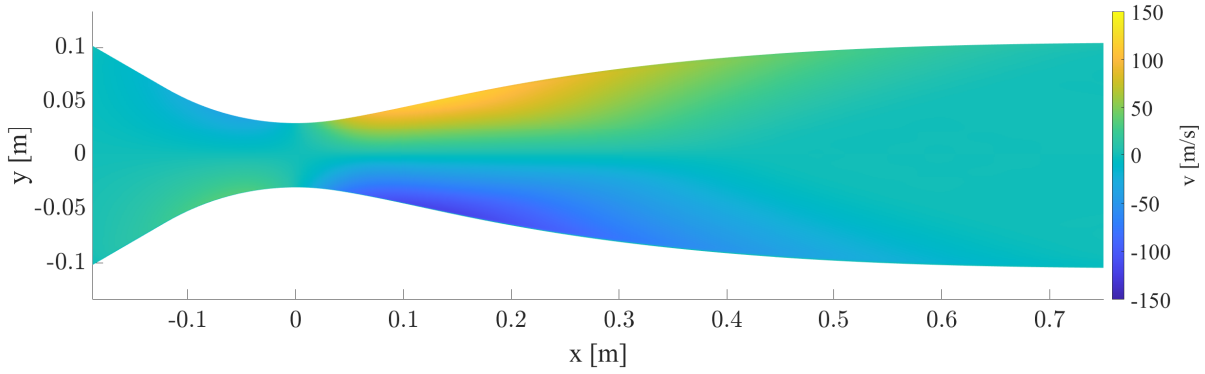

Figure 2.21: Y-component of velocity in the MIST Mach-4 nozzle.

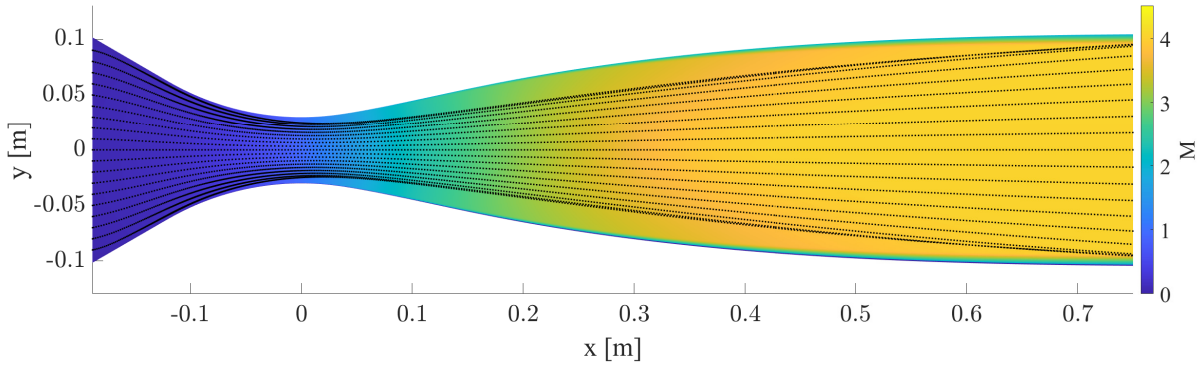

Figure 2.22: Streamlines of the 15.6 μm droplets overlaid on the Mach number profile of the MIST nozzle (p_{fill} = 0.7 bar).

the exit velocity of the gas and the nozzle exit radius, we obtain a Stokes number of 18.3 for the 15.6 μm diameter particle. It is also evident that, although the particles were initialized with equal radial spacing, the path-line spacing at the nozzle exit is compressed further away from the nozzle centerline. Examining Fig. 2.22, we see this compression actually originates near the throat, where the local Stokes number becomes large enough that the particles no longer follow the fluid path, and this continues out into the diverging section. For reference, a Stokes number of Stk = 0.1 is congruous with an RMS slip velocity of approximately 1% [89].

A comparison of the trajectories of a selection of the particle sizes is presented in Fig. 2.23 the smallest, largest, and median particle sizes achievable with the MDG 1530 were chosen, each initialized at the same locations at the nozzle entrance (y = 0, ±0.04, and ±0.09 m). The 4.11 μm, 10.6 μm, and 15.6 μm diameter particles have Stokes numbers at the nozzle exit of Stk = 1.27, 8.46, and 18.3, respectively. The difference in trajectories is most noticeable close to the nozzle wall, where the 4.11 μm particles exhibit curved trajectories in the expansion region of the nozzle that more closely follow the shape of the nozzle. In comparison, the 15.6 μm particles follow almost linear paths in the same region, while the 10.6 μm particle paths show signs of some curvature. The spread of the streamlines at the nozzle exit shows a strong dependency on

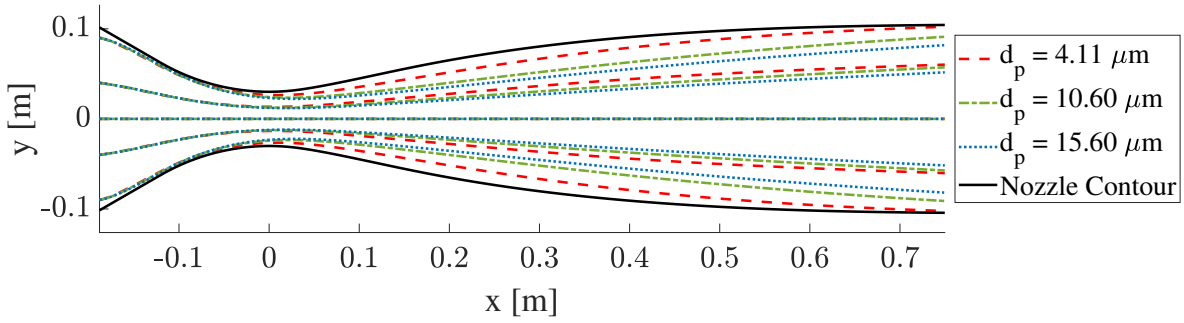

Figure 2.23: Particle trajectories in the MIST nozzle for 4.11 μm, 10.6 μm, and 15.6 μm diameter particles (p_{fill} = 1 bar).

the particle Stokes number. The smallest particles that were initialized at y = ±0.09 m, actually impinge on the nozzle wall before the nozzle exit, while the corresponding particle path-lines for the 10.6 μm and 15.6 μm particles exit at y = ±0.091 m and y = ±0.082 m, respectively.

2.4 Multi-phase Flow Visualization

Two optical visualization techniques were employed to confirm the presence of particles in the freestream. With the equipment available in the HAPL lab, however, using the images to ascertain the particle concentration in the freestream proved to be difficult, and an alternative approach was found to be necessary.

2.4.1 Visualization using Mie Scattering

Initial particle visualization was conducted by taking advantage of the Mie scattering effect using a 280 W Cavitar Cavilux HF laser with a 646±10 nm wavelength and a 2.49 μs pulse width. A Cavitar Cavilux HF Light Sheet Optic was used to produce a vertical 0.85 mm thick laser sheet

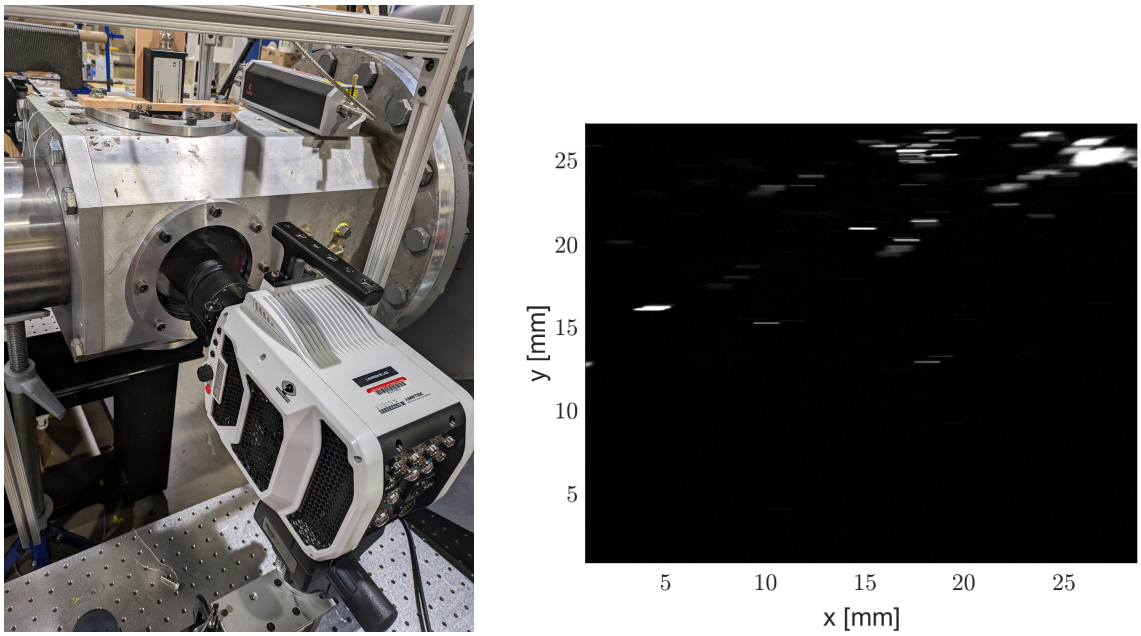

(a) (b)

Figure 2.24: (a) Laser sheet and camera setup for the Mie-scattering visualization in the MIST test section and (b) a snapshot of 11.6 μm droplets in the Mach 4 flow.

aligned streamwise with the flow. A Vision Research Phantom v2640 high-speed camera with a 150 mm focal length Irix Dragonfly Macro lens was set up normal to the light sheet, as shown in Fig. 2.24a. The camera frame rate was 8,000 frames per second with a pixel resolution of 1024 $\times$ 976 pixels (35.7 pixels/mm) and an exposure time of 3 μs to minimize the background noise in the images. Frames were collected under flow-off conditions as well as during clean-flow runs without the particles to establish a baseline for comparison. For these tests, MIST was operated at room temperature and a 1 bar fill pressure, leading to the freestream conditions provided in Tab. 2.4. A medium particle size of 11.6 μm was chosen for the initial visualization attempts as this represented a compromise between maximizing the amount of light scattered into each pixel by the particle and maintaining a relatively long settling time to ensure that particles remained suspended in the charge tube during the seeding process. Other runs with 15.6 μm and 8.75 μm particles were attempted but resulted in poor quality images.

Table 2.4: Run Conditions for Particle Visualization.

M_∞	Re_∞ ($\times 10^6$ m^{-1})	v_∞ (m/s)	p_∞ (Pa)	T_∞ (K)	ρ_∞ (kg/m^3)
4.12	4.68	684	640	69.8	0.031

2.4.2 Mie Scattering Visualization Results

Figure 2.24b shows a snapshot obtained using the Mie scattering setup from the steady test time. We observe a significant number of 11.6 μm particles streaking through the frame: these particles appear as lines due to the long-exposure effect produced by the long pulse width of the laser. By dividing the streak length by the pulse width, the resultant particle speed was measured as 562 m/s. This is well below both the freestream flow speed of 684 m/s and the expected particle speed of 668 m/s from Tab. 2.3, although we note that the image resolution is a source of large errors, as one pixel accounts for a difference in speed of 11.2 m/s. Images such as this one were obtained sporadically throughout the shot; however, such streaks only appeared during the flow time and not during either the flow-off time or the no-particle runs, indicating that they did represent passing droplets. Choosing the largest particle diameter (15.6 μm) to attempt to increase the amount of light scattered by the particle had an adverse effect on the particle density in the flow, since it was more difficult to keep these particles suspended in the charge tube. In particular, these particles had a settling time on the order of 30 seconds, whereas the MDG 1530 needed to be run for a much longer time to produce the desired particle concentration for this specific droplet size. Furthermore, the effective laser sheet thickness (insofar as it produced detectable particle illumination) was somewhat less than the nominal 0.85 mm because of the rapid drop-off in the Gaussian intensity profile away from the centerline. Attempts to visualize smaller, 8.75 μm diameter particles, which would have likely produced a higher particle density

in the flow, were unsuccessful as the signal to noise ratio was too low, probably due to the pixel area being 57 times larger than the droplet cross-sectional area in this case.

2.4.3 Visualization using Magnified Schlieren and Shadowgraphy

A second technique for particle visualization employed a magnified Z-type schlieren setup with a horizontal knife edge, as shown in Fig. 2.25. The light source was the same Cavilux HF laser, but now pulsed at 30 ns and focused through a 1.5 mm diameter pupil for this configuration. On the light source side of the test section, a spherical mirror with a diameter of 152.4 mm and a focal length of 1524 mm was placed to collimate the light through the test section. On the camera side, a second, identical mirror refocused the laser light. To maximize the magnification, this mirror was placed as far away from the test section as possible, given other laboratory constraints - in practice, this meant 2032 mm from the test-section centerline. The light was then reflected off a planar mirror and focused down to a horizontal knife edge. A 2000 mm focal length, 25.4 mm diameter plano-convex lens was placed beyond the focal point in order to refocus the magnified image onto the 150 mm focal length Dragonfly IRIX macro lens that was attached to the Phantom Research v2640 camera. The resultant magnification produced a resolution of approximately 28 pixels/mm ($\sim 36\ \mu$m/pixel). The limitation on the magnification was due to the physical limit on the distance at which the camera could be placed from the knife edge (see Fig. 2.25). Although this magnification still resulted in the pixel width being on the order of twice the particle diameter, a bench-top test, shown in Fig. 2.26, where the particle generation column was mounted directly on top of the test section, showed that the droplets were in fact visible. For shadowgraph visualization, an identical setup was employed but with the knife edge removed.

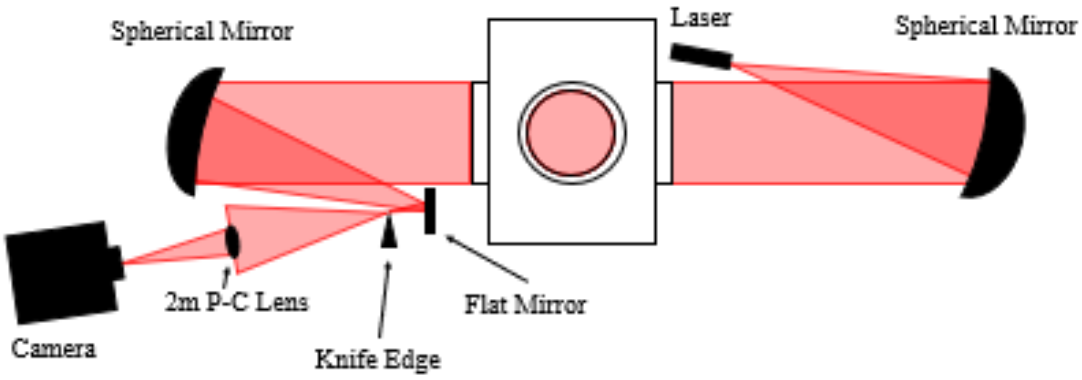

Figure 2.25: Magnified schlieren visualization setup.

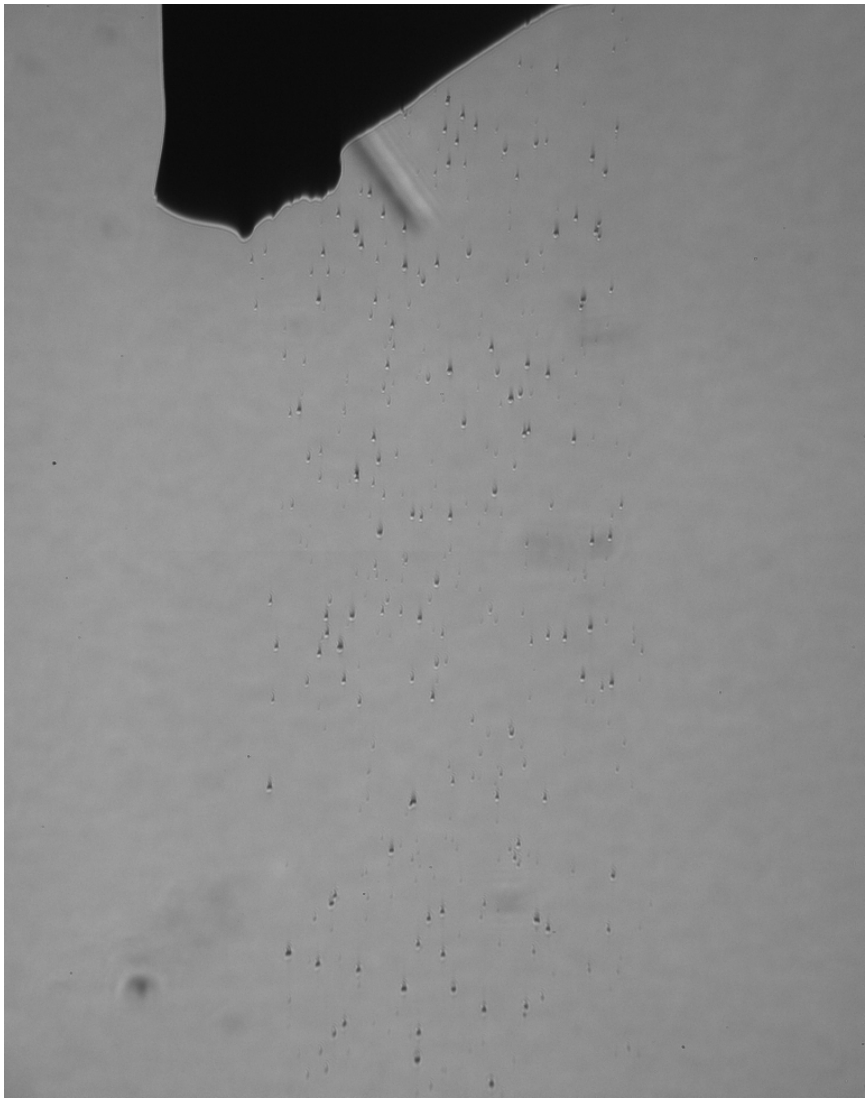

Figure 2.26: 15.6 μm diameter particles injected directly into the test section and visualized using magnified schlieren.

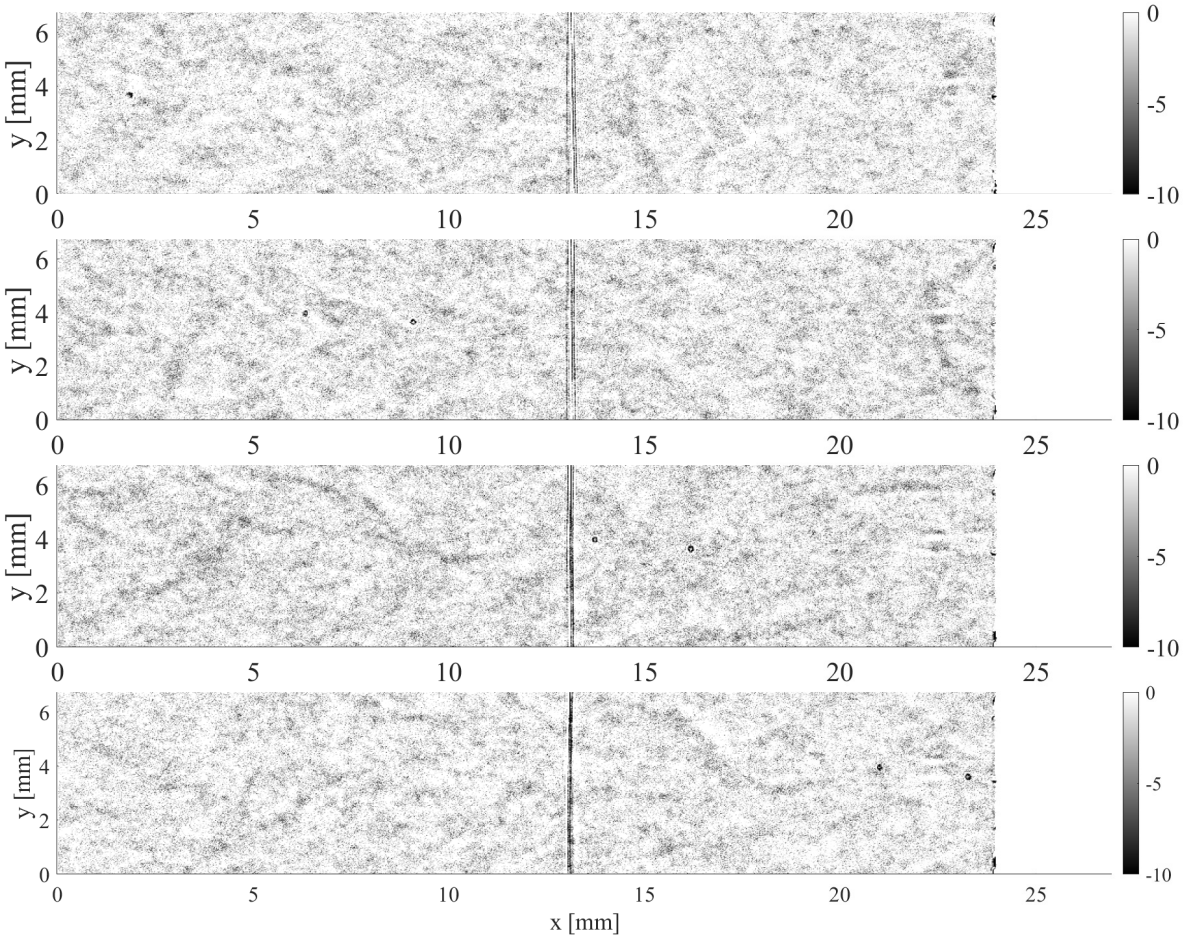

Figure 2.27: Magnified shadowgraphy of two d_p = 11.6 μm droplets taken during the fluorescent sampling experiments described in Section 2.5. The frame rate for this imaging sequence is 79 kHz.

2.4.4 Magnified Schlieren and Shadowgraphy Results

With the magnified schlieren and shadowgraph setups, it proved to be even more challenging to obtain useful particle visualizations during wind-tunnel tests. The disturbances caused by the high-speed flow generated significant background noise, making it difficult to discern if a pixel was darkened by the presence of a particle or the fluid itself. However, in some cases particles were clearly visible: in Fig. 2.27, for example, a series of frames collected at 79 kHz with a resolution of 1024×256 pixels shows two $d_p = 11.6\ \mu$m droplets traveling through the test section towards the impact board used in the particle concentration characterization tests described in Section 2.5. The particles appear as dark ellipses at $y \approx 4$ mm on the indicated coordinates. These images were reference subtracted to improve the image quality and show both the normal shock in front of the impact board at $x \approx 13$ mm as well as the impact board itself at $x \approx 24$ mm. The short pulse width of the laser enables the particles to be essentially frozen in time. Dividing the distance traveled by the time between frames, the speed of the particle is found to be 560 m/s, corroborating the speed of the particles measured using the Mie scattering visualization. Since the particles do not slow down when they appear to cross the shock, it is highly probable that they are displaced laterally outside of the region of influence of the board, since it is a fraction of the total width of the test section. Although both visualization techniques have large sources of error, the measured particle speeds, which are significantly lower than those predicted, are an area of concern. In the present work, the particle speed is important for the study presented in Ch. 3; however, the knowledge of the actual particle speed does not affect the measurements made, but more so how to understand the physics behind what is observed and to possibly computationally reproduce the experiments.

2.5 Multi-phase Flow Characterization

The optical methods just described revealed the presence of particles in the freestream but could not be used to provide reliable concentration measurements. Therefore, a technique previously applied in low speed flows was utilized to measure the concentration of particles in the flow, based on the deposition of fluorescein-doped particles on a rectangular target placed in the test section.

2.5.1 Sizing of Fluorescein-doped Droplets

Uranine (fluorescein) has been used in prior studies involving low-speed aerosol flow applications to measure deposition [90, 91]. The aerosol, in these cases oleic acid, was doped with less than 1% uranine by mass; a fluorometric analysis then produced a quantifiable measurement for the aerosol deposition. Based on the working principle of these studies, a similar experiment for application to high-speed wind tunnels was designed.

The solution was prepared by adding 1 gram of fluorescein per 500 ml of the 5% DEHS in methanol mixture. To ensure that the change in solution properties was minimal and that the MDG continued to produce monodisperse droplets of the same size as the non-doped solution, the particle sizes were again measured with an APS on a benchtop setup, replicating the measurements at the University of Minnesota (Fig. 2.6). In this configuration, the droplet generation column, described in Section 2.1.3, was placed directly on top of the MIST test section, and the APS was placed directly below. For comparison, results for the six largest droplet sizes produced in the MIST test section are shown in Fig. 2.28. The amount of debris and dust in the wind tunnel is immediately evident, with high counts of small diameter particles spanning from d_p = 0.5 μm

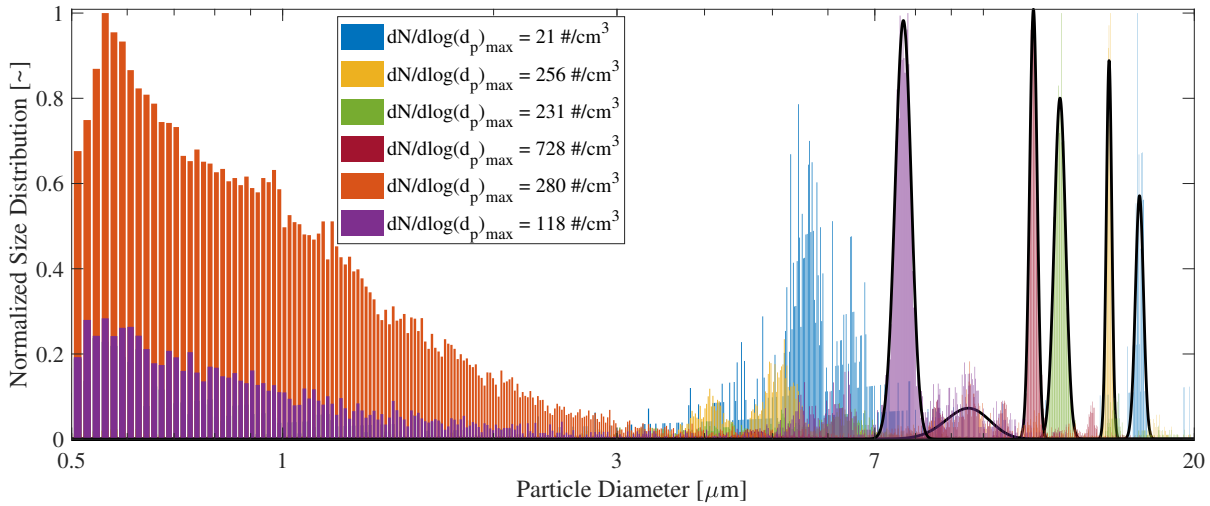

Figure 2.28: Geometric particle size distribution by number count normalized by the maximum bin value for each case with a Gaussian curve fitted to each data set for the DEHS droplets measured in the HAPL lab.

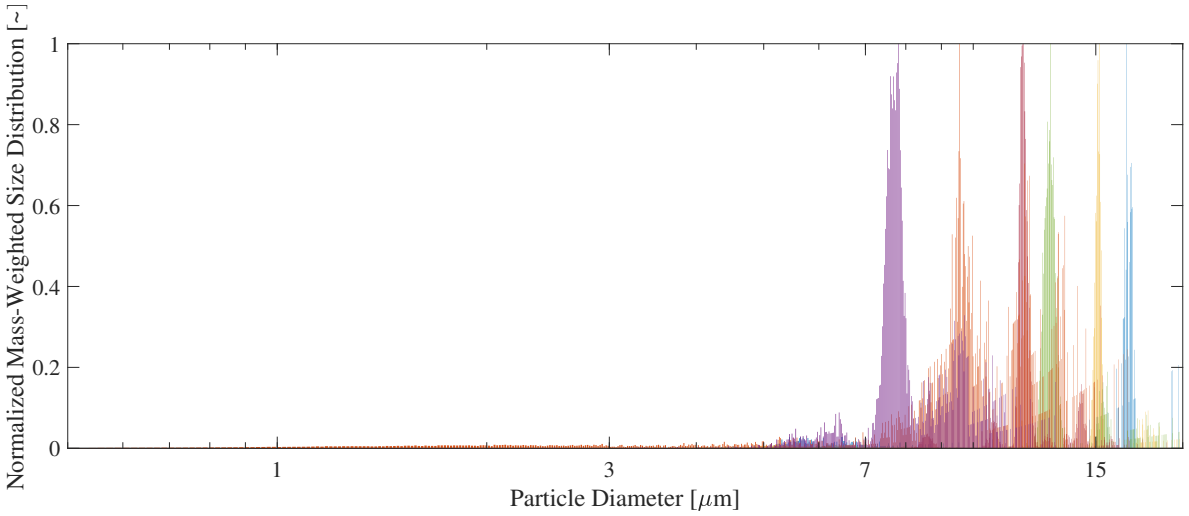

Figure 2.29: Geometric mass-weighted particle size distribution normalized by the maximum bin value for each case for the DEHS droplets measured in the HAPL lab.

Table 2.5: Mean particle diameter of pure DEHS, measured both at the University of Minnesota and University of Maryland, and fluorescein-doped DEHS droplets.

UMN DEHS d_p (μm)	UMD DEHS d_p (μm)	DEHS with Fluorescein d_p (μm)
6.95	7.69	7.90
8.75	9.52	9.72
10.6	11.8	11.7
11.6	12.9	12.9
13.5	15.1	15.2
15.6	16.7	16.6

to $d_p \approx 3$ μm. To suppress these contaminants, the number counts were mass-weighted and then normalized by the largest bin. The mass-weighted data (Fig. 2.29) show six semi-monodisperse distributions: debris and doublets are still present in the results but the majority of the particle sizes detected for each nominal droplet size fall well within a narrow range. The mean diameters for each case, provided in Tab. 2.5, are consistently on the order of 1 μm larger than those measured previously at the University of Minnesota. The most likely cause for this increase in diameter size is the aging shelf life of the DEHS and methanol mixture. Over time and as the vessel containing the 5% DEHS mixture was opened and closed during tests, the methanol slowly evaporates off, leaving behind an effectively higher concentration of DEHS. The study conducted at the University of Minnesota was performed with freshly mixed DEHS and methanol, whereas the results presented in Section 2.5 were obtained from a mixture that was approximately one month old.

The fluorescein was mixed into a fresh batch of 5% DEHS in methanol solution and the resulting droplet diameters for the same MDG settings are presented in Fig. 2.30. Due to the continued presence of dust and debris in the test section, the mass-weighted distributions are again used to determine the uniformity of the particle sizes (Fig. 2.31). The non-uniformity

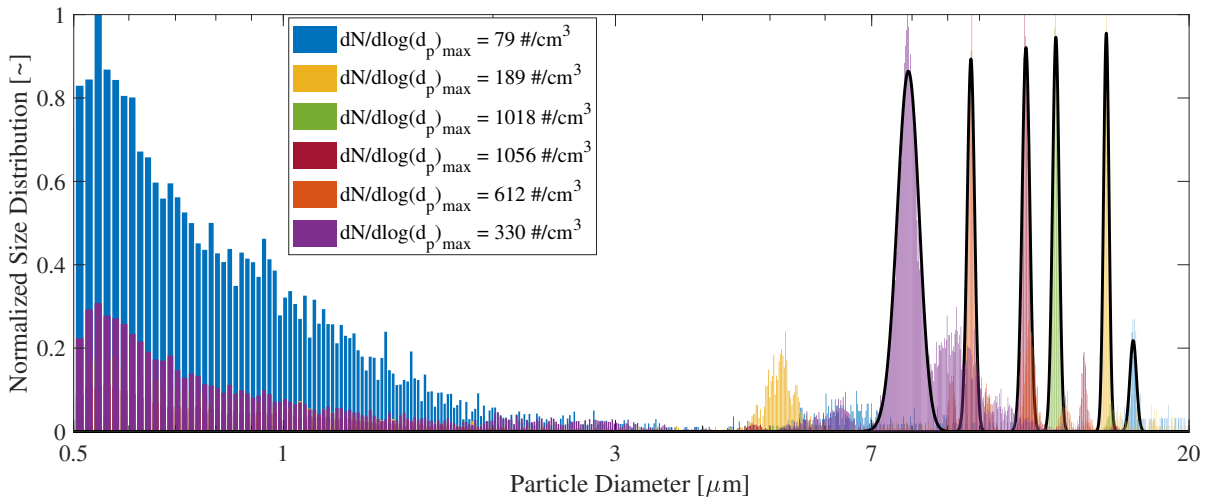

Figure 2.30: Geometric particle size distribution by number count normalized by the maximum bin value for each case with a Gaussian curve fitted to each data set for the fluorescein-doped DEHS droplets.

of the particle sizes produced is evident for the d_p = 11.7 μm and d_p = 7.90 μm droplets; a doublet is produced at $d_p \approx 14$ μm for the former, and a broad spectrum of sizes ranging from 7-12.5 (albeit the dominant size is noticeably at 7.9 μm) for the latter. The fluorescein-doped DEHS droplets are comparable in size to the pure DEHS droplets measured using the month-old solution, and also on average 1 μm larger than those measured using the test rig at the University of Minnesota. Since the measurements made at the University of Minnesota were under the most ideal conditions (sealed, clean chamber), those are likely the most accurate representation of the actual particle diameters produced by the MDG 1530.

2.5.2 Methodology

In the wind-tunnel tests, the fluorescein samples were collected by mounting a wooden board covered with a piece of filter paper in the test section so that it would be exposed to the particle-laden flow, shown in Fig. 2.32. Filter paper was chosen for its high strength and absorp-

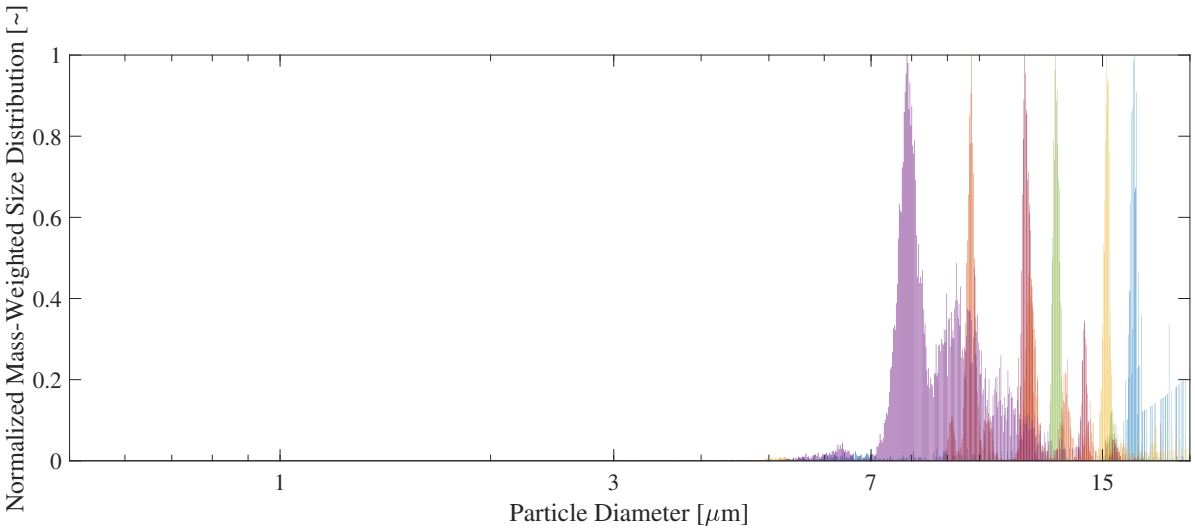

Figure 2.31: Geometric mass-weighted particle size distribution normalized by the maximum bin value for each case for the fluorescein-doped DEHS droplets.

tion, as it would need to capture the particles while not being torn apart by the high-speed flow. The board was centered in the test section and had a frontal cross-section measuring 19 mm × 254 mm (0.75 in × 10 in), with the longer dimension aligned vertically. After each multi-phase test, the filter paper was divided into 19 mm × 10 mm segments and the segments were placed in a 3 ml bath of highly diluted sodium hydroxide solution and agitated to release the fluorescein. A 0.25 ml volume of the resulting sample was then pipetted into a VWR Avantor 96 well microplate. The relative fluorescence of each well in the microplate was read by a Tecan Spark® multimode microplate reader.

Since the Tecan Spark® outputted the fluorescence reading in terms of a relative fluorescence, a set of calibration solutions were prepared for data conversion to allow quantitative concentrations to be determined. To account for the sodium hydroxide in the fluid used to extract the fluorescein from the filter paper, fluorescein was added directly to the same dilute sodium hydroxide solution and further diluted with water to achieve a set of solutions with varying quantities of fluorescein. An exponential curve was fitted to the data and Fig. 2.33 shows this function to be

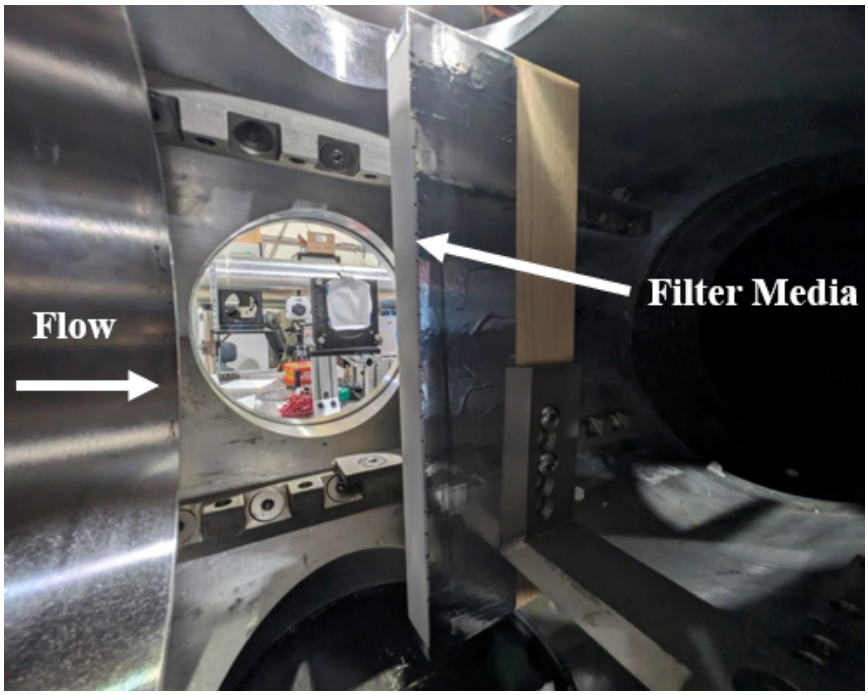

Figure 2.32: Particle impact board placed inside the MIST test section.

in good agreement with the measured values. Control solutions were also created to measure the fluorescence of the filter paper, pure DEHS, and DEHS in methanol: in each case, the measured relative fluorescence was on the order of unity meaning that they do not emit a green wavelength when excited with a violet/blue wavelength. Therefore, the relative fluorescence measured by the Tecan Spark® comes only from the fluorescein itself.

The particle count was obtained by dividing the mass of fluorescein deposited on each filter paper sample (obtained from the relative fluorescence to fluorescein concentration conversion) by the mass of fluorescein in a particle. This was found by multiplying the pre-evaporated droplet volume with the mass concentration of fluorescein in the aerosol mixture. The extant droplet volume was calculated from the theoretical droplet diameter based on the operating conditions of the MDG:

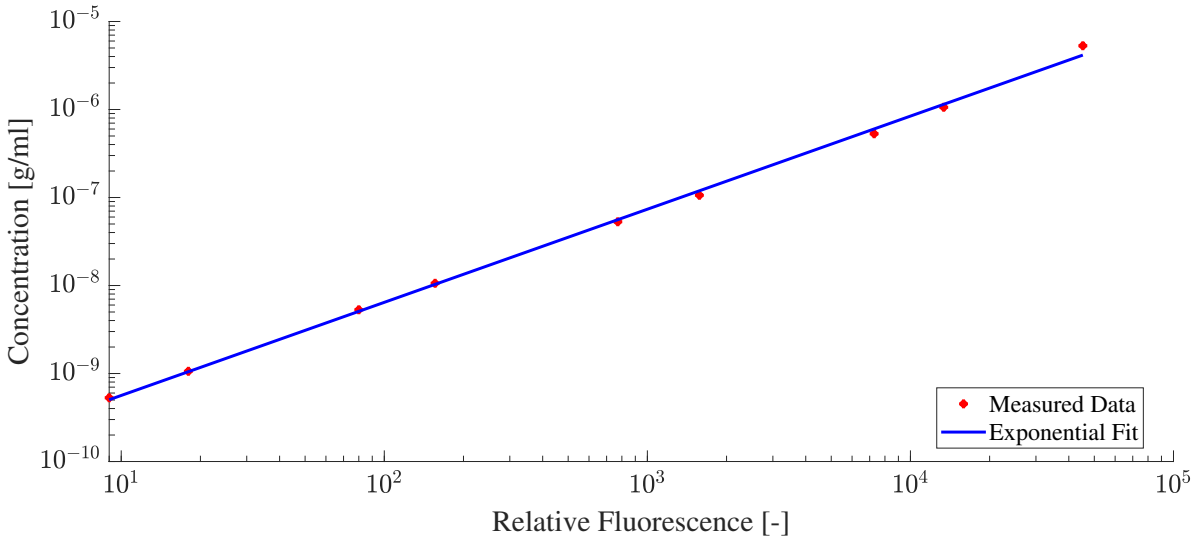

Figure 2.33: Calibration curve for converting relative fluorescence of fluorescein in dilute sodium hydroxide to a known concentration.

$$d_d = \left(\frac{6Q}{\pi f}\right)^{\frac{1}{3}} \quad , \tag{2.16}$$

where Q is the liquid flow rate and f is the frequency. Once the total number of particles on a sample was found, the particle concentration was calculated by dividing the particle count by the volume of gas impacting the sample during the test time.

The volume of gas was obtained using the pitot rake pressure traces (described in section 2.2): the pressure trace was then converted into a velocity profile (see Figs. 2.34 and 2.35), which was integrated over the test time from flow start-up to flow unstart using the information from the sensor at r = 22.8 mm. To simplify the calculation during tunnel start-up, a linear fit was used for the velocity from flow arrival to the steady flow velocity. The volume was then calculated by numerically integrating the velocity profile such that

$$Volume = A \int u\, dt \quad . \tag{2.17}$$

The total flow volume through the tunnel from start-up to unstart was compared to the total available volume of aerosolized gas in the charge tube (from the nozzle throat to the butterfly valve) to ensure that it was an accurate representation of the multi-phase flow. It was found that the aerosolized portion of the flow is consumed approximately 20 ms before the unstart shock arrives. Therefore, the volume of the available aerosolized gas, which was comparable to the volume of fluid generated in the first 60 ms of flow from flow arrival, was used for the calculations.

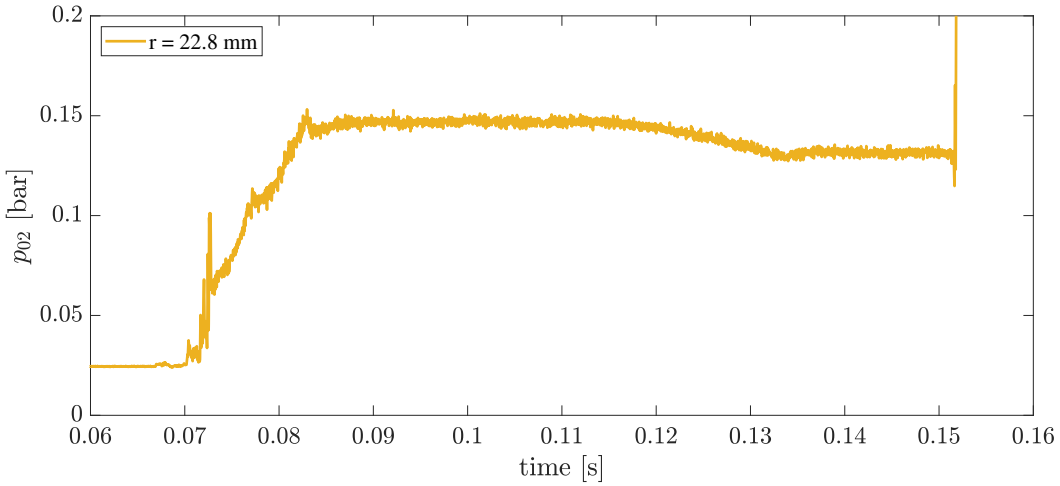

Figure 2.34: Pitot rake pressure traces for a charge tube pressure of 1 bar at the nozzle exit.

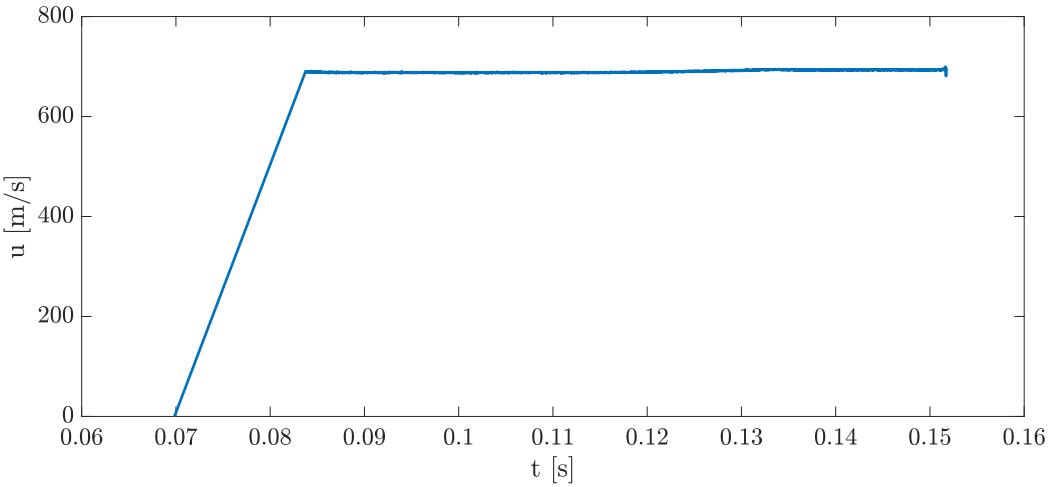

Figure 2.35: Assumed velocity profile based on the pressure trace from tunnel start to unstart for the probe at r = 22.8 mm, with a linear fit from flow arrival to the steady flow velocity.

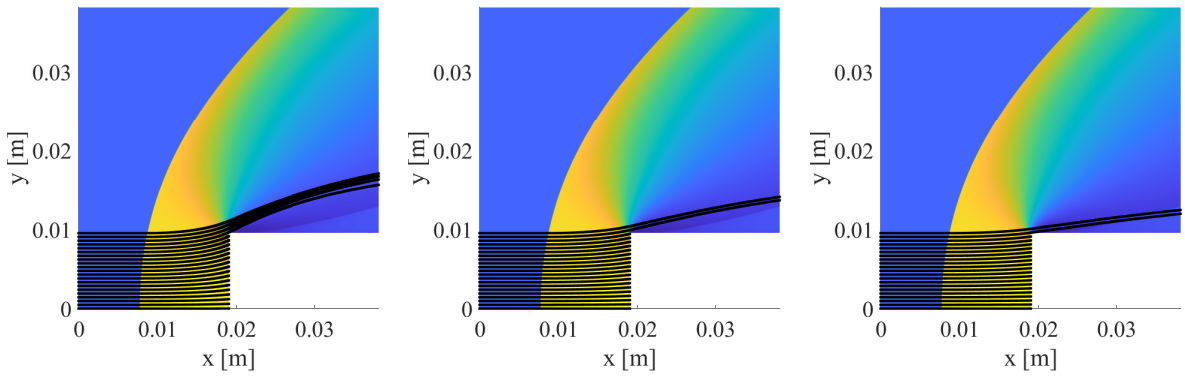

Figure 2.36: Particle pathlines for (a) d_p = 6.95 μm, (b) d_p = 10.6 μm, and (c) d_p = 15.6 μm in the Mach-4 flowfield of the impact board, overlaid on the flow density profile.

2.5.3 Correction for Particle Concentration due to Particle Deflections

The target board for the collection of the fluorescein-doped particles produces a large bow shock in Mach-4 flow, and the flowfield behind this bow shock can force the particles to deviate from a linear path. A calculation was therefore performed in order to quantify the percentage of particles that were expected to impact the board. For these calculations, a two-dimensional flowfield, for a fill pressure of p_{fill} = 0.7 bar and T_{fill} = 296 K, was generated with the AMROC (Adaptive Mesh Refinement in Object-oriented C++) software developed by Deiterding [92], and following the methods of Laurence et al. [93]. 201 equally-spaced particles were then initiated upstream of the board and the path-lines were traced following the same methods as in Section 2.3. Some example path-lines for simulations with different particle sizes are shown in Fig. 2.36. The resulting percentage of particles that impact the board are summarized in Tab. 2.6 for the various particle sizes. For the freestream particle concentration calculations, the resultant concentration obtained from the calculations performed in the section above are then divided by the impact percentage to yield the actual freestream particle concentrations.

Table 2.6: Particle Impact Percentage.

d_p (μm)	Impact Percentage (%)
6.95	83.6
8.75	88.1
10.6	90.1
11.6	91.5
15.6	94.0

2.5.4 Particle Concentration Measurements

Wind-tunnel concentration measurements were obtained for a variety of droplet sizes and durations of MDG operation, and were related to the equivalent pure DEHS droplet diameter since that is the important parameter for aerodynamic testing involving multi-phase flows in MIST. To begin with, the mean profile of the particle concentration for the various available droplet diameters is presented in Fig. 2.37, where y = 0 mm is the nozzle center line and the charge tube was filled to p_{fill} = 0.7 bar. Each profile is shown based on the discrete sample locations and is therefore not presented as a smooth curve. For each run, the MDG was operated long enough to result in a theoretical concentration of 50 particles/cc in the freestream, assuming no losses due to deposition in the tunnel or particle settling time. For the larger droplets ($\geq$ 10.6 μm), this was evidently an inaccurate assumption, with measured concentrations below 30/cc. This might be expected, since the lower frequency for particle generation (on the order of 70 kHz) for these sizes meant that the MDG needed to be run for longer, and the larger diameters meant that the settling time was significantly shorter (on the order of one minute), both resulting in greater difficulty for keeping the particles airborne in the charge tube during the required filling time. The results improve as the particles get smaller and even exceed the desired concentration. To calculate the theoretical MDG operation time for the production of 50 particles/cc, the settling

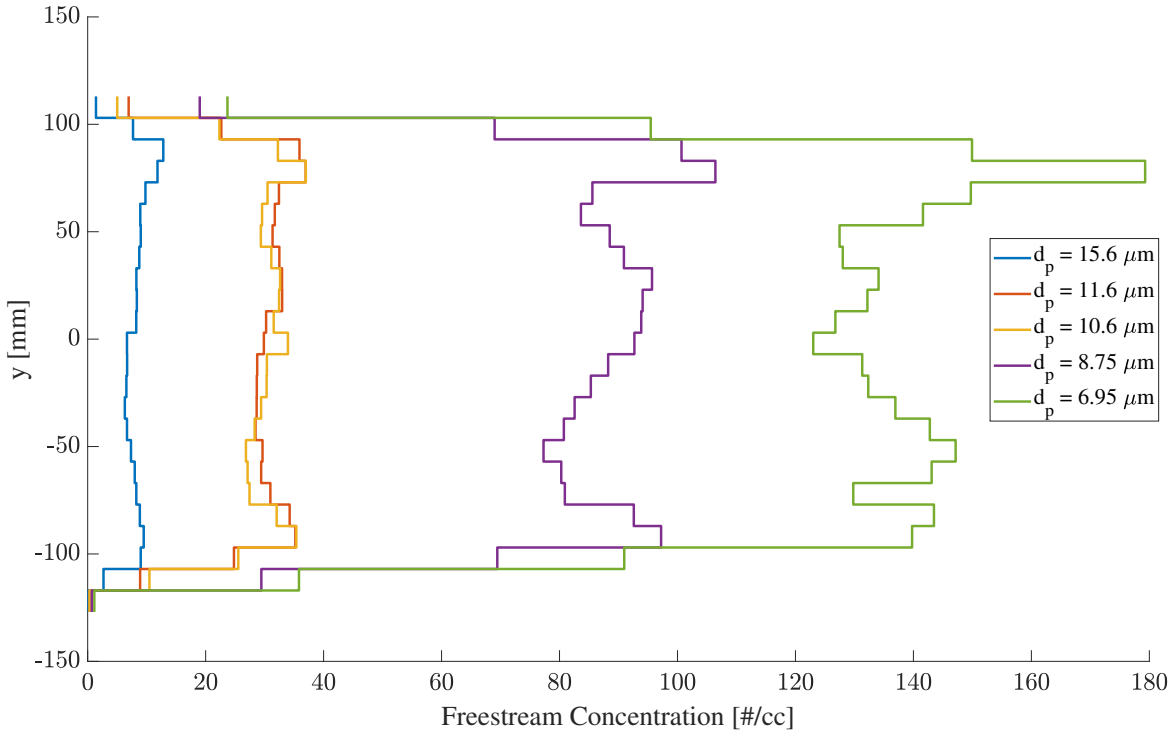

Figure 2.37: Profile of the freestream particle concentration for various particle diameters driven by a charge tube pressure of p_{fill} = 0.7 bar.

time for the particles to travel from the MDG head down the drying column and into the charge tube was added to the time of production for the total required number of particles. However, with the addition of the suction system lining the top of the charge tube, the particle flow into the charge tube was accelerated compared to simply relying on gravitational settling. The original target of 50 particles/cc was therefore no longer the limiting case and higher concentrations than expected could be obtained.

The mean particle concentration distributions of the d_p = 15.6 μm and d_p = 11.6 μm particles have a shallow concave shape, where the particle count towards the edge of the free jet is slightly higher than at the center. This shape is consistent with the results from the two-dimensional simulations in Section 2.3.3, in which an unfocused path through the nozzle due to

the larger particle Stokes number for these sizes resulted in a conical dispersion, and thus concentrating the particles towards the edge of the free jet. The d_p = 10.6 μm particle profile takes the shape of a shallow 'W', where the concentration is higher at the edges, but rather than having a minimum at the center line, the concentration initially decreases towards the center and then increases to a local maximum. This profile is amplified for the d_p = 8.75 μm, accompanying a sharp rise in the particle concentration; this indicates an increased efficacy of the ventilation system in the charge tube (see Section 2.1.3) for the smaller particle sizes. The rise in concentration towards the center line could be caused by the presence of the plug valve mechanism in the center of the charge tube. As the particles make their way around the piston housing, the smaller Stokes number allows the smaller particles to follow the streamlines that carry them back towards the center of the charge tube, increasing their presence at the center of the nozzle exit. The d_p = 6.95 μm particles exhibit a more irregular distribution along the nozzle exit profile although at much higher concentrations since they are more buoyant and have a smaller particle Stokes number, and thus are more receptive to minor changes in the operation settings of MIST. The much increased concentration for this particle diameter can be attributed to a higher production rate (on the order of 120 kHz).

A repeatability study of the mean particle concentration and distribution in MIST was performed using a charge tube fill pressure of p_{fill} = 0.7 bar. Figure 2.38(a) shows typical results for d_p = 15.6 μm particles. Operational times of 35 and 50 minutes were chosen in order to produce theoretical freestream concentrations of 100 and 150 particles/cc, respectively. In each case, at least one repetition was performed. Clearly, the obtained particle concentrations for this particle diameter are again well below the theoretical values that ignore deposition and settling, but the tunnel nevertheless appears to produce generally repeatable conditions. The exception to this is

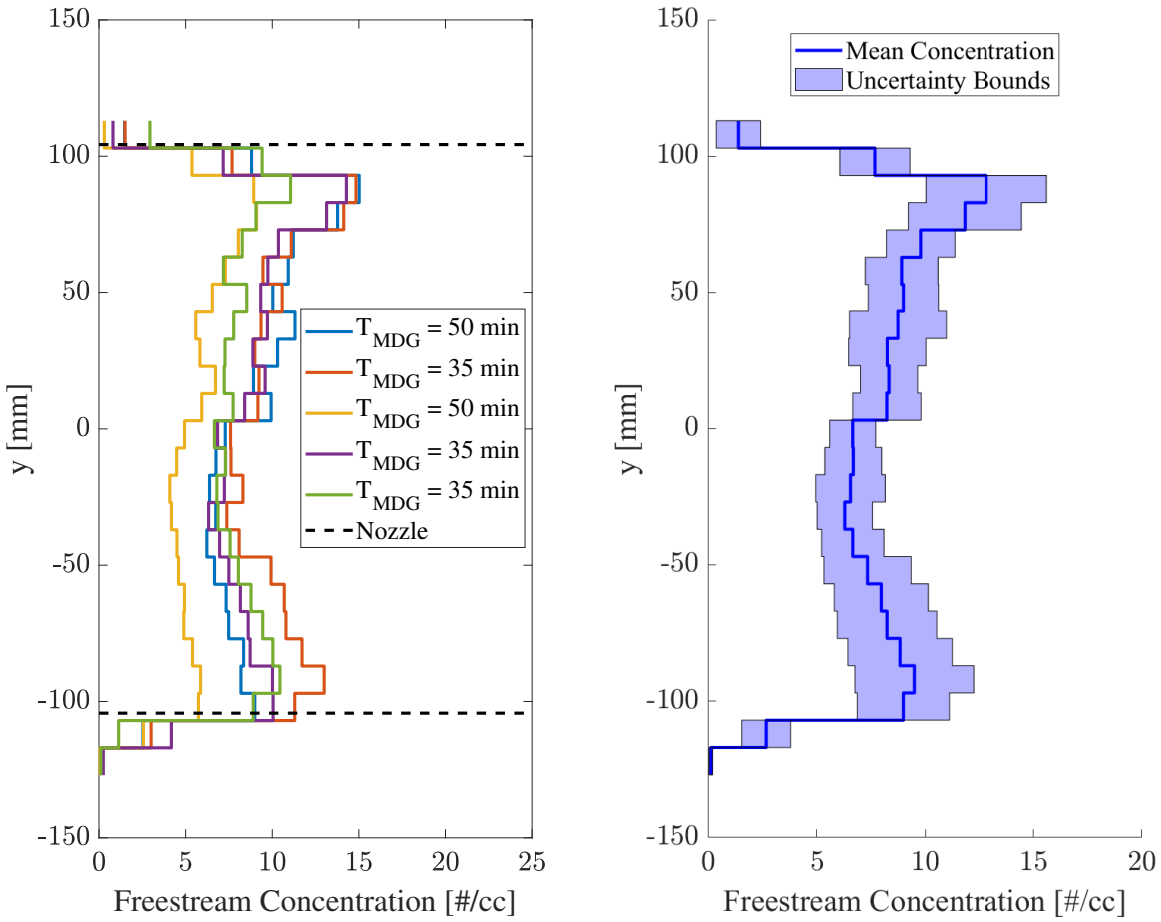

Figure 2.38: Profile of the freestream particle concentration for (a) repeated tests using d_p = 15.6 μm and MDG run times of 35 and 50 minutes and (b) the mean profile with uncertainty bounds for a 95% confidence interval.

Table 2.7: Freestream particle concentrations along the MIST test section centerline.

d_p (μm)	C (#/cm^3)
6.95±0.23	123±49.3
8.75±0.25	92.7±10.3
10.6±0.35	34.0±7.21
11.6±0.45	29.9±5.22
15.6±0.88	6.67±1.07

the yellow curve, which diverges somewhat from the others. There is evidence of MIST reaching a limiting particle production since both the 35 and 50 minute operation of the MDG produce essentially the same concentrations. By averaging over these tests, a mean concentration profile is shown in Fig. 2.38(b), with the uncertainty bounds for a 95% confidence interval indicated. The standard deviation is strongly affected, however, by the outlying yellow curve noted earlier; the mean concentration and uncertainty at the nozzle centerline change from 6.67 ± 1.07 particles/cc to 7.10 ± 0.51 particles/cc when this result is excluded.

The same procedure was repeated for the other particle sizes: the results are presented in Figs 2.39 - 2.42. In each case, a minimum of three repetitions were performed and all but one particle diameter conditions are shown to be generally well reproducible. Of the concentration profiles, the d_p = 6.95 μm is the least reproducible as the uncertainty is shown to be at 40% of the mean. Although experiments using this condition must account for the large concentration uncertainty, they could still provide useful insight into certain flow physics as well. Since most experiments in MIST are conducted at or near the centerline of the test section, the concentrations for each particle diameter and their respective uncertainties are summarized in Tab. 2.7. The uncertainty in the concentration of particles in the freestream along the test section centerline for the four larger particles presented ranges from 11-21% of the mean value.

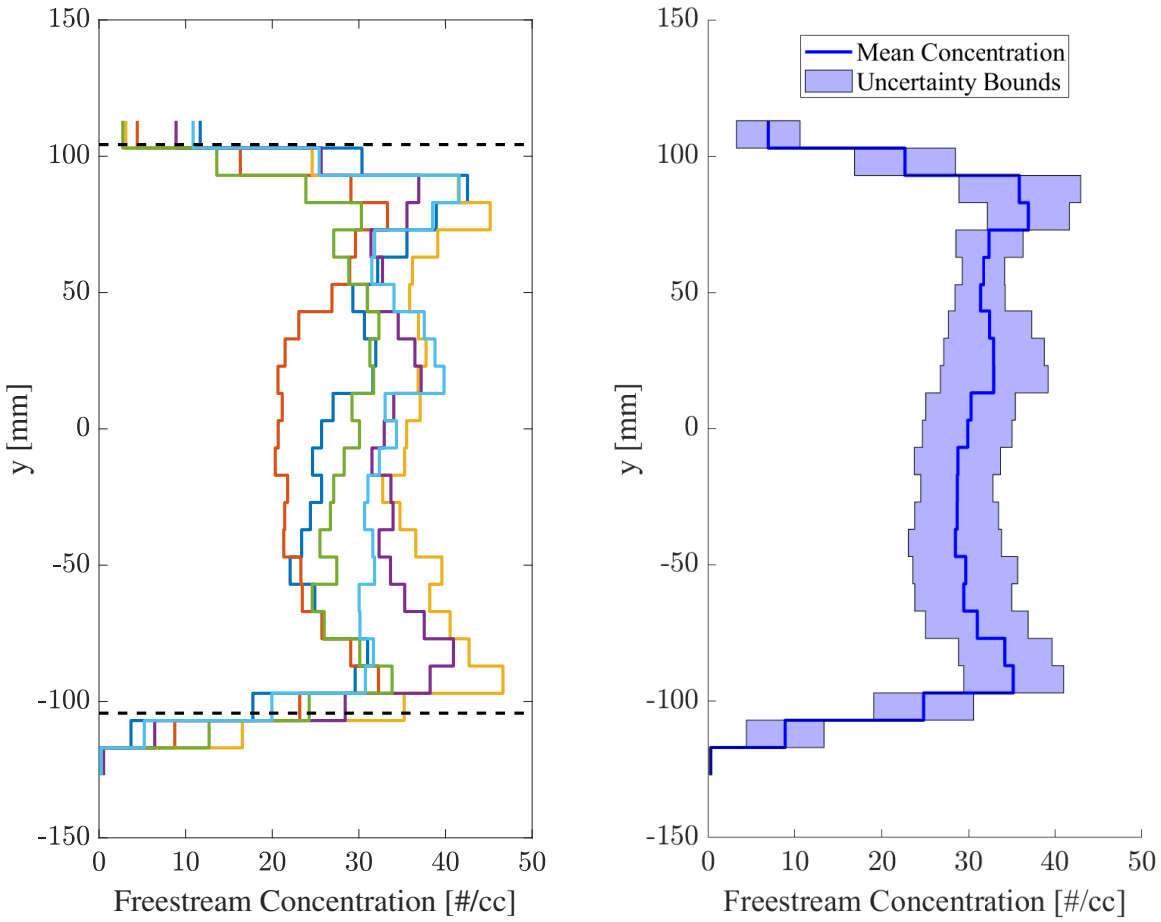

(a) (b)

Figure 2.39: Profile of the freestream particle concentration for (a) repeated tests using d_p = 11.6 μm and MDG run times of 20 minutes, and (b) the mean profile with uncertainty bounds for a 95% confidence interval.

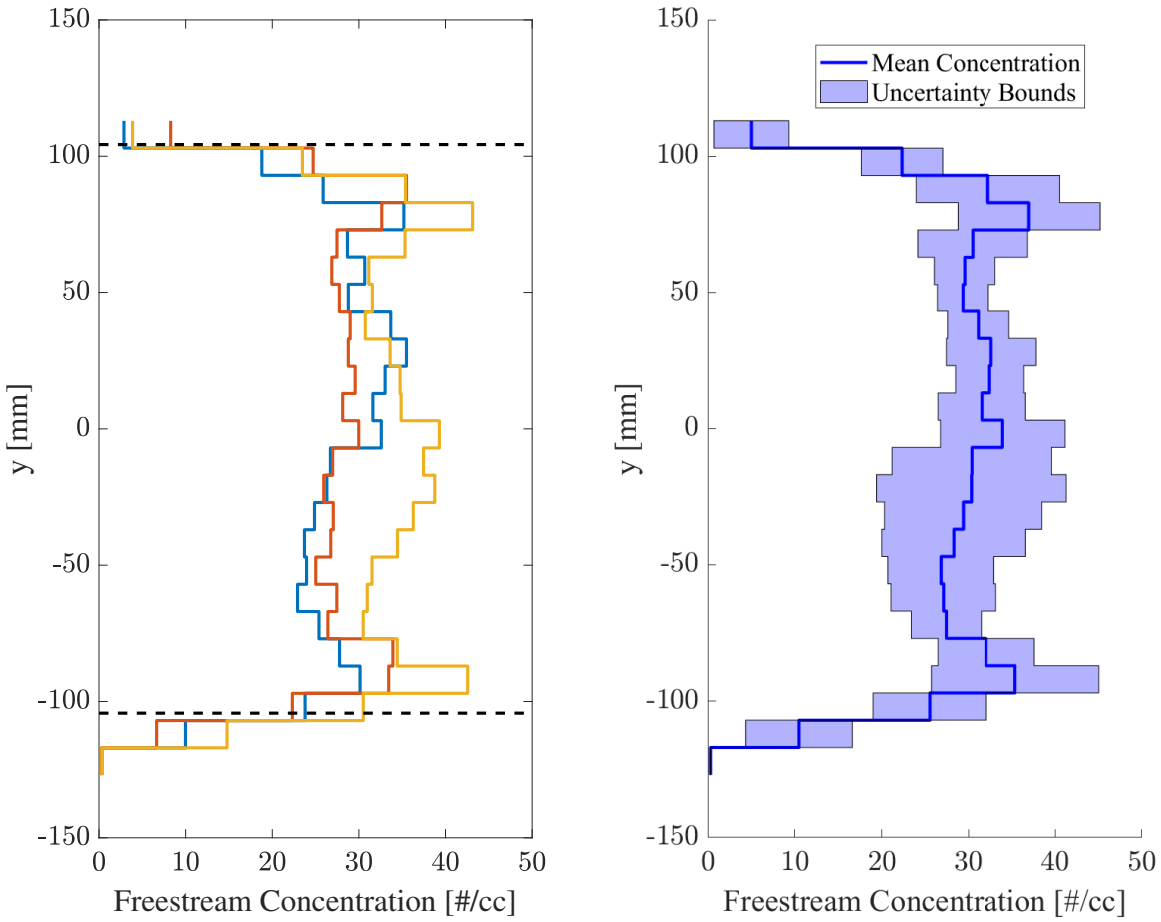

(a) (b)

Figure 2.40: Profile of the freestream particle concentration for (a) repeated tests using d_p = 10.6 μm and MDG run times of 27 minutes, and (b) the mean profile with uncertainty bounds for a 95% confidence interval.

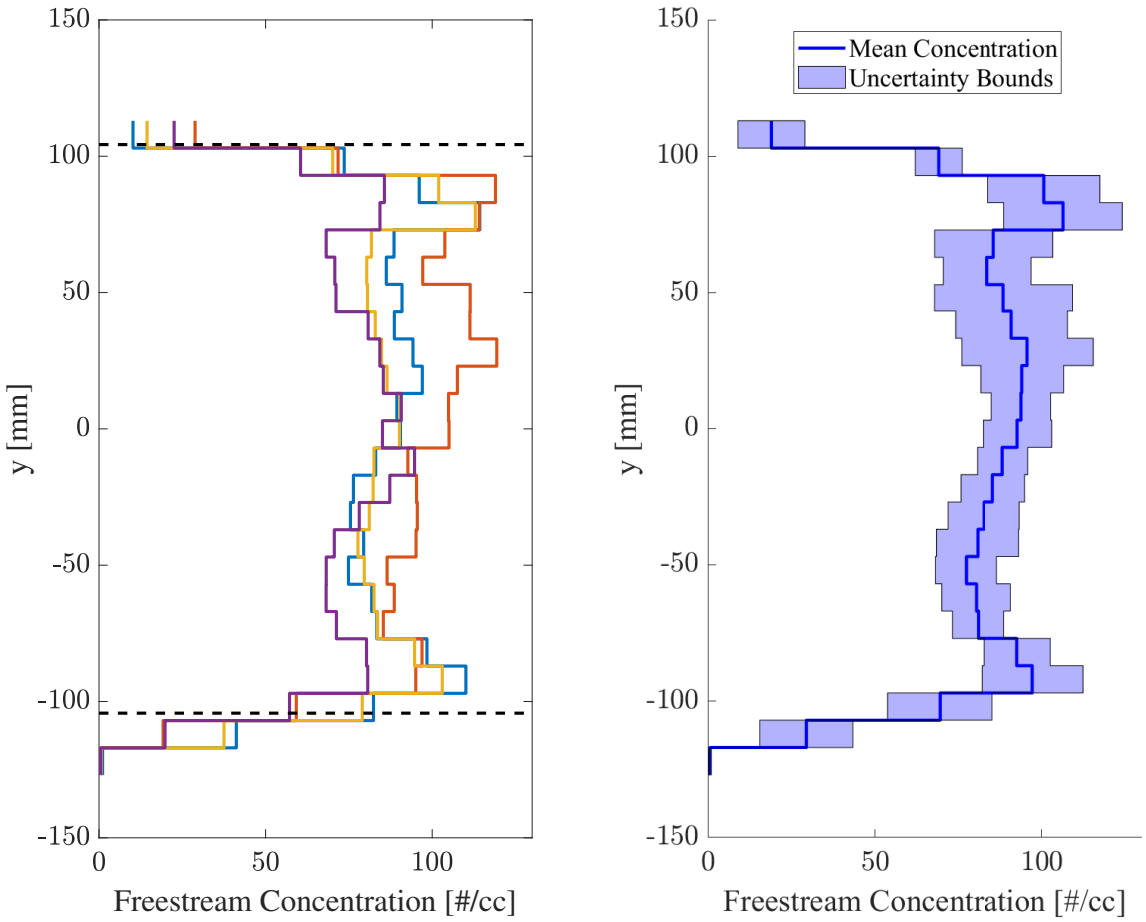

(a) (b)

Figure 2.41: Profile of the freestream particle concentration for (a) repeated tests using d_p = 8.75 μm and MDG run times of 24 minutes, and (b) the mean profile with uncertainty bounds for a 95% confidence interval.

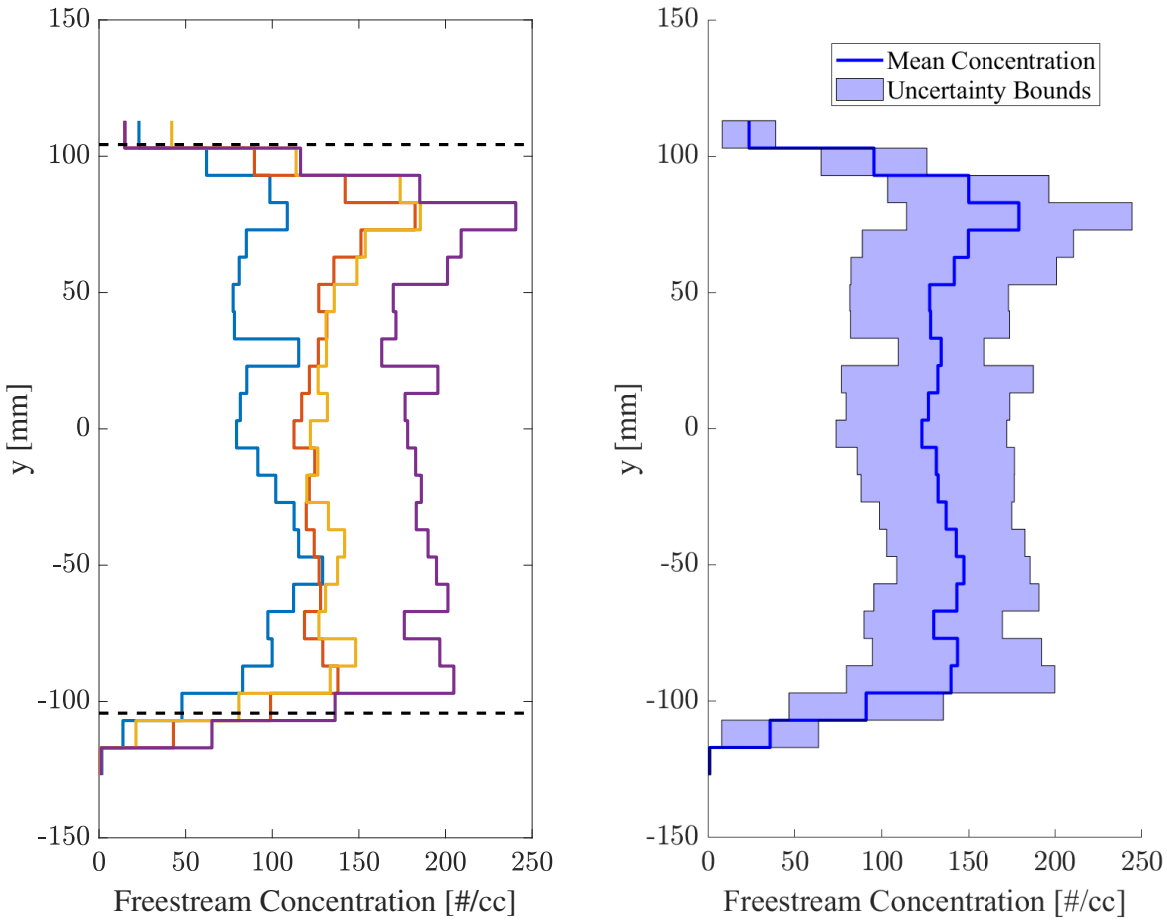

Figure 2.42: Profile of the freestream particle concentration for (a) repeated tests using d_p = 6.95 μm and MDG run times of 32 minutes, and (b) the mean profile with uncertainty bounds for a 95% confidence interval.

2.6 Conclusions

The commissioning of MIST will allow for experimental investigations of multi-phase flow phenomena at high-supersonic speeds. MIST is a Mach-4 Ludwieg tube with a fast-acting plug valve to ensure reliable and repeatable operation. The wind tunnel is operational at Mach 3.75-4 and has been calibrated under clean test conditions using a pure nitrogen test gas for unit Reynolds numbers spanning $\sim 2.5\times10^6$ m^{-1} to $\sim 24\times10^6$ m^{-1}. Steady test times ranged from 30 to 40 ms, with an average startup time of 15 ms. The pitot rake study indicated a 160 mm diameter core flow at the nozzle exit that reduces to 140 mm at the middle of the tunnel viewing window. An analysis of the pressure fluctuations at various radial locations indicated that the wake of the plug valve produces no significant adverse effects on the flow.

With the incorporation of the TSI 1530 aerosol generator, MIST is capable of multi-phase flows with both liquid and solid particles, though the latter has not yet been implemented. A characterization study established seven monodisperse particle sizes that can be produced using a solution of 5% DEHS by volume in methanol ranging from 4.11 μm to 15.6 μm with a standard deviation in each case of less than a micron. A series of visualization methods confirmed the presence of particles in the freestream and were also used to estimate the particle velocities in the freestream. These values were found to be on the order of 100 m/s lower than the expected nozzle exit velocities of the particles. This difference in velocity is concernedly large, however, several factors can lead to large uncertainties in the measurements with the given setup.

One- and two-dimensional particle trajectory simulations utilizing computationally generated flowfields and spherical particle drag models were applied to study the transport of particles through the nozzle. The one-dimensional simulations were used during the wind-tunnel

design phase to establish survivable particle sizes that could be used in MIST by comparing predicted Weber numbers with a limiting critical value obtained from the available literature. A two-dimensional study was conducted to predict the particle profiles and velocities at the nozzle exit for comparison to the experimentally obtained results. The results showed that the largest particles within the available range do not closely follow the path of the fluid due to their high Stokes numbers: the particles are funneled towards the throat in the converging section of the nozzle and then show a delayed response to the rapid expansion in the diverging section. Smaller particles, on the other hand, tracked the fluid streamlines more closely, resulting in a more even distribution at the exit.

Lastly, a unique experimental study involving fluorescent particles was used to characterize the particle concentration in the freestream. The DEHS/methanol solution used to generate the particles was doped with fluorescein and an impact beam covered with filter paper was placed in the wind-tunnel test section. During tunnel operation, the fluorescein-doped particles were deposited onto the paper, and this deposited material was subsequently removed using a sodium hydroxide bath and analyzed using fluorescence spectroscopy. The measured intensity of the fluorescence was converted into a known value of fluorescein mass using a predetermined calibration. From this measurement, the amount of particles needed to deposit this mass was extracted and the particle concentration and distribution profiles were determined for the various particle diameters. Repeatability tests were carried out for each particle diameter tested showing that MIST can produce reproducible, particle-laden flows for five of the seven characterized DEHS particle diameters. The freestream particle number concentrations increased as the particle diameter decreased, which was expected due to the increase in buoyancy of the smaller particles. Furthermore, the nitrogen ventilation system was shown to assist with keeping the particles airborne

in the test section, allowing for a greater accumulation of particles in the test section. This was represented by the smaller particle diameters showing a number concentration much greater than the theoretically expected value when gravitational settling of the particle was considered.

With the development and characterization of MIST, experimental high-speed, particle-laden flow studies can now be conducted which will contribute to closing the knowledge gap on this field of study. MIST is the only facility in open literature capable of producing multi-phase flows with droplet sizes ranging from 4.11-15.6 μm and flow Mach numbers of 3.75-4. The extensive characterization studies provide useful data for comparison with computational results as nearly all characteristics of the fluid, particles, and particle concentrations are accounted for.

Chapter 3: Force Measurements on Free-Flying Spheres in a Supersonic, Particle-Laden Flow

3.1 Overview

In this chapter, MIST is used to investigate the effect of particle-laden flow on the drag force experienced by a free-flying sphere. Bi-telecentric visualization and an improved edge-tracking technique are employed to determine the sphere's trajectory in the wind tunnel from which the drag acceleration, and thus drag force, are calculated. A comparison of the drag coefficients for spheres exposed to the five particle-laden flows characterized in Sec. 2.5.4 to that of spheres in a baseline, clean flow is presented. The results are also compared to the expected drag coefficient calculated using the Loth drag model and assuming an effective flow density for the particle-laden flow. Lastly, contributions of individual particle impacts to the drag coefficient augmentation were estimated based on the bulk data.

3.2 Facility

For these experiments MIST was operated at two free-stream unit Reynolds numbers: $Re_\infty = 3.41 \times 10^6$ m^{-1} and $Re_\infty = 4.73 \times 10^6$ m^{-1} ($p_{fill} = 0.7$ bar and $p_{fill} = 1$ bar, respectively), in both cases using nitrogen as the test gas. The charge-tube fill pressures were kept at these relatively low

Table 3.1: Run Conditions.

M_∞	Re_∞ ($\times 10^6$ m^{-1})	v_∞ (m/s)	p_∞ (Pa)	T_∞ (K)	ρ_∞ (kg/m^3)
3.79±0.02	3.41±0.03	676	579	76.7	0.025
3.85±0.02	4.73±0.03	679	756	74.8	0.034

Table 3.2: Particle characteristics for the various MDG conditions.

Condition	d_p (μm)	C (#/cm^3)	u_{slip} (m/s)
D7	6.95	123±49.3	-6
D9	8.75	92.7±10.3	-11
D11	10.6	34.0±7.21	-16
D12	11.6	29.9±5.22	-20
D16	15.6	6.67±1.07	-36

values due to the operational limits of the MDG. The higher Reynolds number test condition was used only for experiments with particle-free flow while establishing a baseline drag coefficient for the spheres. The MDG was operated for the lower Reynolds number condition shown in Tab. 3.1 resulting in the concentrations and free-stream slip velocities presented in Tab. 3.2. The slip velocities were obtained by subtracting the nozzle exit velocities of the particles provided in Tab. 2.3 from the gas exit velocity in the simulations. Although the simulated conditions do not perfectly match the actual conditions obtained from the pitot rake study, it is assumed that the slip velocity would be of the same order of magnitude. Furthermore, these slip velocities represent a lower bound as the results from Sec. 2.4 indicate that the slip velocities are likely greater.

Three sizes of Delrin® acetal resin spheres were used for the freeflight measurements, with the goal of assessing if the particle diameter to sphere diameter ratio had an effect on the drag force augmentation: 12.7 mm, 19.05 mm, and 25.4 mm diameter, in each case with a tolerance of ±0.0254 mm (0.5 in, 0.75 in, and 1 in diameter, with a tolerance of ± 0.001 in). The spheres were suspended in front of the nozzle, upstream of the test section windows, using a weak release

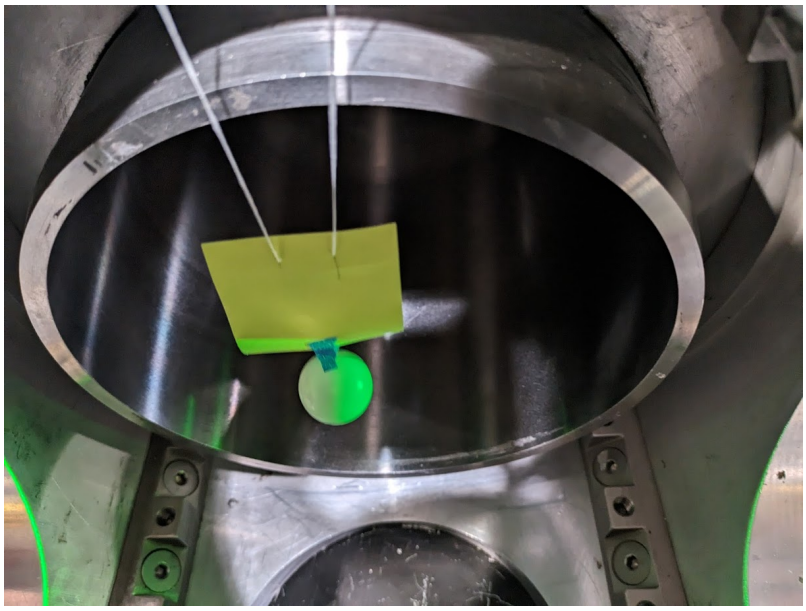

Figure 3.1: View from above of the suspended sphere in front of the nozzle with the weak release mechanism.

system consisting of dental floss, a paper rectangle, and 3M Scotch 2090 masking tape as shown in Fig. 3.1. The floss is fed through the paper rectangle such that the face of the paper is oriented normal to the flow. A thin strip of masking tape, chosen so as not to leave any adhesive residue behind, connects the sphere to the paper. Upon flow arrival, the large drag force generated by the paper detaches the tape from the sphere and rapidly sweeps the suspension system downstream. Although this process imparts a small initial impulse on the sphere in the flow-normal direction, the resulting sphere velocity is negligible in comparison to, and normal to, the flow velocity. Since the spheres were suspended upstream of the test section viewing windows, by the time they became visible the suspension mechanism had been swept well downstream and the spheres were travelling independently. Furthermore, the entirety of the visible sphere flight occurred during the steady flow time. In order to obtain reliable statistics and assess run-to-run variation, a minimum of four experiments were conducted with each particle diameter and sphere diameter combination.

3.3 Diagnostic Techniques

3.3.1 Bi-telecentric Visualization

The spheres in free flight were imaged using a bi-telecentric visualization system consisting of a parallel-light illuminator and bi-telecentric lens. A bi-telecentric lens receives mostly parallel rays of light from the object being inspected and then projects mostly parallel rays of light onto the camera, while providing constant perspective and constant magnification of the object [94] with minimal optical distortions. As a result, bi-telecentric imaging provides improved tracking accuracy over, for example, focused shadowgraphy (another parallel-light method that has been commonly used in such applications) [95]. The bi-telecentric system used in these experiments is shown in Fig. 3.2. On the left, light from a MORITEX Corporation MTI-150-CG-070 high-performance parallel-light illuminator (working distance of 300 mm) is projected into the test section, while on the right, the image is collected with a MORITEX Corporation MTL-15035P-023 bi-telecentric lens (working distance of 300 mm, magnification factor of 0.233, and field of view of 150 mm diameter) and projected into a Vision Research Phantom v2640 high-speed camera. The product of this method is a well defined silhouette of the sphere with negligible dilation and distortion as it traverses the entirety of the test-section window. The illuminator was controlled using a Metaphase Technologies universal LED controller ULC-2 and operated in continuous mode. For the clean flow and 15.6 μm particle cases, the images were sampled at 31,000 frames per second with a pixel resolution of 1024×768 pixels and an exposure time of 15 μs. The remainder of the particle-laden flow cases were sampled at 36,000 fps with a pixel resolution of 1024×576 pixels and an exposure time of 10 μs. This resulted in 470-730

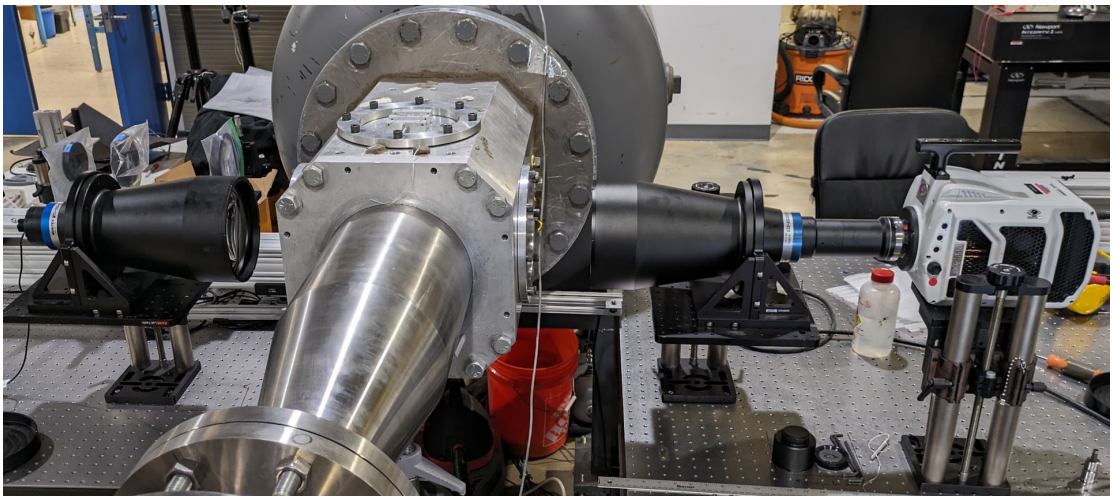

Figure 3.2: Upstream view of the bi-telecentric visualization setup.

frames per test depending on the sphere size and frame rate used. The image resolution remained constant along both settings at 8.62 pixels/mm.

3.3.2 Edge Tracking

Edge tracking is an optical-tracking technique that has been used extensively to determine the forces and moments of free-flying bodies in high-speed flows [93, 95–102]. This method first uses an edge-detection algorithm to identify the edge of the object's silhouette in the image at the pixel or sub-pixel level. Possible algorithms include the Canny [103] or partial area [104] methods, with recent work by Duchene et al. showing that the partial area method improved the accuracy of the edge detection compared to other subpixel techniques [102]. Once the edges of the object's silhouette have been identified, an appropriate geometric shape is fitted to the locus of edge points to identify relevant pose parameters (location and orientation). For a sphere, a circle of the form $r^2 = x^2 + y^2$ it typically fit. However, Duchene et al. [102] made use of a routine that fits a super-ellipse [105], given as

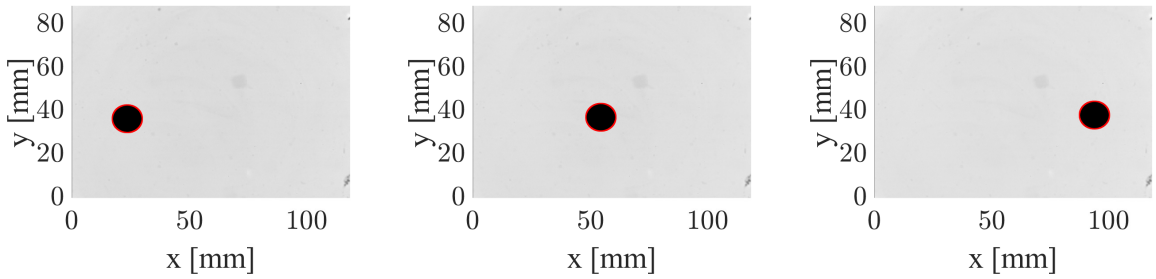

Figure 3.3: Free-flying sphere with a superimposed super-ellipse edge fit in red for three frames in a Mach-4 experiment.

$$r^2 = \frac{(x - x_0)^{\frac{2}{m}}}{a} + \frac{(y - y_0)^{\frac{2}{m}}}{b} \quad , \tag{3.1}$$

and found that it was more accurate than a circle at identifying the center of the silhouette of a sphere due to the slight optical distortions that are still present from misalignment in the setup of the bi-telecentric visualization apparatus. The edge-tracking technique implemented here thus used the partial area method for edge detection and an edge fit using the super-ellipse method. All routines were implemented in MATLAB; an example of a tracked sphere over a sequence of images is shown in Fig. 3.3.

Once the centroid location is identified in every image, the x and y components of the sphere tranjectory can be reconstructed, together with its effective radius. Performing a least squares fit of a circle to the locus of edge points provides the diameter of the sphere in pixels, which is then compared to the known physical diameter of the sphere to obtain a scaling factor. This scaling factor is then applied to the sub-pixel accurate coordinates of the centroid of the sphere from each image that was obtained with the more accurate super-ellipse fitting routine to determine the accurate physical trajectory of the sphere. An example is shown in Fig. 3.4. The primary quantity of interest is the acceleration in the x-direction, representing the acceleration

due to the drag force. To obtain this value, a second-order polynomial is fit to the x-position data such that $x = \frac{a_x}{2}t^2 + u_0 t + x_0$. The error in the measured acceleration using this method scales approximately with $1/\sqrt{n-1}$, where n is the nymber of images within the measurement time Δt, and is given as

$$\frac{S(a)}{a} = \frac{12\sqrt{5}\,(n-1)^2}{\sqrt{(n-3)(n-2)n(n+1)(n+2)}}\frac{s}{a\Delta t^2} \quad , \tag{3.2}$$

where $S(a)$ is the standard error in the acceleration a and s is the standard deviation in the residuals to the quadratic fit [97, 100]. This process makes use of the assumption that the acceleration remains constant throughout the test time. In this case, it is necessary that the velocity of the sphere be much less than that of the flow. After performing the analysis, it was found that the sphere entered the test-section viewing window with approximately $u_s = 0.005u_\infty$ and exited with approximately $u_s = 0.012u_\infty$ for each case. Furthermore, the polynomial fitting technique resulted in errors on the order of $S(a) = 0.001a$.

3.4 Prediction of Drag Augmentation

3.4.1 Drag Augmentation

To first gain an estimate of the effects expected in the experiments, the drag coefficient amplification of the sphere was modeled using the Loth drag model (see Appendix A). This model has been well validated at high Mach numbers and Reynolds numbers above 10,000 [85, 106], and thus at the conditions relevant to these tests. To account for the presence of the particles, the multi-phase flow was treated as a single fluid with the equivalent density of the combined

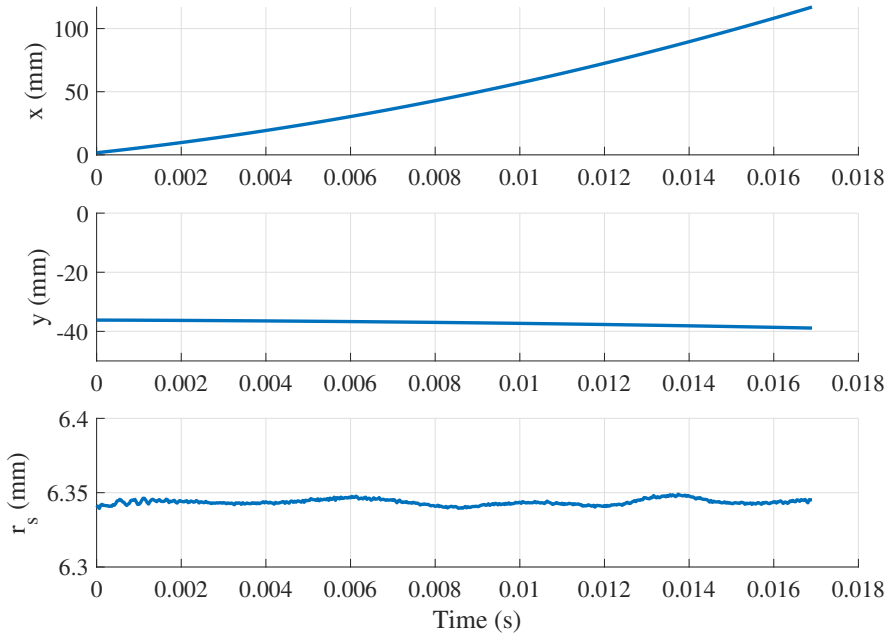

Figure 3.4: Example displacement profiles determined using edge tracking.

particles and gas given by

$$\rho_{eff} = \frac{\rho_{DEHS} \times V_{particles} + \rho_{N_2} \times V_{N_2}}{V_{particles} + V_{N_2}} \quad . \tag{3.3}$$

Here we have effectively assumed that the effect of the particles is to increase the momentum flux of the flow. The drag coefficient then is calculated for each particle diameter in Tab. 3.2 using the experimental flow conditions for $\mathrm{Re}_\infty = 3.41 \times 10^6$ m^{-1}. The modeled spheres have the same density as the experiments, with $\rho_{sphere} = 1.34$ g/cm^3, while the sphere diameter was varied to obtain the drag coefficient at a range of sphere Reynolds numbers (Re_s). Time scales of the experiments are assumed to be too short for any thermal exchange between the flow and the spheres, therefore the sphere temperature was kept constant at $\mathrm{T}_{sphere} = 296$ K. In order to compare the numerically obtained drag coefficient to that measured in experiments, the drag coefficient is normalized by the flow density assuming pure nitrogen gas such that $C_\mathrm{D} = C_\mathrm{D}|_{\rho_{eff}} \times$

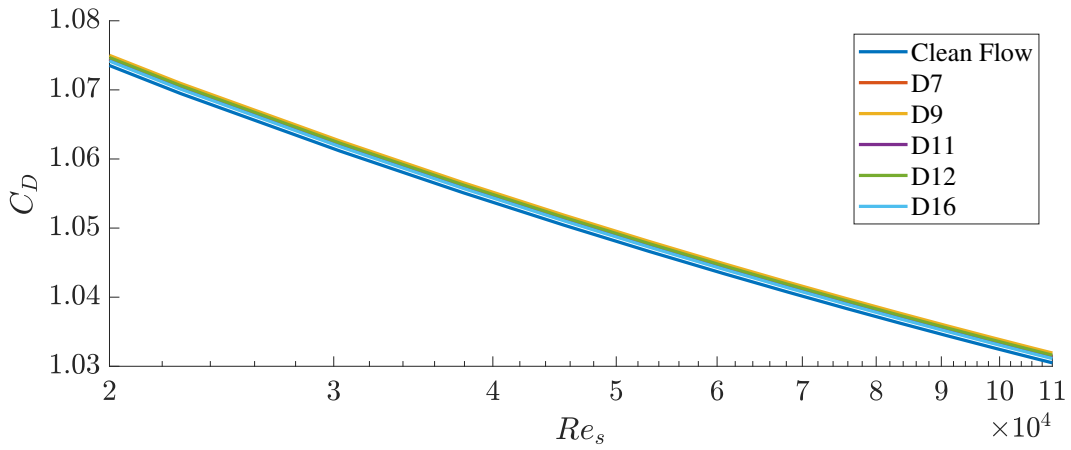

Figure 3.5: Drag coefficient for spheres exposed to supersonic, multi-phase flows calculated using the Loth drag model.

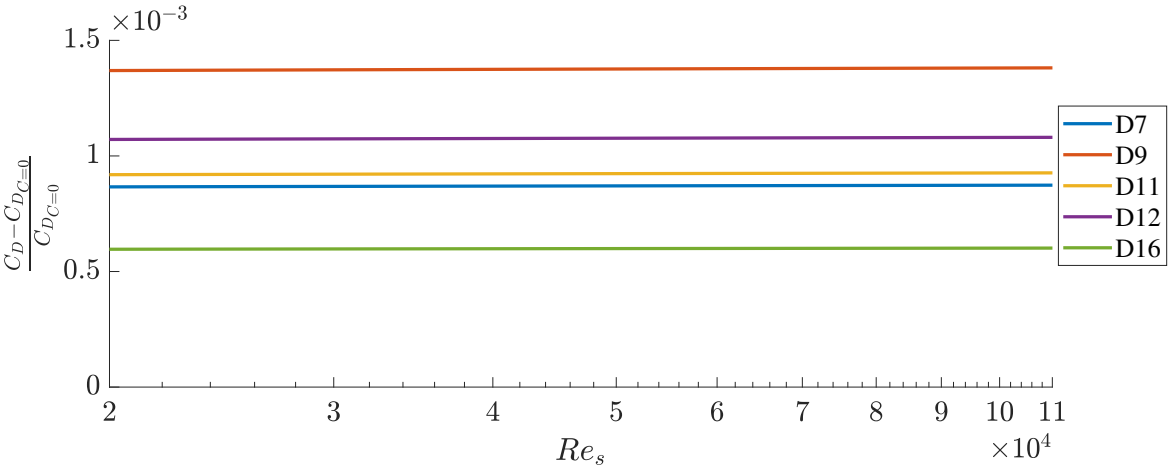

Figure 3.6: Drag coefficient augmentation for spheres exposed to supersonic, multi-phase flows calculated using the Loth drag model.

ρ_{eff}/ρ_∞.

The numerical results, presented in Figs. 3.5 and 3.6, show a slight increase in the drag coefficient for each case of particle-laden flow. By assuming that the flow can be modeled as a higher density fluid, the effect of the multi-phase flow is shown to be constant across the Reynolds numbers of interest. Given the conditions that have been characterized for MIST, it is expected that the combination of particle size and concentration for condition B (d_p = 8.75 μm and C = 81.6 #/cm^3) will produce the largest increase in drag coefficient.

3.4.2 Particle Impingement

The simple method of accounting for the presence of the particles introduced in the previous subsection is unlikely to be accurate if direct impact of the particles with the sphere occurs. Not all particles are expected to hit the spheres, however, since some will be deflected around the body by the flow, but this effect will clearly become less pronounced for larger particles, as they will have larger particle Stokes numbers. To predict the impingement of the particles on the spheres, a process similar to that employed in the nozzle particle simulations was used.

The two-dimensional flowfield around a sphere was generated using the same methods of Laurence et al. [93], with the AMROC (Adaptive Mesh Refinement in Object-oriented C++) software developed by Deiterding [92]. The particles, from each condition in Tab. 3.2, were initialized upstream of the sphere with their respective relative slip velocities. The particle concentrations were not modeled, i.e., the particles were treates as isolated, since the desired outcome of this study is simply to understand if the particle originating from a given upstream location will impact or not. The two-dimensional particle trajectories were calculated using the same methods as those used in Sec. 2.3. Since there was the possibility that the bow shock would produce a strong enough force to break up the particles, an additional layer of calculations was added to the analysis. To simplify the model, the droplets were assumed to remain intact, but the increase in the droplet cross-sectional area was modeled using the equations from Chou and Faeth [107]. For the relevant range of parameters ($13 < We < 20$, $0.0043 < Oh < 0.0427$, $633 < \epsilon < 893$, and $1550 < Re < 2150$), the following equations are applicable:

$$\frac{d_{cro}}{d_0} = 0.5\tau + 1.0 \qquad 0 < \tau < 2 \tag{3.4}$$

$$\frac{d_{cro}}{d_0} = 0.25\tau^2 - 0.18\tau + 1.43 \qquad 2 < \tau < 4 \tag{3.5}$$

$$\frac{d_{cro}}{d_0} = 1.79\tau - 2.51 \qquad 4 < \tau < 5 \tag{3.6}$$

where

$$\tau = t\frac{u_0}{\epsilon^{0.5} d_0} \quad . \tag{3.7}$$

Here τ is the dimensionless time, u_0 is chosen to be the initial velocity of the particle, ϵ is the density ratio of the droplet and the gas, and d_0 is the initial droplet diameter. When the particles are not exposed to the conditions that would allow for the use of these equations, the droplet cross-sectional area was modeled using Eqn. 2.8 and applying the same treatment for larger Ohnesorge number as in Sec. 2.3.

Representative pathlines for the particles entering the region of influence around the sphere are shown in Fig. 3.7. For illustrative purposes, a simulation with smaller 1 μm particles was run in addition to the diameters used in experiments. While most particles of 1 μm diameter are deflected around the sphere, increasing to the smallest experimental diameter (d_p = 6.95 μm) results in impacts except for particles initiated very close to the outermost edge of the sphere.

Impact contour maps are presented in Figs. 3.8-3.10; these indicate whether or not a particle that is initialized at a certain radial position upstream of the sphere would hit the sphere (head-on view). Simulations were run for each particle and sphere size using a distribution of 51 particles along a single radial direction, given the axisymmetric nature of the sphere. The green

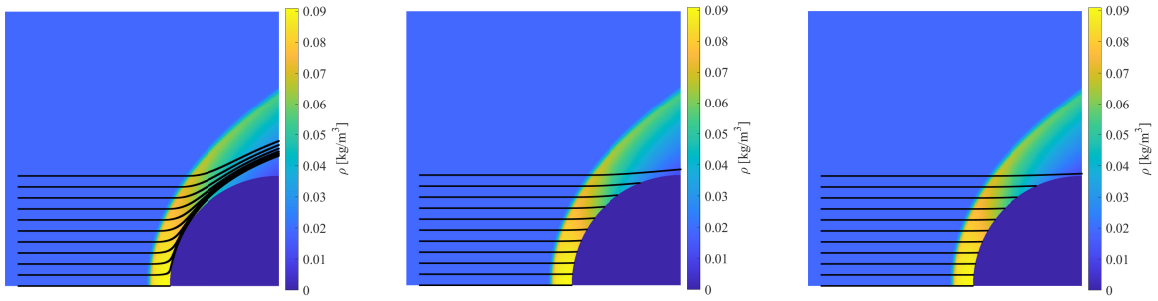

(a) (b) (c)

Figure 3.7: Particle trajectories for (a) d_p = 1 μm, (b) d_p = 6.95 μm, and (c) d_p = 15.6 μm in the flowfield of a 25.4 mm diameter sphere at Mach 4 overlaid on the flow density profile.

Table 3.3: Percentage of particles in a volume that will impact each sphere used in the experiments.

d_s (mm)	d_p = 6.95	d_p = 8.75	d_p = 10.6	d_p = 11.6	d_p = 15.6
12.7	94.1%	94.1%	98%	98%	98%
19.05	90.1%	94.1%	94.1%	94.1%	98%
25.4	89.3%	91.2%	93.2%	94.1%	95%

zone represents particle hits and the blue zone misses. The impact area for each sphere and particle size, as a fraction of the sphere frontal area, is given in Tab. 3.3. Clearly, in all cases, a majority of particles are predicted to impact the sphere. Considering that momentum transfer from directly impacting particles is likely to be more efficient than from flow-following particles, it is anticipated that the drag augmentation will be larger than that predicted by the simulations from the previous subsection in which the particle-laden flow was treated as a fluid with a higher effective density. With 90% or more of the particles impacting the sphere for all but one case, it is expected that the direct momentum transfer from these impacts will have a non-negligible effect on the measured drag coefficient in the experiments.

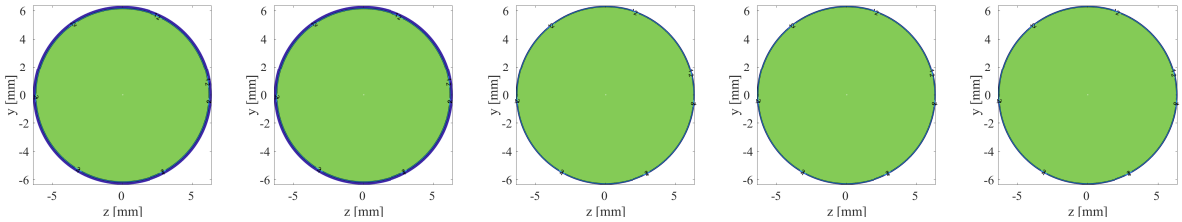

(a) (b) (c) (d) (e)

Figure 3.8: Impact maps showing whether or not particles will hit a 12.7 mm diameter sphere for (a) d_p = 6.95 μm, (b) d_p = 8.75 μm, (c) d_p = 10.6 μm, (d) d_p = 11.6 μm, and (e) d_p = 15.6 μm where green represents a particle hit and blue represents a miss.

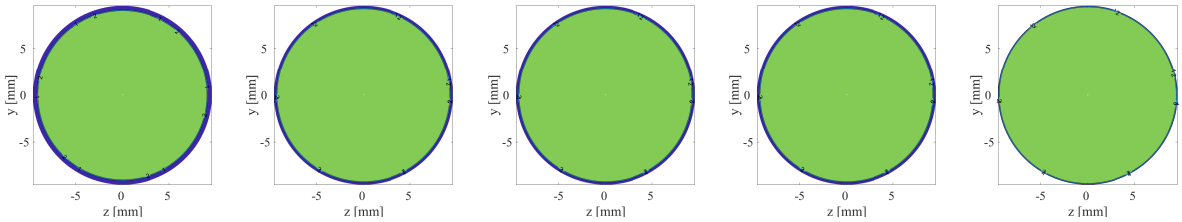

(a) (b) (c) (d) (e)

Figure 3.9: Impact maps showing whether or not particles will hit a 19.05 diameter sphere for (a) d_p = 6.95 μm, (b) d_p = 8.75 μm, (c) d_p = 10.6 μm, (d) d_p = 11.6 μm, and (e) d_p = 15.6 μm where green represents a particle hit and blue represents a miss.

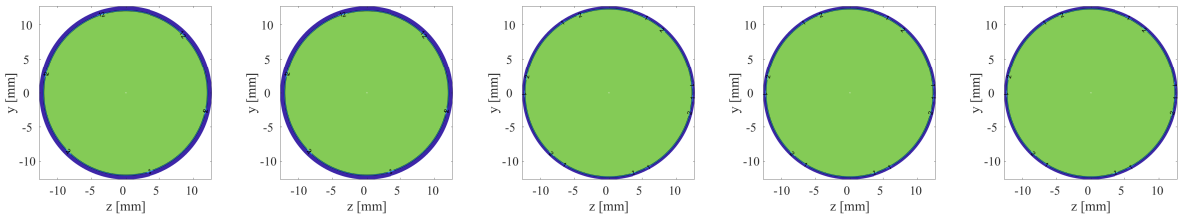

(a) (b) (c) (d) (e)

Figure 3.10: Impact maps showing whether or not particles will hit a 25.4 mm diameter sphere for (a) d_p = 6.95 μm, (b) d_p = 8.75 μm, (c) d_p = 10.6 μm, (d) d_p = 11.6 μm, and (e) d_p = 15.6 μm where green represents a particle hit and blue represents a miss.

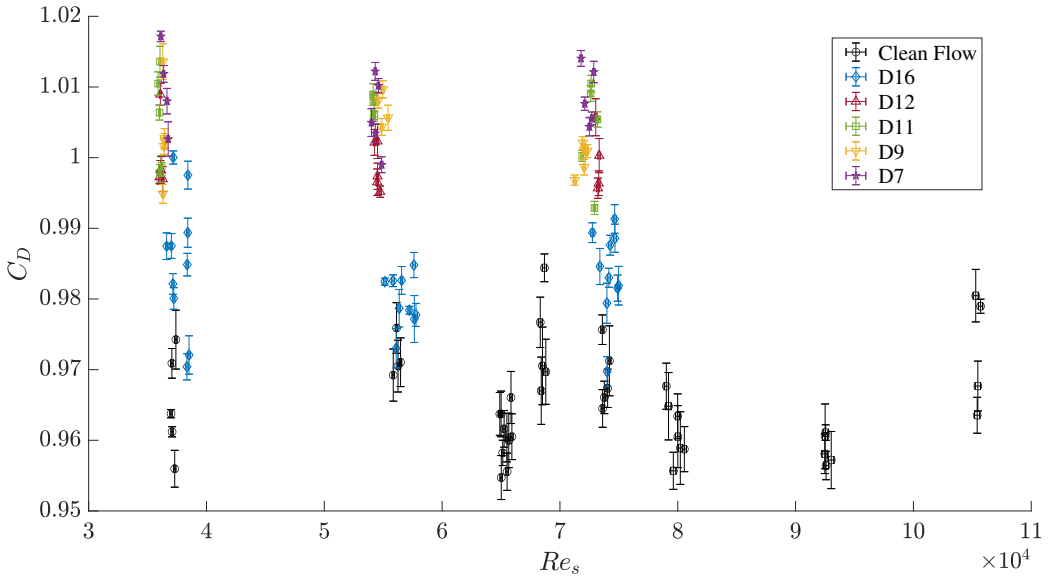

Figure 3.11: Drag coefficient measurement for all runs with their respective uncertainty bars.

3.5 Experimental Results

The drag coefficients over all tests are presented in Fig. 3.11; in each case the drag force measured using optical tracking is normalized by the respective particle-free dynamic pressure and sphere cross-sectional area for the given wind tunnel conditions. This highlights the direct effect of the particle-laden flow on the forces experienced by the sphere. A noticeable, albeit small, increase in the drag coefficient is evident for each droplet size. The low number density of the D16 case appears to limit the drag coefficient increase (~1.75%) compared to the particle-free case, whereas for the other cases (D7-D12) the combination of the particle size and number density balances the results such that they all exhibit a 3.5%-4.5% increase. We see that these measured coefficients are significantly higher than predicted in the previous section. Given this unexpectedly high drag coefficient increase, it is imperative to note that the repetitions at each condition show a consistency of the results.

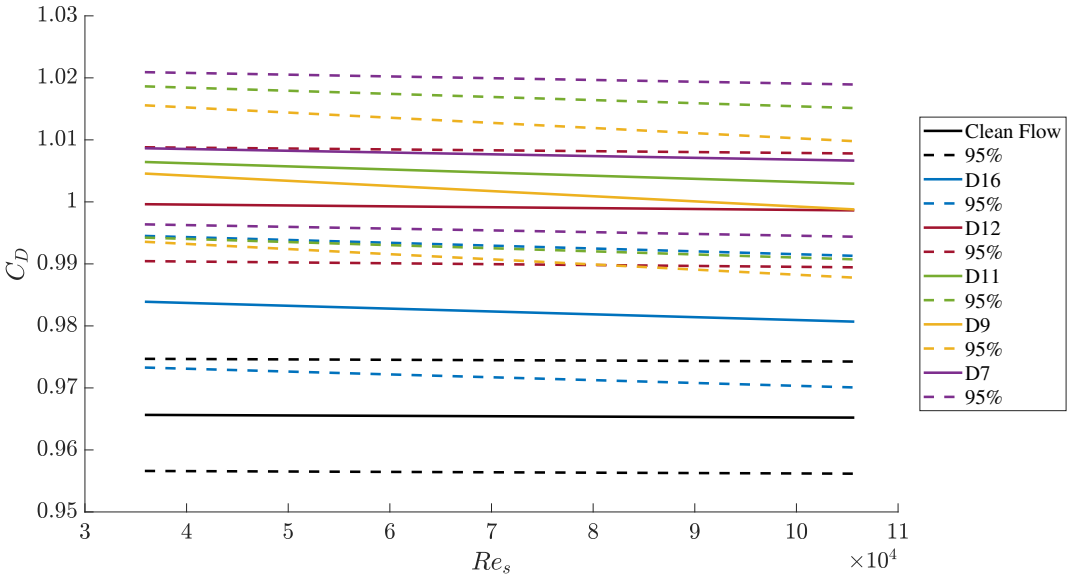

Figure 3.12: Linear fit to each data set (solid line) with their respective upper and lower bounds of the 95% confidence interval (dashed lines).

For the small Reynolds number span of the data ($Re_s \approx 3.5 \times 10^4 - 10.5 \times 10^4$), a linear regression was performed on each data set to deduce trends in the results. The ensuing functions are plotted with their respective 95% confidence interval bounds in Fig 3.12. The mean trend line of the d_p = 15.6 μm particle data set lies outside of the confidence interval for the particle-free control case, suggesting that the former results show a distinct data set with an increase in drag coefficient. However, the lower bound of the d_p = 15.6 μm confidence interval resides within the particle-free confidence interval bounds: this indicates that the observed drag coefficient increase is not statistically significant with 95% confidence, but that it likely would be with the use of a lower confidence interval. The remaining cases show clear statistically significant differences from the particle-free values..

To isolate the increase in drag coefficient caused by mechanisms that are not related simply to the increased density of the flow, a drag increment using the estimated coefficients from the previous section was defined as

$$\Delta C_D = C_{D_{meas}} - \frac{C_{D,\rho_{eff}}}{C_{D,\rho_\infty}} \times C_{D_{Clean}} \quad , \tag{3.8}$$

where $C_{D_{meas}}$ is the experimentally measured drag coefficient for the particle-laden cases, $C_D|_{Clean}$ is the measured drag coefficient for the particle-free case, $C_D|_{\rho_{eff}}$ is the estimated drag coefficient for the higher effective density flow from section 3.4.1, and $C_D|_{\rho_\infty}$ is the corresponding drag coefficient for the particle-free flow. Fig. 3.13 shows both the this drag increment for the various particle diameters (dashed line) as well as the estimated increment caused by the higher effective density for each case, i.e., $C_D|_{\rho_{eff}}$ - $C_D|_{\rho_\infty}$ (solid line). The increase from the higher effective fluid density is orders of magnitude smaller than that from the other mechanisms and is essentially negligible. This result indicates that simple estimates for the drag increase based on assuming a higher effective density were highly inaccurate, the method used to calculate the concentration of the particles in the free-stream grossly underestimated the particle population (though this would need to be by orders of magnitude), and/or there are other mechanisms present that are increasing the drag on the sphere. A possible explanation for this drag augmentation is that the particles are approaching the sphere at supersonic speeds relative to the local flowfield and therefore have a bow shock of their own. The pressure wave generated by the supersonic particle would then impart a greater force on the sphere, adding to the momentum transfer from the particle impact. Regardless of the mechanisms at play, the repeated results show the consistency in the higher measured drag coefficient for the spheres subject to particle-laden flows.

To compare the particle-wise contributions for the different diameters, the net drag-coefficient increment, ΔC_D, was divided by the number density of the particles; the resulting value represents the effect a single particle per cubic centimeter would have on the drag experienced by the sphere.

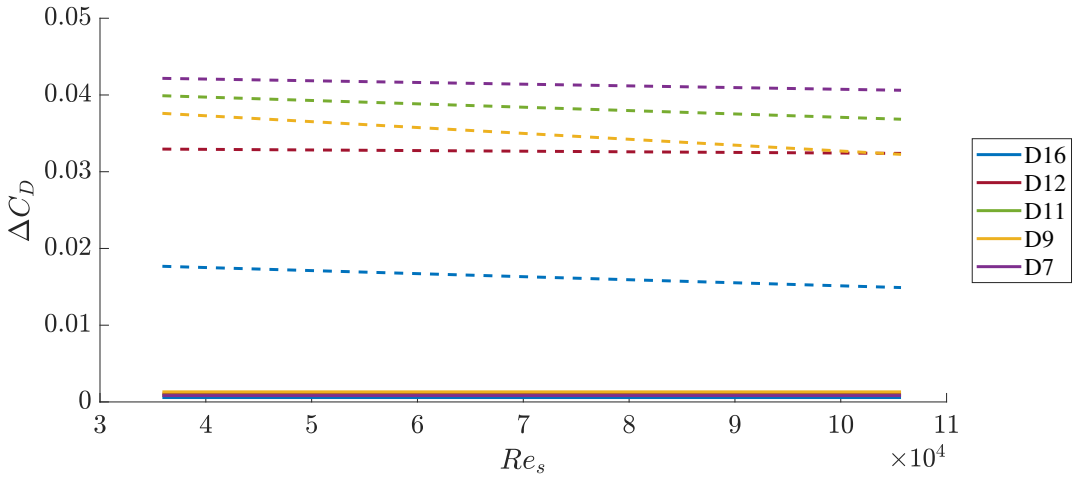

Figure 3.13: Net contribution to the drag coefficient augmentation based on the effective fluid density increase (solid line) and other means (dashed line).

A representative result for a single Reynolds number is shown in Fig. 3.14, with the particle-wise drag increment plotted versus the particle diameter. An approximately linear increase with the particle diameter is observed, which is somewhat contrary to expectations. If momentum transfer from the particles either to the fluid or directly to the sphere were responsible for the drag increase, we would expect the particle-wise drag increment to increase linearly with the particle mass, i.e., as d_p^3. This supports the possibility of the observed drag increase originating from another mechanism.

Finally, it was postulated that the particle-sphere diameter ratio would have an effect on the drag augmentation. A larger sphere will in turn force the bow shock further away from the surface and thus have a longer distance over which the particle trajectories can be influenced. Fig. 3.15 shows the data from all the experiments with an overlaid linear fit. The linear trend suggests that the drag coefficient increases with d_p/d_s, however, it is clear that data over a larger domain is necessary to truly understand the behavior of this trend.

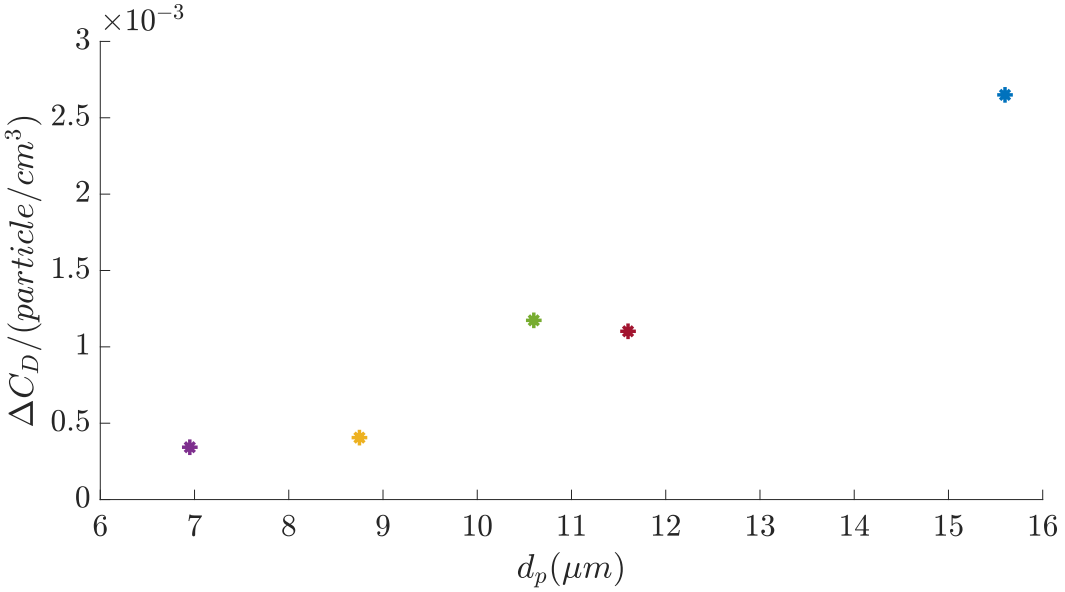

Figure 3.14: Particle-wise drag-coefficient augmentation versus particle diameter for a representative Reynolds number of ~35,900.

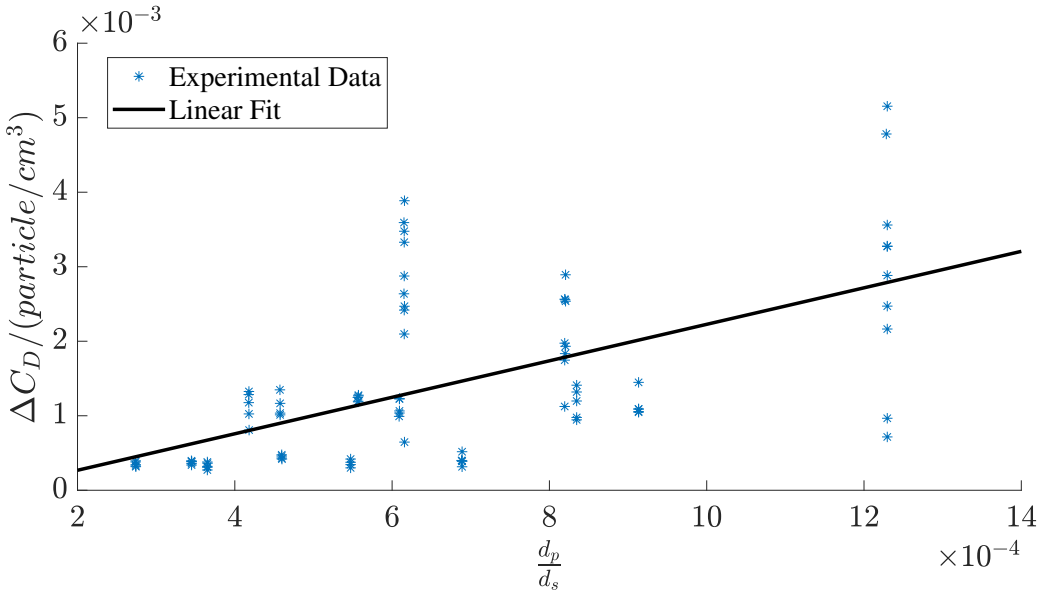

Figure 3.15: Particle-wise drag-coefficient augmentation versus the particle diameter to the sphere diameter ratio.

3.6 Conclusions

In this chapter, the newly-developed Multi-phase Investigations Supersonic Tunnel was employed to study the drag augmentation of spheres exposed to high-supersonic, particle-laden flows. Tests were carried out using five separate particle diameter and concentration conditions for three different sphere sizes. Simple estimates of the drag augmentation from particle-laden flow incorporating higher effective density predicted a drag increase of less than 1% for each condition generated by MIST. The experimental results showed, however, that this model severely under-predicted the actual drag coefficient at such conditions, which was up to 4.5% higher than the particle-free case, several orders of magnitude higher than estimated. A possible explanation for this increase is that the supersonic particles, with their own bow shock, produce a high-pressure wave as they impact the sphere, thus increasing the force imparted on the sphere. Particle trajectory simulations showed that almost all the particles lying within the upstream streamtube corresponding the sphere cross-sectional area would impact the sphere at the tested conditions due to the large Stokes number. To the knowledge of the author, this is the first experimental study in which aerodynamic forces have been measured in high-supersonic, liquid-particle-laden flows. Additional studies are necessary to understand the mechanism behind the large increase in drag coefficient.

Chapter 4: Attenuation of Acoustic Disturbances in a High-Supersonic Wind Tunnel Nozzle with Multi-phase Flows

4.1 Overview

The free-stream acoustic disturbance environment in MIST is investigated in this chapter. Focused Laser Differential Interferometry (FLDI) is used in both the clean and particle-laden flow environments to compare the disturbance spectrum and amplitudes. The intent of these measurements was to inform the results of the cone transition experiments in Ch. 5. Interesting observations from these experiments are discussed.

4.2 Facility

For these experiments, MIST was operated at two free-stream unit Reynolds numbers, Re_∞ = 4.73 $\times 10^6$ m^{-1} and Re_∞ = 5.82 $\times 10^6$ m^{-1} (p_{fill} = 1 bar and p_{fill} = 1.25 bar, respectively), using nitrogen as the test gas. The free-stream properties associated with these Reynolds numbers are presented in Tab. 4.1. Values for the Re_∞ = 5.89 $\times 10^6$ m^{-1} condition were obtained by linearly interpolating the results from the pitot-rake study (Sec. 2.2), since no pitot measurements at a fill pressure of 1.25 bar were available. For the particle-laden flows, the same particle-concentration combinations were chosen as those from Ch. 3, resulting in the concentrations and free-stream

Table 4.1: Run Conditions.

M_∞	Re_∞ ($\times 10^6$ m^{-1})	v_∞ (m/s)	p_∞ (Pa)	T_∞ (K)	ρ_∞ (kg/m^3)
3.85±0.02	4.73±0.03	679	756	74.8	0.034
3.89±0.02	5.82±0.03	681	898	73.9	0.041

Table 4.2: Particle Conditions.

Condition	d_p (μm)	C (#/cm^3)	u_{slip} (m/s)
D7	6.95	123±49.3	-6
D9	8.75	92.7±10.3	-11
D11	10.6	34.0±7.21	-16
D12	11.6	29.9±5.22	-20
D16	15.6	6.67±1.07	-36

slip velocities presented in Tab. 4.2. The slip velocities were obtained by subtracting the nozzle exit velocities of the particles provided in Tab. 2.3 from the gas exit velocity in the simulations. Although the simulated conditions do not perfectly match the actual conditions obtained from the pitot rake study, it is assumed that the slip velocity would be of the same order of magnitude since the flow velocity remains relatively constant across all conditions for the nozzle and that these values represent the lower bound of the slip velocity.

4.3 Focused Laser Differential Interferometry

FLDI has been shown to be a useful technique for characterizing the disturbance levels in high-speed wind tunnels [47, 51]. The high frequency response, spatial resolution, and signal-to-noise ratio of FLDI make it suitable for measuring the high-frequency, weak acoustic disturbances that are typically the dominant source of noise in high-speed wind tunnels. Furthermore, FLDI is designed to be more sensitive at the focal point and less sensitive along the remaining beam path, such that the disturbances from the tunnel-wall boundary layers and shears layers are attenuated,

allowing for more accurate core-flow measurements [54]. In these experiments a single-point FLDI setup was used to measure the core-flow disturbances in MIST for the clean flow and particle-laden flow conditions.

4.3.1 FLDI Setup

The configuration of the single point FLDI system is shown in Fig. 4.1. A Cobalt Samba diode pumped laser (LS) was used to provide continuous 532 nm light at 100 mW. The narrow spectral linewidth (±0.3 nm), long coherence length (>100 m), and low noise output (<0.1% RMS) of this laser make it excellent for use in FLDI systems. C_1 is a plano-convex lens with a 20 mm focal length and H is a half-wave plate (Thorlabs model number WPH05M-532). On the other side of the region of interest, W is a custom made Wollaston prism by United Crystals with a splitting angle (ε) of 8 arcmin and C_2 is a 100 mm diameter lens with a 200 mm focal length; P is a linear polarizer. The signal was recorded by a DET36A2 biased Si photodetector terminated with a 50Ω resistor. A 14-bit Picoscope 5444D sampled the signal at 25 MHz. This system is a simplified, single-point version of the four-point FLDI setup previously used by Gillespie et al. [51] in the same test section, although at the time the tunnel was configured as a reflected shock tunnel rather than as a Ludwieg tube. The beams were located at the center of the MIST test-section viewing window. The beam spacing was measured using a Newport Corporation LBP2-HR-VIS2 beam profiler and was determined to be $\Delta x_1 = 465 \pm 10\ \mu$m.

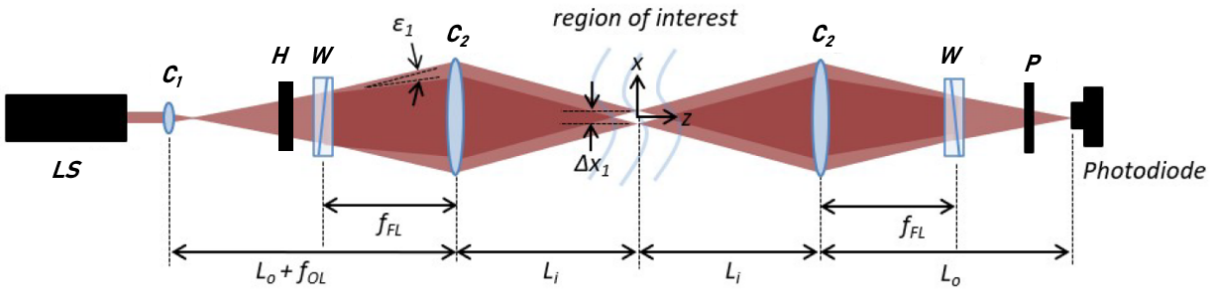

Figure 4.1: Schematic of the single-point Focused Laser Differential Interferometer (adapted from [9].)

4.3.2 Analysis of FLDI Data

Although there have been significant recent improvements in the analysis of an FLDI signal to enable it to be correlated to fluctuations in the density gradient of the flow [49, 52–54], the purpose of the present study was to gain an understanding of how the tunnel noise was affected by the use of an aerosol in comparison to clean flow, with the ultimate intent of informing the subsequent cone transition experiments. Qualitatively, a comparison between the clean-flow case and the various particle-laden flow cases was sufficient to shed light on some of the interesting behaviors seen in the boundary-layer experiments later described. For this reason, only the raw voltage signals are compared, with no attempt to convert to quantitative density fluctuations. To calculate the power spectral densities during the test time then, Welch's method [108] is employed by averaging 125,000-point segments of the voltage signal with 50% overlap.

4.4 Results

In Fig. 4.2a we present the power spectral densities for clean flow and each particle size for the $\mathrm{Re}_\infty = 4.73 \times 10^6$ m^{-1} condition. A 3-point moving average filter has been applied twice

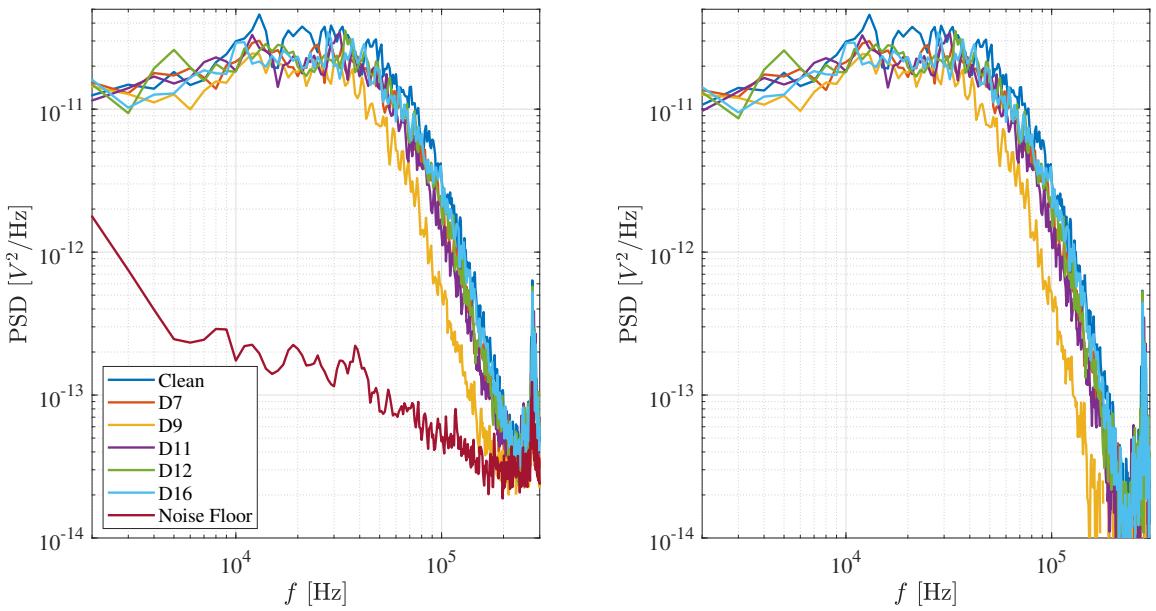

Figure 4.2: Fluctuation voltage power spectral densities of the FLDI signal in the free-stream for all particle diameters with a free-stream unit Reynolds number of $\mathrm{Re}_\infty = 4.73 \times 10^6$ m^{-1} with (a) the raw voltage signal and (b) the background-noise-subtracted signal.

to these spectra to help clarify the trends. The flow-off noise floor is also presented for reference. Although it is evident that the background noise levels are slightly elevated compared to the similar measurements of Gillespie et al. [51]. The flow-on signals remain well above the noise floor out to frequencies over 100 kHz.

There is little difference between the various flow-on spectra below 10 kHz, but at higher frequencies we note that the clean flow spectrum lies consistently above those for the particle-laden flows. This is an unexpected result: if anything, we might expect the particles passing through the laser beams to produce additional noise. Although their influence would depend greatly on the particle concentration and the probability that the particles would be passing directly through the focal point of the beams. The effect is most pronounced for case D9, where the attenuation at high frequencies can reach a factor of approximately 2, but it is present for all

particle diameters (except, perhaps D16, which merges with the clean-flow spectrum at higher frequencies). Note that the sharp peak at roughly 250 kHz is a non-physical artifact: it was present when the laser was turned off, with several different photodiodes, and with a separate picoscope, suggesting it was some form of interference in the laboratory.

To remove the effects of signal noise, the noise floor is subtracted from each case and the resulting spectra are presented in Fig. 4.2b. This slightly enhances the difference between the spectra especially at higher frequencies but the overall observations made above remain unchanged. It is important to remember that the influence of the shear layer becomes increasingly dominant at lower frequencies (see [109, 110], for example) and therefore the attenuation of the free-stream disturbances in the core flow might not be as evident due to the interference of the shear layer on the signal. FLDI experiments on a Mach-4 Ludwieg tube were conducted by Ceruzzi [49] which showed that the sensitivity of the FLDI system would provide confident measurements for wavenumbers above $k = 500$ m^{-1}, which for the present work would correspond to a frequency of 8.8 kHz. In the shock-tube version of the facility used at the University of Maryland, which uses the same test section as MIST, the cut-off wavenumber was measured to be $k = 2100$ m^{-1} [51], corresponding to a cut-off frequency of 368 kHz for MIST, although the shock tunnel used a Mach 6 nozzle. By considering these cut-off frequencies as upper and lower bounds, it would be reasonable to expect that the cut-off frequency for the present work would lie somewhere between these values. The presented results suggest that this occurs at some point on the order of the tens of kHz range.

Previously discussed in Sec. 1.4, Knudsen et al. [60] postulated that the reduction of sound wave amplitudes through fog and smoke was caused by particle relaxation. This was later confirmed by Temkin and Dobbins [61] who produced a model to predict this behavior which showed

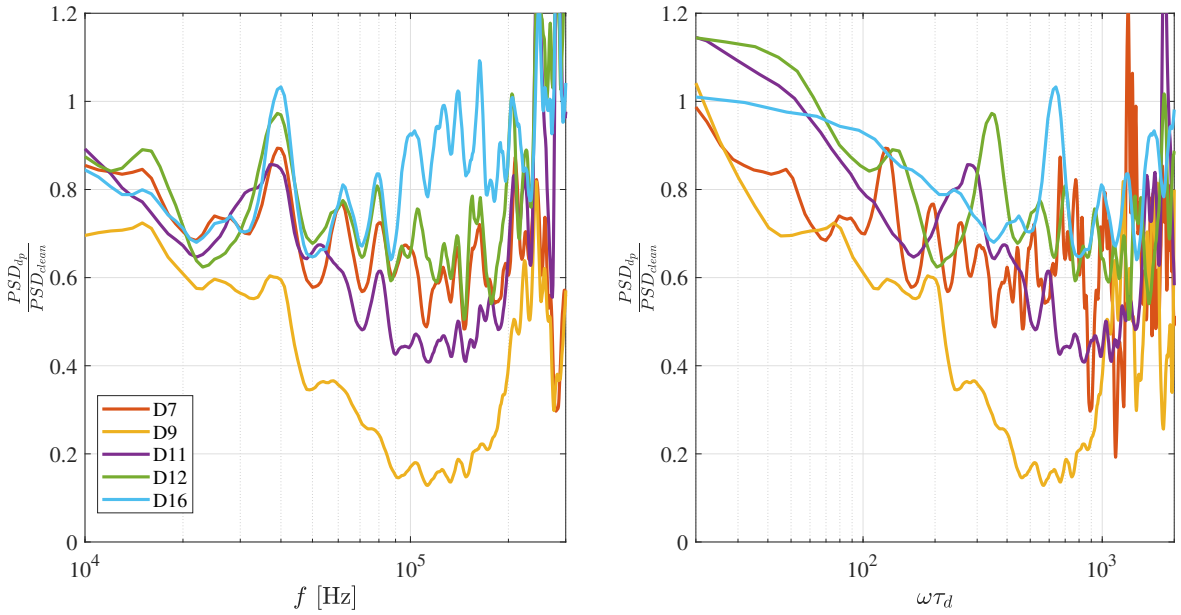

(a) (b)

Figure 4.3: Ratio of the particle-laden to particle-free spectra of the free-stream disturbances for all particle diameters with a free-stream unit Reynolds number of $\mathrm{Re}_\infty = 4.73 \times 10^6$ m^{-1} as a function of (a) the frequency and (b) the circular frequency and particle dynamic relaxation time.

that the maximum attenuation occurs where $\omega\tau_d$ is near unity. Here, ω is the circular frequency and τ_d is the particle dynamic relaxation time defined as

$$\tau_d = \frac{d_p^2 \rho_p}{18\mu_g} \quad , \tag{4.1}$$

where ρ_p is the density of the particle and μ_g is the dynamic viscosity of the gas, in this case nitrogen. Without the relevant length scale, the attenuation coefficient is difficult to calculate and therefore the attenuation is represented by the ratio of the fluctuation spectra for the particle-laden cases to the clean-run case, shown in Fig. 4.3. In the frequency domain, the greatest difference between the particle-laden and clean flow fluctuation spectra occurs consistently around 100-150 kHz for the D7-D12 conditions; the D9 case shows a maximum reduction in the spectra by

a factor of 5. The attenuation for the D16 case appears to remain low over a broad spectrum of frequencies. By multiplying the circular frequency with the characteristic dynamic particle relaxation time, the maximum attenuation is shown to occur approximately three orders of magnitude higher than that predicted by the Temkin and Dobbins results.

The $Re_\infty = 4.73 \times 10^6$ m^{-1} condition has a relatively low freestream density, which compromises the signal-to-noise ratio in the FLDI measurement. To enhance the signal quality then, another series of experiments was performed at $Re_\infty = 5.82 \times 10^6$ m^{-1}. It was thought that the higher density in the flow at this condition would result in a stronger signal and make the attenuation more apparent. Unfortunately, as noted in Ch. 2, a limitation with MIST is the operating pressure of the MDG, which cannot operate at pressures much higher than 1 bar, making it unable to run in the multi-phase configuration at much higher pressures. Indeed in Fig.4.4 we see that the attenuation for the various particle diameters at this condition is much more evident. Again, maximum attenuation is observed for D9, with a clear difference in signal from the particle-free case over the 20-200 kHz frequency range; for the 70-200 kHz range, the decrease is consistently almost a full order of magnitude. Comparing the other particle diameters, in each case we see a significantly damped spectrum at higher frequencies: in order of decreasing attenuation, these are D9, D11, D7, D12, and D16. Subtracting the noise floor simply reinforces these trends.

A comparison of the particle-laden to particle-free spectra in Fig 4.5 shows that particle condition D9 can achieve a maximum reduction in the noise level by a factor of 10. Similar to the lower Reynolds number flow condition, the peak attenuation occurs for frequencies in the 100-200 kHz range. However, unlike the lower Reynolds number flow condition, here the D16 spectra now shows significant attenuation across a wide range of frequencies. When computing the circular frequency and introducing the particle dynamic relaxation time, the maximum re-

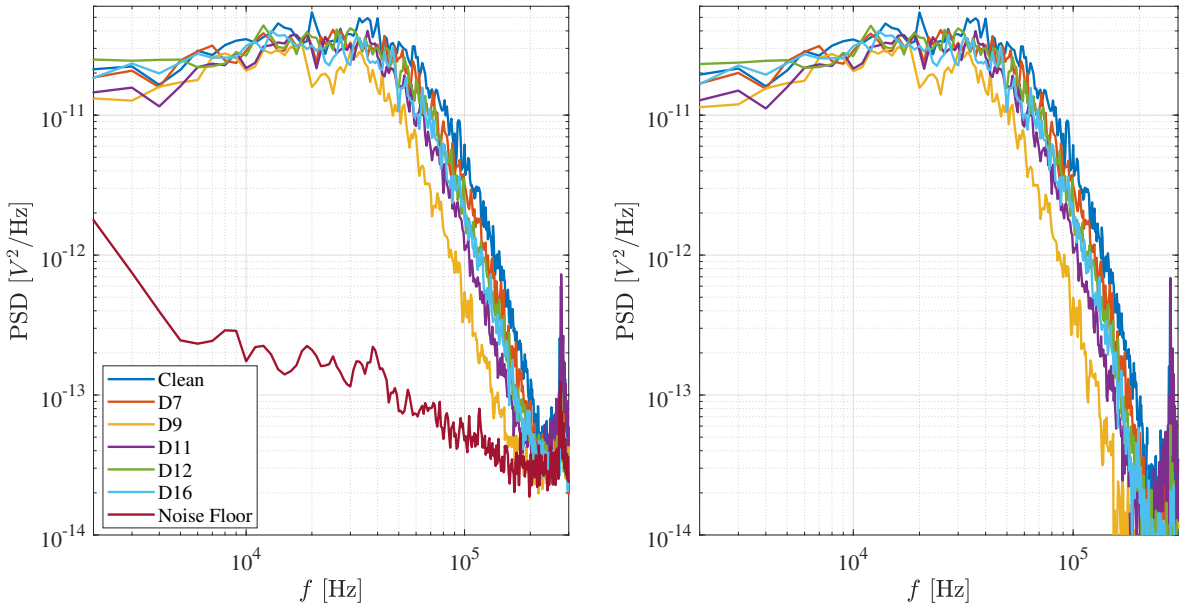

Figure 4.4: Fluctuation voltage power spectral densities of the FLDI signal in the free-stream for all particle diameters with a free-stream unit Reynolds number of $\mathrm{Re}_\infty = 5.82 \times 10^6$ m^{-1} for (a) the raw voltage signal and (b) the background-noise-subtracted spectra.

duction in the spectra is demonstrated again to occur at approximately three orders of magnitude higher $\omega\tau_d$ than what is expected based on the model by Temkin and Dobbins. Further studies will be necessary to understand the deviation from this result as it had been confirmed in other studies, [67] for example. It is important to recall that the FLDI signal is being disturbed by the nozzle shear layer, and therefore the lower frequency disturbances in the freestream are not being measured accurately. It is therefore possible that the peak attenuation could be occuring at a lower frequency which would align with the model by Temkin and Dobbins. Among the other possible mechanisms for the attenuation of sound waves in an aerosol, the particle relaxation mechanism is expected to be dominant as MIST is a cold tunnel (freestream static temperatures on the order of 75K) and therefore particle evaporation is improbable.

Irrespective of the exact attenuation mechanism, this result could have substantial implica-

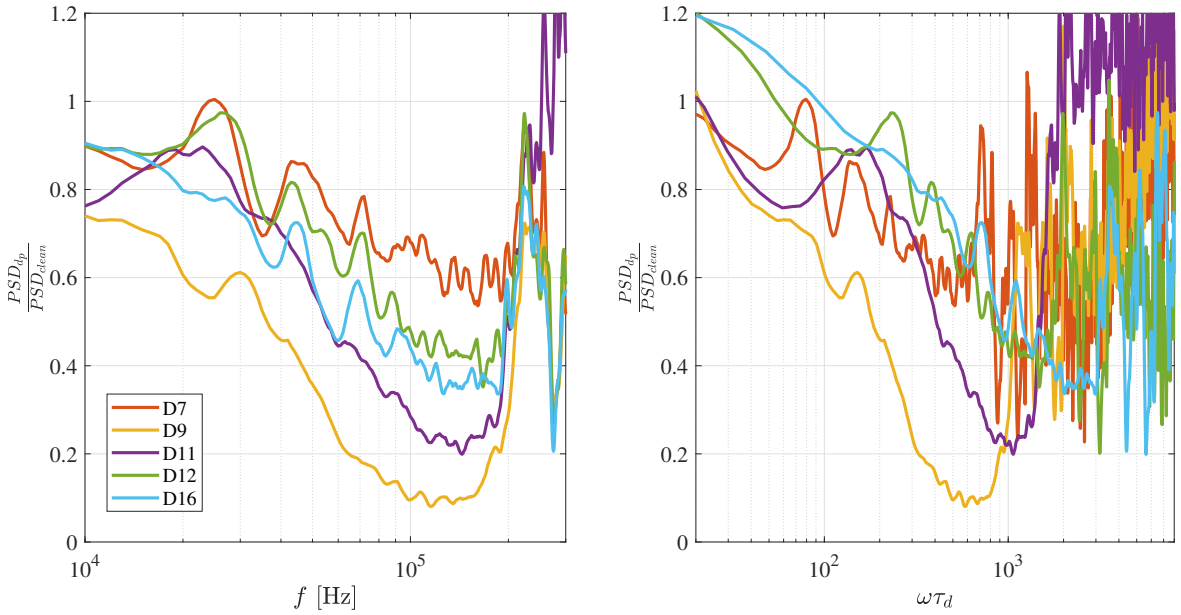

Figure 4.5: Ratio of the particle-laden to particle-free spectra of the free-stream disturbances for all particle diameters with a free-stream unit Reynolds number of $\mathrm{Re}_\infty = 5.82 \times 10^6$ m^{-1} as a function of (a) the frequency and (b) the circular frequency and particle dynamic relaxation time.

tions since it demonstrates a significant decrease in the freestream noise levels in a conventional noisy tunnel. Presumably, aerosols could be introduced into the freestreams of other high-speed wind tunnels and produce a similar decrease in noise levels. The particle production on a shot-by-shot basis is also inexpensive, as the only costly acquisition required is the one-time purchase of the MDG. For example, for one condition D9 shot, 1.6 ml of the 5% DEHS in methanol solution is used, accounting for $0.01 for DEHS and $0.04 for methanol (2024 USA prices). For the most expensive condition (D16), this increases to just over $0.10 per shot. Of course, the drawback of this method of noise attenuation would be that the particles in the flow could disturb the experiments by other means, such as the augmentation of the drag coefficient of a free-flying sphere discussed in Ch. 3, so it depends on the scope of the project as to whether or not this is a useful technique to reduce tunnel free-stream noise.

4.5 Conclusions

In this chapter, the free-stream noise levels in MIST were measured using FLDI at two Reynolds numbers. At each Reynolds number, a particle-free case as well as five distinct particle-laden flow cases were studied. The raw voltage signal of the FLDI was analyzed for qualitative comparisons. A surprising result was the attenuation of free-stream disturbances along a broad frequency spectrum for all particle-laden flow cases. The condition with d_p = 8.75 μm particles reduced the fluctuation spectra the most for both freestream Reynolds numbers tested, by a factor of 5 for $Re_\infty = 4.73 \times 10^6$ m^{-1} and 10 for $Re_\infty = 5.82 \times 10^6$ m^{-1}. While the d_p = 15.6 μm particle condition did not appear to attenuate the acoustic disturbances at the lower Reynolds number, it showed a significant attenuation at the higher Reynolds number. Open literature suggests that the particle relaxation process is a dominant contributor to the dampening of the disturbance amplitude. The main implication here is that particles can be introduced into the flows of conventional noisy wind tunnels to quieten them. A simple calculation on the cost of each shot shows that a reduction of the noise level in the flow can be generated at about $0.10 per shot - an inexpensive method for producing quieter flow in ground test facilities.

Since these were preliminary studies to help understand the results in the following chapter on boundary layer transition, more work is required to fully understand the physical processes at work. First of all, improvements to the FLDI system would enable enhanced signal-to-noise at higher frequencies. Additionally, a multi-point FLDI system would allow for the calculation of the attenuation coefficient such as was performed by Gillespie [58]. Transfer functions such as those developed by Ceruzzi and Cadou [9] should also be developed for the MIST nozzle and test section to provide quantifiable data from the experiments. At these low frequencies, the shear

layer from the nozzle free-jet in the test section likely dominates the FLDI signal, therefore it would be beneficial to introduce flow deflectors that would remove the shear layer from the FLDI optical path. Finally, these tests should be expanded to all test conditions that will be utilized in MIST.

Chapter 5: Boundary Layer Transition on a Cone in High-Supersonic, Particle-Laden Flow

5.1 Overview

In this chapter, the boundary layer instabilities and transition behavior on a 5° half-angle cone are studied in high-speed, particle-laden flows. High-speed Schlieren visualization is used to observe the dominant instability structures and frequencies and deduce approximate transition locations. A comparison of the boundary layer exposed to multi-phase flows to that of a clean flow is presented.

5.2 Experimental Apparatus

5.2.1 Facility

MIST was operated at a range of freestream unit Reynolds numbers, corresponding to charge tube fill pressures of 0.7, 0.85, 1, 1.1, and 1.25 bar, using nitrogen as the test gas (see Tab. 5.1). To provide particle-laden flow, a subset of particle-concentration combinations from earlier chapters was chosen, resulting in the particle diameters, concentrations, and freestream slip velocities presented in Tab. 5.2 (maintaining consistent labeling with previous chapters). These conditions were chosen such that there would be one small particle/high concentration, one

Table 5.1: Run Conditions.

M_∞	Re_∞ ($\times 10^6$ m^{-1})	v_∞ (m/s)	p_∞ (Pa)	T_∞ (K)	ρ_∞ (kg/m^3)
3.79±0.02	3.41±0.03	676	579	76.7	0.025
3.83±0.03	4.10±0.04	678	670	75.6	0.030
3.85±0.02	4.73±0.03	679	756	74.8	0.034
3.86±0.02	5.16±0.03	680	813	74.4	0.037
3.89±0.02	5.82±0.03	681	898	73.9	0.041

Table 5.2: Particle Conditions.

Condition	d_p (μm)	C (#/cm^3)	u_{slip} (m/s)
D9	8.75	92.7±10.3	-11
D12	11.6	29.9±5.22	-20
D16	15.6	6.67±1.07	-36

medium particle/medium concentration, and one large particle/low concentration combination. As before, the slip velocities are obtained by subtracting the nozzle exit velocities of the particles provided in Tab. 2.3 from the gas exit velocity in the simulations.

5.2.2 Wind Tunnel Model

A 5-degree half-angle cone with a nominally sharp tip, shown in Fig. 5.1, was used to study the effect of particle-laden flows on boundary-layer transition. The model is made up of a 260-mm-long stainless steel frustum with a 150-mm-long stainliss steel sharp nose-tip (the nose-tip radius is approximately 0.1 mm), followed by a 76.2-mm-long plastic extension. Using a digital protractor, the cone pitch angle was measured to be 0±0.1 degrees. The model axis was raised 4.8 mm above the centerline of the nozzle to avoid any disturbances from the plug-valve wake, although the pitot-rake study in Sec. 2.2 suggested such disturbances to be minimal. Instrumentation ports for PCB 132B38 pressure transducers are available on the frustum and extension of the cone model, however, no sensors were instrumented for these tests.

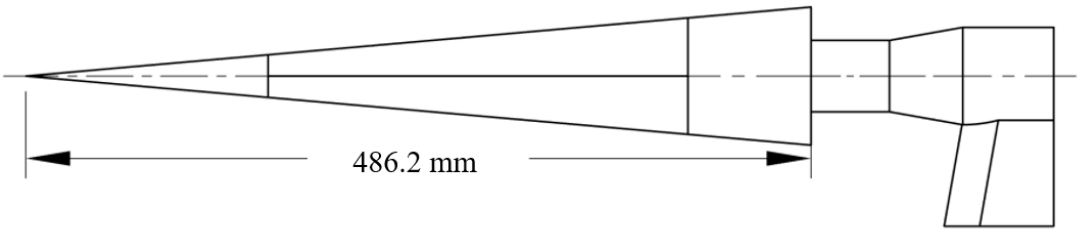

Figure 5.1: Schematic of the 5 degree half-angle cone (adapted from [10].)

5.2.3 Schlieren Visualization

A Z-type Schlieren setup (example shown in Fig. 5.2) with a horizontal knife edge was used to image the boundary layer. A continuously excited green LED (530 nm) served as the light source and was focused using a plano-convex lens to reduce the divergence angle; however, doing so resulted in a non-uniform background intensity profile. On the light-source side of the test section, a spherical mirror with a diameter of 152.4 mm and a focal length of 1524 mm was placed such that the light was collimated before passing through the test section. On the camera side of the test section, an identical mirror refocused the light, which was reflected off a planar mirror to the camera. A horizontal knife edge was placed at the focal point meaning density gradients in the approximate wall-normal direction were visualized. A Vision Research Phantom v2640 camera in high-speed binned mode was used to record images at 200 kHz with a Tamron lens (16-300 mm focal length), a 768 $\times$ 64 pixel resolution (0.138 mm/pixel), and 3.38-4.5 μs exposure time. The camera imaged the top surface of the cone and was rotated so that the cone edge appeared horizontal in images. The field of view remained constant at 330 mm to 435 mm along the surface from the cone tip.

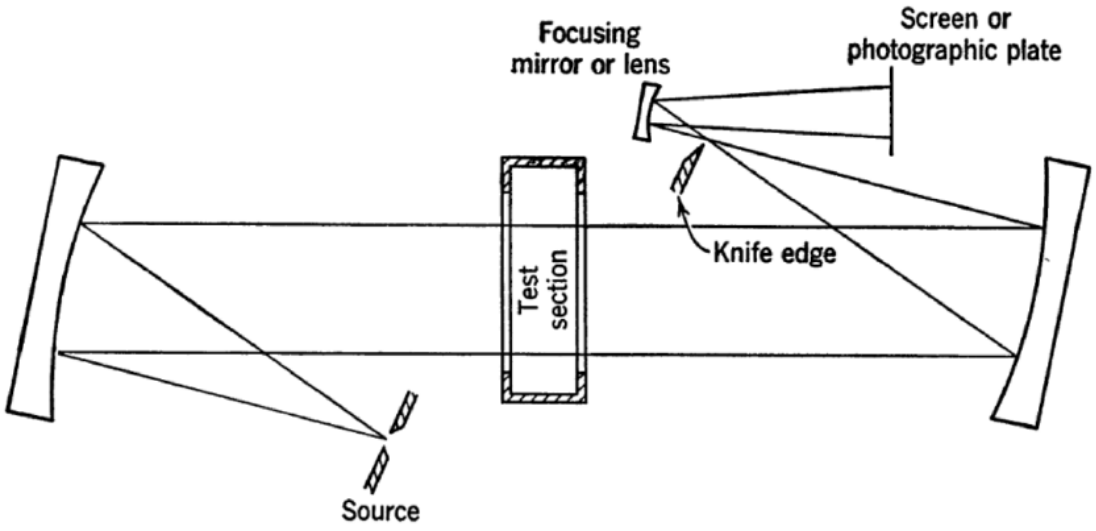

Figure 5.2: Schematic of the Z-type Schlieren setup [11].

5.3 Results

Previous work by Benjamin Jones investigated the boundary-layer transition of the same cone model in MIST under particle-free flow conditions [10]. The results indicated the first mode to be the dominant instability mode with frequencies ranging from 10 to 40 kHz. Additionally, he identified the transition process to begin somewhere in the region of Re_x = 900,000. Due to the limitations of the freestream Reynolds number that can be produced in MIST while operating the MDG, the positioning of the wind tunnel nozzle and cone were such that a further aft section of the cone could be visualized compared to the experiments by Jones.

For each run, a 20 ms time segment during the steady test time was chosen for analysis, corresponding to 4000 frames. The Schlieren images were not calibrated, and therefore the comparison between the particle-free and particle-laden flow cases is primarily qualitative in nature. Each image in a given sequence was reference-normalized by first dividing the pixelwise intensity by the corresponding flow-off intensity to account for nonuniformities in the background inten-

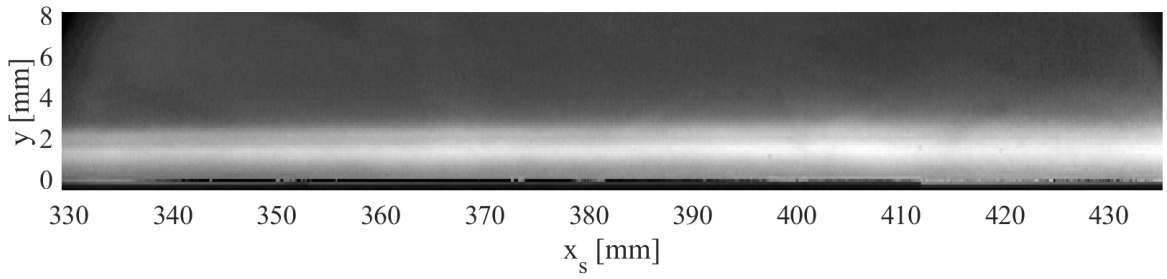

Figure 5.3: Mean Schlieren intensity during the steady test time of a particle-free, Re_∞ = 3.41±0.03 ×10^6 m^{-1} shot.

sity. Then the pixels in each frame were divided by a moving average intensity of the freestream, calculated by finding the mean pixel intensity from a section of pixels within the freestream using 30 frames before and after. This was done to account for the change in background intensity over time produced by the light source, as the power supply unit did not maintain a steady voltage and current, resulting in a temporally undulating brightness.

To begin, average schlieren images over the steady test time are used to assess the mean state of the boundary layer. For these average images, x_s represents the distance along the cone surface from the tip, and y represents the surface normal direction. Fig. 5.3 shows the mean intensity of a particle-free, Re_∞ = 3.41×10^6 m^{-1} shot. The fully laminar boundary layer is evident from the well-defined contrast between the brighter, (lower density) region indicating the fluid within the boundary layer and the darker (higher density) freestream. A transitional or intermittently turbulent boundary layer would result in a more diffuse edge in the average image than is seen here. This image provides a baseline for comparison to the particle-laden flow experiments. To approximate the boundary-layer height, a sobel filter is applied to the average image and a straight line is fit to the data points identified as edge points. At x_s = 330 mm, the boundary layer height measures $\delta \approx 2.3$ mm, and increases to $\delta \approx 3.2$ mm at x_s = 430 mm.

Increasing the freestream unit Reynolds number to Re_∞ = 4.73±0.03 ×10^6 m^{-1} causes the

boundary layer to become transitional for the particle-free case, presented in Fig. 5.4a.The transitional/intermittently turbulent boundary layer appears as a weaker intensity gradient extending to $\delta \approx 4.5$ mm at $x_s = 330$ mm and growing to $\delta \approx 6.0$ mm at $x_s = 430$ mm. In the image, Mach waves are visible emanating from the unused PCB sensor locations at $x_s = 380$ mm and $x_s = 400$ mm as well as an expansion wave caused by the slight backwards step at the cone-extension attachment location at $x_s = 411$ mm. Individual snapshots of the boundary layer, separated by 2.5 ms across the steady test time, are presented in Fig. 5.5 to provide an understanding of how the mean image is composed from the individual frames. Half of the selected frames show a fully turbulent boundary layer while the other half show transitional behavior at diferent stages along the transition process.

In Fig. 5.4b and 5.4c, the mean Schlieren intensities are shown for the $Re_\infty = 4.73\times10^6$ m^{-1} and particle conditions D9 and D12, respectively. Both show an initially laminar boundary layer, with a smearing of the boundary-layer edge indicating the onset of transition occurring roughly half-way through the image. This smearing effect produced in the average image is produced from the intermittent turbulence bursts that originate from within a long section of the cone surface. The use of the large particles, $d_p = 15.6$ μm and C = 6.67±1 #/cm^3, produces an entirely laminar boundary layer at this unit Reynolds number (Fig. 5.4d). For each particle-laden case, we thus conclude that the attenuation of the freestream acoustic disturbances is dominant over the additional disturbances produced by particles interacting with the cone shock and boundary layer. Corresponding sets of individual frames from the Schlieren visualization are presented in Figs. 5.6-5.8 for the D9-D16 cases, respectively. The snapshots for the D9 and D12 conditions depict the boundary layer to be predominately in a transitional state, at various stages of the transition process. However, there are some instances of a fully laminar or turbulent boundary layer. As is

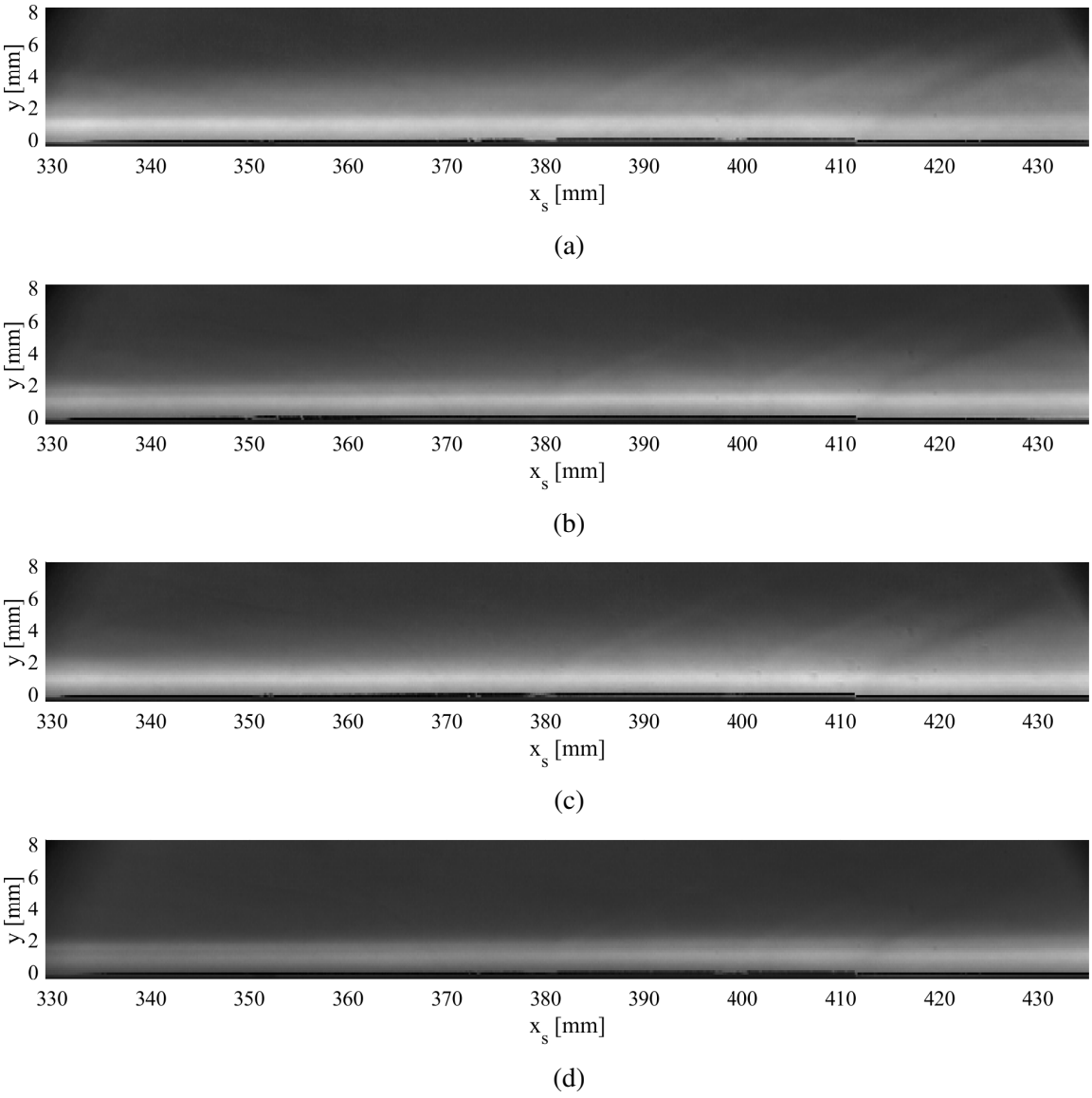

Figure 5.4: Mean Schlieren intensity during the steady test time of a $Re_\infty = 4.73 \pm 0.03 \times 10^6$ m^{-1} shot and (a) particle-free flow, (b) D9, (c) D12, and (d) D16 conditions.

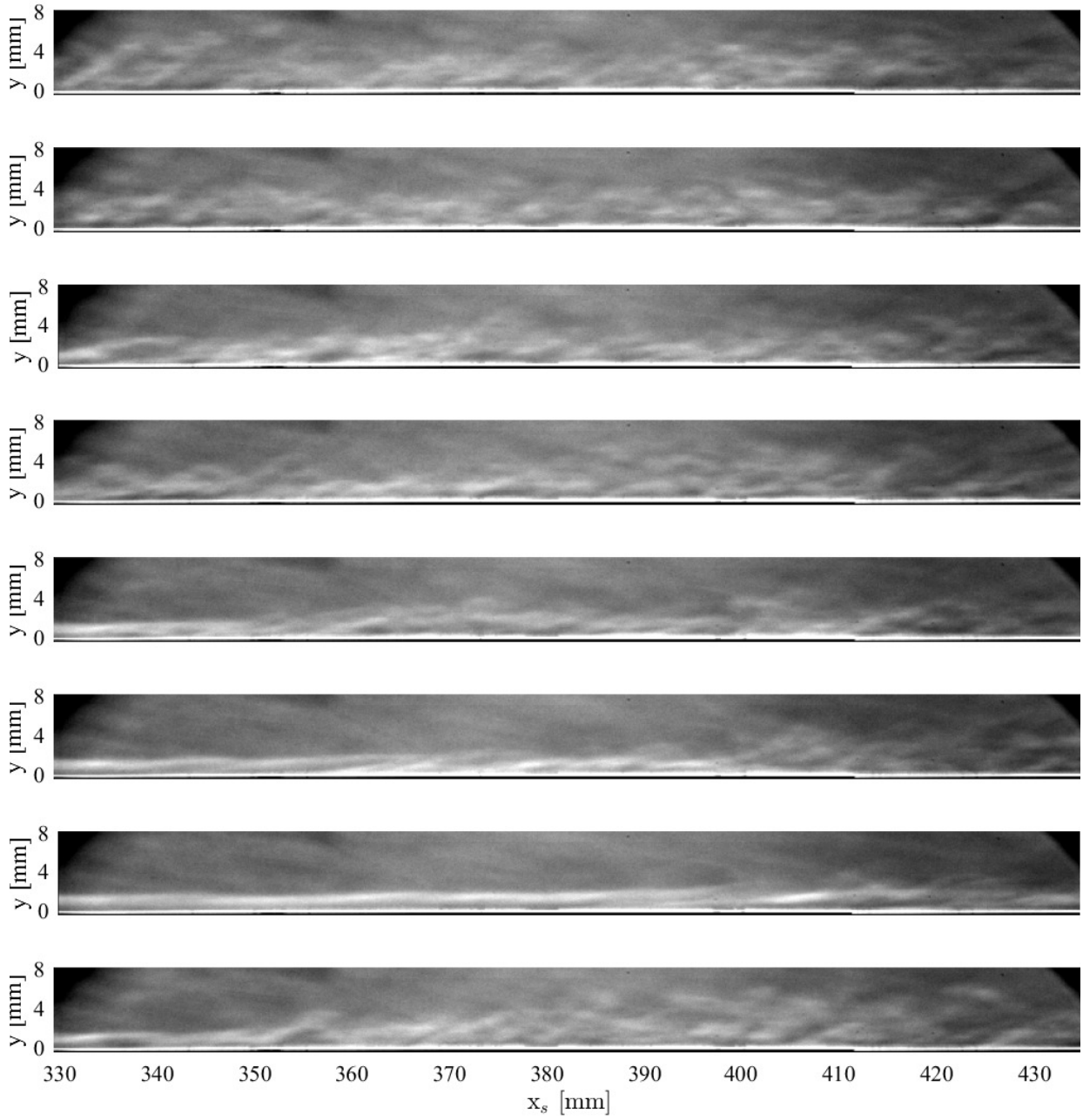

Figure 5.5: Sequence of schlieren images, Δt = 2.5 ms, for the particle-free, Re_∞ = 4.73±0.03 $\times 10^6$ m^{-1} condition.

expected by the state of the mean Schlieren image for the D16 condition, the individual frames show a laminar boundary layer in each case, although there appear to be initial signs of first mode structures in the lower three frames of Fig. 5.8.

At the highest freestream unit Reynolds number tested, $Re_\infty = 5.82\times10^6$ m^{-1}, the mean Schlieren image depicts a mostly turbulent boundary layer for the particle-free case, presented in Fig. 5.9a. A visual inspection of the footage revealed that for the majority of the steady flow time, the boundary layer was fully turbulent; however, the boundary layer would occasionally show signs of behavior representative of an earlier stage in the transition process. The particle-laden flows with particle conditions D9 and D12 produce intermittent turbulent bursts, which when the Schlieren images are averaged over the entire steady test time, these bursts result in a thick but weak band of higher intensity pixels above the laminar boundary layer height that was estimated from Fig. 5.3. Fig. 5.9d shows the mean image for particle condition D16. Here the boundary layer appears to be in the initial phases of the transition process with a similar profile to those of Figs. 5.4b and 5.4c which were produced at a lower freestream unit Reynolds number. A complete set of snapshot series and mean Schlieren figures is presented in Appendix B.

An alternative way of depicting the boundary-layer development is through the disturbance spectra; in particular, as the boundary layer transitions to turbulence, we would expect a tendency towards broader-band fluctuations in the spectra. The power spectral densities (PSD) of the fluctuating intensity in the Schlieren images were calculated using Welch's method [108]. At each streamwise position along the cone surface, the PSDs are averaged over 15 pixels from the cone surface in the y-direction, corresponding to a 2.07 mm portion of the boundary layer, chosen based upon the analysis of the laminar boundary layer heights identified from Fig. B.21. Since there was some shot-to-shot variation in tunnel conditions, PSD results are only presented over

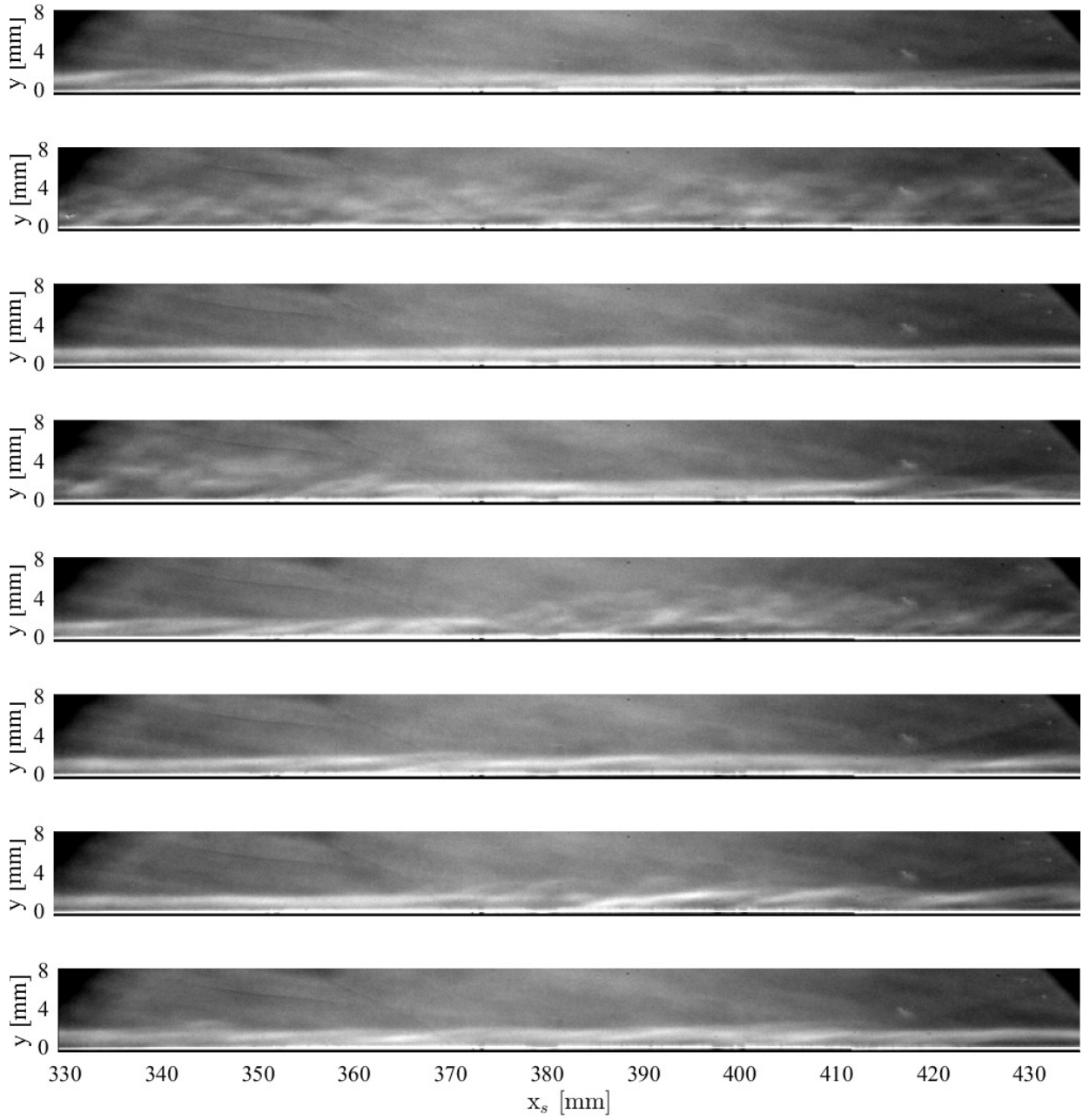

Figure 5.6: Sequence of schlieren images, Δt = 2.5 ms, for the D9, $Re_\infty = 4.73 \pm 0.03 \times 10^6$ m^{-1} condition.

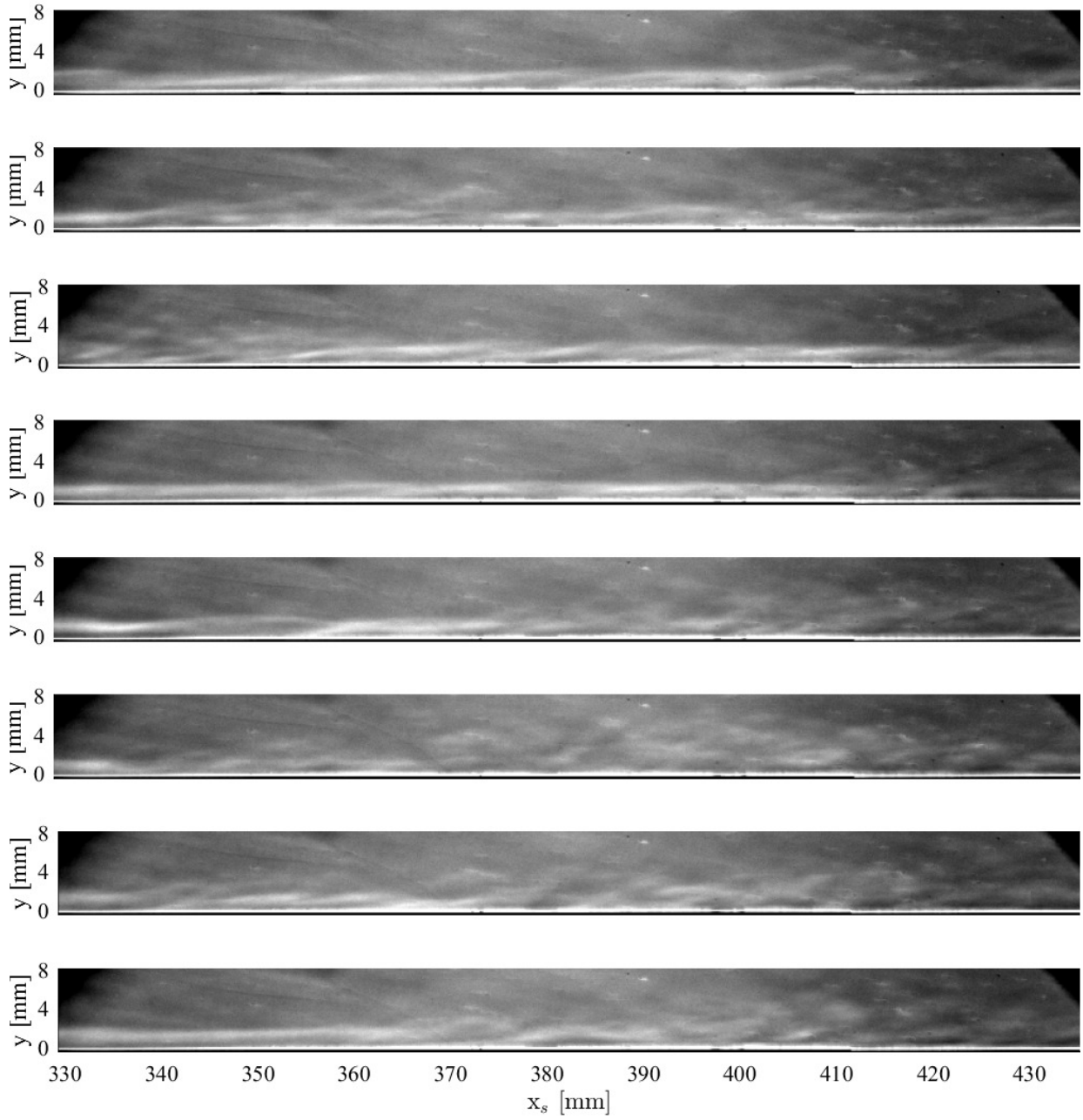

Figure 5.7: Sequence of schlieren images, Δt = 2.5 ms, for the D12, $Re_\infty = 4.73 \pm 0.03 \times 10^6$ m^{-1} condition.

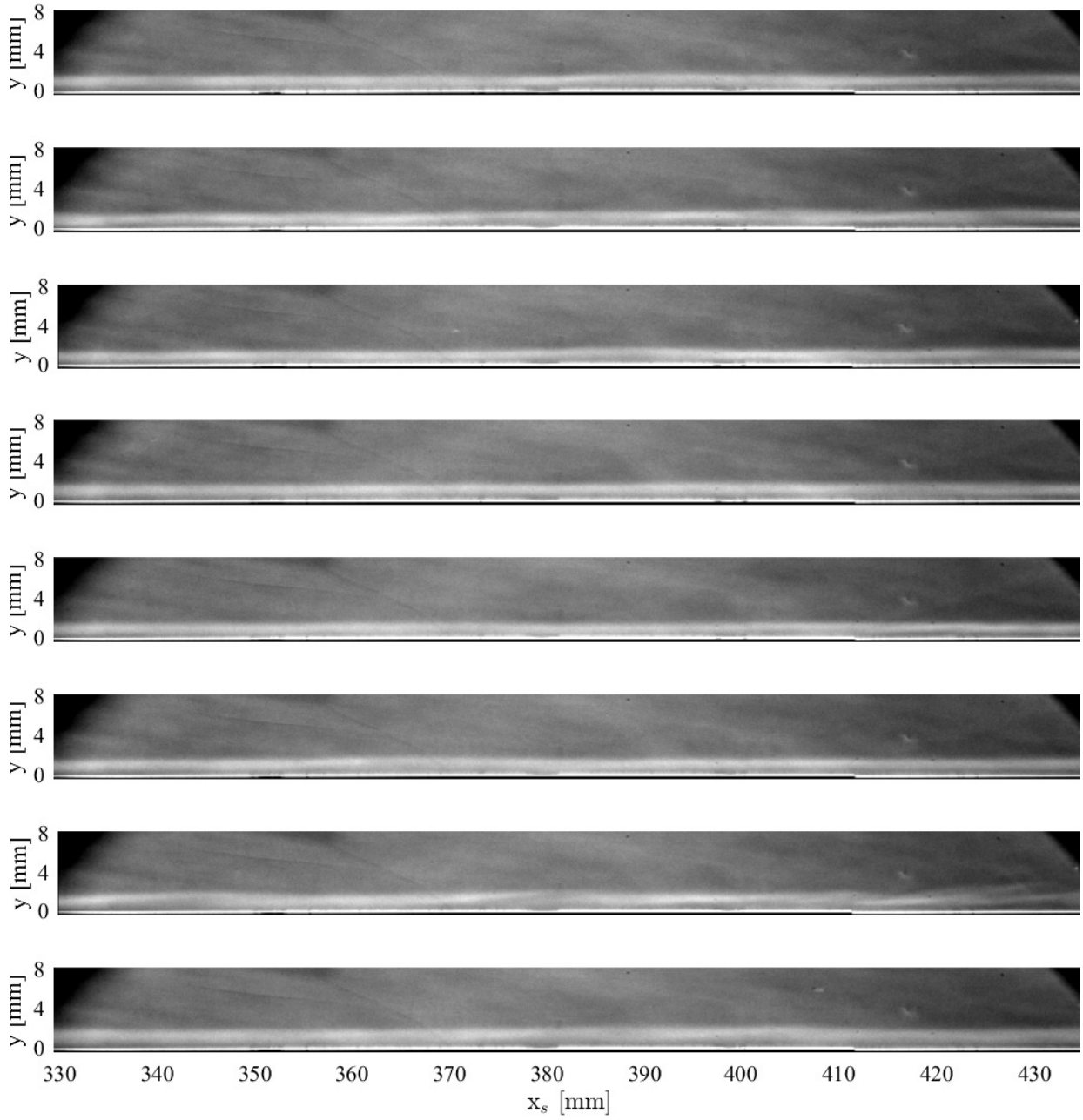

Figure 5.8: Sequence of schlieren images, Δt = 2.5 ms, for the D16, $Re_\infty = 4.73 \pm 0.03 \times 10^6$ m^{-1} condition.

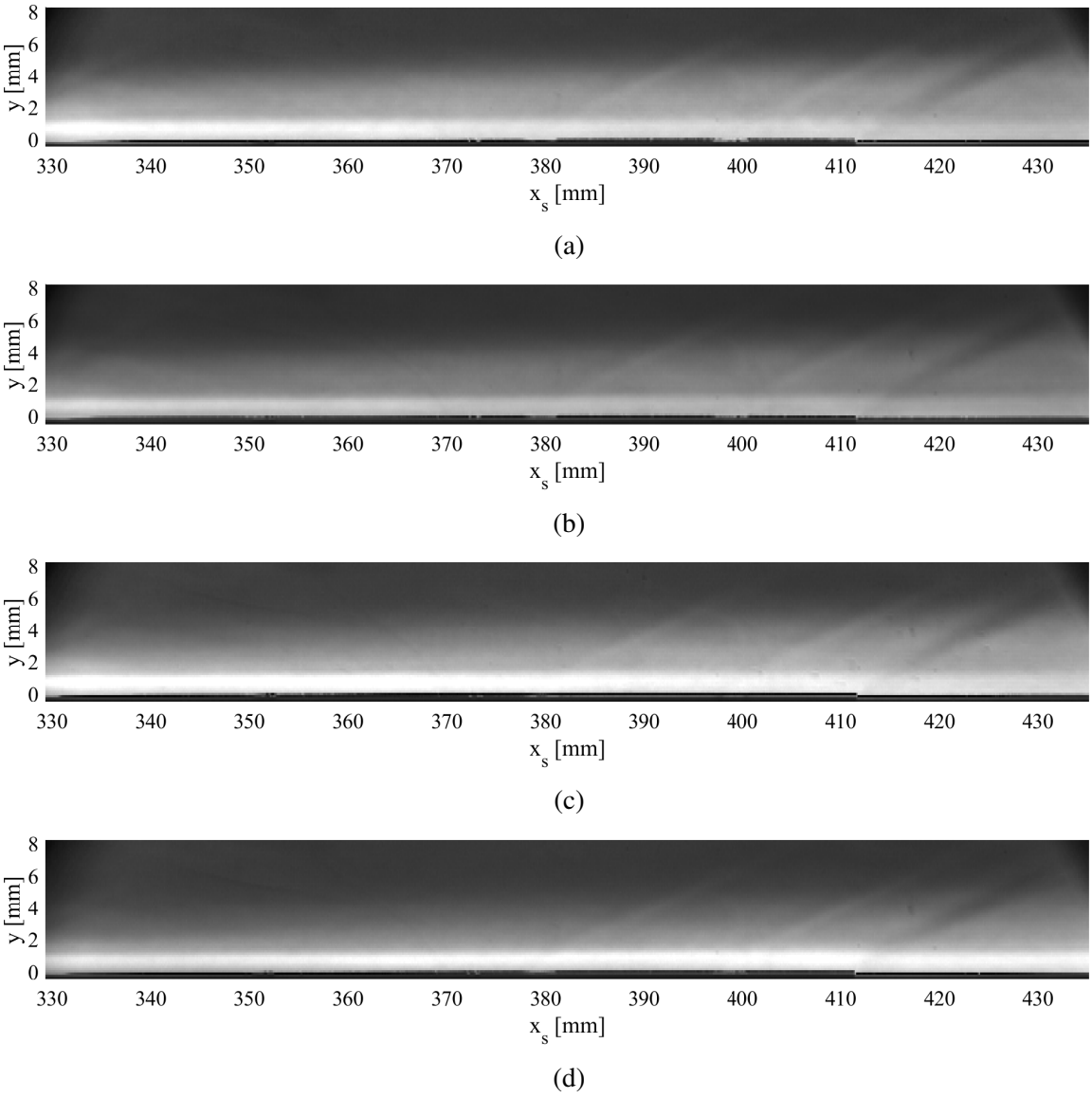

Figure 5.9: Mean Schlieren intensity during the steady test time of a $Re_\infty = 5.82 \pm 0.03 \times 10^6$ m^{-1} shot and (a) particle-free flow, (b) D9, (c) D12, and (d) D16 conditions.

regions of the cone with overlapping local Reynolds numbers.

Beginning with the lowest freestream unit Reynolds number condition (Re_∞= 3.41×10^6 m^{-1}) in Fig. 5.10, the top plot shows the PSD for the particle-free case and the plots below show the particle-laden flow cases, in order of increasing particle diameter. Although the boundary layer remains laminar in each case, the attenuation of the higher-frequency freestream disturbances for the particle-laden flows in Ch. 4 is still reflected in these spectra, with reduced amplitudes in the higher-frequency bands of the corresponding PSDs. This would suggest that the attenuation of the tunnel acoustic waves by the particles has a stronger effect than any particle impingement, especially given the relatively low concentrations of particles in the flow.

At the next highest freestream Reynolds number tested (Re_∞= 4.10×10^6 m^{-1}), the boundary layer in the particle-free case begins to show signs of transition with intermittent first-mode structures and turbulent bursts represented by a slight increase in the intensity near the boundary-layer edge in the mean image provided in Appendix B, Fig. B.22a. This is reflected in the top plot of Fig. 5.11 by the increase in power of the boundary-layer fluctuations over a broad range of frequencies. We note that the color scale for these PSD plots is the same within each figure but different across the various figures: this makes it easier to distinguish between the different particle cases for a given Reynolds number. The three particle-laden cases continue to show spectra consistent with a laminar boundary layer, although the D12 shot (second from bottom) shows some increase in the disturbance amplitude of the lower frequencies compared to the other particle-laden cases.

As discussed previously, at Re_∞= 4.73×10^6 m^{-1}, the boundary layer of the cone in particle-free flow has a high occurrence of turbulent bursts whereas the particle-laden cases remain primarily laminar. This behavior is reflected in the mean top plot of Fig. 5.12, which shows sig-

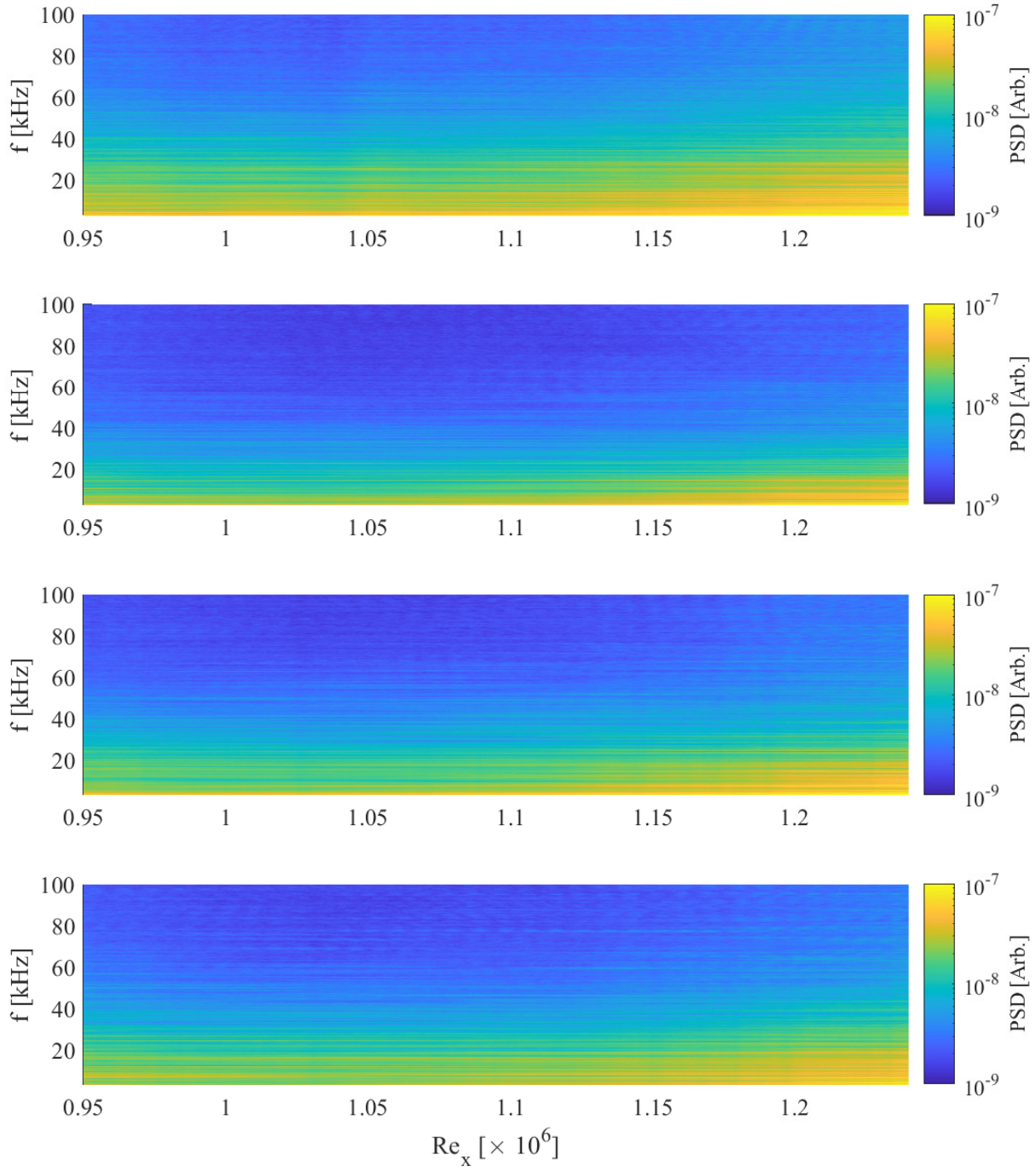

Figure 5.10: Spatially resolved PSDs along the cone for the particle-free, D9, D12, and D16 flow cases in order from top to bottom (Re_∞= 3.41±0.03×10^6 m^{-1}).

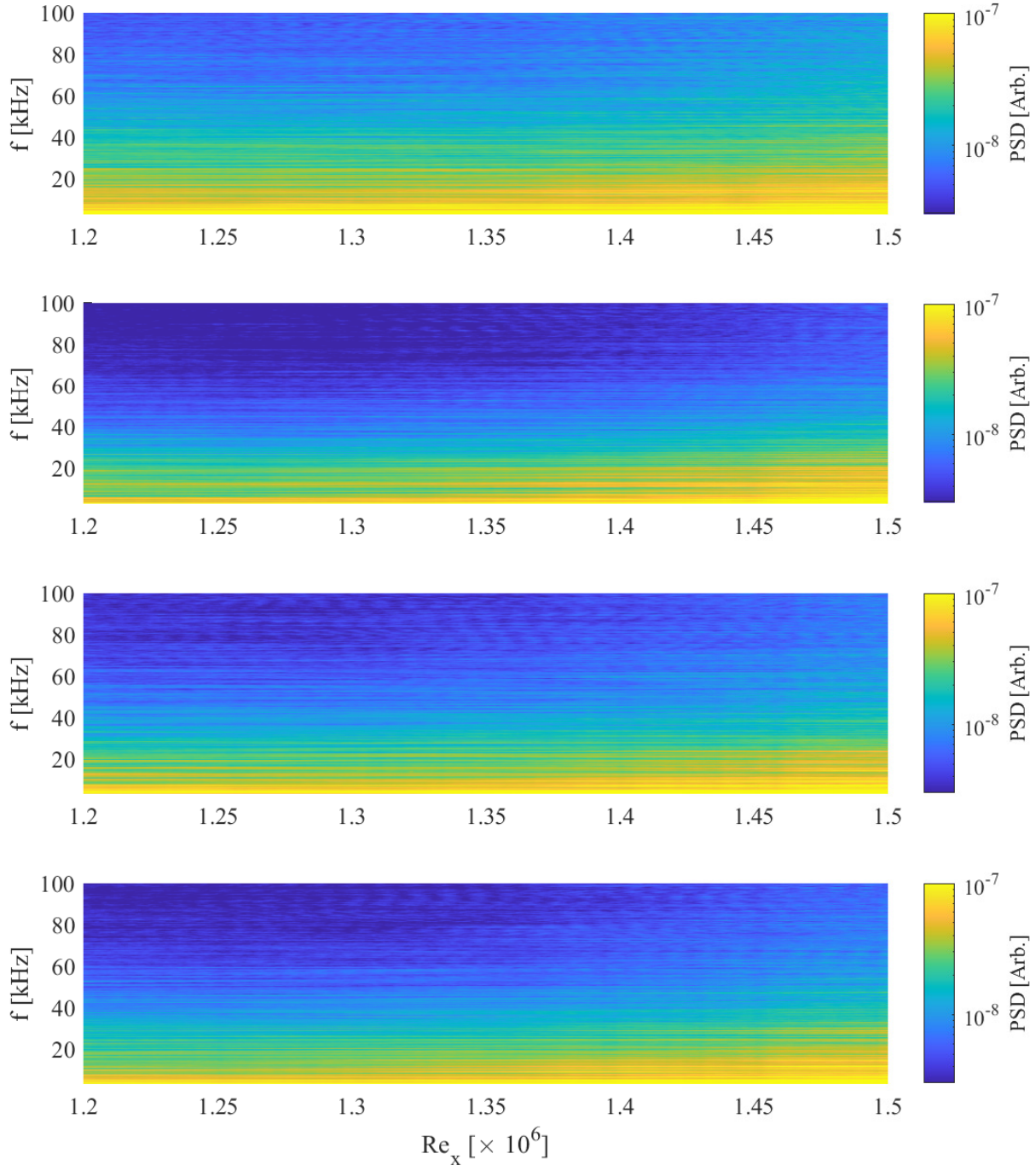

Figure 5.11: Spatially resolved PSDs along the cone for the particle-free, D9, D12, and D16 flow cases in order from top to bottom ($Re_\infty = 4.10 \pm 0.04 \times 10^6$ m^{-1}).

nificantly elevated disturbance amplitudes across the entire spectrum. The middle two plots, representing particle conditions D9 (above) and D12 (below), show that the boundary layers in these cases are intermittently transitional. The spectra have a similar amplitude in the 0-10 kHz range as the particle-free case, but slight attenuation of the higher-frequency fluctuations is present. The attenuation in the 10-40 kHz range on the upstream portion of the plots, for which the disturbances are associated with the first mode [10], is reflected in Fig. 5.4 where the upstream portion of the mean boundary layer appears laminar and the downstream portion shows signs of intermittent transitional behavior, reflected in the increase in the amplitude of the 10-40 kHz disturbances. An unexpected result is the level of attenuation of the freestream disturbances in the 10-40 kHz range in the particle condition D16 case. The freestream disturbance measurements in Ch. 4 had shown that the particle condition D9 case attenuates the disturbances the most, however condition D16 appears to have a stronger effect in suppressing the boundary layer disturbances. Given the differing particle sizes and number concentrations it is difficult to discern which variable is dominant in generating this phenomenon.

Increasing the Reynolds number slightly to $Re_\infty = 5.16\times10^6$ m^{-1} is enough to force transition/intermittent turbulent bursts for particle conditions D9 and D12 along the length of the cone visible with the camera, as shown in Fig. B.24. This is embodied in the PSD plots presented in Fig. 5.13 where the PSDs for those two conditions appear similar to that of the particle-free case, albeit with a reduction in power at higher frequencies. On the other hand, the particle-laden flow with particle diameter $d_p = 15.6\ \mu$m continues to exhibit a laminar boundary layer with relatively low amplitudes across the entire measured bandwidth. This particle condition finally shows signs of transition at the highest freestream Reynolds number tested ($Re_\infty = 5.82\times10^6$ m^{-1}), as shown in the lowermost plot of Fig. 5.14. At this Reynolds number, the power associated with the frequen-

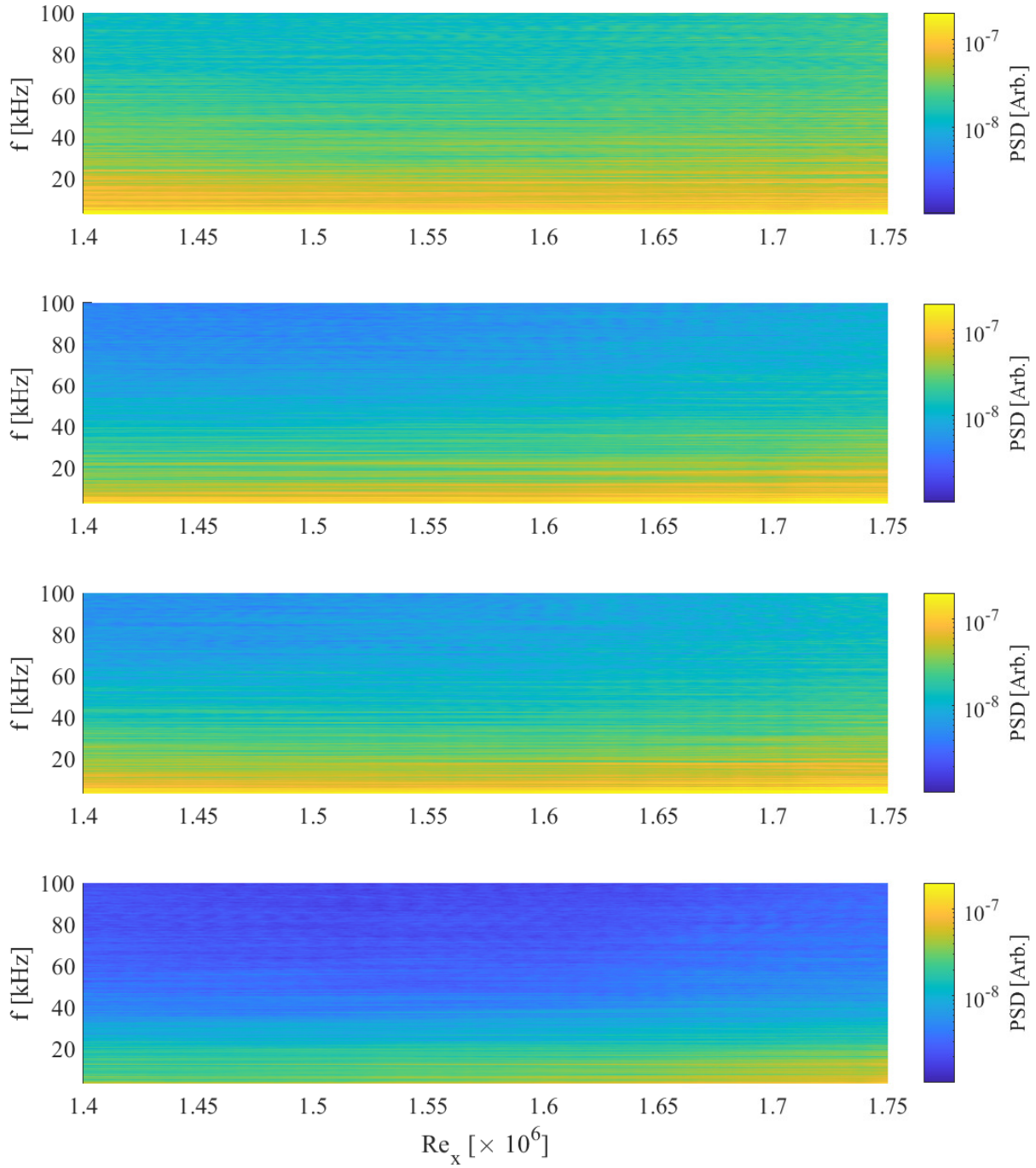

Figure 5.12: Spatially resolved PSDs along the cone for the particle-free, D9, D12, and D16 flow cases in order from top to bottom ($Re_\infty = 4.73 \pm 0.03 \times 10^6$ m^{-1}).

cies below 30 kHz is relatively consistent across the different particle conditions, but attenuation at higher frequencies is still apparent for all particle-laden cases and most notably for condition D16.

To provide a clearer comparison of the boundary-layer behavior with the various particle diameters, spectra were extracted at specific locations spanning local Reynolds numbers of $Re_x = 1.1\times10^6$ to $Re_x = 2.1\times10^6$ and are presented in Fig. 5.15. Similar results for other local Reynolds numbers can be found in Appendix B. The evolution in the growth of the disturbance amplitudes across the measured frequencies can be easily traced in these plots. The spectrum marked in black in each case is from the particle-free flow and consistently shows either similar or greater power across the plotted frequency range compared to the particle-laden cases. The increase in the higher frequency band (20-100 kHz) of the particle-free spectrum between $Re_x = 1.1\times10^6$ and $Re_x = 1.5\times10^6$ coincides with the change in boundary-layer state from purely laminar to transitional as discussed previously. For the particle-laden cases, conditions D9 (blue) and D12 (red) diverge from the profile of condition D16 (green) at $Re_x = 1.5\times10^6$ and begin to approach the PSD of the particle-free case, suggesting the onset of transition in both cases. At $Re_x = 1.7\times10^6$, particle conditions D9 and D12 exhibit spectra nearly identical to that of the particle-free case, indicating turbulent flow. At higher Reynolds numbers, the power at higher frequencies at these conditions again decreases as the turbulence becomes more fully developed.

Particle condition D16 is the most interesting case. The spectrum for this condition remains nearly unchanged until $Re_x = 1.7\times10^6$, indicating that the boundary layer is fully laminar. At $Re_x = 1.9\times10^6$, we begin to see the broadband growth consistent with the onset of transition, while at $Re_x = 2.1\times10^6$, the amplitude of the lower-frequency content for this condition follows that of all the other cases, including the particle-free case, while the higher-frequency content still shows

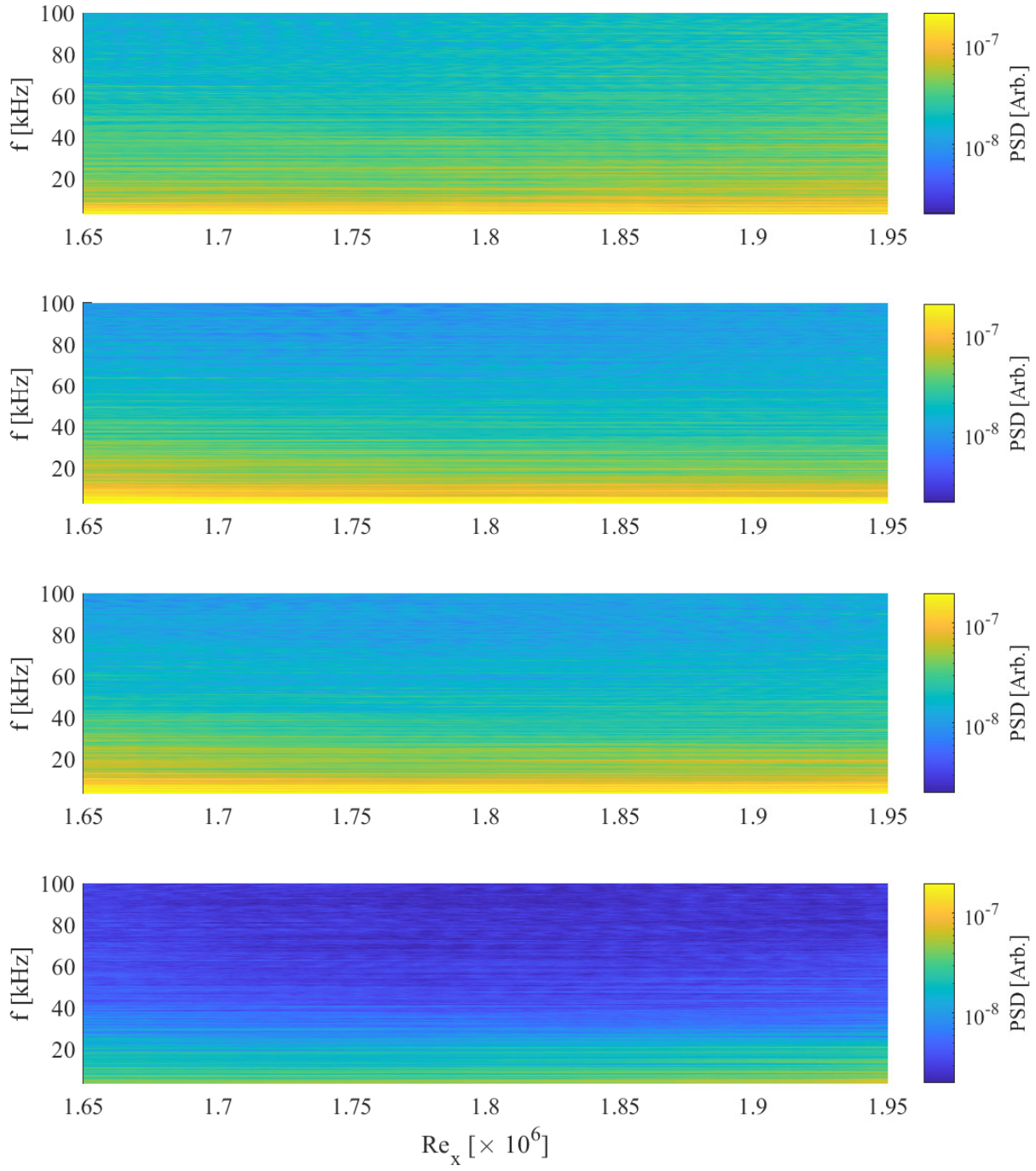

Figure 5.13: Spatially resolved PSDs along the cone for the particle-free, D9, D12, and D16 flow cases in order from top to bottom (Re_∞= 5.16±0.03×10^6 m^{-1}).

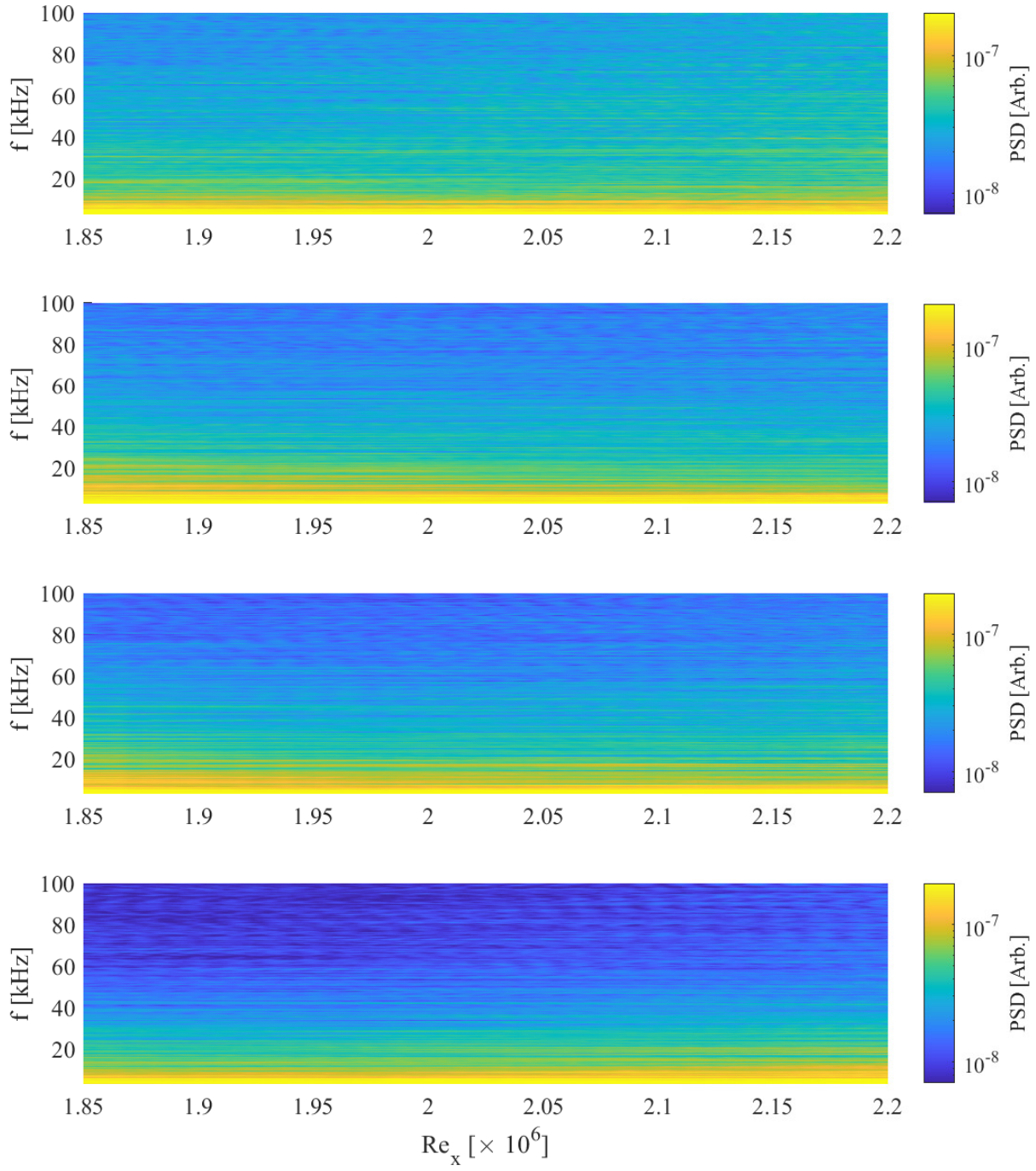

Figure 5.14: Spatially resolved PSDs along the cone for the particle-free, D9, D12, and D16 flow cases in order from top to bottom ($Re_\infty = 5.82 \pm 0.03 \times 10^6$ m^{-1}).

clear signs of attenuation. It is not clear whether this apparent attenuation is a result of the flow still not having reached a fully turbulent state, or if the reduced free-stream disturbance levels are also being reflected in the turbulent spectrum. In any case, assuming the onset of transition to occur at $Re_x = 1.3\times10^6$ for the clean flow and $Re_x = 1.8\times10^6$ for condition D16, this would correspond to an increase of 38% in the transition Reynolds number.

5.4 Conclusions

In this chapter, the effects of the presence of free-stream particles on boundary-layer transition were investigated on a 5° half-angle cone. Over a range of freestream unit Reynolds numbers, the boundary-layer behavior for three different types of particle-laden flows was compared to the baseline, particle-free, flow case using Schlieren visualizations. Mean Schlieren intensity images as well as derived PSD within the boundary layer were used to understand the influence of the particles on the onset of transition to turbulence.

The previous chapter had shown how the freestream particles lead to attenuation of the freestream acoustic disturbances generated by the nature of turbulent nozzle boundary layers. Based on those results, it appeared that condition D9 should have been the most successful at delaying the transition Reynolds number of the cone, as this combination of particle diameter and number concentration led to the greatest attenuation of freestream disturbances. However, as has been suggested in open literature, particles impinging on, or even approaching close enough to disturb the boundary layer through the generation of pressure waves [4,5,18] can actually force early onset of transition. Overall, this means that the particles should introduce competing effects on the transition behavior, that may depend on the particle diameters and concentrations.

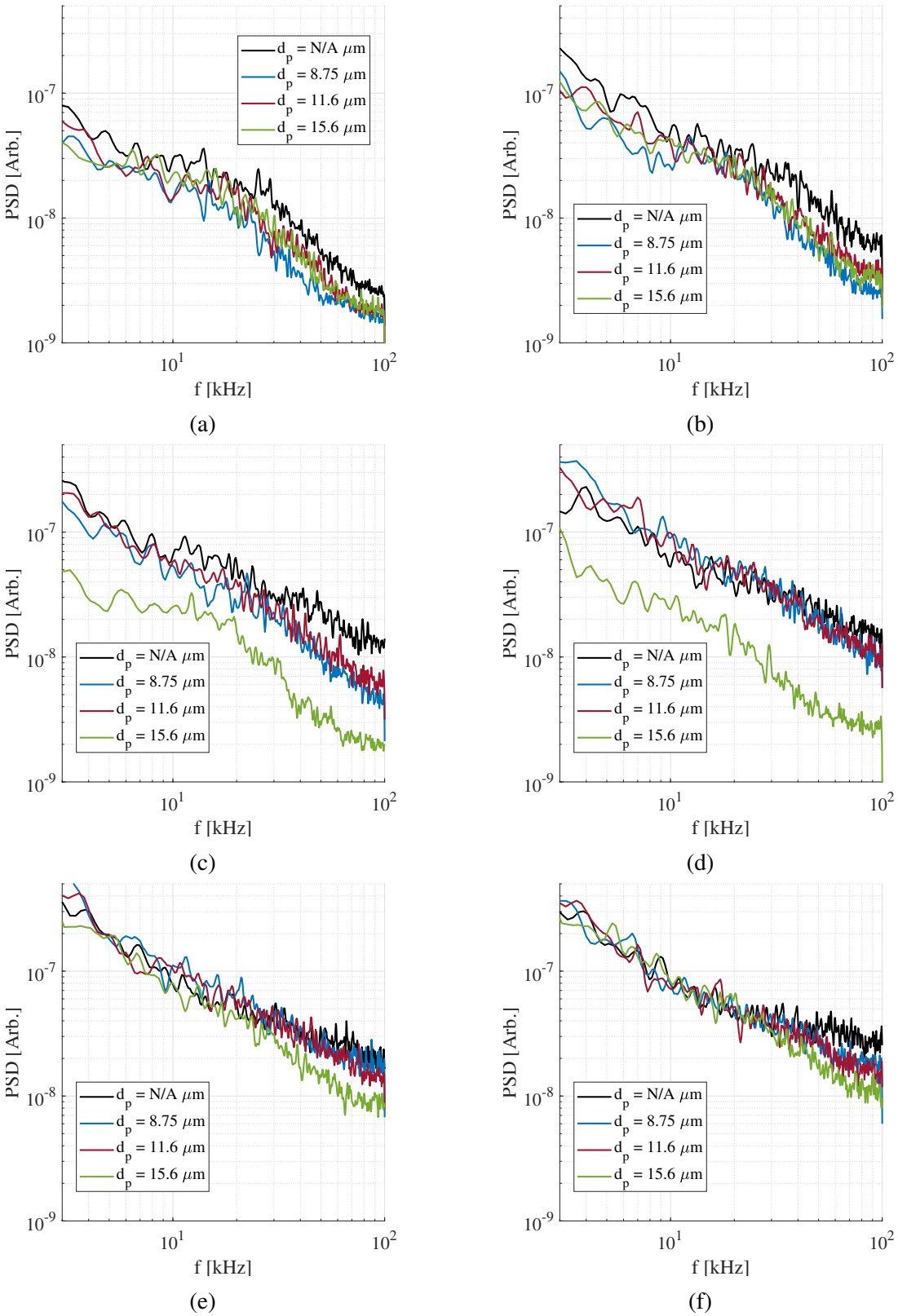

Figure 5.15: Comparison of the mean fluctuation density PSD in the boundary layer during the steady test time at cone Reynolds numbers of (a) Re_x= 1.1×10^6, (b) Re_x= 1.3×10^6, (c) Re_x= 1.5×10^6, (d) Re_x= 1.7×10^6, (e) Re_x= 1.9×10^6, and (f) Re_x= 2.1×10^6.

The mean Schlieren intensity images from the steady test time indicate that a freestream unit Reynolds number of $Re_\infty = 4.10 \pm 0.04 \times 10^6$ m^{-1} led to the boundary layer transition for the cone in Mach 3.83, particle-free flow. This corresponds to a Reynolds number of $Re_x = 1.35 \times 10^6$. The boundary layer transition for flow with particle conditions D9 and D12 does not appear to occur until $Re_\infty = 5.16 \pm 0.03 \times 10^6$ m^{-1} ($Re_x = 1.7 \times 10^6$), and it is delayed even further to $Re_\infty = 5.82 \pm 0.03 \times 10^6$ m^{-1} ($Re_x = 1.92 \times 10^6$) for condition D16. A PSD analysis was used to understand the differences in the disturbance spectra within the boundary layer at each condition. Across the entire experimental campaign, the particle-free cases consistently exhibited high, if not the highest, levels of boundary-layer fluctuations across the measured frequency spectrum. Seemingly as a result of the higher-frequency freestream acoustic disturbances being attenuated by the presence of particles, the boundary-layer PSDs for the particle-laden flows also showed reduced power at higher frequencies. Although condition D9 was shown to dampen the freestream acoustic disturbances the most, condition D16 produced the least disturbed boundary layer and most significant transition delay. This suggests a trade-off between the ability to attenuate freestream disturbances with a higher concentration of particles versus the effect that particle impingement has on tripping the boundary layer.

To improve our understanding of this behavior, additional experiments are necessary to cover a wider domain for all variables used, especially the particle diameters and concentrations. Furthermore, given the shot-to-shot variation in particle concentrations and unit Reynolds numbers, further repetitions of the experiments would be greatly beneficial to produce a more reliable representation of the results. Nevertheless, the present results provide compelling evidence that particle-laden flows, in a conventionally noisy wind-tunnel, can lead to a delay in boundary-layer transition through the attenuation of freestream acoustic disturbances. While tailoring MIST to

expand the testing parameters is left for future work, these results provide a previously unavailable data set on a highly relevant phenomenon for computational validation.

Chapter 6: Conclusion

6.1 Summary

This work was motivated by the desire to gain a better understanding on how high-speed vehicles are affected by the multi-phase nature of the atmosphere. Liquid particles ranging from sub-micron sized aerosols to millimeter-diameter rain droplets are found throughout the various layers of Earth's atmosphere. Irrespective of the mission, high-speed vehicles will traverse, or even operate in the lower atmosphere where cloud encounters expose them to droplets in the 5-20 μm diameter range. Furthermore, advanced sea- or ground-launched weapons systems, such as railguns, that need to operate in any weather condition (rain, fog, mist, etc.) can be strongly impacted by particles. To study the high-speed multi-phase flows that will be encountered in such situations, the Multi-phase Investigation Supersonic Tunnel (MIST) was designed and built at the University of Maryland.

MIST is a Mach 3.75-4 Ludwieg tube that is capable of producing high-speed, particle-laden flows with monodisperse particle diameters ranging from 4-16 μm. The DEHS droplets were produced by a TSI 1530 monodisperse droplet generator using a 5% DEHS in methanol mixture where the methanol evaporated once the droplets were produced to leave behind a pure DEHS, smaller droplet. To characterize the particles themselves, a TSI aerodynamic particle sizer was used to measure the droplet diameters under quiescent conditions; this led to the identifica-

tion of seven distinct DEHS particle sizes after the methanol had evaporated off. One- and two-dimensional simulations of particle flight through the nozzle were performed to inform the nozzle design as well as understand the behavior of the droplets as they accelerate to high-supersonic speeds. The nominal, particle-free flow conditions of the tunnel were well characterized by an extensive pitot rake study. Characterizing the particle-laden flow inside the wind tunnel proved more challenging. Two visualization techniques were employed to confirm the presence of particles in the flow and provide approximate measurements of the particles; however, measurements of in situ particle concentration proved impossible with these techniques. Therefore, an alternative methodology was developed that involved doping the particles with a fluorescent dye and inferring the particle number concentration based on the amount of fluorescent material deposited on a target; while similar methodologies have been used previously in subsonic flows, here it was performed in a supersonic flow for the first time. The freestream number concentration and particle distribution for five of the seven particle sizes were characterized with this method.

Using this newly developed and fully characterized wind tunnel, an investigation into how the particle-laden flow affects the drag on a sphere was performed. Spheres of three different sizes were suspended in the wind tunnel and exposed to particle-laden flows with all five characterized particle sizes and concentrations, as well as particle-free flow for comparison. High-speed bi-telecentric imaging was used to capture the flight of the sphere and an edge-fitting routine allowed the trajectory to be determined, from which the drag could be derived. Each condition was repeated five times to allow statistics to be calculated. The drag coefficient for spheres exposed to particle-laden flow was measured to be 1.75-4.5% higher that generated by particle-free flow, depending on the particle diameter and concentration combination. This was significantly higher than the expected increase obtained from estimates based on a drag model assuming the multi-

phase flow behaved as a single-phase fluid with an equivalent effective density. Simulations showed that nearly all particles would impact the sphere rather than being deflected around it by the flowfield at the tested conditions, but direct momentum transfer from particle impacts would still result in a drag-coefficient increase orders of magnitude below that which was measured. This would suggest that either the model is inaccurate or there are other physical phenomena at play. One possible explanation is that the particles are impacting the sphere at supersonic speeds, and therefore will impart a high pressure wave on the sphere as a result of the presence of their bow shock, thus increasing the force on the sphere.

In addition to force measurements, MIST was also used to study the behavior of boundary layers in high-speed, multi-phase flows. Boundary layer transition has always been an area of concern for high-speed vehicles due to the significant pressure and thermal loads associated with the process. Previous numerical studies concluded that particles in the flow advance transition by disturbing the boundary layer through direct impacts or indirectly by the pressure wave produced from the particles entering the near-body flowfield. Before a transition study could be performed, the noise environment in MIST needed to be characterized since the acoustic disturbances in ground test facilities play a major role in determining the transition behavior. Focused Laser Differential Interferometry (FLDI) was used to measure the freestream density fluctuations under various conditions. All five particle-laden flow conditions were compared to the particle-free case at two different unit Reynolds numbers. The multi-phase flow was shown to produce a quieter noise environment in the MIST freestream in all cases. The D9 particle condition (d_p = 8.75 μm and C = 92.7 #/cm^3) attenuated the disturbances the most, reducing the power of the PSD spectra by up to a factor of 5 for the $Re_\infty = 4.73 \times 10^6$ m^{-1} condition and 10 for the $Re_\infty = 5.82 \times 10^6$ m^{-1} condition. Based on open literature, particle relaxation is expected to be

the dominant mechanism for attenuating the acoustic disturbances. The experiments showed a higher frequency for the peak attenuation, however, this discrepancy could be due to the presence of the lower-frequency shear layer disturbances in the FLDI measurements.

Leveraging the unique capabilities of MIST, an experimental investigation on the influence of multi-phase flow on the boundary layer transition on a sharp, 5° half-angle cone was performed. Three particle diameter and concentration combinations were chosen to compare to the particle-free flow case at five different freestream unit Reynolds numbers. Contrary to expectations, the particle-laden flow led to a delay in the boundary-layer transition with up to a 38% increase in transition Reynolds number. This was attributed to the attenuation of the freestream acoustic disturbance environment noted above. When comparing between the particle-laden flow cases, maximum delay was observed for the largest (15.6 μm diameter) particles, whereas the boundary layer transitioned earlier for the cases with smaller particles but higher particle concentrations; this was despite one of those cases having shown the strongest attenuation of higher-frequency freestream disturbances. Previous experiments indicated that the first mode (in the 10-40 kHz range) dominated the transition process on the same cone model in MIST. Unfortunately, the measured attenuation of the disturbances in this frequency band from the FLDI experiments are likely corrupted from the presence of the shear layer in the MIST test section, and therefore do not represent the true magnitude of attenuation in the freestream disturbances by the particle-laden flows.

6.2 Contributions

This work has led to a series of contributions on the behavior of high-speed, multi-phase flows. To begin with, the design of MIST is unique in the open literature and it currently is the only wind tunnel capable of producing high-supersonic, liquid-particle-laden flows using cloud-sized droplets. An extensive wind-tunnel-characterization campaign ensured that the properties of the wind tunnel and the particles used in the multi-phase flow were well established. In connection with the development of the wind tunnel, a novel application of fluorescence spectroscopy was utilized to characterize the freestream particle-number concentration. This technique had been used previously only in subsonic flows and was fundamental in determining the particle concentration, a key parameter used in the presented.

Pertaining to the scientific contributions, each investigation presented in this paper was a first of its kind. The measurement of the increase in drag coefficient in high-speed, particle-laden flows was enabled because of the development of MIST and therefore is unique to this work. While most facilities avoid introducing any type of particulate, and flight trajectory estimations tend to neglect weather encounters due to the small percentage of the overall flight path that they usually occupy, the results showed that an adjustment to the drag coefficient in the calculations for any vehicle traveling at high speeds and low altitudes is recommended. These results also provide valuable experimental data for the validation of more complex computational models as the simple model used in this work, where the multi-phase flow was treated as a single fluid with a modified effective density, was shown to be inaccurate.

A significant contribution is the discovery of the attenuation of high-speed wind tunnel acoustic disturbances using particle-laden flows. There have been major investments in methods

for reducing noise in wind tunnels and the results from this work have shown a relatively cheap method for attenuating the freestream disturbances. While the phenomenon of aerosolized gases reducing the amplitude of acoustic waves has been previously observed, this is the first demonstration of this effect in a high-speed wind tunnel. This discovery could be potentially leveraged to develop a "quasi-quiet" wind tunnel.

Finally, the experimental study on the effect of particle-laden flows on the transition of a high-speed boundary layer is the first of its kind in open literature, to the author's knowledge. While the FLDI study demonstrated that a conventionally noisy wind tunnel could be made quieter with the use of particle-laden flows, the cone study showed conclusively that the onset of the boundary-layer transition on a sharp cone could be successfully delayed. This work also provides much needed experimental results for the validation of computational methods, several of which have already been used to study a similar problem.

6.3 Future Work

While various aspects of high-speed, particle-laden flows have been explored in the present work, the new gaps identified need to be explored. To begin with, the capabilities of MIST can be expanded. This includes the establishment and characterization of additional test conditions. Specifically, new test points for different freestream number concentrations of the particles would help advance the understanding of how this parameter affects the various aerodynamic measurements offered by MIST. Further verification of these concentration measurements would also be beneficial. Improving the visualization techniques would allow for corroboration of the values obtained from the fluorescence spectroscopy technique.

On top of adding additional data points based on the particle concentration, the work examining the increase in drag coefficient of the sphere would benefit from a larger Reynolds number domain. In this work, only a linear function was fit to the data, but this expansion would allow for a better defined function to be obtained. While this type of study on a sphere is highly useful, most aircraft and projectiles have at least one asymmetric axis, and therefore studying the effect of particle-laden flows on a lifting body, such as a cone, would help inform how the moment coefficients are affected. This is significant because we would expect more particle impacts near the front of the body than the rear, which would lead to an unbalanced pitching moment.

With regards to the freestream noise measurements, significant improvements need to be made to the FLDI setup in order to obtain calibrated data. The plots presented in this work showed the attenuation of the disturbances, but for CFD validation or other quantitative uses of the data, actual physical values are necessary. The investigation was unable to use the entire range of capabilities of the FLDI setup, as the signal to noise ratio did not exceed unity for frequencies much higher than 100 kHz, whereas previous FLDI measurements have shown the potential for much higher bandwidths. Furthermore, producing a model of the shear layer generated by the MIST nozzle would allow for the development of transfer functions, such as that developed by Ceruzzi [49], that lead to an accurate physical representation of the density fluctuations in the freestream.

As with all of the results obtained using MIST in its multi-phase flow configuration, repetition of shots is highly recommended for statistical purposes. This would be useful for both the FLDI measurements of the freestream acoustic disturbances as well as the visualization of the boundary layer transition of the cone. Boundary layer transition is already quite variable by nature and the repetitions would not only benefit by reducing the propagation of uncertainty from

the particle concentration measurements, but also help establish at which Reynolds number transition is most likely to occur. Additionally, exploring optimal combinations of particle diameter and concentrations to maximize the transition delay could assist in the design of "quieter tunnels". Lastly, modifying MIST for a higher Mach number would allow for the examination of the second-mode dominated transition which is highly relevant for vehicles and projectiles traveling at hypersonic speeds.

Appendix A: Sphere Drag Models

The drag force is the dominant force driving the particle trajectories in MIST; the minuscule time scales render gravitational and buoyant forces negligible. For the purposes of simulating the droplet trajectories through the nozzle and over the wind tunnel models, each droplet was treated as a sphere and the drag coefficient was calculated using the Singh [86] and Loth [85] drag models. A summary of the drag models is presented in this section. For a complete description, the reader is directed to the respective papers.

A.1 Singh Drag Model

The physics-based expressions for the generalized drag model are presented here, keeping consistent with the notation from Singh.

$$C_d = C_d^c\left(M_\infty, Re_\infty\right) f_{Kn_\infty, W_r} \frac{1}{1 + Br^\eta} + Cd_{fm} \frac{Br^\eta}{1 + Br^\eta} \tag{A.1}$$

where

$$Br = W_r^T \frac{M_\infty^{2\omega-1} + 1}{M_\infty^{2\omega-1}} \tag{A.2}$$

$$W_r^T = W_r \left(1 + \frac{T_p}{T_s}\right)^{\omega} \qquad M_\infty > 1 \tag{A.3}$$

$$W_r = \frac{M_\infty^{2\omega}}{Re_\infty} = Kn_\infty M_\infty^{2\omega-1} \sqrt{\frac{2}{\pi\gamma}} \tag{A.4}$$

$$f_{Kn_\infty, W_r} = \frac{1}{1 + Kn_\infty \left[A_1 + A_2 \exp\left(-A_3/Kn_\infty\right)\right]} \frac{1}{1 + \alpha_{hoc} W_r^T} \tag{A.5}$$

$$C_{d,fm} = \frac{\left(1 + 2s^2\right) exp\left(-s^2\right)}{s^3 \sqrt{\pi}} + \frac{\left(4s^4 + 4s^2 - 1\right) erf(s)}{2s^4} + \frac{2}{3s} \sqrt{\pi \frac{T_p}{T_\infty}} \tag{A.6}$$

$$s = M_\infty \sqrt{\frac{\gamma}{2}} \tag{A.7}$$

$$C_d^c = C_1 \left(1 - \alpha \frac{U_s}{U_\infty}\right) + C_0 \Theta_s \left(1 + \frac{\delta_0}{\left(\tilde{R}e_s\right)^{1/2}}\right)^2 \tag{A.8}$$

$$\Theta(M) = \left[1 + (\gamma - 1)\frac{M^2}{2}\right]^{\gamma/(\gamma-1)} \tag{A.9}$$

$$\tilde{R}e_s = Re_\infty \left[\frac{1}{\alpha^2} \frac{T_\infty}{T_s}\right]^{\omega} \Theta\left(M\right)^{(\gamma+1/2\gamma)-(\gamma-1/\gamma)\omega} \tag{A.10}$$

$$C_1 = \frac{C_d^{M_\infty} - C_0 \left\{1 + \left[\frac{(\gamma-1)^2}{4\gamma}\right]\right\}^{\gamma/(\gamma-1)}}{1 - \left(\frac{1}{\alpha_0 M_\infty}\right)\left(\frac{\gamma-1}{\gamma+1}\right)} \tag{A.11}$$

$$\alpha = \frac{1}{\alpha_0 M_\infty + 1 - \alpha_0} \tag{A.12}$$

A.2 Loth Drag Model

The equations for the Loth drag model, keeping consistent with the notation from Loth, are presented here. For the compression dominated regime,

$$C_D = \frac{24}{Re_p}\left(1 + 0.15Re_p^{0.687}\right)H_M + \frac{0.42C_M}{1 + \left(\frac{42500}{Re_p^{1.16C_M}}\right) + \left(\frac{G_M}{Re_p^{0.5}}\right)} \qquad 45 < Re_p < Re_{p,crit} \tag{A.13}$$

where

$$C_M = 1.65 + 0.65\tanh\left(4M_p - 3.4\right) \qquad \text{for } M_p < 1.5 \tag{A.14}$$

$$C_M = 2.18 - 0.13\tanh\left(0.9M_p - 2.7\right) \qquad \text{for } M_p > 1.5 \tag{A.15}$$

$$G_M = 166M_p^3 + 3.29M_p^2 - 10.9M_p + 20 \qquad \text{for } M_p < 0.8 \tag{A.16}$$

$$G_M = 5 + 40M_p^{-3} \qquad \text{for } M_p > 0.8 \tag{A.17}$$

$$H_M = 0.0239M_p^3 + 0.212M_p^2 - 0.074M_p + 1 \qquad \text{for } M_p < 1 \tag{A.18}$$

$$H_M = 0.93 + \frac{1}{3.5 + M_p^5} \qquad \text{for } M_p > 1 \tag{A.19}$$

For the rarefaction-dominated regime,

$$C_D = \frac{C_{D,Kn,Re}}{1 + M_p^4} + \frac{M_p^4 C_{D,fm,Re}}{1 + M_p^4} \qquad \text{for } Re_p \leq 45 \tag{A.20}$$

where

$$C_{D,Kn,Re} = \frac{24}{Re_p}\left(1 + 0.15 Re_p^{0.687}\right) f_{Kn} \tag{A.21}$$

$$f_{Kn} = \frac{1}{1 + Kn_p\left[2.514 + 0.8\exp(-0.55/Kn_p)\right]} \tag{A.22}$$

$$C_{D,fm,Re} = \frac{C_{D,fm}}{1 + \left[\left(C_{D,fm}/J_M\right) - 1\right]\sqrt{\left(Re_p/45\right)}} \tag{A.23}$$

$$J_M = 2.26 - \frac{0.1}{M_p} + \frac{0.14}{M_p^3} \qquad \text{for } M_p \leq 1 \tag{A.24}$$

$$J_M = 1.6 + \frac{0.25}{M_p} + \frac{0.11}{M_p^2} + \frac{0.44}{M_p^3} \qquad \text{for } M_p \geq 1 \tag{A.25}$$

$$C_{D,fm} = \frac{\left(1 + 2s^2\right)\exp\left(-s^2\right)}{s^3\sqrt{\pi}} + \frac{\left(4s^4 + 4s^2 - 1\right)\mathrm{erf}(s)}{2s^4} + \frac{2}{3s}\sqrt{\pi} \tag{A.26}$$

$$s \equiv M_p \sqrt{\frac{\gamma}{2}} \tag{A.27}$$

Appendix B: Additional Data

B.1 Schlieren snapshot sequences for all test cases

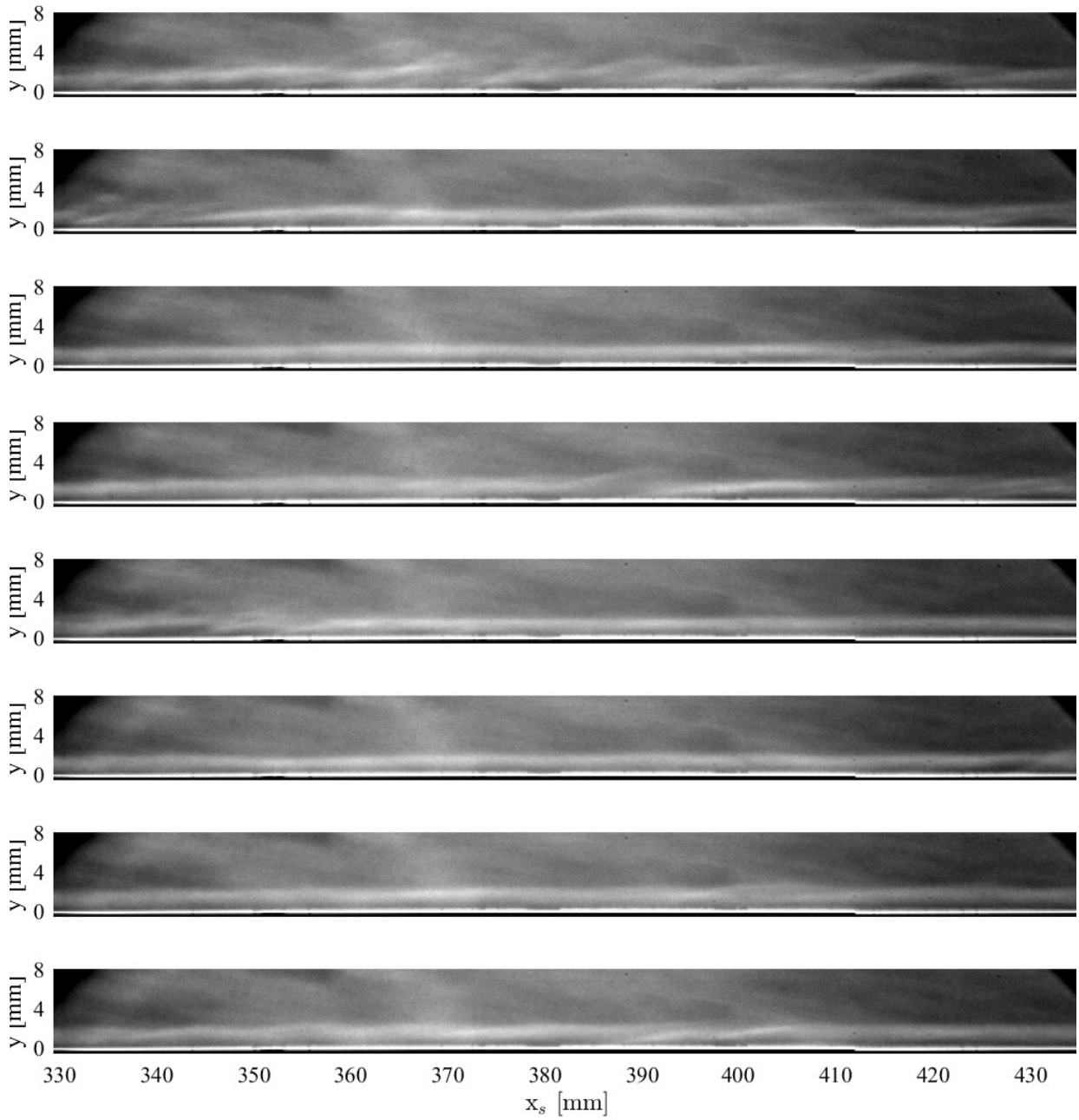

Figure B.1: Sequence of schlieren images, Δt = 2.5 ms, for the particle-free, Re_∞ = 3.41±0.03 $\times 10^6$ m^{-1} condition.

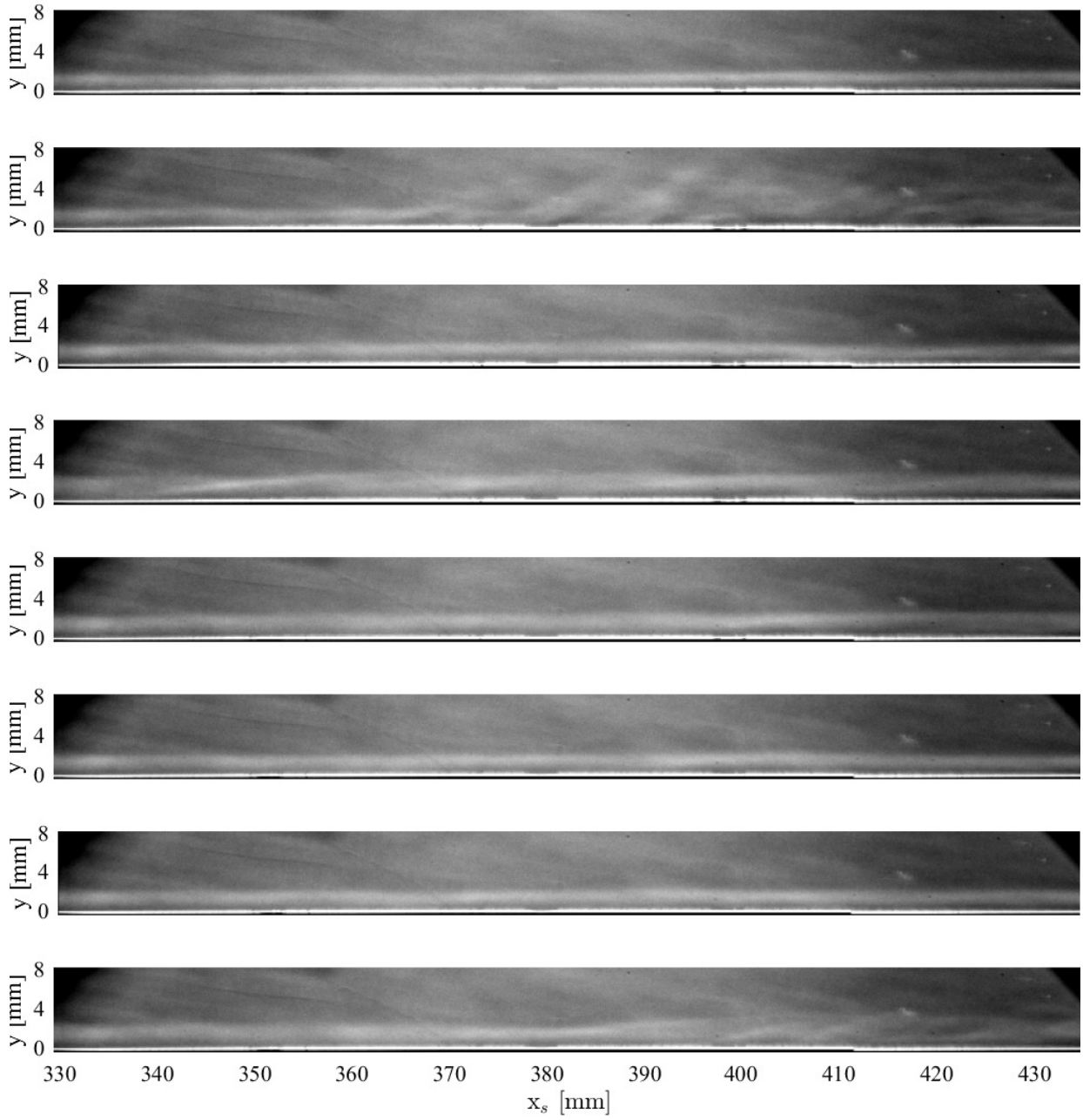

Figure B.2: Sequence of schlieren images, Δt = 2.5 ms, for the D9, $Re_\infty = 3.41 \pm 0.03 \times 10^6$ m^{-1} condition.

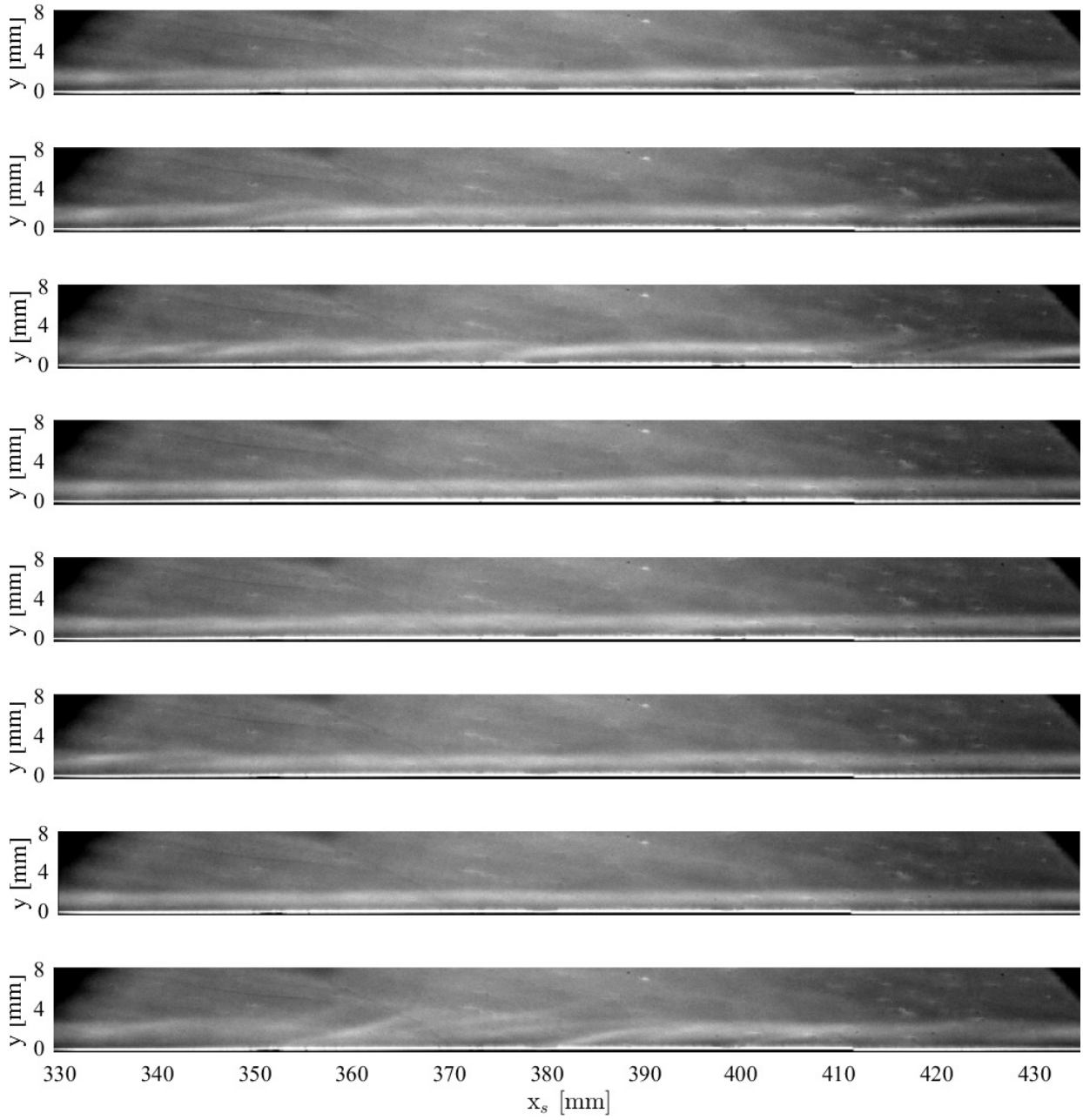

Figure B.3: Sequence of schlieren images, Δt = 2.5 ms, for the D12, $Re_\infty = 3.41 \pm 0.03 \times 10^6$ m^{-1} condition.

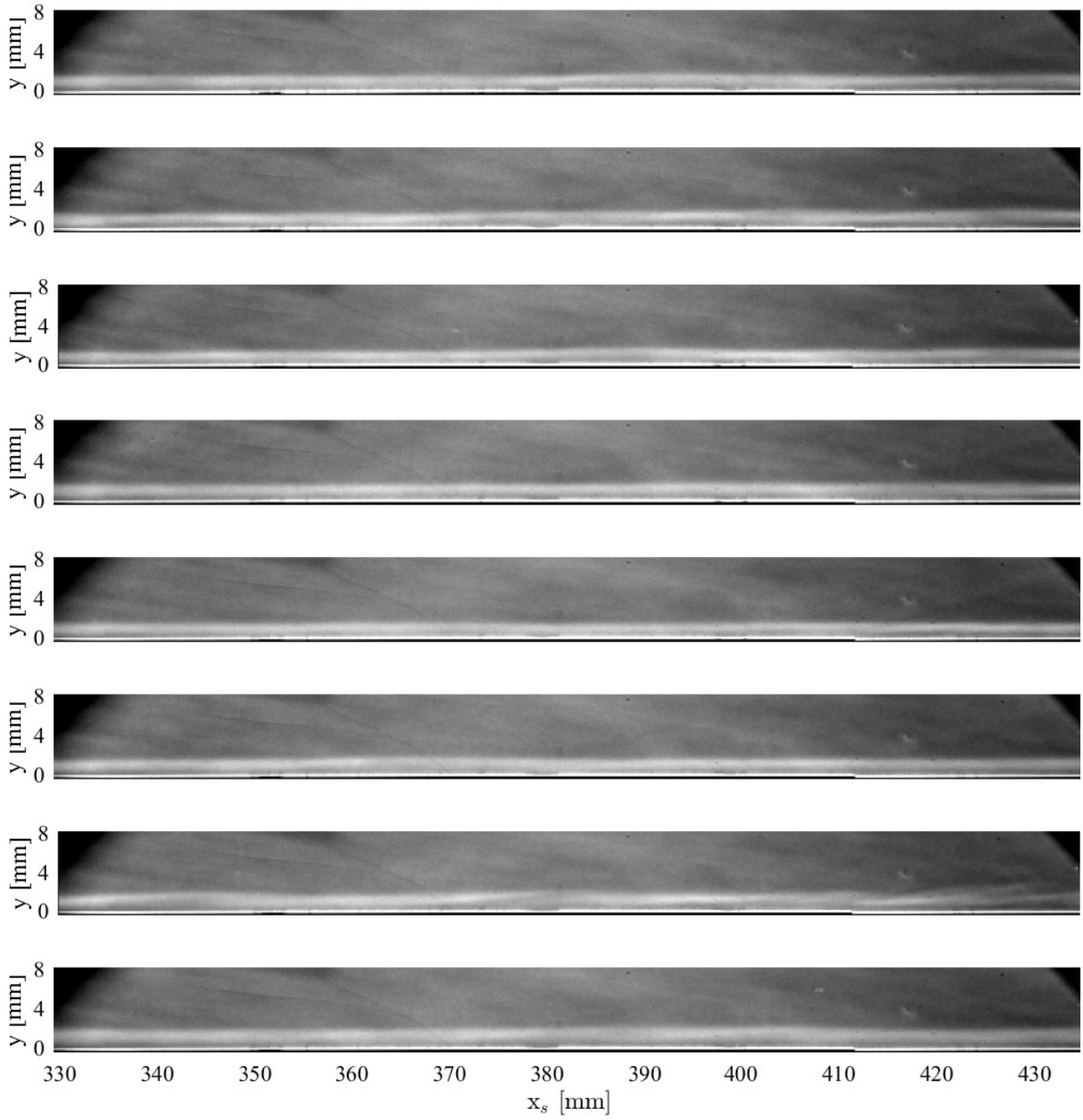

Figure B.4: Sequence of schlieren images, Δt = 2.5 ms, for the D16, $Re_\infty = 3.41 \pm 0.03 \times 10^6$ m^{-1} condition.

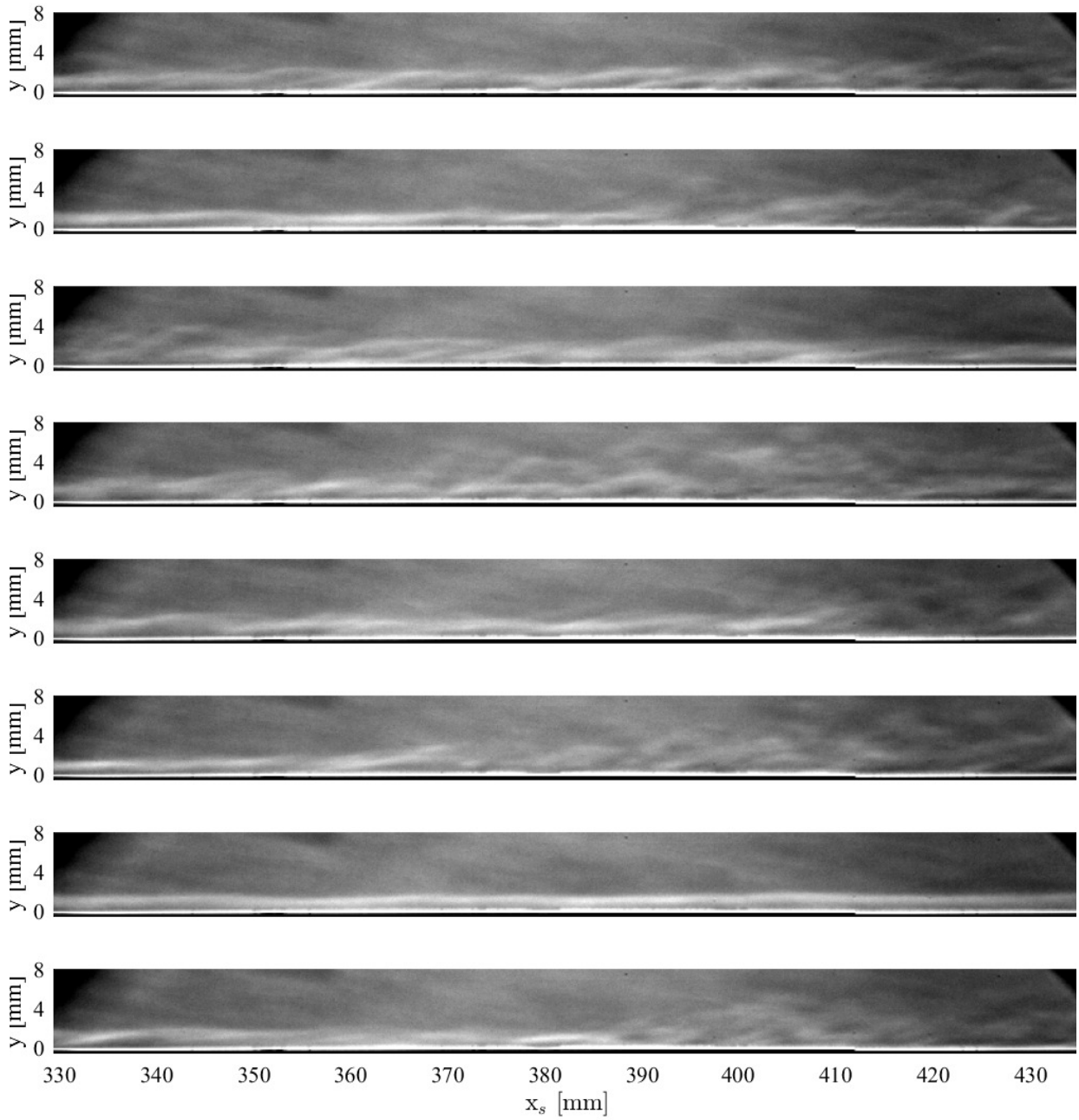

Figure B.5: Sequence of schlieren images, Δt = 2.5 ms, for the particle-free, Re_∞ = 4.10±0.04 $\times 10^6$ m^{-1} condition.

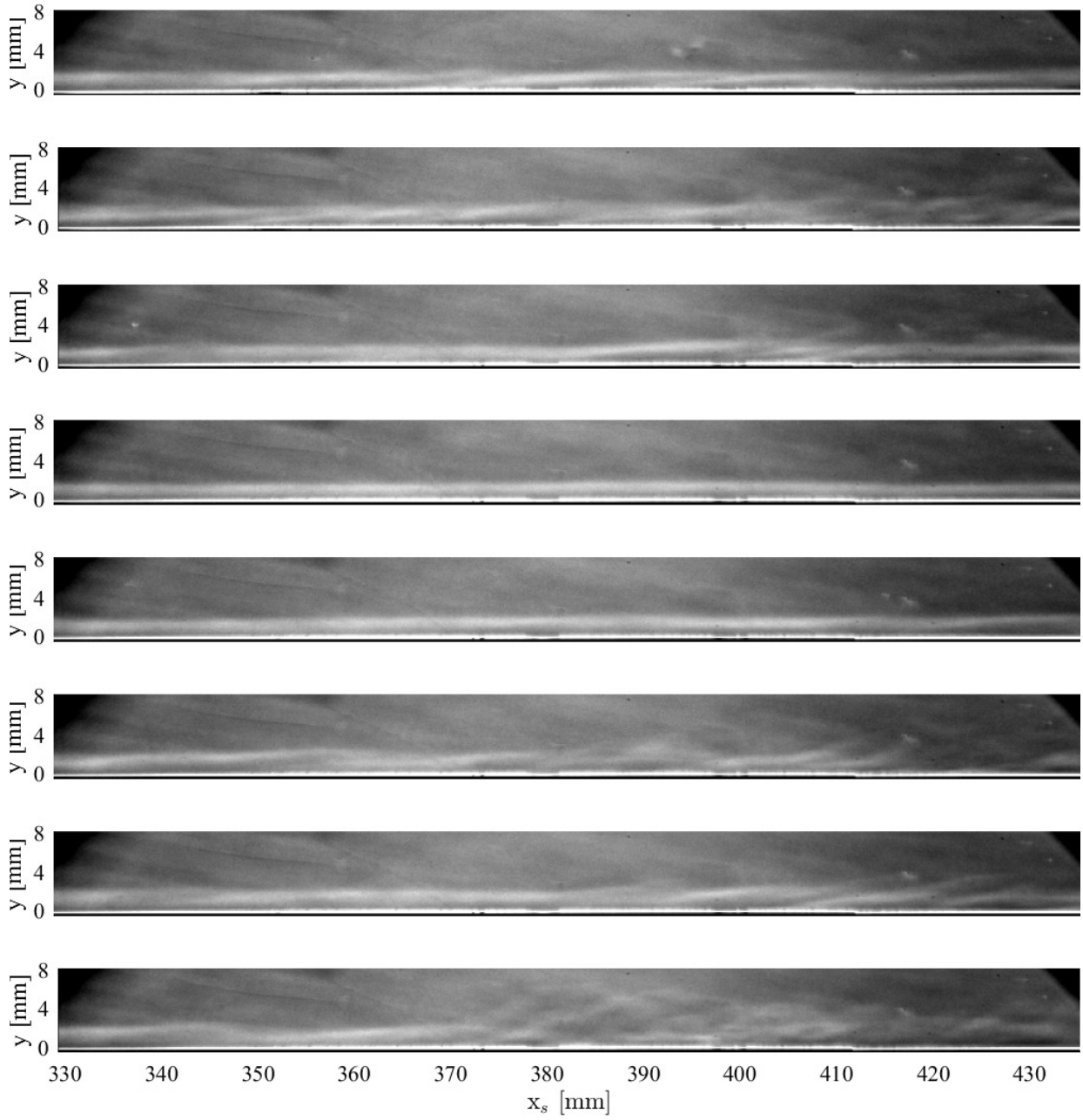

Figure B.6: Sequence of schlieren images, Δt = 2.5 ms, for the D9, $Re_\infty = 4.10 \pm 0.04 \times 10^6$ m^{-1} condition.

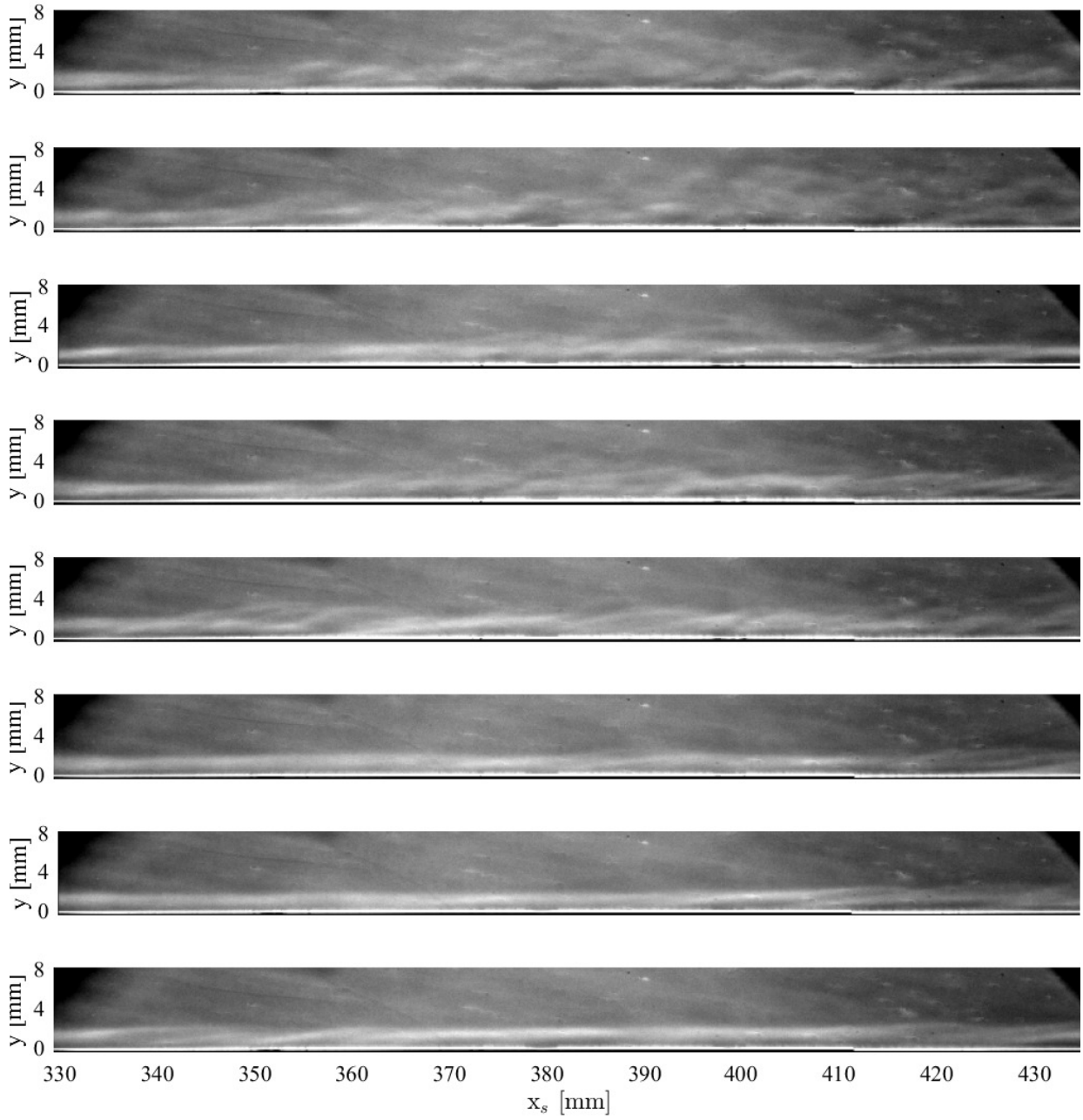

Figure B.7: Sequence of schlieren images, Δt = 2.5 ms, for the D12, $Re_\infty = 4.10 \pm 0.04 \times 10^6$ m^{-1} condition.

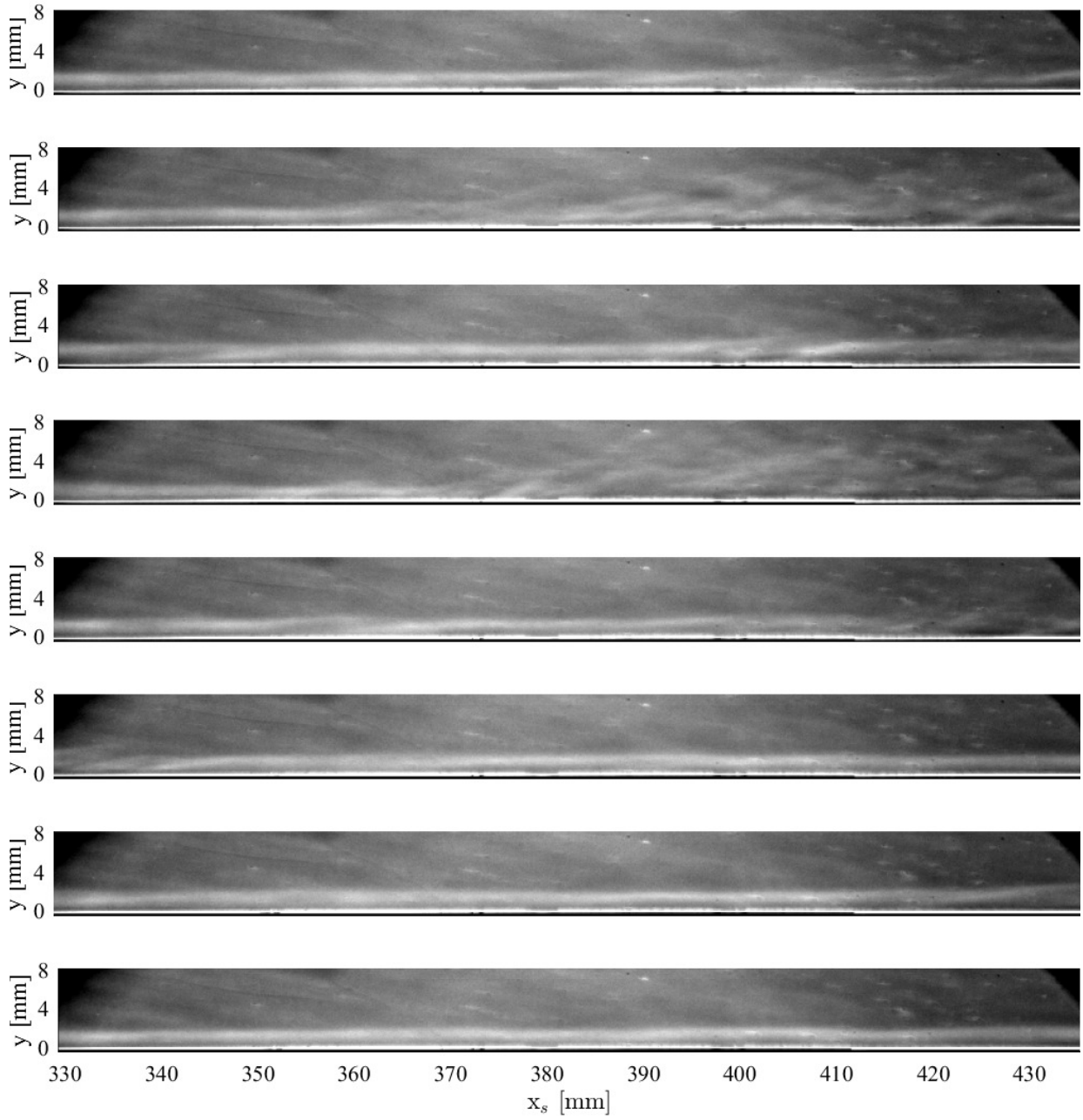

Figure B.8: Sequence of schlieren images, Δt = 2.5 ms, for the D16, $Re_\infty = 4.10 \pm 0.04 \times 10^6$ m^{-1} condition.

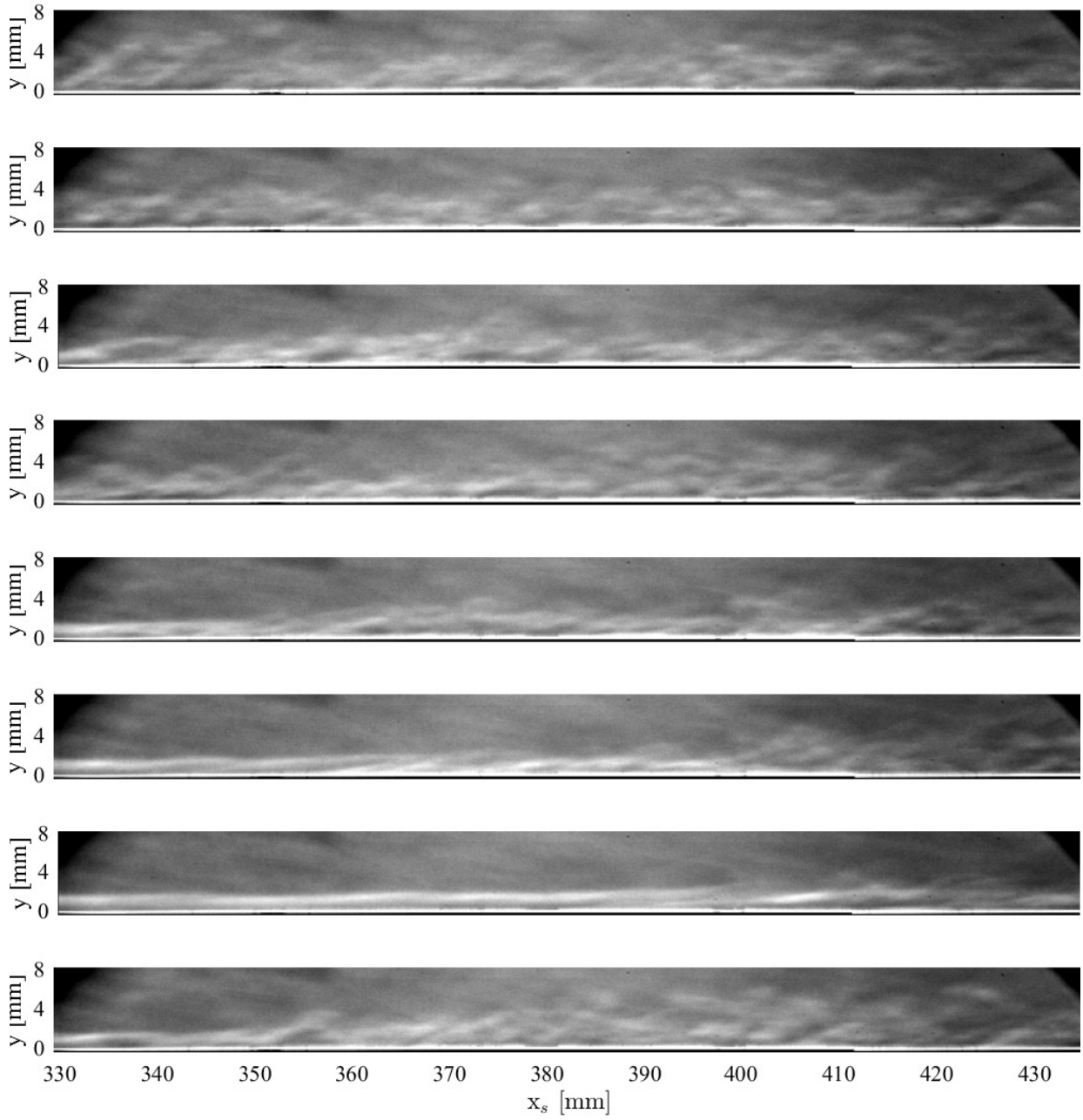

Figure B.9: Sequence of schlieren images, Δt = 2.5 ms, for the particle-free, Re_∞ = 4.73±0.03 $\times 10^6$ m^{-1} condition.

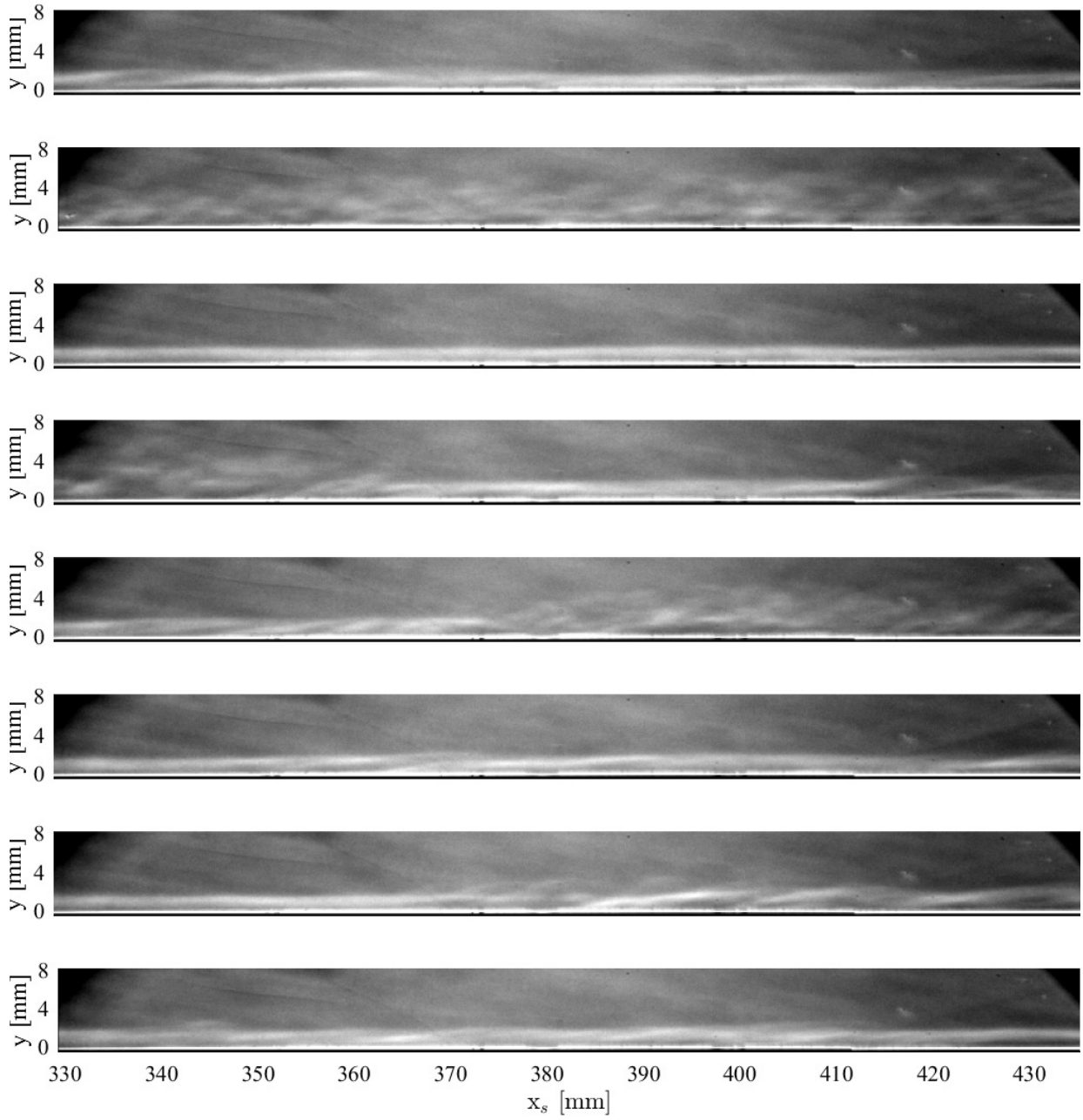

Figure B.10: Sequence of schlieren images, Δt = 2.5 ms, for the D9, $Re_\infty = 4.73 \pm 0.03 \times 10^6$ m^{-1} condition.

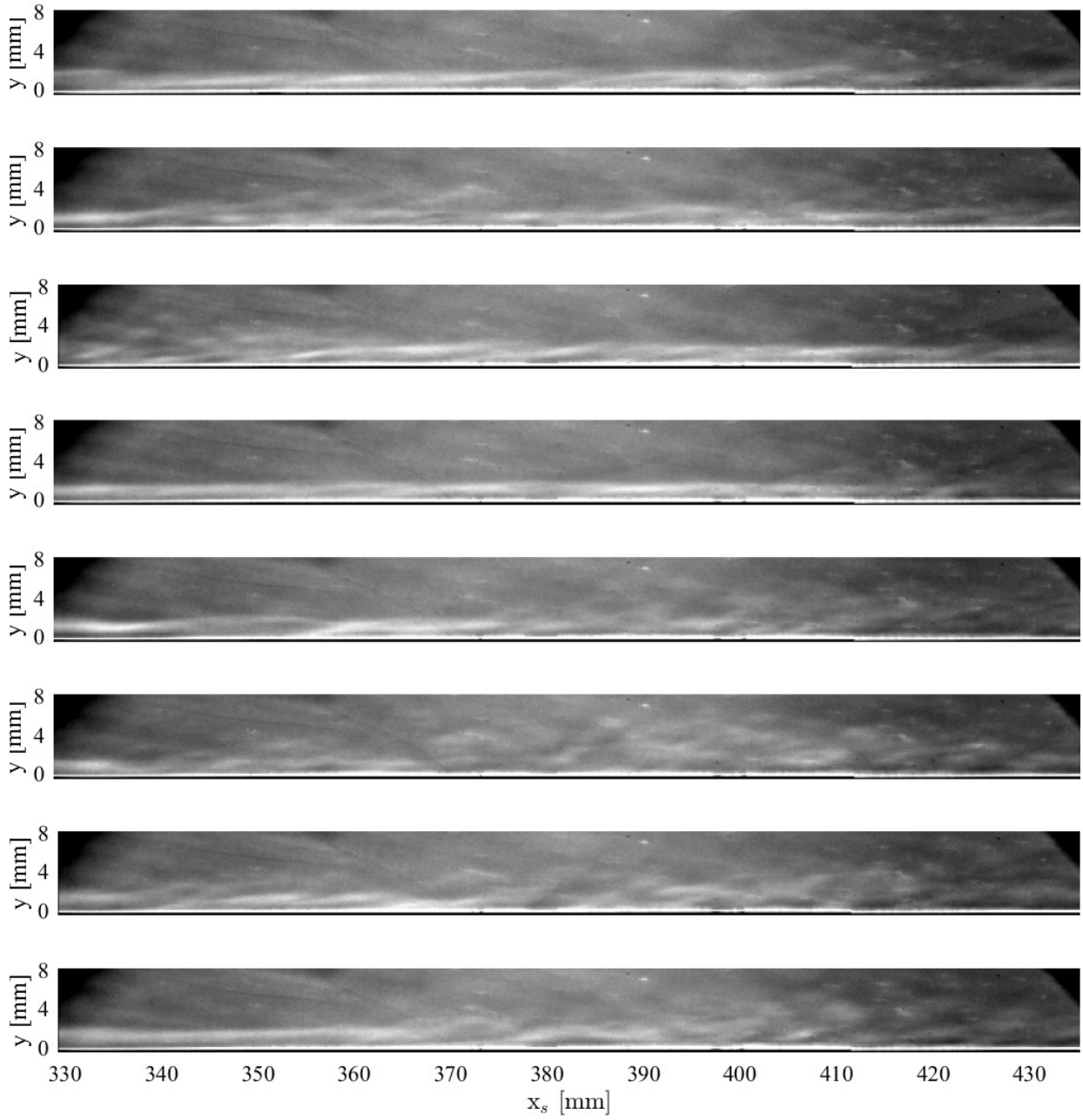

Figure B.11: Sequence of schlieren images, $\Delta t = 2.5$ ms, for the D12, $Re_\infty = 4.73 \pm 0.03 \times 10^6$ m^{-1} condition.

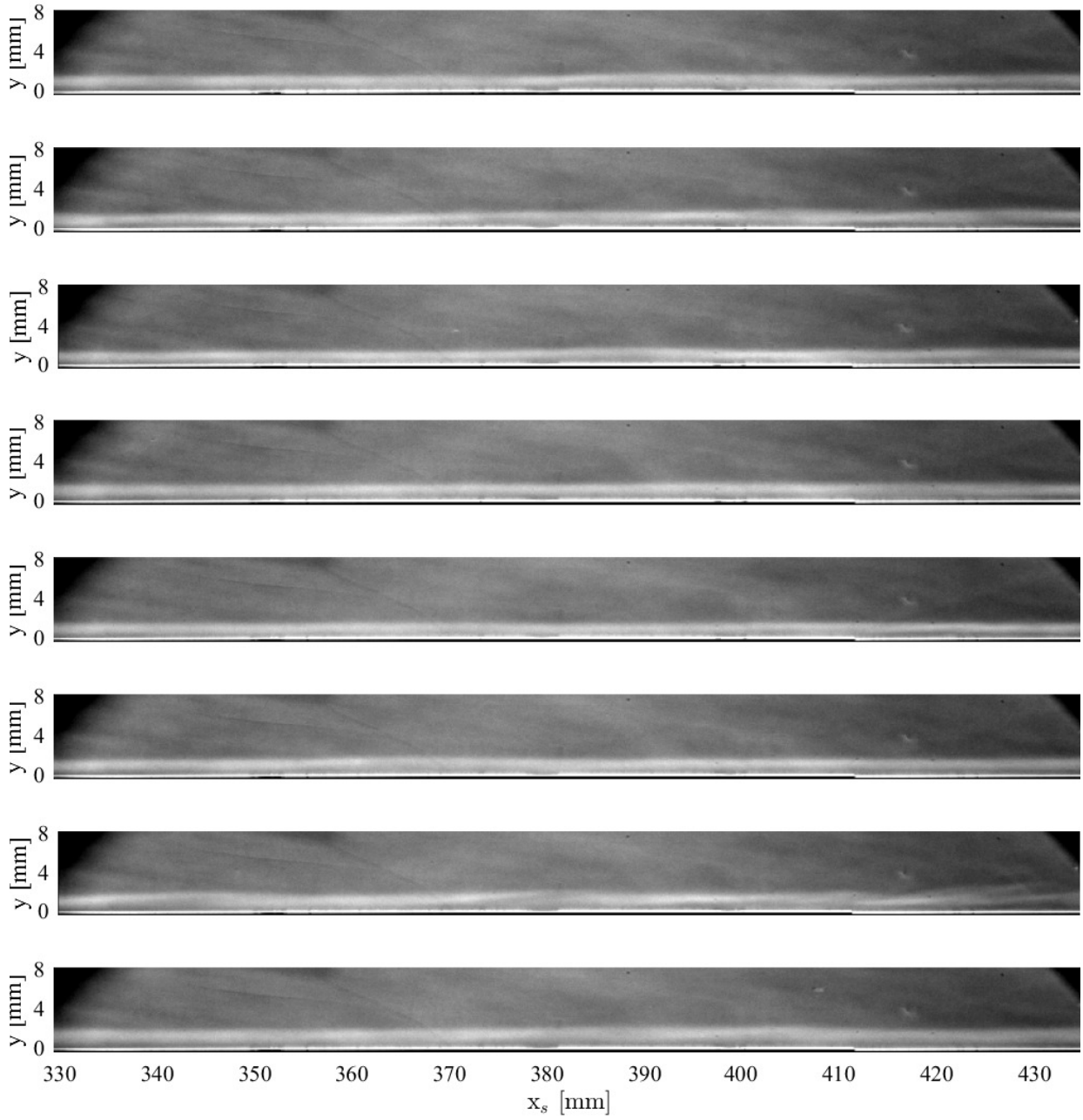

Figure B.12: Sequence of schlieren images, $\Delta t = 2.5$ ms, for the D16, $Re_\infty = 4.73 \pm 0.03 \times 10^6$ m^{-1} condition.

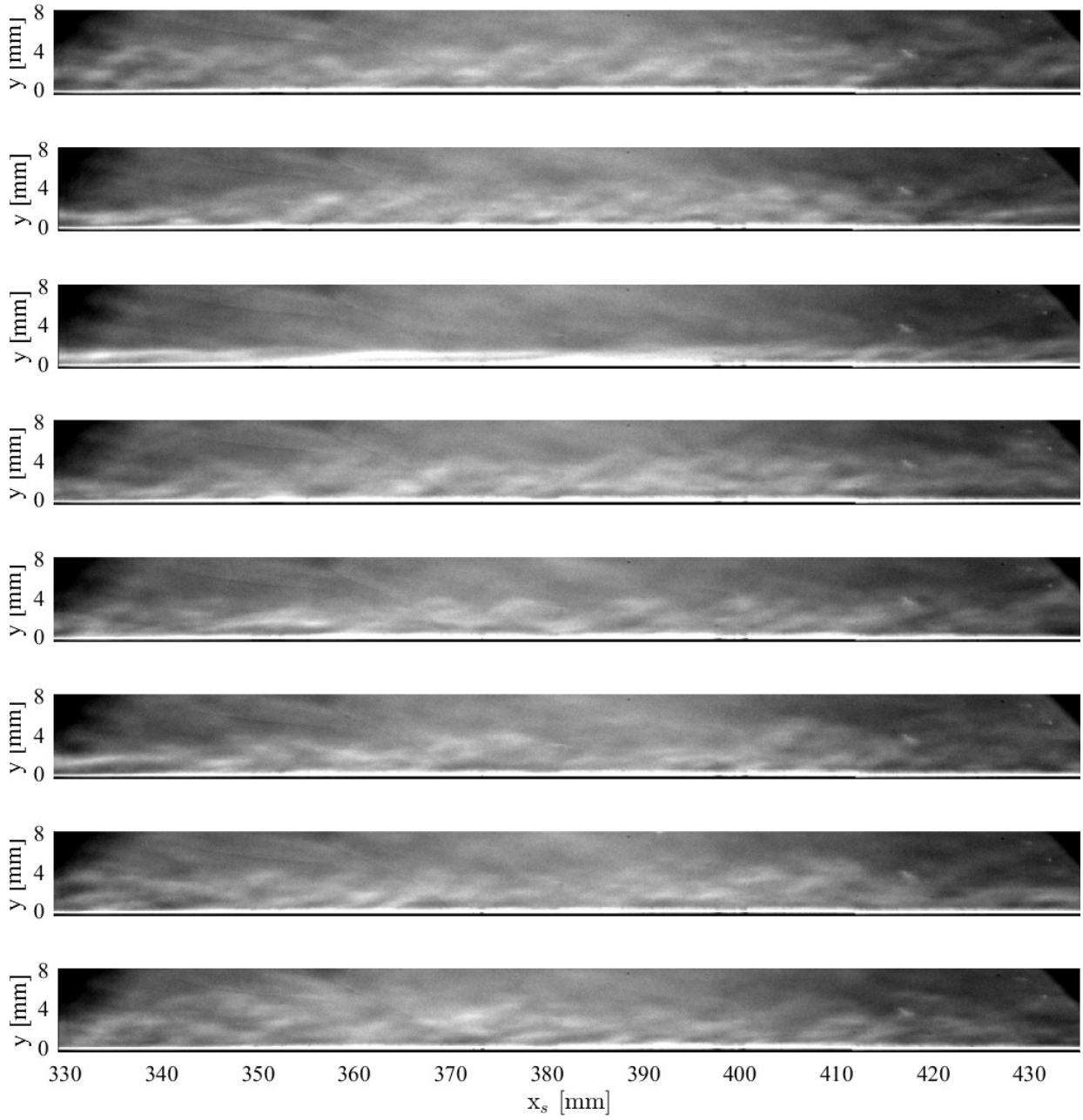

Figure B.13: Sequence of schlieren images, Δt = 2.5 ms, for the particle-free, Re_∞ = 5.16±0.03 $\times 10^6$ m^{-1} condition.

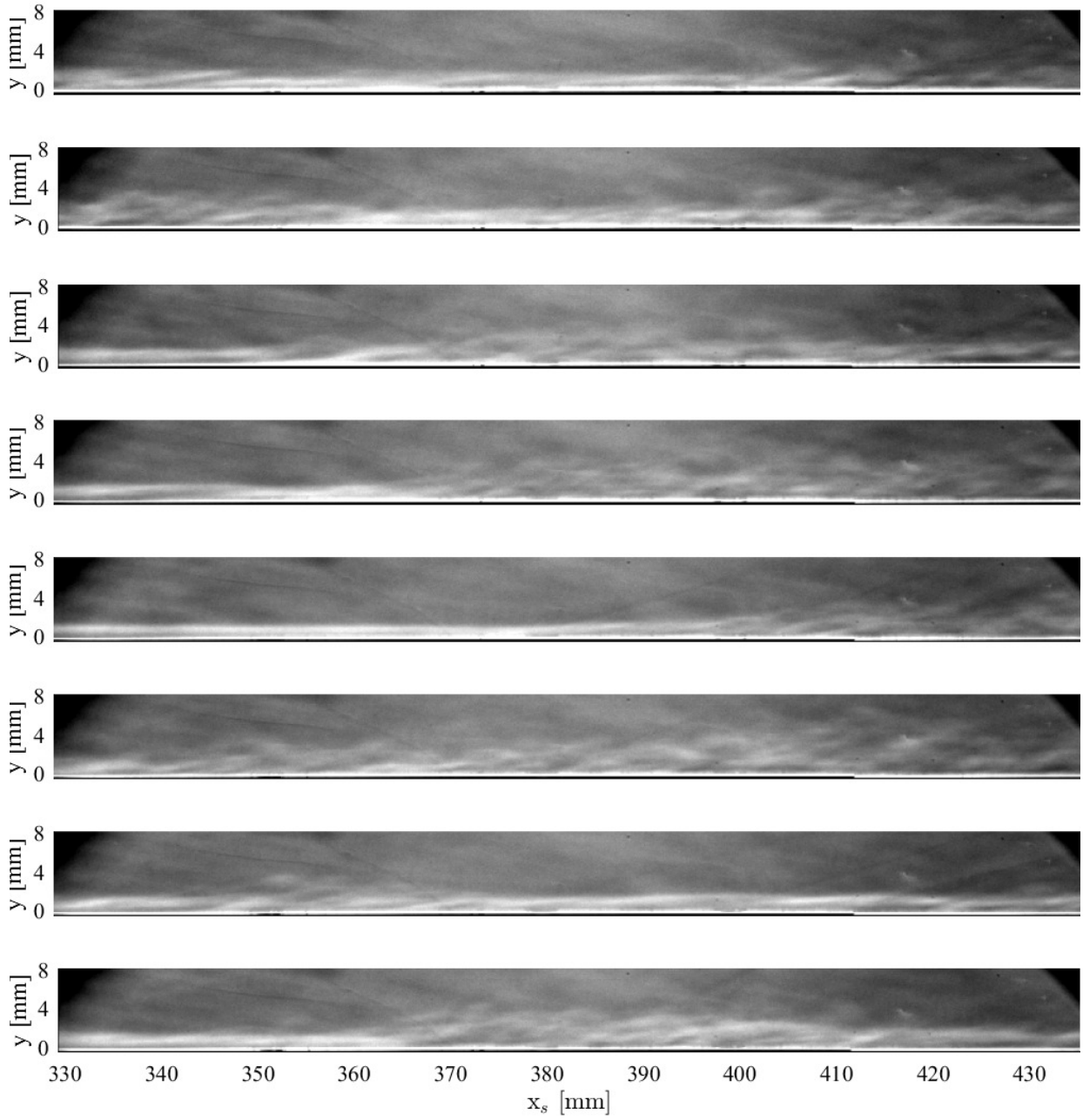

Figure B.14: Sequence of schlieren images, Δt = 2.5 ms, for the D9, $Re_\infty = 5.16 \pm 0.03 \times 10^6$ m^{-1} condition.

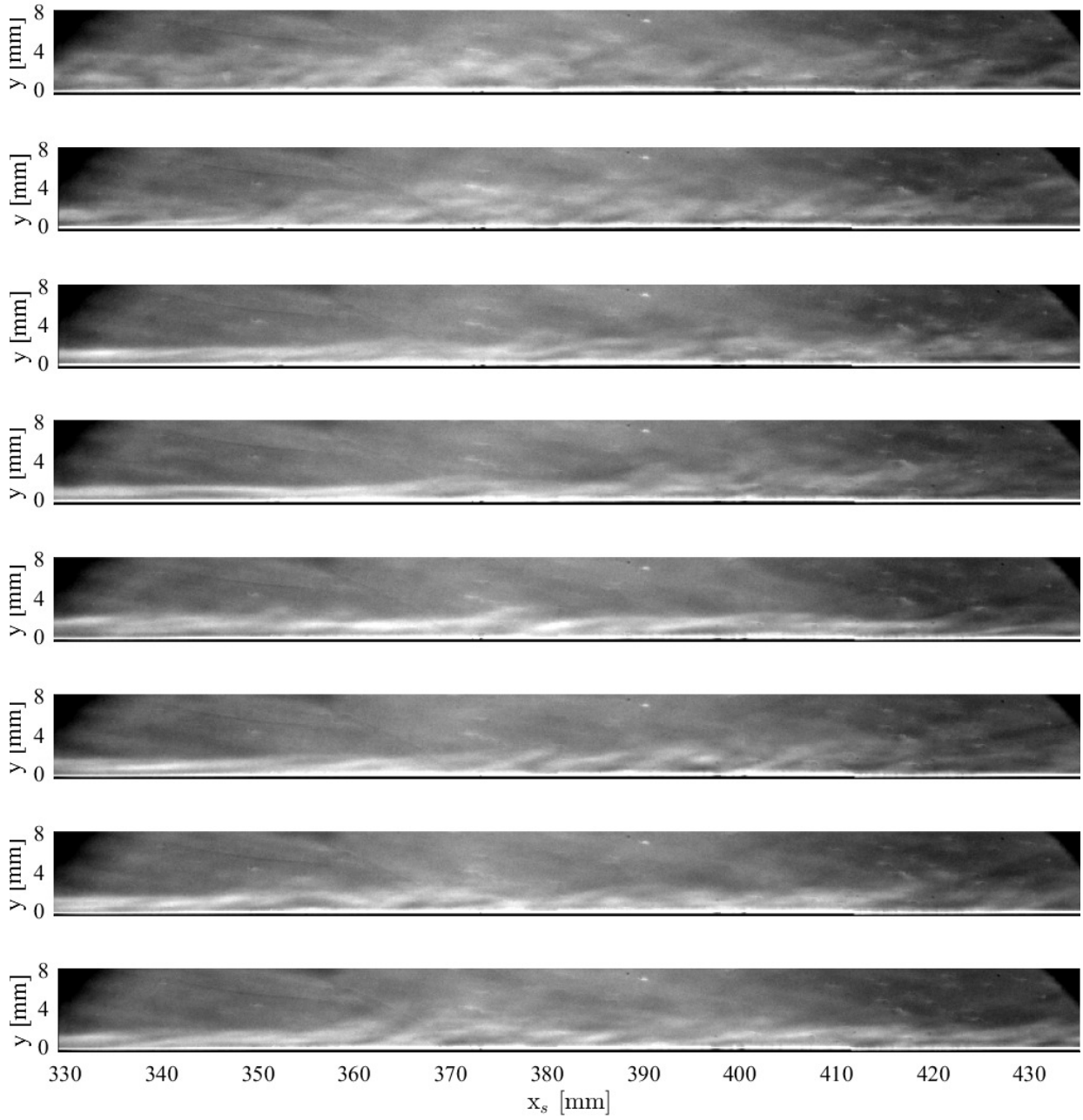

Figure B.15: Sequence of schlieren images, $\Delta t = 2.5$ ms, for the D12, $Re_\infty = 5.16 \pm 0.03 \times 10^6$ m^{-1} condition.

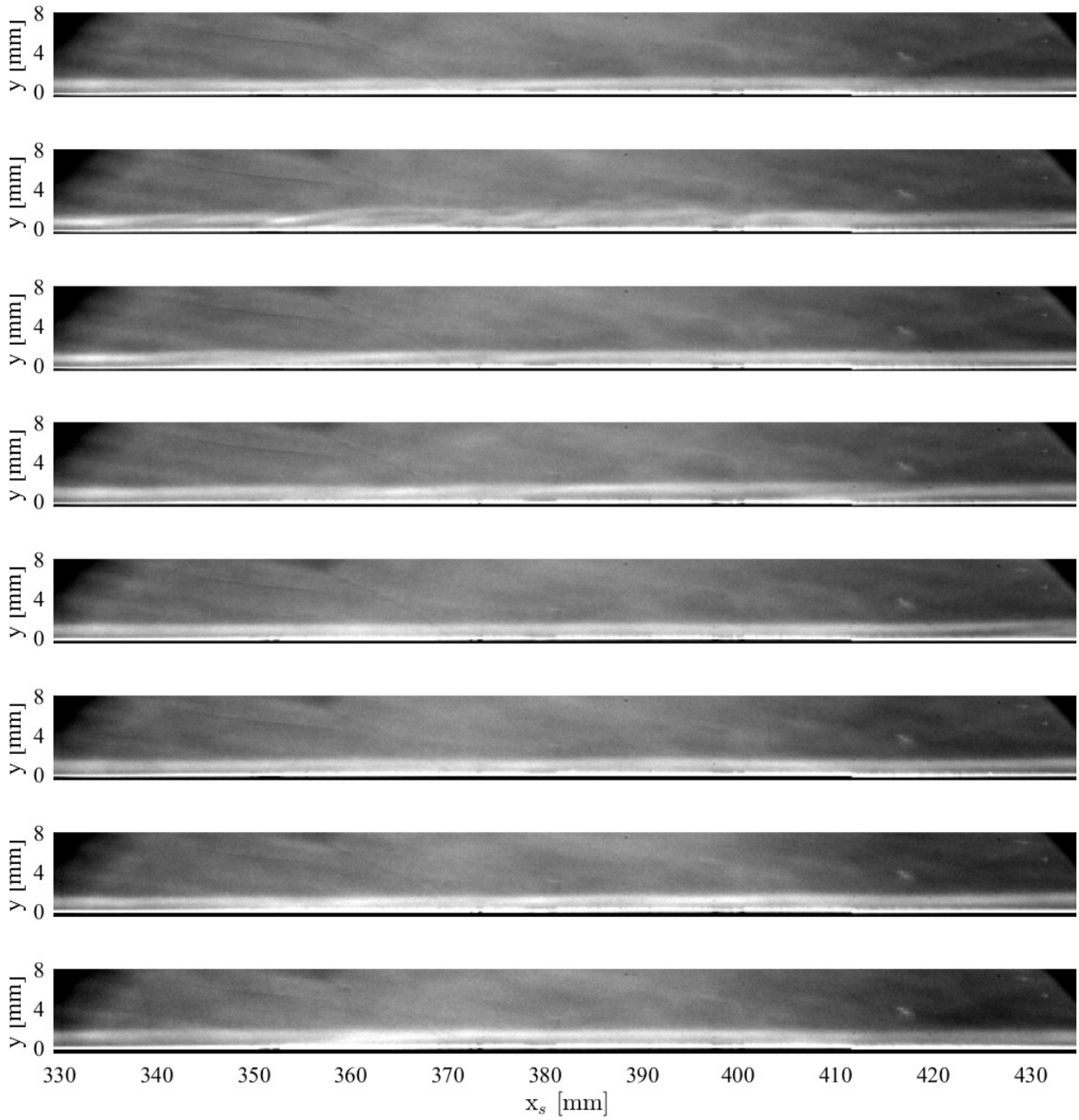

Figure B.16: Sequence of schlieren images, $\Delta t = 2.5$ ms, for the D16, $Re_\infty = 5.16 \pm 0.03 \times 10^6$ m^{-1} condition.

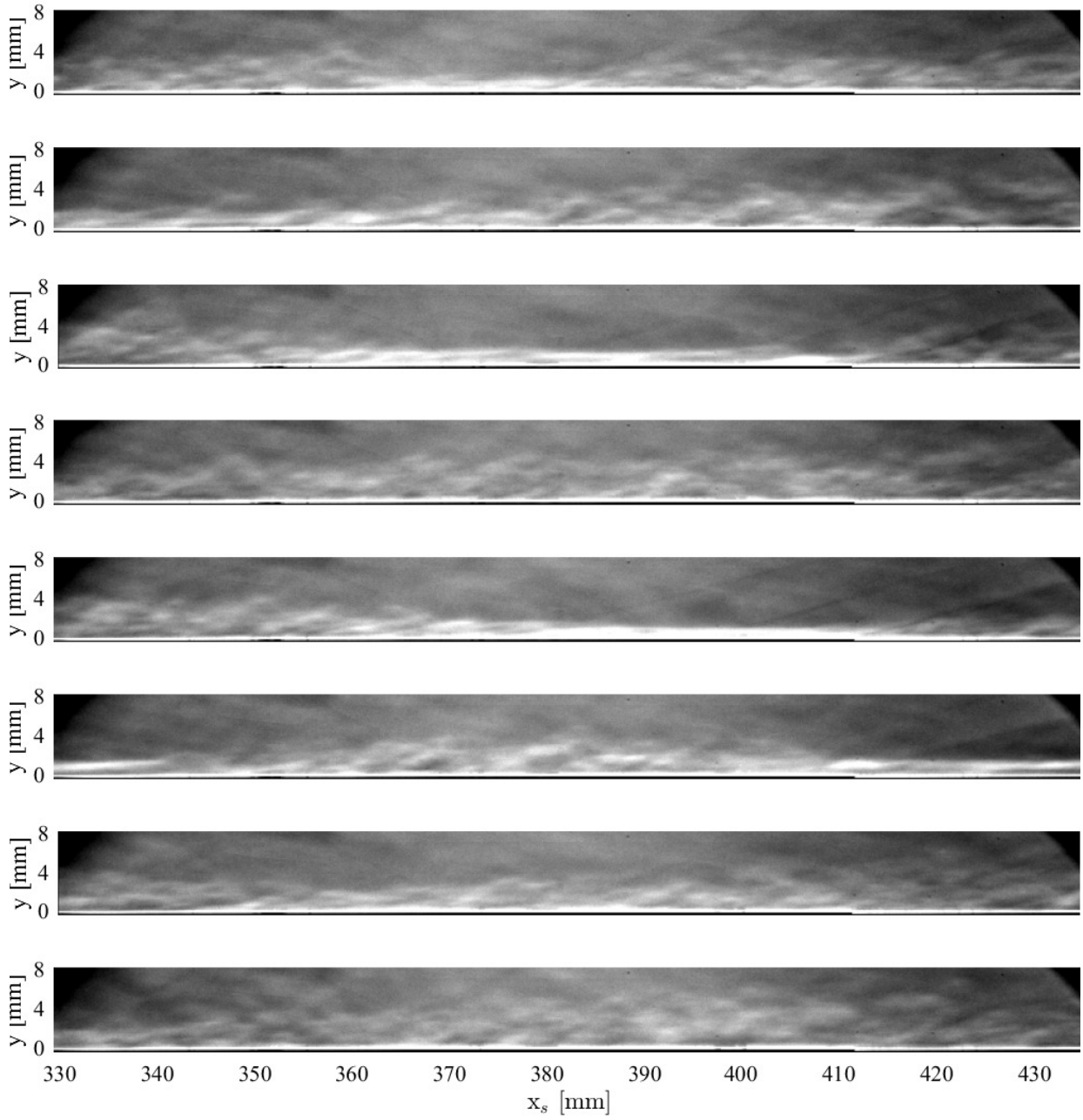

Figure B.17: Sequence of schlieren images, Δt = 2.5 ms, for the particle-free, Re_∞ = 5.82±0.03 $\times 10^6$ m^{-1} condition.

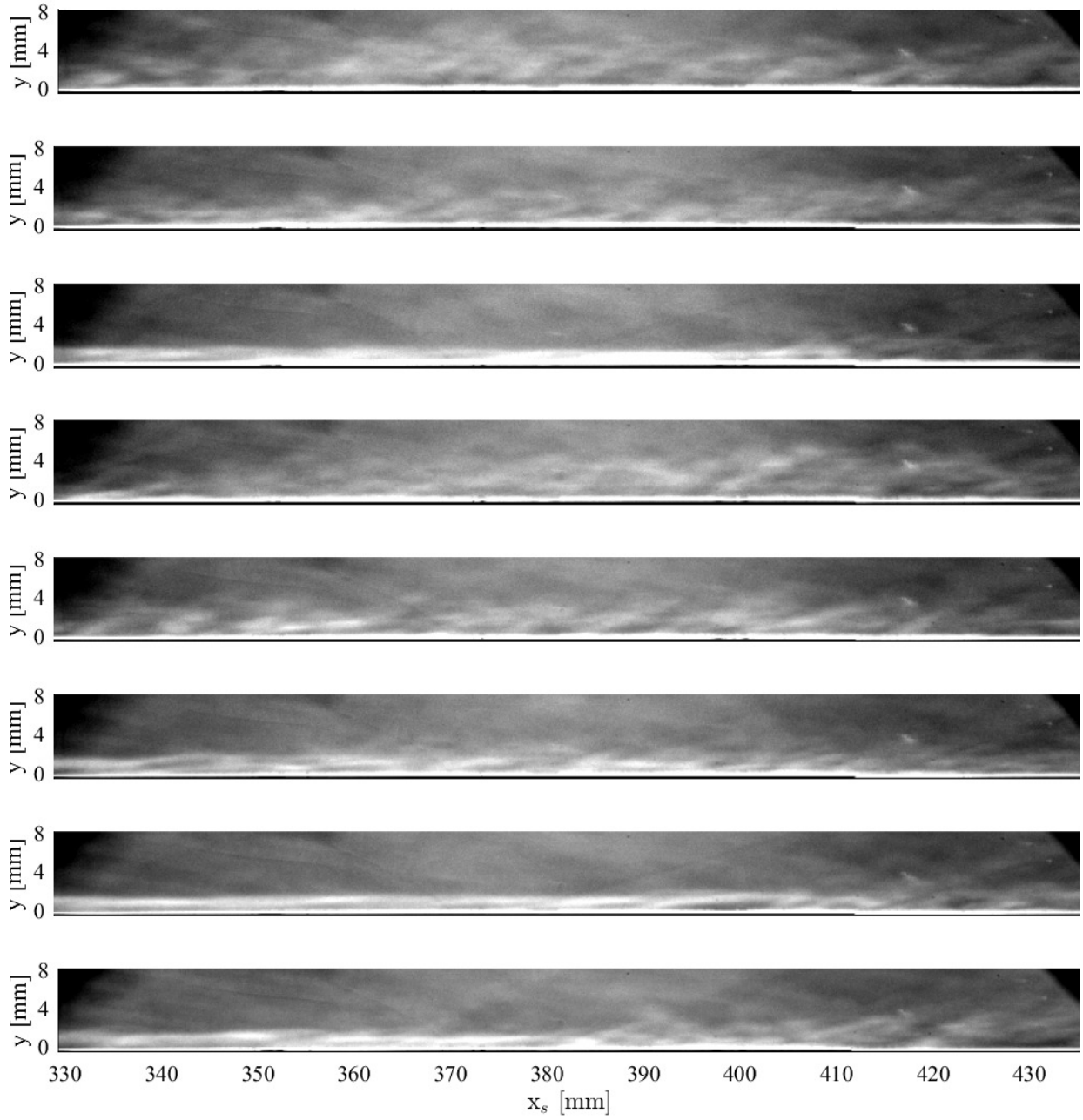

Figure B.18: Sequence of schlieren images, Δt = 2.5 ms, for the D9, $Re_\infty = 5.82 \pm 0.03 \times 10^6$ m^{-1} condition.

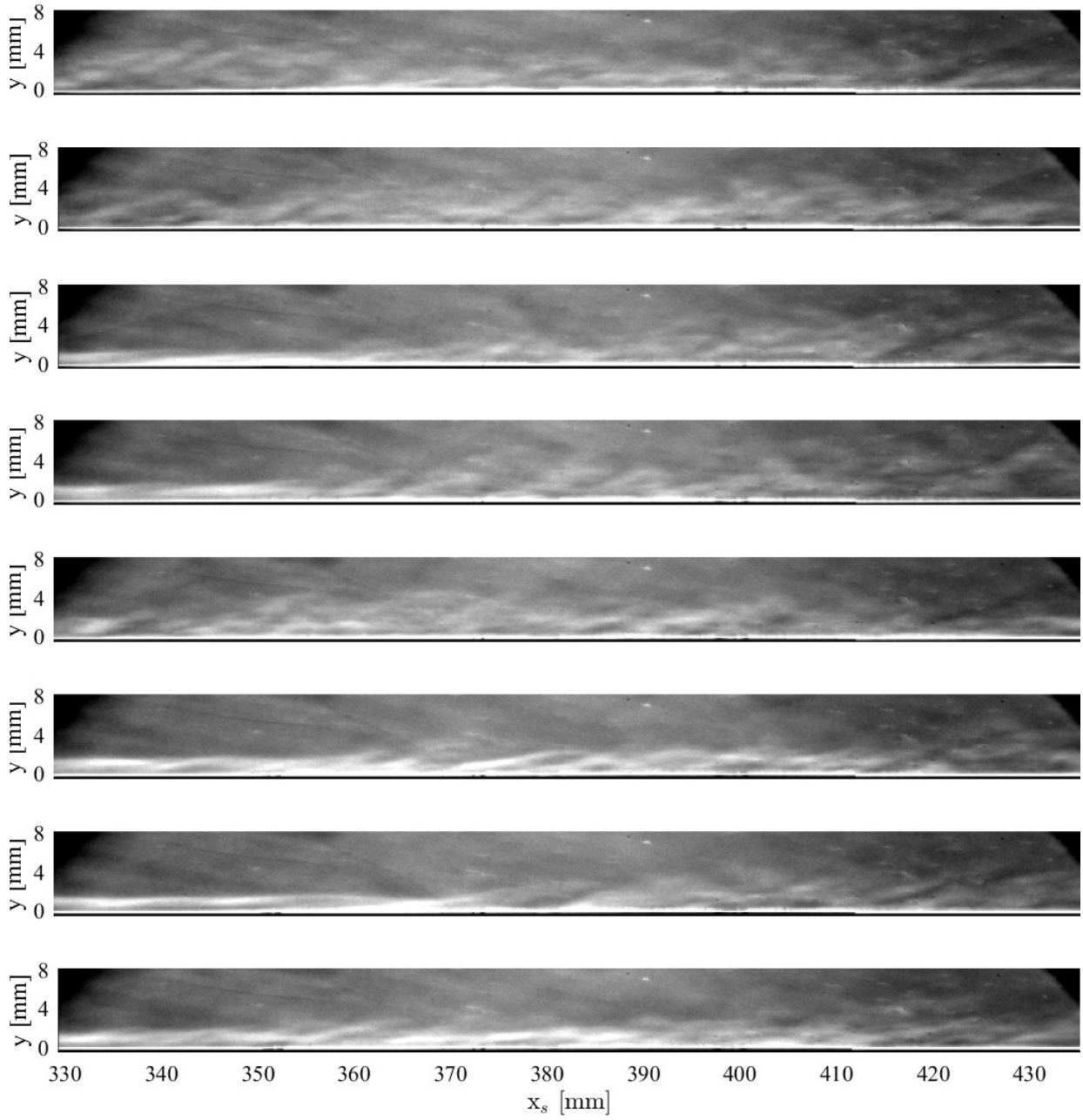

Figure B.19: Sequence of schlieren images, $\Delta t = 2.5$ ms, for the D12, $Re_\infty = 5.82 \pm 0.03 \times 10^6$ m^{-1} condition.

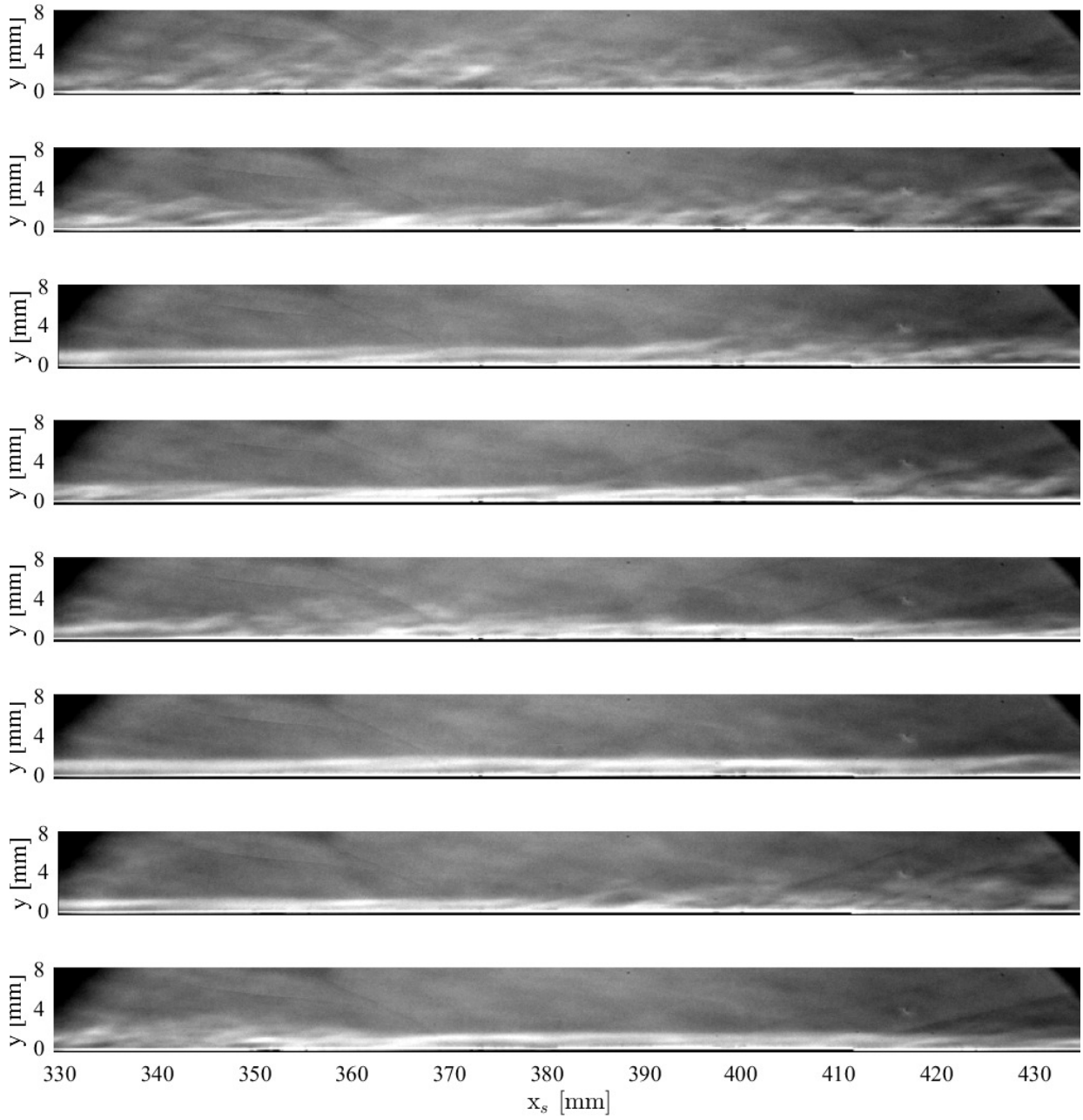

Figure B.20: Sequence of schlieren images, Δt = 2.5 ms, for the D16, $Re_\infty = 5.82 \pm 0.03 \times 10^6$ m^{-1} condition.

B.2 Mean Schlieren intensity images for all test cases

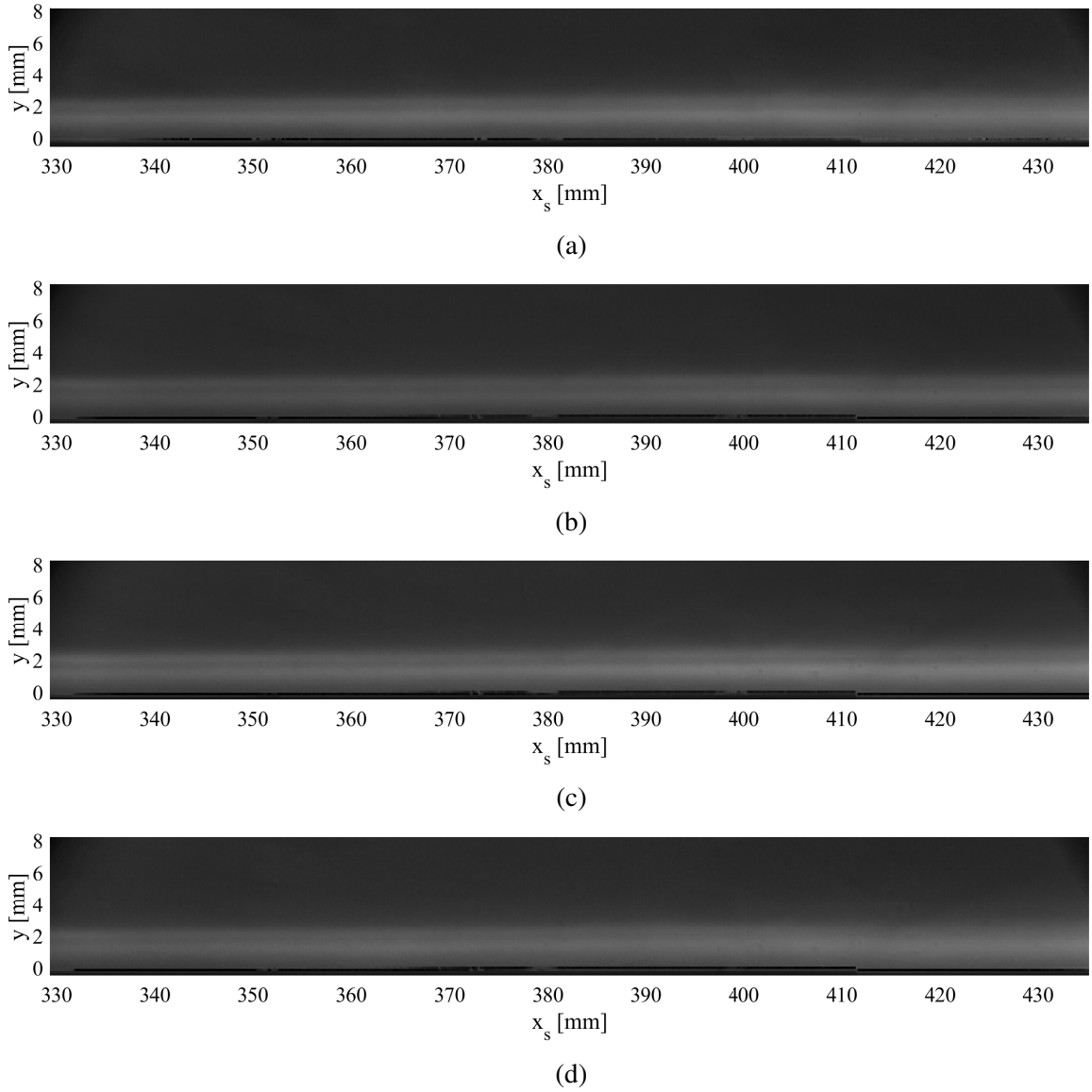

Figure B.21: Mean Schlieren intensity during the steady test time of a $Re_\infty = 3.41 \pm 0.03 \times 10^6$ m^{-1} shot and (a) particle-free flow, (b) D9, (c) D12, and (d) D16 conditions.

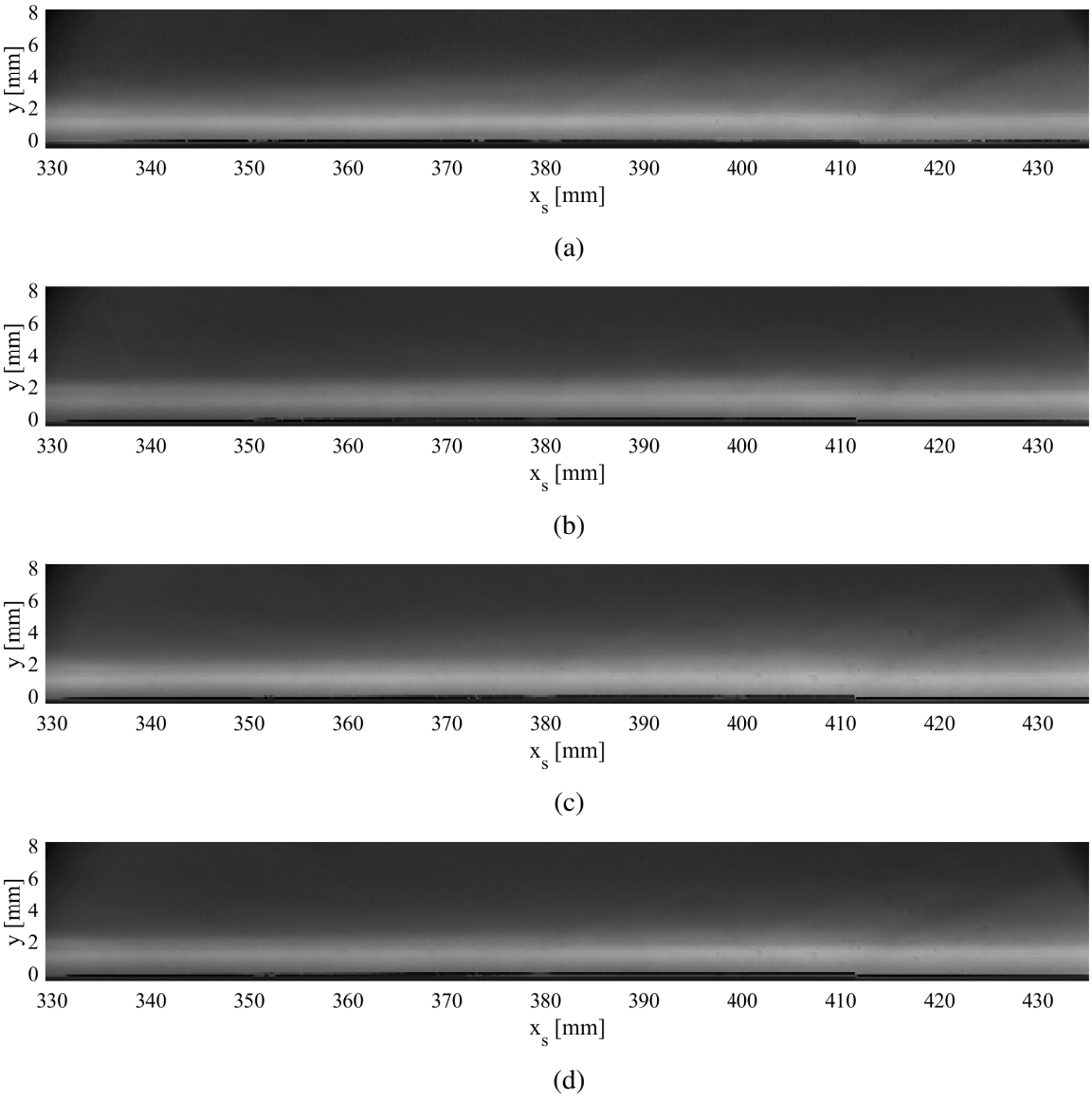

Figure B.22: Mean Schlieren intensity during the steady test time of a $Re_\infty = 4.10 \pm 0.04 \times 10^6$ m^{-1} shot and (a) particle-free flow, (b) D9, (c) D12, and (d) D16 conditions.

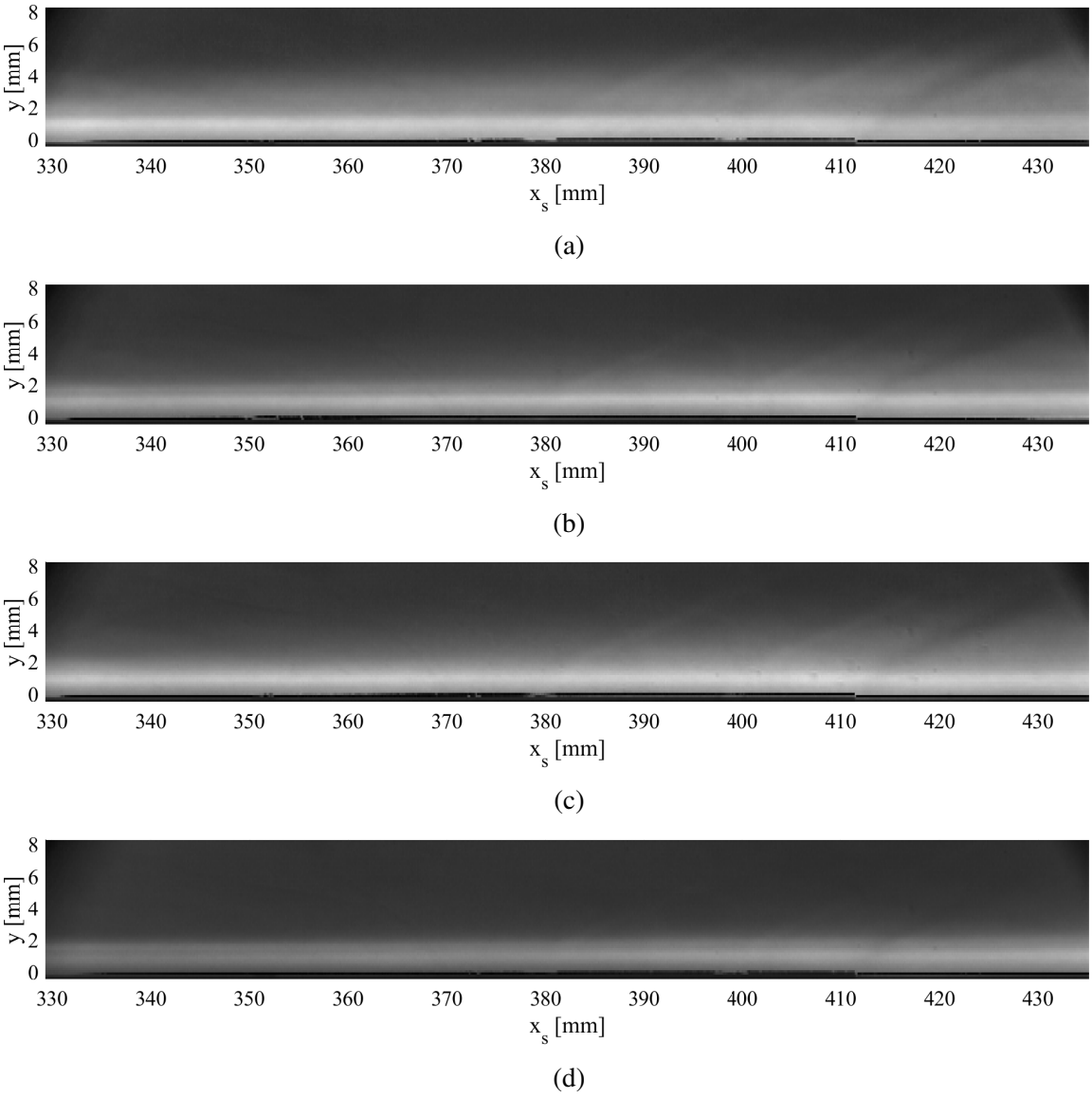

Figure B.23: Mean Schlieren intensity during the steady test time of a $Re_\infty = 4.73 \pm 0.03 \times 10^6$ m^{-1} shot and (a) particle-free flow, (b) D9, (c) D12, and (d) D16 conditions.

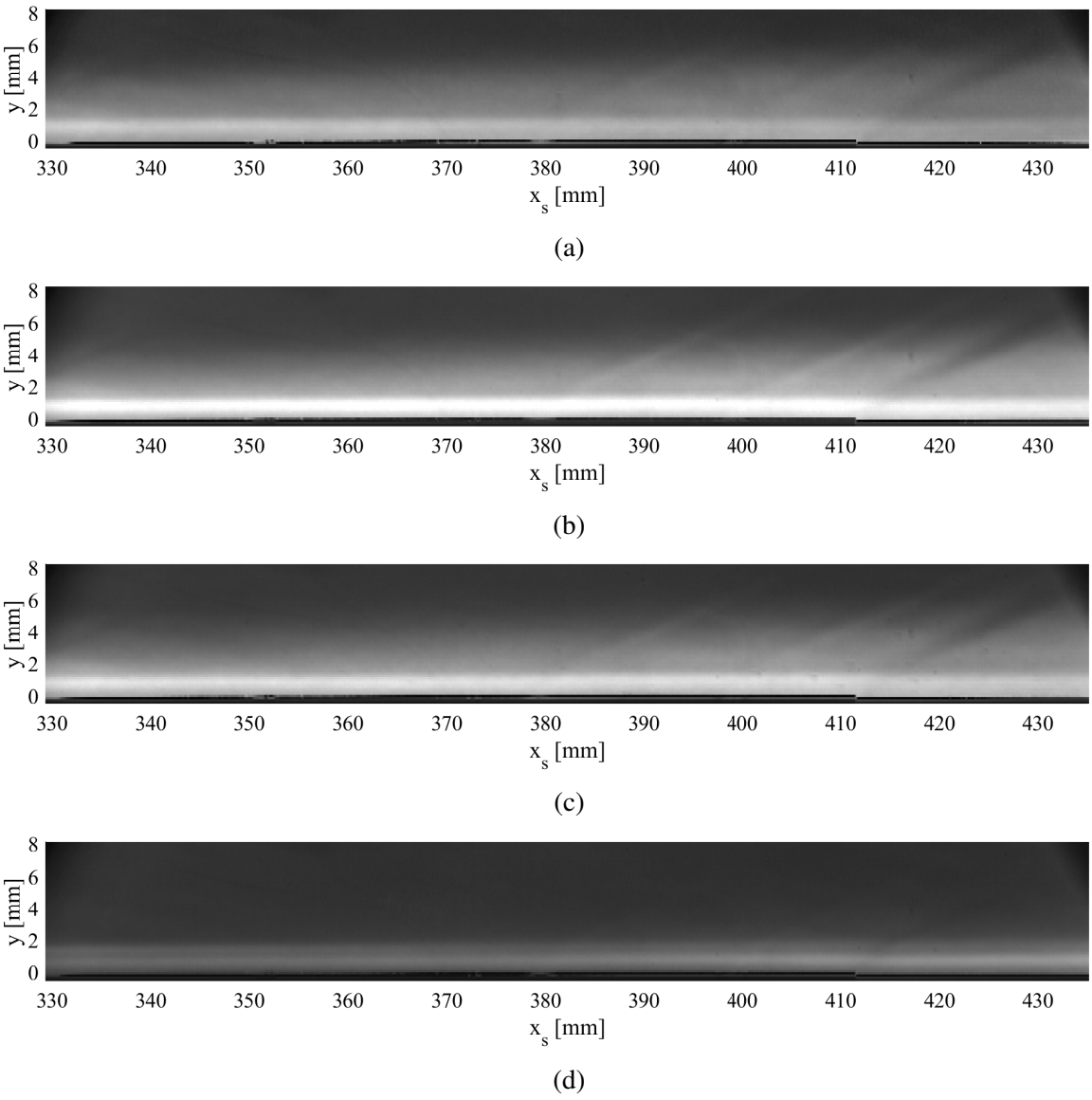

Figure B.24: Mean Schlieren intensity during the steady test time of a $Re_\infty = 5.16 \pm 0.03 \times 10^6$ m^{-1} shot and (a) particle-free flow, (b) D9, (c) D12, and (d) D16 conditions.

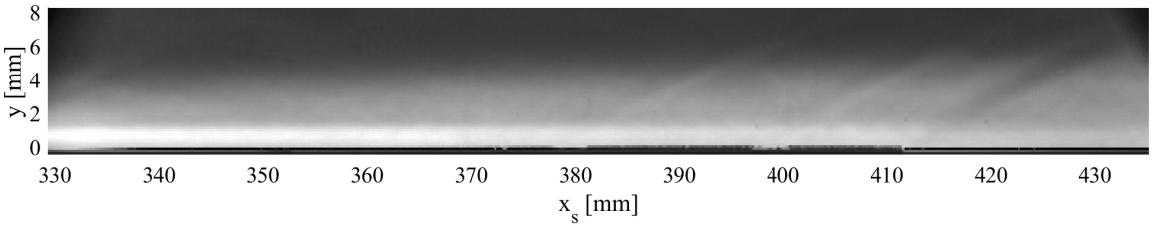

(a)

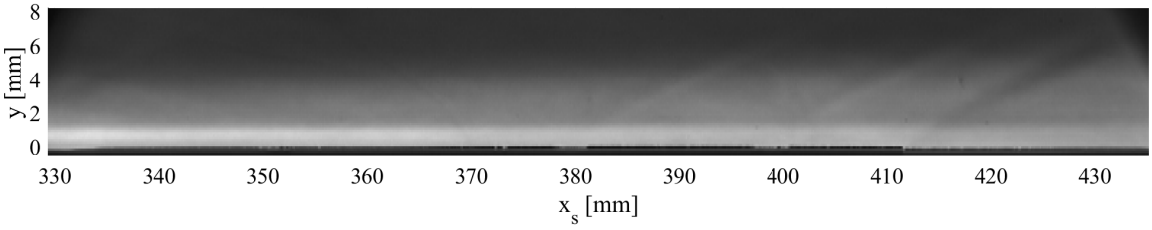

(b)

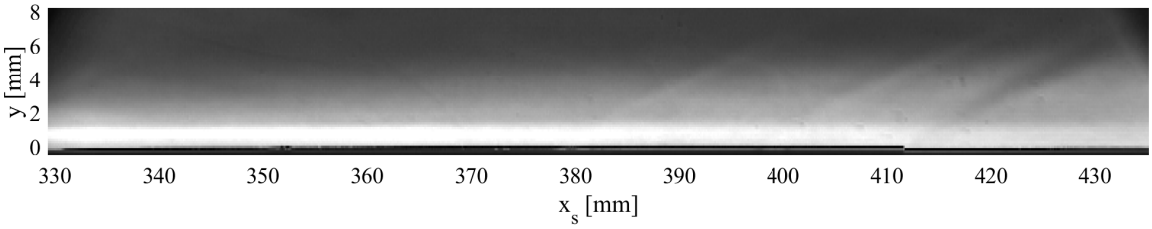

(c)

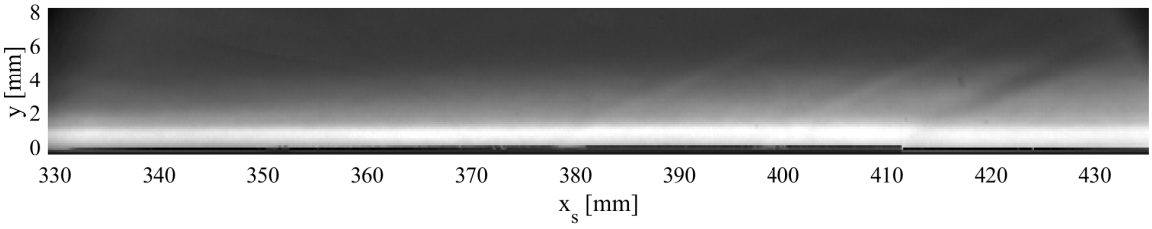

(d)

Figure B.25: Mean Schlieren intensity during the steady test time of a $Re_\infty = 5.82 \pm 0.03 \times 10^6$ m^{-1} shot and (a) particle-free flow, (b) D9, (c) D12, and (d) D16 conditions.

B.3 Comparison of the mean fluctuation density PSD in the sharp-Cone boundary layer

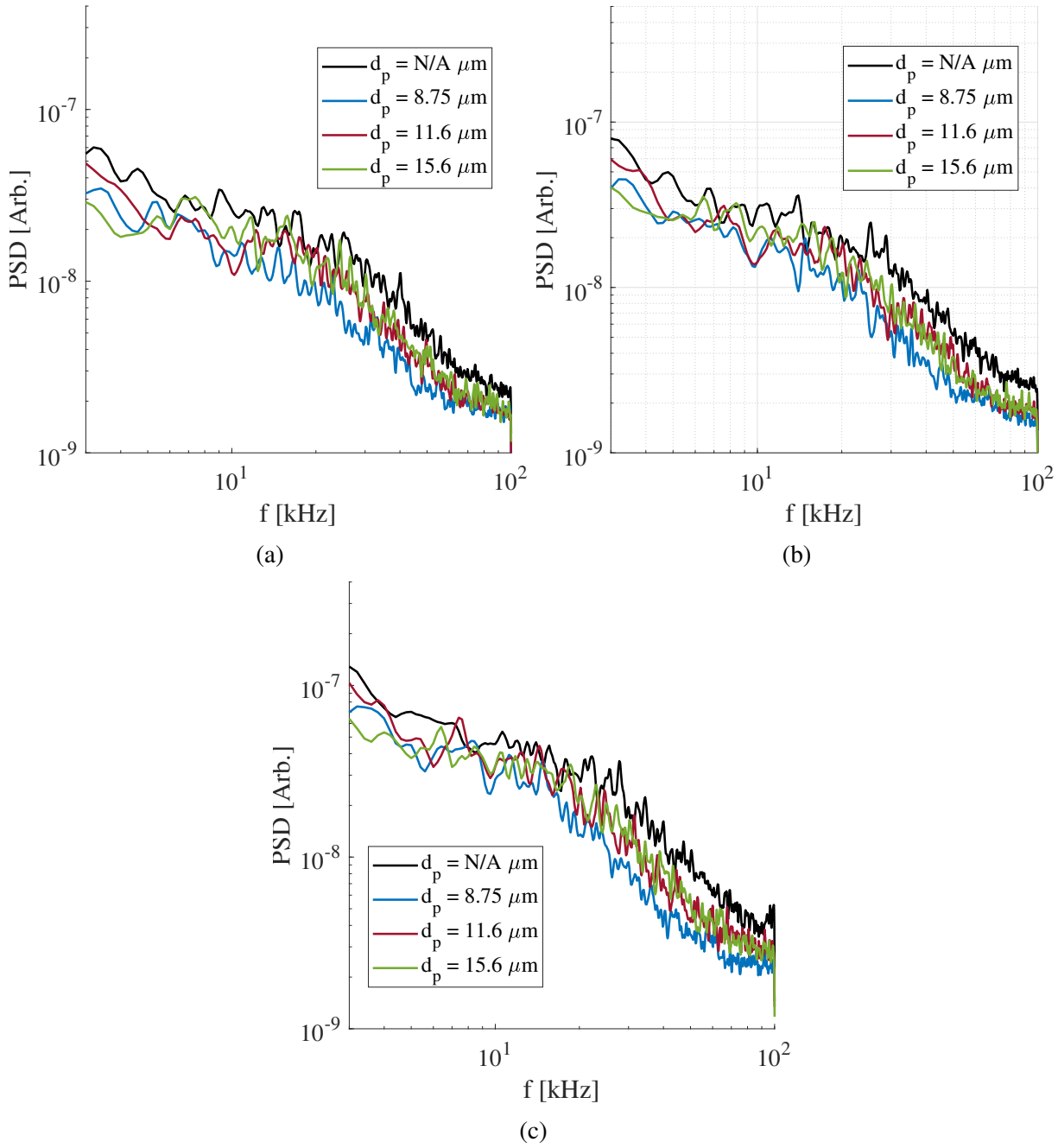

Figure B.26: Comparison of the mean fluctuation density PSD in the boundary layer during the steady test time of a $Re_\infty = 3.41 \pm 0.03 \times 10^6$ m^{-1} shot at cone Reynolds numbers of (a) $Re_x = 1.0 \times 10^6$, (b) $Re_x = 1.1 \times 10^6$, and (c) $Re_x = 1.2 \times 10^6$.

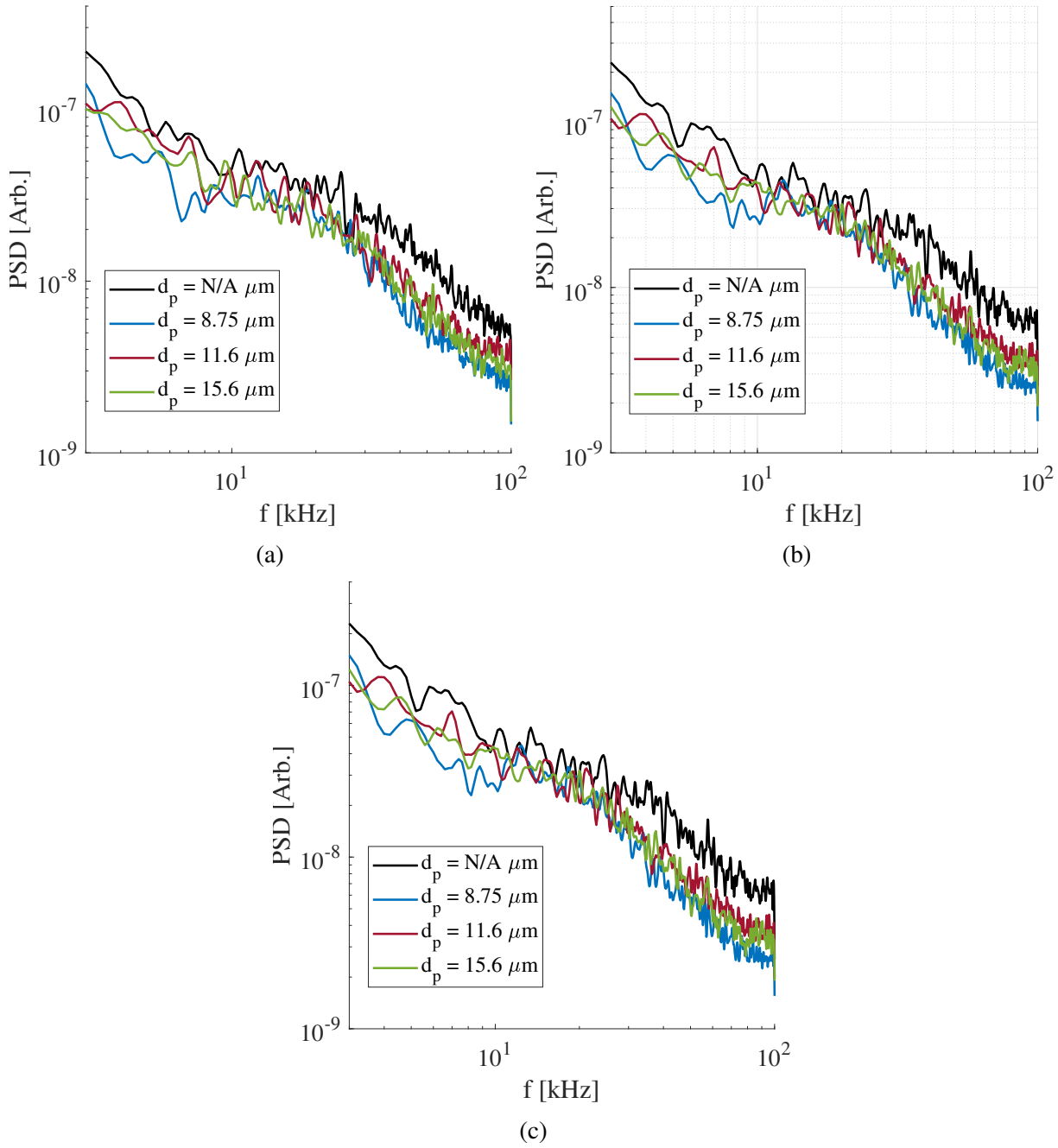

Figure B.27: Comparison of the mean fluctuation density PSD in the boundary layer during the steady test time of a Re_{∞} = 4.10±0.04 ×10^6 m^{-1} shot at cone Reynolds numbers of (a) Re_x= 1.2 ×10^6, (b) Re_x= 1.3 ×10^6, and (c) Re_x= 1.4 ×10^6.

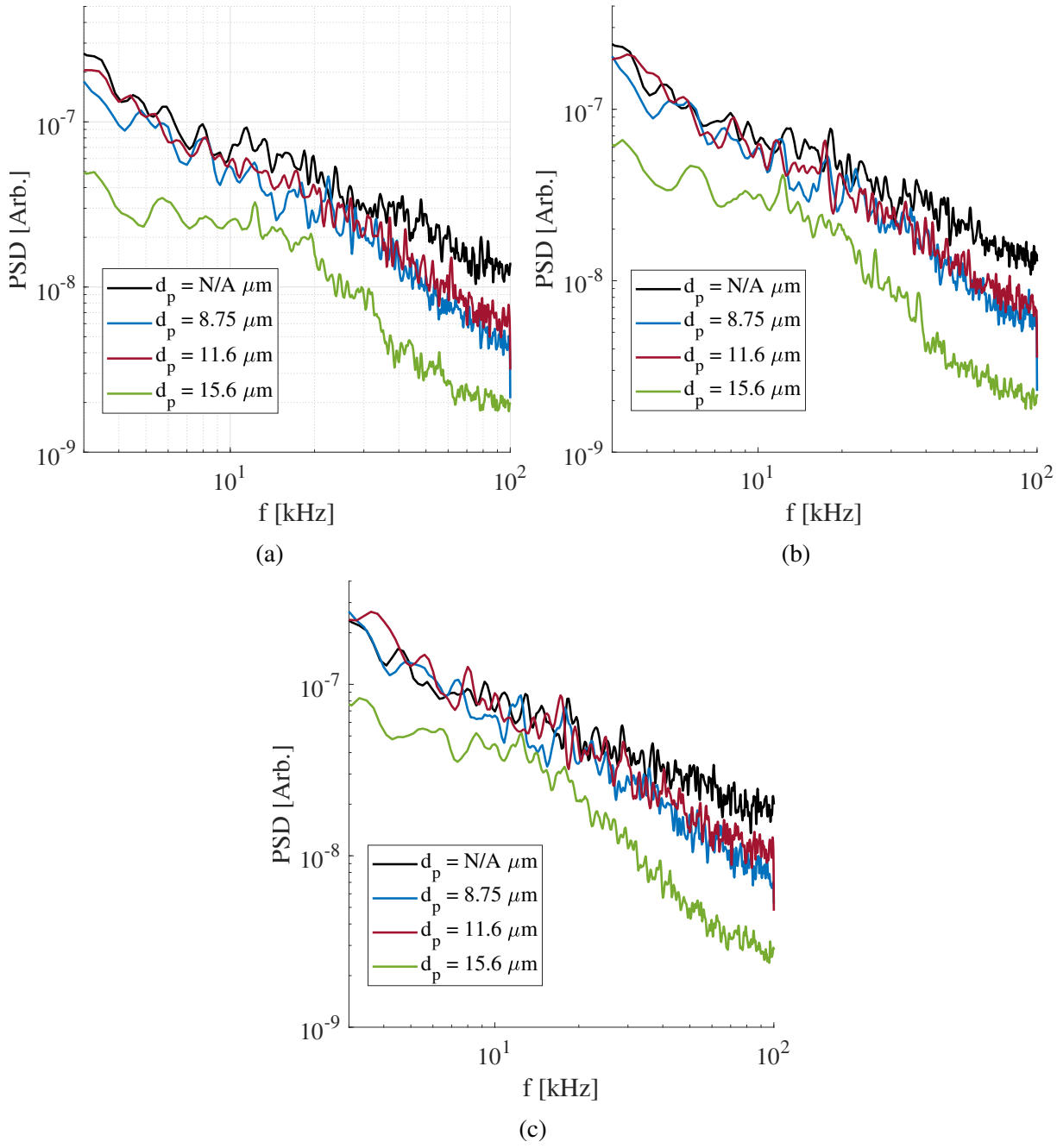

Figure B.28: Comparison of the mean fluctuation density PSD in the boundary layer during the steady test time of a Re_∞ = 4.73±0.03 $\times 10^6$ m^{-1} shot at cone Reynolds numbers of (a) Re_x= 1.5 $\times 10^6$, (b) Re_x= 1.6 $\times 10^6$, and (c) Re_x= 1.7 $\times 10^6$.

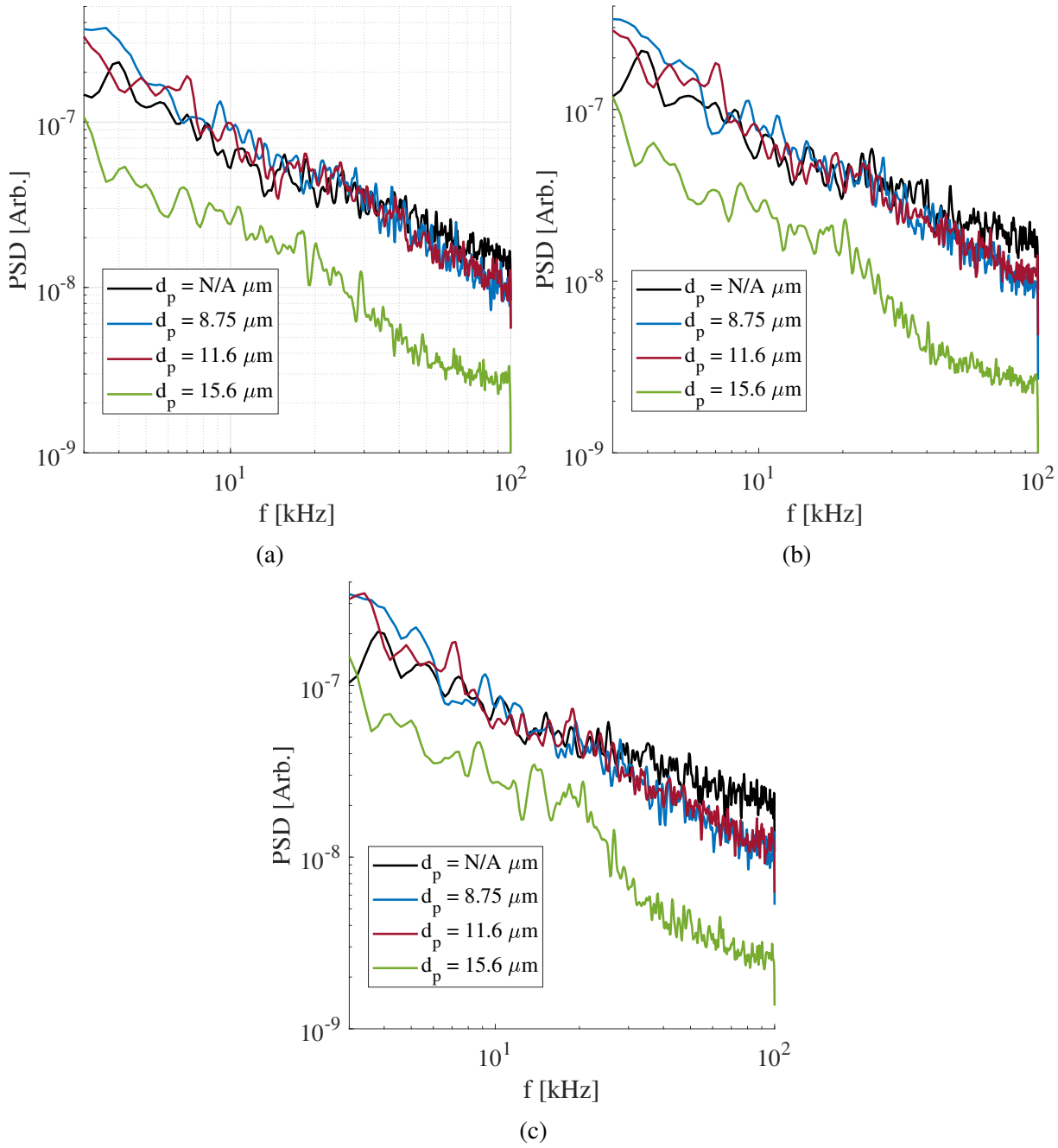

Figure B.29: Comparison of the mean fluctuation density PSD in the boundary layer during the steady test time of a Re_{∞} = 5.16±0.03 ×10^6 m^{-1} shot at cone Reynolds numbers of (a) Re_x= 1.7 ×10^6, (b) Re_x= 1.8 ×10^6, and (c) Re_x= 1.9 ×10^6.

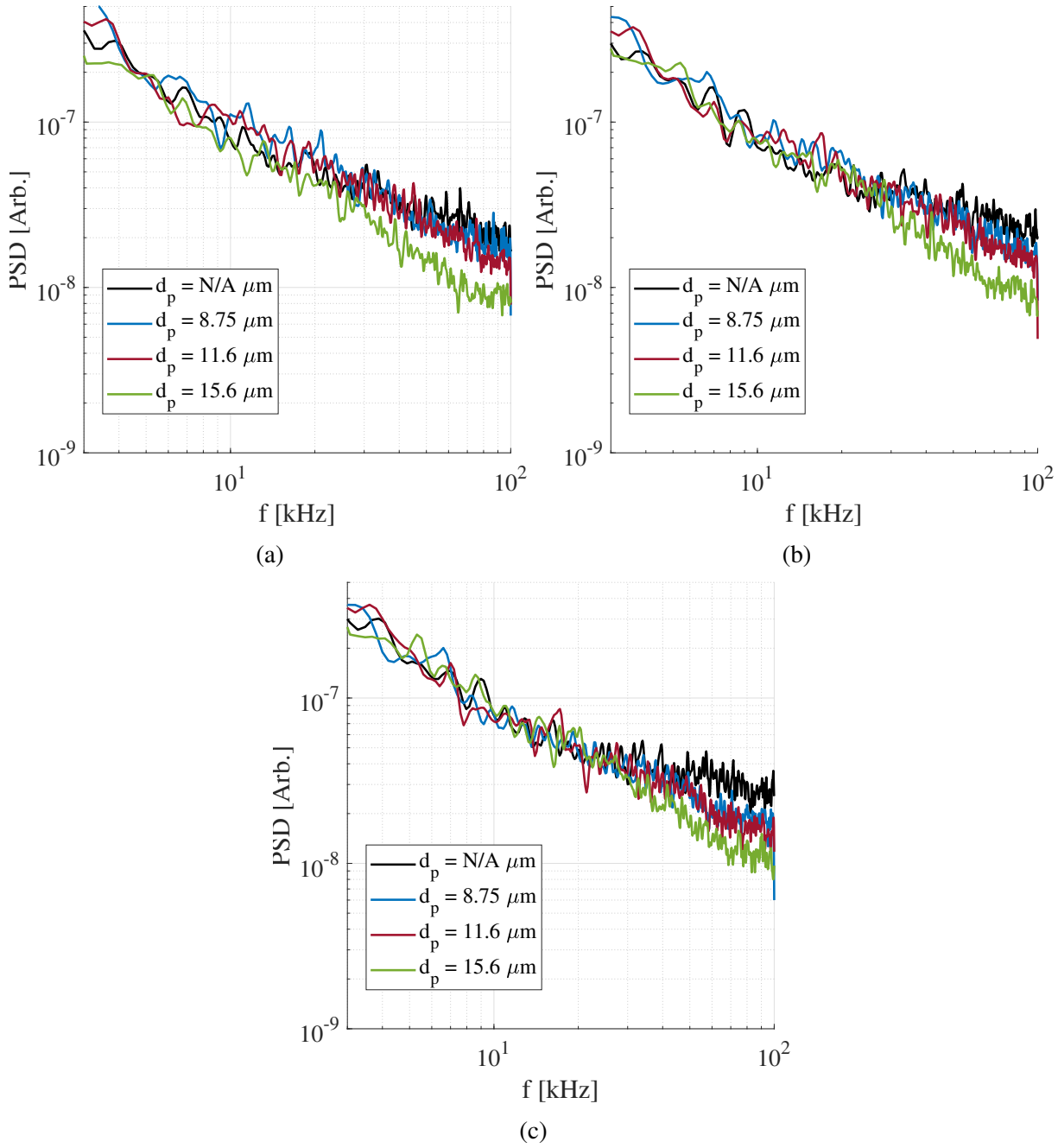

Figure B.30: Comparison of the mean fluctuation density PSD in the boundary layer during the steady test time of a Re_{∞} = 5.82±0.03 $\times 10^6$ m^{-1} shot at cone Reynolds numbers of (a) Re_x= 1.9 $\times 10^6$, (b) Re_x= 2.0 $\times 10^6$, and (c) Re_x= 2.1 $\times 10^6$.

Bibliography

[1] Stefanie Kremser, Larry W Thomason, Marc von Hobe, Markus Hermann, Terry Deshler, Claudia Timmreck, Matthew Toohey, Andrea Stenke, Joshua P Schwarz, Ralf Weigel, et al. Stratospheric aerosol—observations, processes, and impact on climate. *Reviews of Geophysics*, 54(2):278–335, 2016.

[2] Steven P Schneider. Development of hypersonic quiet tunnels. *Journal of Spacecraft and Rockets*, 45(4):641–664, 2008.

[3] Eli Reshotko. Transition issues for atmospheric entry. *Journal of Spacecraft and Rockets*, 45(2):161–164, 2008.

[4] Vincenzo Russo, Sayed Mohammad Abdullah Al Hasnine, and Christoph Brehm. Towards understanding particle cloud interactions with high-speed boundary layer flows. In *AIAA AVIATION 2021 FORUM*, page 2829, 2021.

[5] Sayed Mohammad Abdullah Al Hasnine, Vincenzo Russo, Oliver M Browne, Anatoli Tumin, and Christoph Brehm. Disturbance flow field analysis of particulate interaction with high speed boundary layers. In *AIAA Aviation 2020 Forum*, page 3046, 2020.

[6] M Pilch and CA Erdman. Use of breakup time data and velocity history data to predict the maximum size of stable fragments for acceleration-induced breakup of a liquid drop. *International journal of multiphase flow*, 13(6):741–757, 1987.

[7] L-P Hsiang and Gerard M Faeth. Drop deformation and breakup due to shock wave and steady disturbances. *International Journal of Multiphase Flow*, 21(4):545–560, 1995.

[8] DR Guildenbecher, C López-Rivera, and PE Sojka. Secondary atomization. *Experiments in Fluids*, 46(3):371–402, 2009.

[9] Andrew P Ceruzzi and Christopher P Cadou. Interpreting single-point and two-point focused laser differential interferometry in a turbulent jet. *Experiments in Fluids*, 63(7):112, 2022.

[10] Benjamin Rhys Jones. Experimental investigation of boundary-layer transition on a slender cone at mach 4. Master's thesis, University of Maryland, College Park, 2023.

[11] A Roshko and HW Liepmann. *Elements of Gas-dynamics*. Wiley, 1957.

[12] Richard P Turco. Upper-atmosphere aerosols: properties and natural cycles. *NASA, Washington, The Atmospheric Effects of Stratospheric Aircraft: A First Program Report*, 1992.

[13] T Deshler, ME Hervig, DJ Hofmann, JM Rosen, and JB Liley. Thirty years of in situ stratospheric aerosol size distribution measurements from laramie, wyoming (41 n), using balloon-borne instruments. *Journal of Geophysical Research: Atmospheres*, 108(D5), 2003.

[14] Terry Deshler. A review of global stratospheric aerosol: Measurements, importance, life cycle, and local stratospheric aerosol. *Atmospheric Research*, 90(2-4):223–232, 2008.

[15] Jean-Baptiste Renard, Colette Brogniez, Gwenaël Berthet, Quentin Bourgeois, Bertrand Gaubicher, Michel Chartier, Jean-Yves Balois, Christian Verwaerde, Frédérique Auriol, Philippe Francois, et al. Vertical distribution of the different types of aerosols in the stratosphere: Detection of solid particles and analysis of their spatial variability. *Journal of Geophysical Research: Atmospheres*, 113(D21), 2008.

[16] Jean-Baptiste Renard, Gwenaël Berthet, Verónica Salazar, Valery Catoire, Michel Tagger, Bertrand Gaubicher, and Claude Robert. In situ detection of aerosol layers in the middle stratosphere. *Geophysical Research Letters*, 37(20), 2010.

[17] Joseph B Habeck, James Flaten, and Graham V Candler. High-altitude balloon measurements of atmospheric particulates. In *AIAA Scitech 2020 Forum*, page 1794, 2020.

[18] Bruce Moylan, Brian Landrum, and Gerald Russell. Investigation of the physical phenomena associated with rain impacts on supersonic and hypersonic flight vehicles. *Procedia Engineering*, 58:223–231, 2013.

[19] Natasha L Miles, Johannes Verlinde, and Eugene E Clothiaux. Cloud droplet size distributions in low-level stratiform clouds. *Journal of the atmospheric sciences*, 57(2):295–311, 2000.

[20] Joseph B Habeck, Michael D Kroells, Thomas E Schwartzentruber, and Graham V Candler. Characterization of particle-surface impacts on a sphere-cone at hypersonic flight conditions. In *AIAA SCITECH 2023 Forum*, page 0205, 2023.

[21] Austin Andrews, Devin McGee, Ioannis Pothos, Nathan Bellefeuille, Christopher J Hogan, and Thomas E Schwartzentruber. Characterization of surface erosion from high speed single micrometer impacts on al-6061 t6. In *AIAA SCITECH 2023 Forum*, page 0394, 2023.

[22] W Fleener and R Watson. Convective heating in dust-laden hypersonic flows. In *8th Thermophysics Conference*, page 761, 1973.

[23] P Schneider. Reentry weather erosion simulator. In *10th Aerodynamic Testing Conference*, page 816, 1978.

[24] EB Vasilevskii, AN Osiptsov, AV Chirikhin, and LV Yakovleva. Heat exchange on the front surface of a blunt body in a high-speed flow containing low-inertia particles. *Journal of Engineering Physics and Thermophysics*, 74(6):1399–1411, 2001.

[25] Matthew H Bowman. The history and advancement of the weather encounter capabilities in the aedc hyperballistic range g. In *AIAA Scitech 2021 Forum*, page 1874, 2021.

[26] Richard V Rhode. Some effects of rainfall on flight of airplanes and on instrument indications. Technical report, National Advisory Committee for Aeronautics, 1941.

[27] GAUDY BEZOS, BRYAN CAMBELL, and WEDWARD MELSON. The development of a capability for aerodynamic testing of large-scale wing sections in a simulated natural rain environment. In *27th Aerospace Sciences Meeting*, page 762, 1989.

[28] Hans J. Rasmussen. Operational capability of the holloman test track's rain simulation facility. *Journal of Environmental Sciences*, 1977.

[29] Bruce Emerson Moylan. *Raindrop demise in a high-speed projectile flowfield*. The University of Alabama in Huntsville, 2010.

[30] Lyle E Dunbar, Joseph F Courtney, and Lowell D McMillen. Heating augmentation in erosive hypersonic environments. *AIAA Journal*, 13(7):908–912, 1975.

[31] W Shih. Ballistics range measurements of aerodynamic heating in erosion environments. In *9th Fluid and PlasmaDynamics Conference*, page 319, 1976.

[32] E Vasilevskii and A Osiptsov. Experimental and numerical study of heat transfer on a blunt body in dusty hypersonic flow. In *33rd Thermophysics Conference*, page 3563, 1999.

[33] Periklis Papadopoulos, Michael E Tauber, and I-Dee Chang. Heatshield erosion in a dusty martian atmosphere. *Journal of Spacecraft and Rockets*, 30(2):140–151, 1993.

[34] Abdul Majid, Uwe Bauder, Georg Herdrich, and Markus Fertig. Two-phase flow solver for hypersonic entry flows in a dusty martian atmosphere. *Journal of Thermophysics and Heat Transfer*, 30(2):418–428, 2016.

[35] Michael D Kroells, Amal Sahai, and Thomas E Schwartzentruber. Sensitivity study of dust-induced surface erosion during martian planetary entry. In *AIAA Scitech 2022 Forum*, page 0112, 2022.

[36] Joseph B Habeck, Michael D Kroells, Thomas E Schwartzentruber, and Graham V Candler. Characterization of particle-surface impacts on a sphere-cone at hypersonic flight conditions. *AIAA journal*, 62(2):460–475, 2024.

[37] Manuel Viqueira-Moreira, Alex Dworzanczyk, Nick J Parziale, and Christoph Brehm. Numerical investigation of droplet aerobreakup and impingement experiments at mach 5. In *AIAA AVIATION 2023 Forum*, page 4251, 2023.

[38] Riza K Gonuleri, Manuel Viqueira-Moreira, Joshua R Leigh, Ugur Can, Kyle Watson, Christoph Brehm, and Ibrahim Guven. Cfd-informed rain drop impact damage predictions at hypersonic conditions. In *AIAA SCITECH 2023 Forum*, page 2024, 2023.

[39] Leslie SG Kovasznay. Turbulence in supersonic flow. *Journal of the Aeronautical Sciences*, 20(10):657–674, 1953.

[40] Mark V Morkovin. On supersonic wind tunnels with low free-stream disturbances. 1959.

[41] John Laufer. Aerodynamic noise in supersonic wind tunnels. *Journal of the Aerospace Sciences*, 28(9):685–692, 1961.

[42] G. Smeets and A. George. Gas-dynamic investigations in a shock tube using a highly sensitive interferometer. Technical report, Institut Saint-Louis, 1971.

[43] G Smeets. Laser interferometer for high sensitivity measurements on transient phase objects. *IEEE transactions on Aerospace and Electronic Systems*, (2):186–190, 1972.

[44] G. Smeets and A. George. Laser-differential interferometer applications in gas dynamics. Technical report, Institut Saint-Louis, 1973.

[45] G. Smeets and A. George. Laser-interferometer with phase compensation. Technical report, Institut Saint-Louis, 1975.

[46] G Smeets. Flow diagnostics by laser interferometry. *IEEE transactions on Aerospace and Electronic Systems*, (2):82–90, 1977.

[47] NJ Parziale, JE Shepherd, and HG Hornung. Free-stream density perturbations in a reflected-shock tunnel. *Experiments in Fluids*, 55:1–10, 2014.

[48] Ahsan Hameed, Nick J Parziale, Laura A Paquin, Cameron Butler, and Stuart J Laurence. Hypersonic slender-cone boundary-layer instability in the umd hyperterp shock tunnel. In *Aiaa scitech 2020 forum*, page 0362, 2020.

[49] Andrew Ceruzzi. *Development of two-point focused laser differential interferometry for applications in high-speed wind tunnels*. PhD thesis, University of Maryland, College Park, 2022.

[50] Brett F Bathel, Joshua M Weisberger, Gregory C Herring, Rudolph A King, Stephen B Jones, Richard E Kennedy, and Stuart J Laurence. Two-point, parallel-beam focused laser differential interferometry with a nomarski prism. *Applied optics*, 59(2):244–252, 2020.

[51] Graeme I Gillespie, Andrew P Ceruzzi, and Stuart J Laurence. A multi-point focused laser differential interferometer for characterizing freestream disturbances in hypersonic wind tunnels. *Experiments in Fluids*, 63(11):180, 2022.

[52] Matthew R Fulghum. *Turbulence measurements in high-speed wind tunnels using focusing laser differential interferometry*. The Pennsylvania State University, 2014.

[53] Bryan E Schmidt and JE Shepherd. Analysis of focused laser differential interferometry. *Applied optics*, 54(28):8459–8472, 2015.

[54] Joel Michael Lawson. *Focused laser differential interferometry*. California Institute of Technology, 2021.

[55] Keisuke Fujii and Hans G Hornung. Experimental investigation of high-enthalpy effects on attachment-line boundary-layer transition. *AIAA journal*, 41(7):1282–1291, 2003.

[56] Ivett Leyva, Stuart Laurence, Amy Beierholm, Hans Hornung, Ross Wagnild, and Graham Candler. Transition delay in hypervelocity boundary layers by means of co2/acoustic instability interactions. In *47th AIAA Aerospace Sciences Meeting Including the New Horizons Forum and Aerospace Exposition*, page 1287, 2009.

[57] Joseph Jewell, Ross Wagnild, Ivett Leyva, Graham Candler, and Joseph Shepherd. Transition within a hypervelocity boundary layer on a 5-degree half-angle cone in air/co2 mixtures. In *51st AIAA Aerospace Sciences Meeting Including the New Horizons Forum and Aerospace Exposition*, page 523, 2013.

[58] Graeme I Gillespie and Stuart J Laurence. Attenuation of the acoustic noise radiated by a compressible boundary layer through injection of a vibrationally active gas. *Experiments in Fluids*, 65(2):18, 2024.

[59] CJT Sewell. Vii. the extinction of sound in a viscous atmosphere by small obstacles of cylindrical and spherical form. *Philosophical Transactions of the Royal Society of London. Series A, Containing Papers of a Mathematical or Physical Character*, 210(459-470):239–270, 1911.

[60] Vern O Knudsen, John V Wilson, and Neal S Anderson. The attenuation of audible sound in fog and smoke. *The Journal of the Acoustical Society of America*, 20(6):849–857, 1948.

[61] Samuel Temkin and Richard A Dobbins. Attenuation and dispersion of sound by particulate-relaxation processes. *The Journal of the Acoustical Society of America*, 40(2):317–324, 1966.

[62] Frank E Marble and Sebastien M Candel. Acoustic attenuation in fans and ducts by vaporization of liquid droplets. *AIAA Journal*, 13(5):634–639, 1975.

[63] VI Kalikmanov and R Hagmeijer. Real gas effects in sound wave propagation through two-phase systems. *Physics of Fluids*, 34(6), 2022.

[64] Eric Zoppellari and Daniel Juve. Reduction of hot supersonic jet noise by water injection. In *4th AIAA/CEAS Aeroacoustics Conference*, page 2204, 1998.

[65] A Krothapalli, L Venkatakrishnan, L Lourenco, B Greska, and R Elavarasan. Turbulence and noise suppression of a high-speed jet by water injection. *Journal of Fluid Mechanics*, 491:131–159, 2003.

[66] Max Kandula. Prediction of turbulent jet mixing noise reduction by water injection. *AIAA journal*, 46(11):2714–2722, 2008.

[67] Max Kandula. Spectral attenuation of sound in dilute suspensions with nonlinear particle relaxation. *The Journal of the Acoustical Society of America*, 124(5):EL284–EL290, 2008.

[68] Max Kandula. Broadband shock noise reduction in turbulent jets by water injection. *Applied Acoustics*, 70(7):1009–1014, 2009.

[69] S Sankaran, Jopaul K Ignatius, R Ramkumar, TNV Satyanarayana, Satyanarayanan R Chakravarthy, and NR Panchapakesan. Suppression of high mach number rocket jet noise by water injection. *Journal of spacecraft and rockets*, 46(6):1164–1170, 2009.

[70] Jr. John D. Anderson. *Hypersonic and High-Temperature Gas Dynamics*. American Institute of Aeronautics and Astronauics, 3rd edition, 2019.

[71] Mark V. Morkovin. Recent insights into instability and transition to turbulence in open-flow systems. aiaa paper 88–3675. *1st Nat. Fluid Dyn. Cong., Cincinnati*, 1988.

[72] Eli Reshotko. Boundary-layer stability and transition. *Annual review of fluid mechanics*, 8:311–349, 1976.

[73] Eli Reshotko. Boundary layer instability, transition and control. In *32nd Aerospace Sciences Meeting and Exhibit*, page 1, 1994.

[74] Dennis Bushnell. Notes on initial disturbance fields for the transition problem. In *Instability and Transition: Materials of the workshop held May 15-June 9, 1989 in Hampton, Virgina Volume 1*, pages 217–232. Springer, 1990.

[75] Alexander Fedorov and Mikhail Kozlov. Receptivity of high-speed boundary layer to solid particulates. In *6th AIAA Theoretical Fluid Mechanics Conference*, page 3925, 2011.

[76] Alexander V Fedorov. Receptivity of a supersonic boundary layer to solid particulates. *Journal of Fluid Mechanics*, 737:105–131, 2013.

[77] Pavel V Chuvakhov, Alexander V Fedorov, and Anton O Obraz. Numerical modelling of supersonic boundary-layer receptivity to solid particulates. *Journal of Fluid Mechanics*, 859:949–971, 2019.

[78] Oliver M Browne, Sayed M Al Hasnine, Vincenzo Russo, and Christoph Brehm. Fully-resolved particulate-induced transition simulations for high-speed boundary-layers with an immersed boundary method. In *AIAA Scitech 2020 Forum*, page 1795, 2020.

[79] Leslie M Mack. Boundary-layer linear stability theory. *Agard rep*, 709, 1984.

[80] Hubert Ludwieg. Tube wind tunnel: A special type of blowdown tunnel: Report presented at the 11th meeting of the wind tunnel and model testing panel, scheveningen, holland, 8-12 july 1957. AGARD, 1957.

[81] William C Starshak, Cameron Butler, and Stuart J Laurence. Method of characteristics design of high-temperature wind tunnel nozzles with vibrational relaxation. In *2018 Aerodynamic Measurement Technology and Ground Testing Conference*, page 3565, 2018.

[82] Hwa-Chi Wang and Walter John. Particle density correction for the aerodynamic particle sizer. *Aerosol Science and Technology*, 6(2):191–198, 1987.

[83] GM Faeth, L-P Hsiang, and P-K Wu. Structure and breakup properties of sprays. *International Journal of Multiphase Flow*, 21:99–127, 1995.

[84] L-P Hsiang and Gerard M Faeth. Near-limit drop deformation and secondary breakup. *International journal of multiphase flow*, 18(5):635–652, 1992.

[85] Eric Loth, John Tyler Daspit, Michael Jeong, Takayuki Nagata, and Taku Nonomura. Supersonic and hypersonic drag coefficients for a sphere. *AIAA journal*, 59(8):3261–3274, 2021.

[86] Narendra Singh, Michael Kroells, Chenxi Li, Eric Ching, Matthias Ihme, Christopher J Hogan, and Thomas E Schwartzentruber. General drag coefficient for flow over spherical particles. *AIAA journal*, 60(2):587–597, 2022.

[87] Alex B Liu, Daniel Mather, and Rolf D Reitz. Modeling the effects of drop drag and breakup on fuel sprays. *SAE Transactions*, pages 83–95, 1993.

[88] Frank M White. *Viscous fluid flow*, volume 1. McGraw-Hill New York, 1974.

[89] Andreas Schröder and Christian E Willert. *Particle image velocimetry: new developments and recent applications*. Springer Science & Business Media, 2008.

[90] W John and SM Wall. Aerosol testing techniques for size-selective samplers. *Journal of aerosol science*, 14(6):713–727, 1983.

[91] Christopher J Smith, Chase E Christen, Austin J Andrews, Bernard A Olson, and Christopher J Hogan Jr. A 3d-printed sheathed elutriator for size resolved collection of microparticles and droplets. *Journal of Aerosol Science*, 146:105569, 2020.

[92] Ralf Deiterding. Construction and application of an amr algorithm for distributed memory computers. In *Adaptive Mesh Refinement-Theory and Applications: Proceedings of the Chicago Workshop on Adaptive Mesh Refinement Methods, Sept. 3–5, 2003*, pages 361–372. Springer, 2005.

[93] Stuart J Laurence, Ralf Deiterding, and G Hornung. Proximal bodies in hypersonic flow. *Journal of Fluid Mechanics*, 590:209–237, 2007.

[94] Bruce G Batchelor. *Machine vision handbook*, volume 2. Springer, 2012.

[95] Wenbo Zhu and Stuart J Laurence. Application of regularization methods for recovering unsteady forces and moments from free-flight optical measurements in hypersonic impulse facilities. In *AIAA AVIATION 2023 Forum*, page 3710, 2023.

[96] Stuart J Laurence and HG Hornung. Image-based force and moment measurement in hypersonic facilities. *Experiments in Fluids*, 46:343–353, 2009.

[97] Stuart J Laurence and Sebastian Karl. An improved visualization-based force-measurement technique for short-duration hypersonic facilities. *Experiments in Fluids*, 48:949–965, 2010.

[98] Stuart J Laurence. On tracking the motion of rigid bodies through edge detection and least-squares fitting. *Experiments in Fluids*, 52(2):387–401, 2012.

[99] Stuart J Laurence, Nick J Parziale, and Ralf Deiterding. Dynamical separation of spherical bodies in supersonic flow. *Journal of Fluid Mechanics*, 713:159–182, 2012.

[100] Stuart Jon Laurence, CS Butler, J Martinez Schramm, and K Hannemann. Force and moment measurements on a free-flying capsule in a shock tunnel. *Journal of Spacecraft and Rockets*, 55(2):403–414, 2018.

[101] Thomas J Whalen and Stuart J Laurence. Experiments on the separation of sphere clusters in hypersonic flow. *Experiments in Fluids*, 62:1–19, 2021.

[102] Travis Duchene and Stuart Laurence. The aerodynamics of free-flying cylinders in high supersonic flow. In *AIAA AVIATION FORUM AND ASCEND 2024*, page 3923, 2024.

[103] John Canny. A computational approach to edge detection. *IEEE Transactions on pattern analysis and machine intelligence*, (6):679–698, 1986.

[104] Agustín Trujillo-Pino, Karl Krissian, Miguel Alemán-Flores, and Daniel Santana-Cedrés. Accurate subpixel edge location based on partial area effect. *Image and vision computing*, 31(1):72–90, 2013.

[105] Weixiao Liu, Yuwei Wu, Sipu Ruan, and Gregory S Chirikjian. Robust and accurate superquadric recovery: A probabilistic approach. In *Proceedings of the IEEE/CVF Conference on Computer Vision and Pattern Recognition*, pages 2676–2685, 2022.

[106] E Loth. Compressibility and rarefaction effects on drag of a spherical particle. *AIAA journal*, 46(9):2219–2228, 2008.

[107] W-H Chou and GM Faeth. Temporal properties of secondary drop breakup in the bag breakup regime. *International journal of multiphase flow*, 24(6):889–912, 1998.

[108] Peter Welch. The use of fast fourier transform for the estimation of power spectra: a method based on time averaging over short, modified periodograms. *IEEE Transactions on audio and electroacoustics*, 15(2):70–73, 1967.

[109] Gary S Settles and Matthew R Fulghum. The focusing laser differential interferometer, an instrument for localized turbulence measurements in refractive flows. *Journal of Fluids Engineering*, 138(10):101402, 2016.

[110] Byrenn Birch, David Buttsworth, and Fabian Zander. Measurements of freestream density fluctuations in a hypersonic wind tunnel. *Experiments in Fluids*, 61(7):158, 2020.